國立中央大學天文研究所
鹿林天文台年報

2009

No.7

國立中央大學天文研究所編

目錄

研究報告

Simultaneous observation of Be stars with strong infrared excess

Chien-De Lee, Wen-Ping Chen, Chien-Hui Kao and Li-Wen Hung

We just finished the first time successfully simultaneously observation by LOT's Hayoyu and slt's optical band to observe classical Be (CBe) stars at end of lulin 2009b. Besides, the Japan Okayama Astrophysical Observatory (OAO) had permitted the two runs for us to use their near-infrared camera. One of the run was at same time with my proposal of Lulin 2009b 1/29-1/30. We expected to gain simultaneous data of near-infrared, optical and spectral data. Two graduate students (Kao, Chien-Hui and Hung, Li-Wen) were trained to use spectroscopy in lulin and then I went to Japan for this observation. But the weather was not good at OAO, we did not gain the infrared data.

However, we collected a lot of good data from LOT and slt. 21 out of my total 25 CBe stars have at least twice observations in different day and most of them have simultaneous data with slt. Since there are a lot of spectra to analysis, I have constructed a pipeline to have a quick look for my database. Depend on this we found some CBe stars show quick variation within half hours.

We also had 2 runs in 2009a for CBe stars. The results published in poster of the 2010 Annual Meeting of Physical Society. Fig.1 shows the reduced spectra of CBe stars from different extend of near-infrared excess from LOT and Beijing Xinglong's 2.14m. The spectral characteristic of Hα and Hβ from Lulin's data is consistent with the spectra from Xinglong. Beside CBe stars with Hβ emission show larger near-infrared excess, on the other hand CBe stars with Hα absorption show weaker near-infrared excess (Fig 2).

Spectral Characteristics and NIR Excess

Fig. 1 shows some examples spectra taken with the Xinglong 2.16 m and the LOT. Fig. 2 show the NIR colors.

- CBe star with Hα in absorption have small NIR excess. HD 138749 is such an example *(J-H = 0, J-K = 0)* .
- CBe stars with Hβ in emission always have Hα also in emission, and have large NIR excess. An extreme case is MWC 623, which has very large NIR excess and Hα, Hβ, and Hγ all in emission.

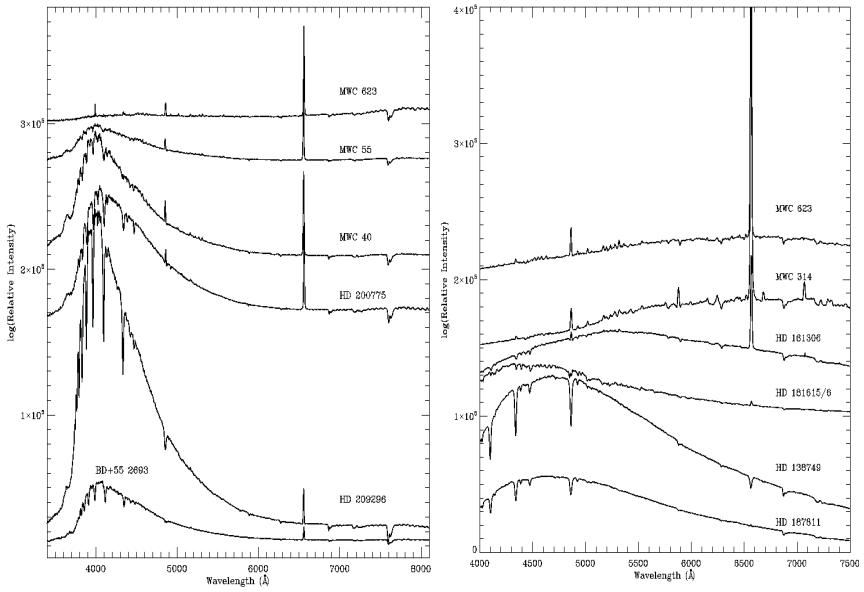

Fig. 1 --- Sample Spectra of CBe stars with different NIR excess. *All stars which Hβ emission, its Hα line also show emission.* ***Left:*** *CBe stars with moderate to large NIR excess (J-H > 0.3 J-K > 0.5) observed by Xinglong 2.16m.* ***Right:*** *CBe stars with small to large NIR excess observed by LOT.*

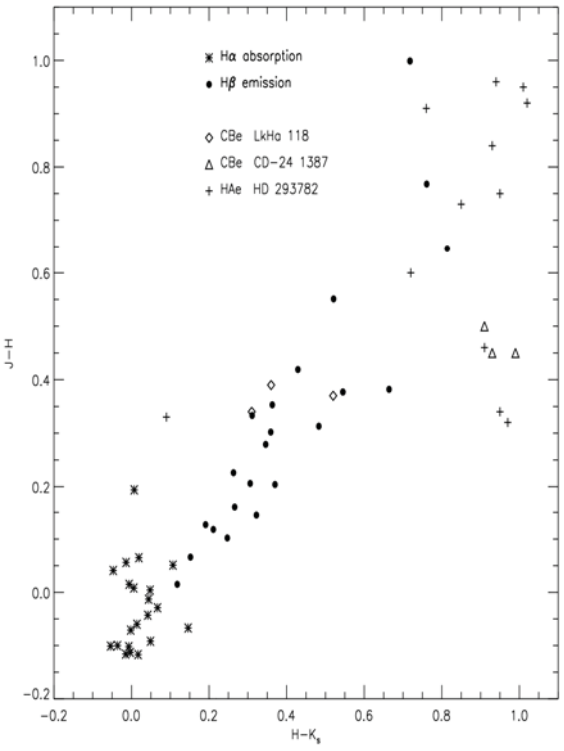

Fig. 2-- Left: *All CBe stars with Hβ in emission show Hα also in emission and large NIR excess. CBe stars that show Hα in absorption tend to have little NIR excess. Be stars are characterized by variable colors, e.g., LkHa 118, CD-24 1387 and the HAe star HD293782. Their spectra may be also highly variable.*

Reference

de Winter, D., et al. 2001, A&A, 380, 609s

The Astronomical Journal, 138:625–632, 2009 August doi:10.1088/0004-6256/138/2/625

THE OUTBURST OF COMET 17P/HOLMES

Zhong-Yi Lin[1,2], Chien-Shien Lin[2], Wing-Huen Ip[2], and Luisa M. Lara[1]
[1] Instituto de Astrofisica de Andalucia—CSIC, Camino Bajo de Huétor 50, 18008 Granada, Spain; zlin@iaa.csic.es
[2] Institute of Astronomy, National Central University, 300 Jungda Road, Jungli City, Taiwan
Received 2009 January 5; accepted 2009 May 17; published 2009 July 8

ABSTRACT

Comet 17P/Holmes had a massive outburst at approximately 2007 October 23.8 and its total brightness reached maximum (from $m = 17$ to $m = 2.5$) around 2007 October 25, about 1.7 days (42 hr) after the event. Following the first report of this extraordinary cometary outburst, comprehensive observations were obtained at the Lulin Observatory until early 2008 January by using broadband filters and narrowband cometary filters. The separation velocity, as projected on the plane of the sky, between the nucleus and the coma blob produced by the outburst has been estimated to be 0.132 ± 0.004 km s^{-1} from October 25.8 to November 1.6. The expansion speed, also projected on the plane of the sky of the dust shell has been found to be constant at a rate of approximately 0.554 ± 0.005 km s^{-1} from October 25.8 to November 1.6. The color on December 10 is slightly redder than that of the Sun. Our narrowband observations provide information on the production rates of gas species on October 31: log Q (CN) = 27.103 and log Q (C_2) = 27.349. The resulting abundance ratios show that the comet 17P can be classified as a "typical comet" in terms of composition.

Key words: comets: general – comets: individual (17P/Holmes)

Online-only material: color figures

1. INTRODUCTION

Comet 17P/Holmes is a periodic comet (orbital period of ∼6.88 years) and is one of the few Jupiter-family comets which have exhibited outbursts enhancing by several magnitudes the brightness of the coma, e.g., 41P/Tuttle–Giacobini–Kresák, 98P/Takamizawa, and 97P/Metcalf–Brewington (Miles 2007). It was first discovered by Edwin Holmes on 1892 November 6 just at the time as it was undergoing an outburst or sudden brightening. On 2007 October 23.8, around six months after the comet had passed its perihelion passage (T = 2007 May 4), the inconspicuous comet suddenly grew much brighter and underwent an outburst from a magnitude of about 17 to about 2.5 mag in just 42 hr (Colas & Lecacheux 2007; Arai et al. 2007). After the initial outburst, the comet brightened up by a million times, and the debris cloud around it grew in angular size to be as large as the planet Jupiter. Sekanina (2007) suggested that breakup of dust particles into small grains within 42 hr after the outburst would be able to explain why the brightness increased so steeply. The large amount of material emitted by comet 17P/Holmes formed an expanding coma over the next few months. Also a coma blob was observed to move away from the central nucleus in the southwesterly direction. The color is slightly bluish according to the measurements by Sostero (Colas & Lecacheux 2007) and the degree of polarization is −0.5% to −0.7% (Arai et al. 2007). The negative polarization at small phase angles (<20°) could be caused by the presence of aggregated dust grains (Petrova et al. 2001) in the coma after the outburst event on 2008 October 24.

In this paper, we describe the broadband and narrowband filter imaging observations of comet 17P/Holmes performed at Lulin Observatory, National Central University, between late 2007 October and early 2008 January. An overview of the observations is presented in Table 1. The photometric nights on October 31 and December 10 were used for determining the Afρ parameter and the gas production rates of CN and C_2 molecules. The observations and their reduction are described in Section 2. In Section 3, we present the morphological evolution of the expanding structure and estimate the corresponding expansion velocity projected on the plane of the sky. In Section 4, we estimate the dust and gas production rates and in Section 5, we study the coma morphology, discuss the implications, and we summarize our results.

2. OBSERVATIONS AND DATA ANALYSIS

The observations were obtained by using the 1 m telescope of the Lulin Observatory, National Central University, Taiwan. The time of our observations began on October 24.5 about 10 hr after the initial outburst reported by Santana (2007). The observations were done by using broadband *R* filter (two different filter systems, Bessel (644/128 nm) and Asahi (674.5/128.5 nm), were used during these observations) and the ESA Rosetta comet filters (CN (387/6 nm), C_2 (514/12 nm), blue continuum (445/4 nm), BC, and red continuum (687.4/6 nm), RC) whose detailed description can be found in Lin et al. (2007b). A PI1300B 1340 × 1300 CCD camera with an effective pixel scale of 0.″515 pixel^{-1} (Kinoshita et al. 2005) was used.

The images' data reduction followed standard procedures. In outline, the procedure began with bias and dark current subtraction and flat-field correction of all frames. Then the night sky contribution was subtracted making use of sky images obtained close to the comet location but far enough away not to contain gas coma emission. The atmospheric extinction in broadband images was corrected by observing Landolt standard stars (1992) at different air masses during the night. Spectrophotometric standard stars, Hz4, GD50, and GD108 selected from the list presented by Oke (1990) were observed in photometric nights and used to convert the measured counting rates into physical units (more details can be seen in Lin et al., 2007b).

3. MORPHOLOGICAL STUDY

After the outburst of comet 17P/Holmes on UT October 23.8 (Hsieh et al. 2007), a series of broadband images in *R*, starting from 2007 October 24 to 2008 January 4, were taken in

Table 1
The Log of Observations of Comet 17P/Holmes at Lulin Observatory

Date	Δ (AU)	r_h (AU)	Pixel Size (km)	P.A. (deg.)	S-T-O (deg.)	Filters
2007 Oct 24	1.636	2.438	611.0695	42.979	16.9	R_1
2007 Oct 25	1.633	2.442	609.9489	41.693	16.6	R_1
2007 Oct 26	1.631	2.446	609.2018	40.365	16.4	R_1
2007 Oct 27	1.629	2.45	608.4541	38.993	16.1	R_1
2007 Oct 28	1.627	2.454	607.7077	37.578	15.9	R_1
2007 Oct 29	1.626	2.458	607.3342	36.116	15.6	R_1
2007 Oct 30	1.624	2.462	606.5871	34.608	15.3	R_1
2007 Oct 31	1.623	2.465	606.2132	33.051	15.1	R_1, N
2007 Nov 1	1.622	2.469	605.8403	31.445	14.8	R_1
2007 Nov 12	1.625	2.513	606.9605	9.898	12.4	R_2
2007 Nov 15	1.63	2.525	608.8279	2.993	11.9	R_2
2007 Nov 16	1.633	2.529	609.9484	0.601	11.8	R_2
2007 Nov 17	1.636	2.533	611.0689	358.169	11.7	R_2
2007 Nov 18	1.638	2.537	611.8160	355.738	11.6	R_2
2007 Nov 19	1.641	2.541	612.9365	353.277	11.5	R_2
2007 Dec 9	1.750	2.622	653.6496	305.825	12.2	R_2
2007 Dec 10	1.758	2.626	656.6377	303.906	12.4	R_2, N
2007 Dec 22	1.871	2.677	698.8447	285.351	14.4	R_2
2008 Jan 1	1.987	2.720	742.1274	275.135	16.2	R_2
2008 Jan 4	2.024	2.732	755.9925	272.810	16.7	R_2

Note : Δ and r_h are the geocentric and heliocentric distances in AU, respectively; P.A. is the position angle of the projected solar direction measured from N towards E, and S-T-O is the Sun-Target-Observer (i.e. phase angle). R_1 is for Bessel broadband filter (644/128 nm), R_2 is for Asahi broadband filter (674.5/128.5 nm) and N is for narrowband cometary filters including CN (387/6 nm), C_2 (514/12 nm), blue continuum BC (445/4 nm) and red continuum RC (687.4/6 nm).

order to follow the morphological evolution of the inner coma. Figure 1 displays a $11' \times 11'$ region of the full frame to study the inner coma of comet 17P/Holmes. On October 24.5, comet 17P/Holmes was a very sizable fuzzy spot, with a bright, hazy nucleus. The circular coma had a sharp edge indicating the abrupt nature of the outburst. In the following days, the bright circular coma becomes larger but no longer as sharply edged as before. The optical center of the extended coma was slightly offset from the assumed nucleus position. With longer exposures the edge of the coma was better defined, allowing us to measure its growth rate. The expansion of the outer edges of the dust coma could be characterized by a constant expansion rate with a projected velocity of 0.554 ± 0.005 km s^{-1} in the radial direction during the time interval between October 25.8 (outer edge at $\rho \sim 6 \times 10^4$ km) and 2007 November 1.6 (outer edge at $\rho \sim 4 \times 10^5$ km). This value is slightly lower than the value of 0.575 km s^{-1} obtained by Colas & Lecacheux (2007) but bracketed by the value of $0.4 \sim 0.6$ km s^{-1} by Snodgrass et al. (2008). The coma diameter on October 30 was nearly the same as the field of view (FOV; 11 arcmin). The noncircularity of the coma became evident as the so-called coma blob moved farther and farther away from the optocenter (i.e., from the nucleus).

A profile cut through the bright circular coma in the Sun-tail direction on October 25.8, shows a brightness asymmetry that is not obvious to the eye (see Figure 2(a)). At the image scale of ∼0.515 arcsec/pixel, the central nuclear region was quite concentrated. The shell-like feature appeared as a bright area offset from the nucleus. The brightness of the inner coma declined more rapidly on the sunward direction than on the tailward direction, apparently because of the solar radiation pressure effect. On the other hand, the profile through the nucleus perpendicular to the Sun-tail axis is nearly symmetrical (see Figure 2(b)). Figure 3 shows log B versus log ρ in the Sun-tail direction and perpendicular to it for the RC images acquired on October 31.7 (right panel) and December 10 (right panel). For long-lived grains expanding isotropically in the cometary coma, the slope of the log B versus log ρ should be around −1. For the case presented here related to October 31, the fits obtained in the range $2500 < \rho < 10{,}000$; $2500 < \rho < 20{,}000$; and $2500 < \rho < 40{,}000$ km are lying between −0.32 and −0.62 in the Sun-tail direction, whereas for the direction perpendicular to it, these values range from −0.47 to −0.60. This clear deviation from a linear fit of slope ∼−1 indicates that either the grains in the coma are not long-lived, that is, they are suffering fragmentation (and thus changing their size) or loosing the volatiles in them, or that the expansion is not isotropic. However, on December 10, the slopes of the log B versus log ρ fits fall in the range −0.78 to −1.18 which is roughly consistent with a ρ^{-1} law for the decrease of the surface brightness profiles as a function of the projected nuclear distance, ρ, in log–log scale.

The outer edge of the shell-like structure and the central condensation can be clearly shown by a simple azimuthally median subtraction routine that enhances any deviation from an isotropic coma. At the same time, the Larson–Sekanina algorithm can be used to bring out the fine structures in the inner coma of comet 17P/Holmes. Figure 4 displays some of the observed comet images (left panels) and the processed ones by the radial renormalization technique (central panels) and by the Larson–Sekanina algorithm (right panels). The images obtained by using the azimuthally median subtraction routine show clearly the evolution of the global structures, especially the elongated features, over several days (October 24 to 31). The ejecta-like feature which appeared on October 24.8 subsequently transformed itself into an extended coma blob with a southwesterly orientation. Its origin can be partly revealed by examining the right-hand side images in Figure 4. On October 24.5, a system of highly collimated dust structures emerged in the position angle between 175° and 185°. This bundle of filamentary structures could very well be the source of the extended coma blob, which moved into P.A. of 210°–220°

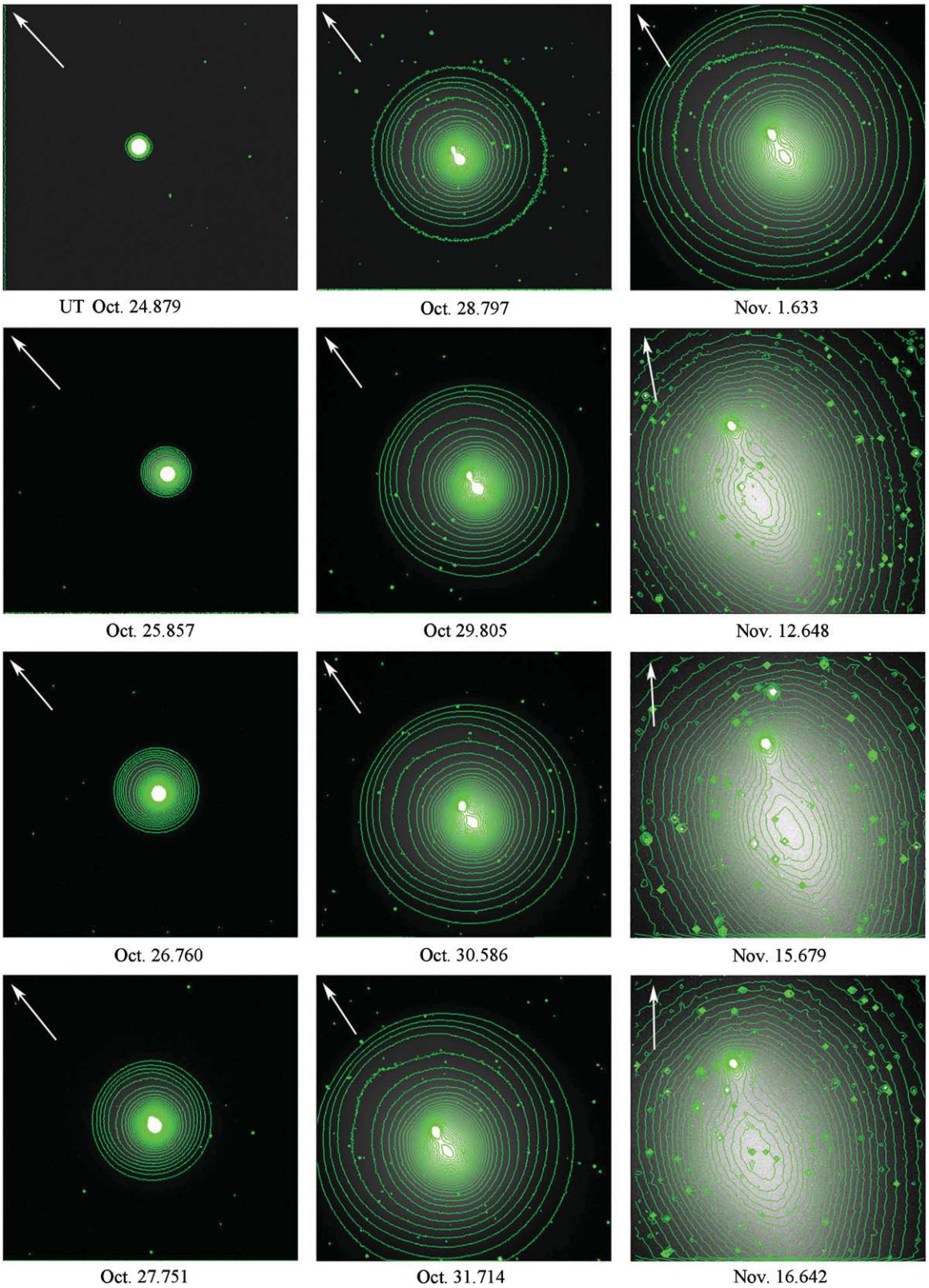

Figure 1. Snapshot of broadband *R* images taken with the Lulin Optical Telescope at the Lulin National Observatory in Taiwan, from October 24 to November 16 showing the time evolution of comet 17P/Holmes. At the very beginning of the observations, comet 17P/Holmes appeared as a very sizable bright fuzz spot. It then progressively expanded and grew in the following days. As shown in the contour plots, the shell-like structure and the coma blob moving away from the central nucleus. In the figure, north is to the top and east is to the left. The arrows indicate the solar direction and the FOV in all images is 11 arcmin × 11 arcmin.
(A color version of this figure is available in the online journal.)

two days later. This coma blob continued to expand and moved away from the comet nucleus with a constant projected speed of 0.132 ± 0.004 km s^{-1} (moving from $\rho \sim 7000$ km on October 25.8 to $\rho \sim 84000$ km on November 1.6). The value derived in

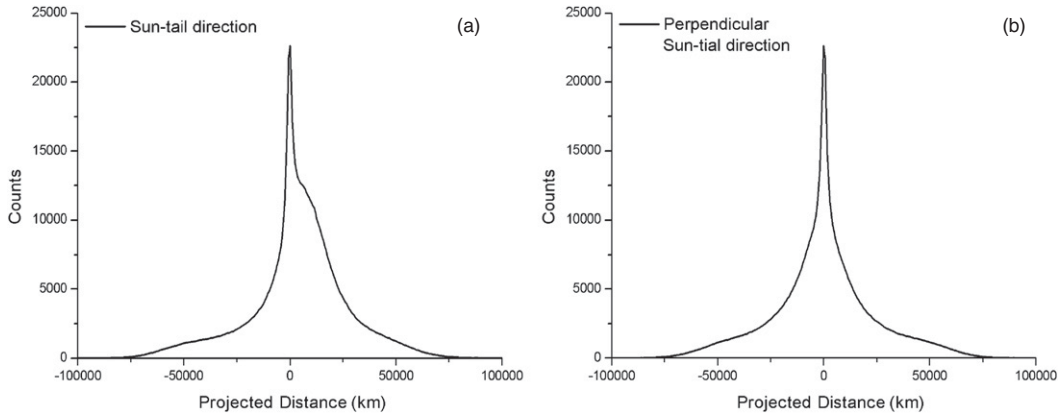

Figure 2. Two profiles cut along the Sun-comet line (a) and perpendicular to the Sun-comet line (b) on 2007 October 25. Note that the asymmetric profile in (a) was caused by the solar radiation pressure effect and the presence of the coma blob. The profile (b) in the perpendicular direction is symmetrical. In the figures, positive distance is counted toward the projected anti-solar direction, negative in the solar direction.

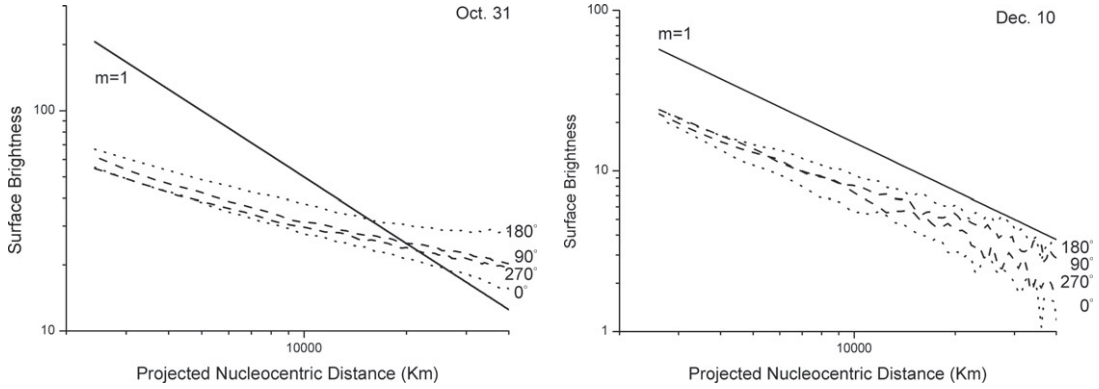

Figure 3. Surface brightness profiles of 17P/Holmes in RC filter on October 31 and December 10. The profiles were obtained from cuts along the Sun-tail direction (dot lines) and perpendicular to Sun-tail direction (dash lines). Dot lines represent the observed profiles measured from the position angle starts from sunward (0°) to tailward (180°) in steps of 90°. The surface brightness, B, is plotted against the projected radius, ρ in double logarithmic representation. The best linear fits verifying $\frac{\mathrm{d(logB)}}{\mathrm{d(log}\rho} = -m$ at $\log \rho \geqslant 3.3$ are $0.32 \sim 0.62$ and $0.78 \sim 1.18$ on October 31 and December 10, respectively.

this work is very close to the measurements in Montalto et al. (2008) who reported 0.135 km s^{-1} .

4. PHOTOMETRIC RESULTS

4.1 Dust Production Rates

To characterize the dust activity of a comet it has become customary to make use of the Afρ parameter introduced by A'Hearn et al. (1984). It is defined as the product of albedo (A), the filling factor of the grains in the FOV (f) within an aperture of projected radius ρ, and the projected radius ρ. It is computed as follows

$$Af\rho \frac{(2r\Delta)^2}{\rho} \frac{F_{\mathrm{com}}}{F_{\mathrm{sun}}}. \quad (1)$$

Here, r [AU] is the comet's heliocentric distance, Δ[cm] is the comet's geocentric distance, ρ [cm] is the aperture radius at the comet distance, F_{com} [erg cm^{-2} s^{-1}] is the measured cometary flux in a continuum filter, and F_{sun}[erg cm^{-2} s^{-1}] is the solar flux at 1 AU. The solar flux was computed by using a high-resolution solar spectrum (Kurucz et al. 1984) convolved with the continuum filter transmission curve. Afρ is related to a stationary model, which assumes that the dust particles are emitted isotropically from the nucleus and move radially outward with a constant velocity in the inner coma. According to this model the dust column density varies as ρ^{-1} and Afρ becomes independent of ρ at large projected cometocentric distances. During the photometric nights on October 31 and December 10, we determined Afρ at three different apertures: 10,000; 20,000; and 40,000 km. The results are listed in Table 2 for the BC and RC filters.

We can also estimate the dust production by using the images acquired with the *R* broadband filter. The filter bandpass mostly covers solar light reflected by the dust grains in the coma and little gas emission (the most important being H_2O^+). The comet was observed with *R* broadband filters (Bessel and Asahi filters) during photometric and non-fully photometric nights. Therefore, the Afρ computed for those nights has to be cautiously considered. To flux-calibrate the images obtained with the *R* broadband filter in non-fully photometric nights, we adopted the following procedure: (1) we observed photometric Landolt stars at different air masses during the night, (2) we compared the atmospheric extinction in those non-fully photometric nights with the one in photometric nights (when also Landolt photometric stars were observed), and (3) under the similar air mass condition, we applied the following formula to compensate for this loss of brightness due to non-fully photometric conditions

$$DN_{np} = \frac{DN_p}{10^{((\Delta Z+\Delta M+\Delta k)/2.5)}}, \quad (2)$$

where the p and np subscript refer to photometric and non-photometric conditions, DN is the measured count rates, ΔZ is

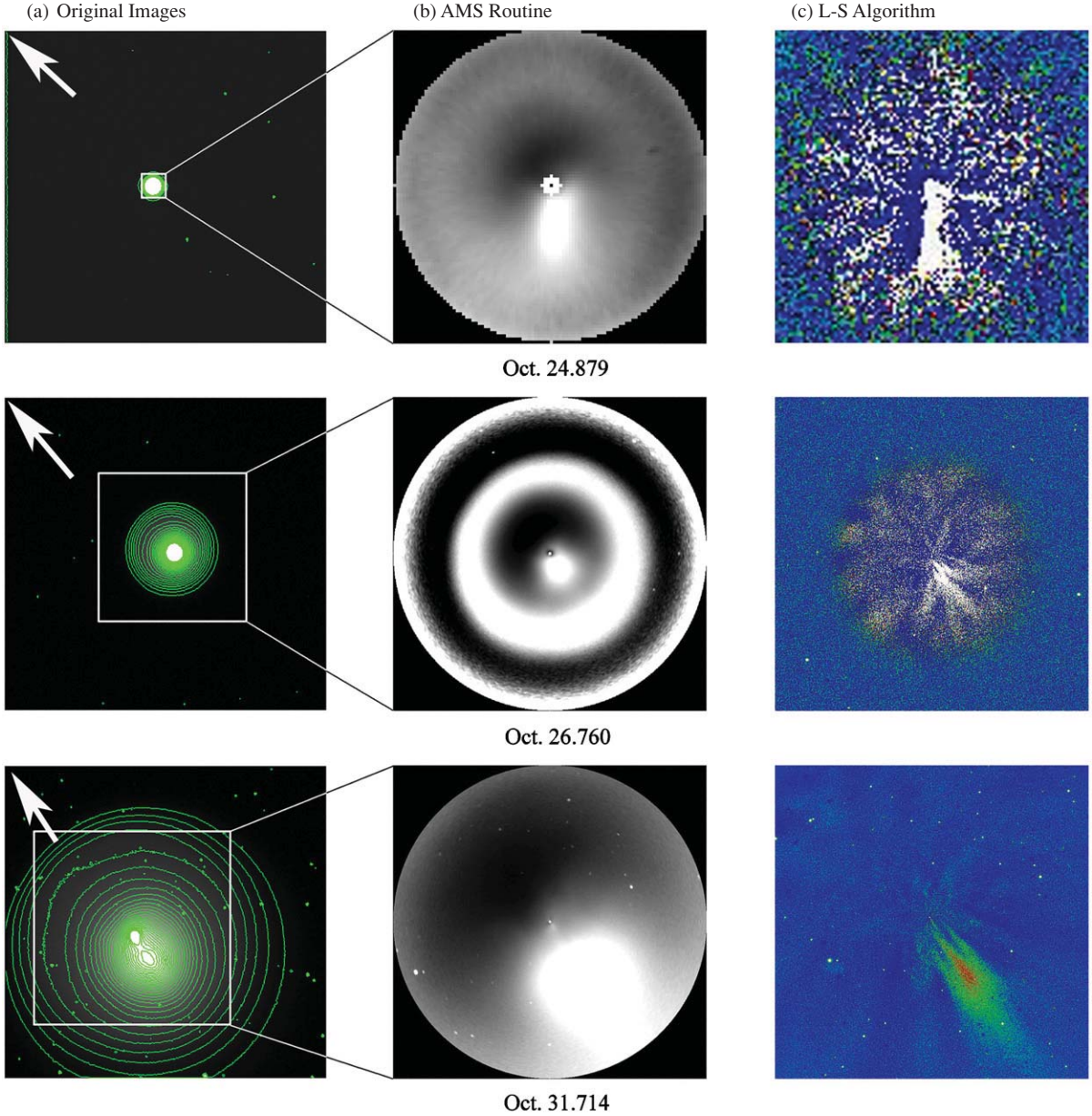

Figure 4. Comparison of the morphological structures on three different times (October 24.879, 26.760, 31.714) obtained by using two different image processing methods. (a) Left-hand side figures: the original broadband *R* images; (b) Middle figures: the azimuthally median subtraction routine; (c) Right-hand side figures: the Larson–Sekanina algorithm. In the figures, North is to the top and East is to the left. The arrows indicate the solar direction. The FOV of the left and right images is 11 arcmin × 11 arcmin.

(A color version of this figure is available in the online journal.)

Table 2
Dust Production Rate (Afρ) and the Normalized Dust Reddening (i.e., Dust Color)

Date	Filter	Δ (AU)	r_h (AU)	Solar Flux (erg cm^{-2} s^{-1})	log(Afρ) (cm)		
					10^4 km	2×10^4 km	4×10^4 km
Oct 31	BC	1.623	2.465	3577.88	4.490	4.682	4.848
	RC	1.623	2.465	8400.38	4.519	4.689	4.854
	Color% per 100 nm				2.76 ± 0.90	0.74 ± 0.92	0.61 ± 0.91
Dec 10	BC	1.758	2.626	3577.88	2.839	2.932	2.968
	RC	1.758	2.626	8400.38	2.883	2.996	3.060
	Color% per 100 nm				4.19 ± 0.89	6.05 ± 0.87	8.70 ± 0.85

the difference in zero point measured at photometric and non-photometric nights $Z_{np} - Z_n$, ΔM is the different instrument magnitude $M_p - M_{np}$, and Δk is the difference in atmospheric extinction $k_p - k_{np}$.

Using this procedure and comparing the Afρ obtained with the broadband filters and the continuum cometary filters for the photometric nights, we found out that the R Bessel and Asahi broadband filters do certainly contain a non-negligible

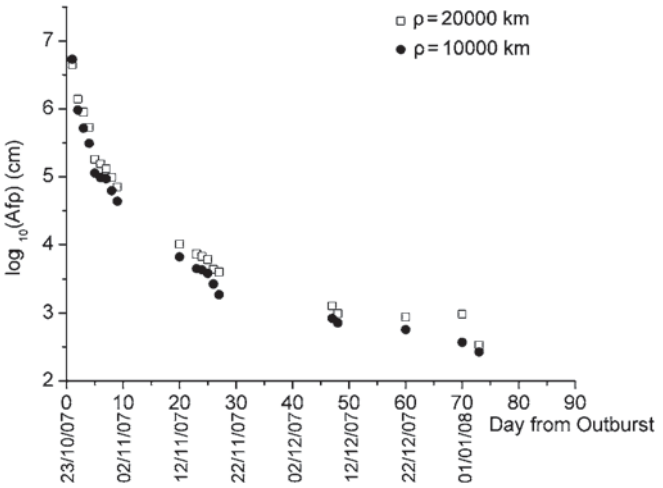

Figure 5. Up-limit Afρ values within an aperture of radius ρ = 20,000 km (open squares) and ρ = 10,000 km (filled circles) for the comet 17P/Holmes from 2007 October 24.8 to 2008 January 4.7. The Afρ measured from the outburst date to the end of November decreased much faster (∼25 times) than that measured after December. The value measured on 2008 January 1 in an aperture of ρ = 20,000 km is higher than that measured on 2007 December 22 due to the presence of a bright star in the considered aperture.

gas emission compared with RC filter on October 31 (as much as 40% of the energy flux measured is due to gas emission of H_2O^+ line and NH_2 bands) and much less on December 10 (∼1%). We therefore show here the upper limit value of dust production rate and plot the evolution of the Afρ parameter since the day of 2007 October 24 (17 hr after the outburst) to 2008 January 4 in Figure 5.

4.2 Dust Colors

The derived Afρ values in the BC and RC filters allow for the determination of the dust color of the cometary dust. The normalized dust reddening, in %/100 nm (Jewitt & Meech 1986) between 445 nm and 687.4 nm (central wavelengths of the BC and RC filters) is computed as (Bonev et al. 2002),

$$color = \frac{Af\rho_{687} - Af\rho_{445}}{\lambda_1 - \lambda_2} \times \frac{2000}{Af\rho_{687} + Af\rho_{445}} \qquad (3)$$

where Afρ_{687} and Afρ_{445} are the Afρ values derived from the comet observations with the BC and RC filters (wavelength 687.4 nm (λ_1) and 445 nm (λ_2), respectively. Table 2 shows the normalized dust reddening on October 31 and December 10 for three aperture radius of 10,000; 20,000; and 40,000 km. On October 31, we notice that the dust reddening decreases with increasing ρ, meaning that the optical properties of the dust grains vary as the grains expand in the coma; in fact the dust grains are getting bluer at larger cometocentric distances. The rapid increase of the coma brightness after the outburst might have been caused by the ongoing fragmentation of large dust grains ($\geqslant$0.9 μm) into smaller and smaller grains thus enhancing the cross sectional area and increasing the intensity detected at shorter wavelengths as a function of ρ (Lara et al. 2001). Therefore, this decrease of the dust reddening at large ρ might be an indirect evidence of the injection of submicrometer dust grains via fragmentation of large grains emitted during the outburst. On the other hand, on December 10, the behavior is reversed and the average dust reddening increases with ρ. According to Storrs et al. (1992), large grains would produce a redder spectrum than smaller ones, thus on December 10, the average size of the dust grains in the coma of comet 17P/Holmes was larger than on October 31.

4.3 Gas Production Rates

To obtain the pure gas emission profiles from the images acquired with the CN and C_2 cometary filters, it is necessary to subtract the contribution of the underlying continuum and the way to get the continuum contribution in the gas filter can be found in detail in Lin et al. (2007b). The CN acquired images have 28% contribution of continuum in the blue range, whereas the C_2 acquired images contain 86% of the blue continuum. Therefore, the gas (CN and C_2) comet images result from the subtraction of the images acquired with the cometary filters and the BC continuum images multiplied by the above-mentioned values ($CN = CN_{obs} - 0.28\ BC_{obs}$, $C_2 = C_2{}^{obs} - 0.86\ BC_{obs}$). Figure 6 shows the CN and C_2 spatial profiles along the Sun-tail before and after the subtraction of the underlying continuum. It is worthy to note that the CN profile shown in Figure 6(a) is relatively symmetric with respect to the optocenter indicating mostly a steady nuclear source of the gas coma. On the other hand, the C_2 profile (seen in Figure 6(b)) has a certain close resemblance to the dust continuum profile in the tailward direction. This could mean that in addition to the nuclear source, C_2 is also produced by the dust in the coma blob. Let us note that C_2 has been long proposed to be formed by two photolytic processes in the gas coma and that no clear gas species has been proposed as the parent species of each of those photolytic processes, not ruling out the refractory material (i.e., the dust) as a likely C_2 source.

In order to determine the gas production rates, the mean radial emission profiles of CN and C_2 have been derived from the images obtained in the corresponding filters. As we are going to determine the gas production rates through the Haser model (Haser 1957) which is only applicable for steady state conditions of comet activity, we have decided to use the average radial brightness profiles CN and C_2, which are at $\pm 45^\circ$ from the sunward direction avoiding the gas+dust blob in the tailward direction. For the conversion of energy flux into column density profiles, the fluorescence efficiency factors (g-factors) of CN (4.2×10^{-13} erg molecule^{-1} s^{-1}, according to Schleicher 1983), and C_2 (4.5×10^{-13} erg molecule^{-1} s^{-1} from and A'Hearn et al., 1995) were used. In the calculations, we have assumed that the g-factors varied with the heliocentric distance r (AU) as $g = g_0\ r^{-2}$ and the gas outflow velocity $V_{gas} = 0.85\ r^{-0.5}$ km s^{-1} (Fray et al. 2005; Tseng et al. 2007).

The column density radial profiles of CN and C_2 profiles were then compared with the theoretical curves of the Haser model (Haser 1957), which describes the isotropic emission of cometary neutral parent molecules and their daughter molecules and radicals. From a best fit of the model output to the observational data, the scale lengths of the parent molecules (l_p) and the daughter molecules (l_d) can be estimated. These quantities determine the shapes of the radial brightness profiles; our best fits provide $l_p = 1.5 \times 10^4$ and $l_d = 1.0 \times 10^5$ for CN and $l_p = 4.2 \times 10^4$ and $l_d = 1.2 \times 10^5$ for C_2. In the case of CN, the parent and daughter scale lengths are similar to the ones commonly used and listed in A'Hearn et al. (1995). However, the C_2 l_p and l_d derived in this work are larger in a factor of 2 than the ones in A'Hearn et al. (1995) likely pointing to the fact that 1-step photolytic model is not the most appropriate to describe the C_2 behaviour in the coma of 17P/Holmes. Making use of the values obtained in this work, the corresponding CN and C_2 production rates (Q) on October 31 are 1.27×10^{27} and

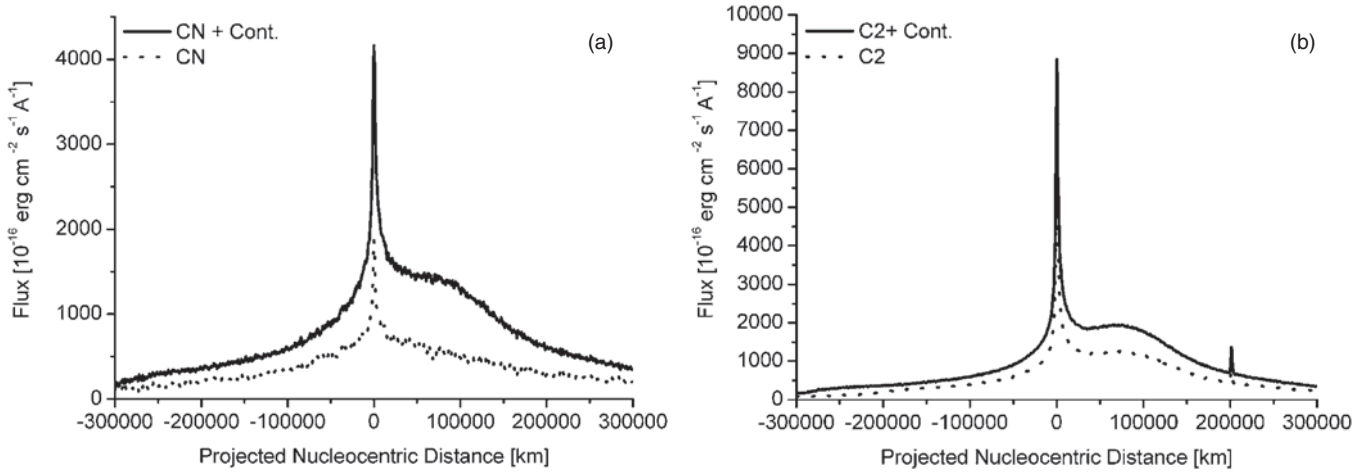

Figure 6. CN (a) and C_2 (b) flux profiles on October 31.7 along the Sun-comet direction. The solid lines show the profiles of CN and C_2 before subtracting the underlying continuum. The dot lines show the CN and C_2 clear gas radial profiles. Positive distance is counted towards the projected anti-solar direction, negative in the solar direction.

2.23×10^{27} s^{-1}, respectively. Therefore, comet 17P/Holmes can be classified as typical in terms of composition according to the classification introduced by A'Hearn et al. (1995), log [Q(CN)/Q(C_2)] being 0.0246, which is in the range of −0.09 to 0.29. For consistency and to ease the comparison with other works which use the scale lengths in A'Hearn et al. (1995), Q (CN) and Q (C_2) turn out to be 1.46×10^{27} and 2.33×10^{27} when (l_p, l_d) are (1.3×10^4, 2.2×10^5) and (2.2×10^4, 6.6×10^4) for CN and C_2, respectively.

It is possible to compare this gas activity with the one shown by very active new comets as C/1995 O1 Hale–Bopp (Rauer et al. 2003); C/1996 B2 Hyakutake (Schleicher & Osip 2002); C/2001 A2 (LINEAR) and C/2004 Q2 (Machholz; see Lin et al. (2007a, 2007b)). For this comparison to be coherent we have to consider Qs at the same heliocentric distance r_h if data are available, or to scale all the available Qs to the same r_h. Although not strictly accurate, when no production rate is available, we have assumed that Q varies as $1/r_h^2$. Bearing all this in mind, we can conclude that comet 17P/Holmes, a Jupiter-family comet, showed an incredibly high activity on 2007 October 31 when it was at 2.465 AU from the Sun. More concisely, focusing on the CN production rates (which can be approximately related to OH and thus to H_2O activity, see A'Hearn et al. 1995), on 2008 October 31 comet 17P/Holmes was a factor of ∼2 more active than C/1995 O1 (Hale–Bopp) and C/2004 Q2 (Machholz), and a factor of ∼4 if compared to C/1996 B2.

5. DISCUSSION AND SUMMARY

In the history of comet observations, only one comet, comet 1P/Halley, underwent a supermassive outburst at a heliocentric distance of 1.44 AU (1 AU closer than 17P) in 1836 January (ICQ 30, Sekanina, Z., 2008). The large increase of optical brightness of 17P/Holmes may have been caused by an impact with a small object capable of punching through the surface crust of nonvolatile material as what had been proposed for its outburst in 1892 (Roberts 1982). The probability of such interplanetary collision is of course very low. The repetition of the outburst event in 2007 led us to consider other possibilities.

One possibility is a fragmentation event like the one suffered by the nucleus of the B component of a 73P/Schwassmann–Wachmann 3 in 2006 (Bertini et al. 2009; Vincent et al. 2008). If this had happened, there should be big fragments trailing the comet nucleus (Bonev et al. 2008). The *Hubble Space Telescope* (*HST*) images, however, do not show any large fragments near the nucleus of comet 17P/Holmes (Weaver et al. 2007). Therefore, this hypothesis must be ruled out.

Another possibility could be that the material eruption was the result of the collapse of a part of the surface of the comet nucleus (Sekanina 2007; Thomas et al. 2007; Belton et al. 2007). Comets have been described as dirty snowballs (Whipple 1950) and comet 17P/Holmes may well have a weak chambered honeycomb structure or a porous internal structure, which had caved in to release the dust and gas cloud around it. Hence, if the upper portion of the nucleus of comet 17P/Holmes happens to have a Swiss cheese-like (or honeycomb) structure with pockets of volatile ice contained in insulating chamber walls made up of fluffy dust, it is a matter of heat transport and material mechanics that individual chamber walls will collapse one after the other thus igniting the eruption event like a firework, but in delayed action. Under this assumption, the high production rates of CN and C_2 molecules as estimated here might possibly be explained. It is clear that the outburst phenomenon of comet 17P/Holmes was extremely interesting but equally enigmatic. We will continue to compare our results with other measurements aiming at obtaining an in-depth understanding of this most unexpected comet explosive event. As a starting point of this further investigation, we believe that (1) the explosion of a highly volatile region should have introduced some anisotropic pattern of dust ejection and (2) a transient outgassing of the whole nucleus should have led to a more isotropic formation of the dust coma. The observations show that the expansion of the dust shell was rather uniform favoring option (2). However, only if the explosion of a highly volatile region occurred such that the emission cone of the dust were facing toward Earth, would it be possible to reconcile the local explosion with the observations then leaving option (1) as the one responsible for the observed coma morphology.

As a summary, the main results from the analysis of the images of comet 17P/Holmes acquired at the Lulin National Observatory in Taiwan can be summarized as follows:

1. After the outburst event on 2007 October 24.8, a number of dust jets emanating from the comet nucleus were found in our time-serious images at P.A. of 175° to 185°. They seem to be sensitive to the solar radiation pressure since they are placed at position angles close to the tail one day later.

2. The expansion of the dust coma generated by the outburst has a constant speed of 0.554 $\pm$ 0.005 km s^{-1} .
3. The separation-projected velocity of the coma blob (produced by the outburst) from the comet nucleus is 0.132 $\pm$ 0.004 km s^{-1}.
4. The average Afρ values at wavelengths of λ_{bc} = 445 nm and λ_{rc} = 687.4 nm are log[Afρ]$_{bc}$ = 4.673 and log [Afρ]$_{rc}$ = 4.687 on October 31 and log[Afρ]$_{bc}$ = 2.913 and log [Afρ]$_{rc}$ = 2.980 on December 10. The dust color on October 31 and December 10 show clear variation with ρ from 10,000 to 40,000 km as measured in the wavelength interval (445 nm, 687.4 nm). These variations are characterized by an obvious bluing on October 31, whereas the behavior is reversed on December 10 (i.e., reddening with increasing projected cometocentric distance).
5. The CN and C_2 Haser production rates determined on October 31 at heliocentric distances 2.465 AU are log Q (CN) = 27.103 $\pm$ 0.054; log Q (C2) = 27.349 $\pm$ 0.057, respectively. Such high gas production rates could be the result of the explosion of a highly volatile region on the surface of comet 17P/Holmes or to a transient outgassing event of the whole nucleus.

This work was based on observations obtained at Lulin Observatory, Taiwan. We thank the staff members and Wen-Sun Hsiao, Ting-Wan Chen, and Yu-Chi Cheng for assistance in the observations. The research carried out was supported by NSC97–2811-M-008–038, NSC97–2112-M-008–011-MY3, and the MoE Grant "Aim for the Top University" of National Central University. Zhong-Yi Lin acknowledges a post-doctoral grant awarded by the Junta de Andalucía through the project P07-TIC-2744. Part of this work has been funded by Ministerio de Ciencia e Innovación through the project ESP2006–02934.

REFERENCES

A'Hearn, M. F., Millis, R. L., Schleicher, D. G., Osip, D. J., & Birch, P. V. 1995, Icarus, 118, 223
A'Hearn, M. F., Schleicher, D. G., Millis, R. L., Feldman, P. D., & Thompson, D. T. 1984, AJ, 89, 579
Arai, et al. 2007, CBETs, 1118
Belton, M. J., et al. 2007, Icarus, 187, 332
Bertini, I., Lara, L. M., Vincent, J.-B., Boehnhardt, H., Küppers, M., & Rodrigo, R. 2009, A&A, 496, 235
Bonev, T., Boehnhardt, H., & Borisov, G. 2008, A&A, 480, 277
Bonev, T., Jockers, K., Petrova, E., Delva, M., Borisov, G., & Ivanova, A. 2002, Icarus, 160, 419
Colas, F., & Lecacheux, J. 2007, CBETs, 1111
Fray, N., Bénilan, Y., Cottin, H., Gazeau, M.-C., & Crovisier, J. 2005, Planet. Space Sci., 53, 1243
Jewitt, D., & Meech, K. J. 1986, ApJ, 310, 937
Haser, L. 1957, Bull. Acad. R. Sci. Leige, 43, 740
Hsieh, H. H., Fitzsimmons, A., & Pollcco, D. L. 2007, IAU Circ., 8897
Kinoshita, D., Chen, C. W., Lin, H. C., Lin, Z. Y., Huang, K. Y., Chang, Y., & Chen, W. P. 2005, Chin. J. Astron. Astrophys., 5, L315
Kurucz, R. L., Furenlid, I., Brault, J., & Testerman, L. 1984, Solar Flux Atlas from 296 to 1300 nm (Sunspot, NM: National Solar Observatory)
Landolt, A. U. 1992, AJ, 104, 340
Lara, L. M., Schulz, R., Stüwe, J. A., & Tozzi, G. P. 2001, Icarus, 150, 124
Lin, Z. Y., Chang, C. P., & Ip, W. H. 2007a, AJ, 133, 1861
Lin, Z. Y., Weiler, M., Rauer, H., & Ip, W. H. 2007b, A&A, 469, 771
Miles, R. 2007, arXiv:0712.3314
Montalto, M., Riffeser, A., Hopp, U., Wilke, S., & Carraro, G. 2008, A&A,
Oke, J. B. 1990, AJ, 99, 1621
Petrova, E. V., Jockers, K., & Kiselev, N. N. 2001, Sol. Syst. Res., 35, 429
Rauer, H., et al. 2003, A&A, 397, 1109
Roberts, I. 1982, MNRAS, 53, 65
Santana, A. H. 2007, IAU Circ., 8886
Schleicher, D. G. 1983, PhD thesis, Univ. Maryland
Schleicher, D. G., & Osip, D. J. 2002, Icarus, 159, 210
Sekanina, Z. 2007, CBET, 1118
Sekanina, Z. 2008, International Comet Quarterly, 63
Snodgrass, C., Fitzsimmons, A., Boehnhardt, H., & Lister, T. 2008, Asteroids, Comets and Meteors, 8278
Storrs, Alex D., Cochran, Anita L., & Barker, Edwin S. 1992, Icarus, 98, 163
Thomas, P. C., et al. 2007, Icarus, 187, 4
Tseng, W. L., Bockelée-Morvan, D., Crovisier, J., Colom, P., & Ip, W. H. 2007, A&A, 467, 729
Vincent, J.-B., Böhnhardt, H., Lara, L. M., & Bertini, I. 2008, Asteroids, Comets, Meteors, 1405, 8022
Weaver, H. 2007, HST Proposal ID #11418. Cycle 16
Whipple, F. L. 1950, ApJ, 111, 375

Mon. Not. R. Astron. Soc. **395,** 1941–1949 (2009) doi:10.1111/j.1365-2966.2009.14729.x

Evidence for energy injection and a fine-tuned central engine at optical wavelengths in GRB 070419A

A. Melandri,[1⋆] C. Guidorzi,[1,2,3] S. Kobayashi,[1] D. Bersier,[1] C. G. Mundell,[1] P. Milne,[4] A. Pozanenko,[5] W. Li,[6] A. V. Filippenko,[6] Y. Urata,[7] M. Ibrahimov,[8] I. A. Steele,[1] A. Gomboc,[9] R. J. Smith,[1] N. R. Tanvir,[10] E. Rol[10] and K. Huang[11]

[1]*Astrophysics Research Institute, Liverpool John Moores University, Twelve Quays House, Egerton Wharf, Birkenhead CH41 1LD*
[2]*Dipartimento di Fisica, Università di Ferrara, via Saragat 1, I-44100 Ferrara, Italy*
[3]*INAF-Osservatorio Astronomico di Brera, via Bianchi 46, I-23807 Merate (LC), Italy*
[4]*Steward Observatory, University of Arizona, 933 North Cherry Avenue, Tucson, AZ 85721, USA*
[5]*Space Research Insitute (IKI), 84/32 Profoyuznaya Str, Moscow 117997, Russia*
[6]*Department of Astronomy, University of California, Berkeley, CA 94720-3411, USA*
[7]*Department of Physics, Saitama University, Saitama 338-8570, Japan*
[8]*Ulugh Beg Astronomical Institute, Tashkent 700052, Uzbekistan*
[9]*Faculty of Mathematics and Physics, University of Ljubljana, Jadranska 19, SI-1000 Ljubljana, Slovenia*
[10]*Department of Physics and Astronomy, University of Leicester, University Road, Leicester LE1 7RH*
[11]*Academia Sinica Institute of Astronomy and Astrophysics, Taipei 106, Taiwan*

Accepted 2009 February 27. Received 2009 February 27; in original form 2009 January 22

ABSTRACT

We present a comprehensive multiwavelength temporal and spectral analysis of the 'fast rise exponential decay' GRB 070419A. The early-time emission in the γ-ray and X-ray bands can be explained by a central engine active for at least 250 s, while at late times the X-ray light curve displays a simple power-law decay. In contrast, the observed behaviour in the optical band is complex (from 10^2 up to 10^6 s). We investigate the light-curve behaviour in the context of the standard forward/reverse shock model; associating the peak in the optical light curve at ∼450 s with the fireball deceleration time results in a Lorenz factor $\Gamma \approx 350$ at this time. In contrast, the shallow optical decay between 450 and 1500 s remains problematic, requiring a reverse shock component whose typical frequency is above the optical band at the optical peak time for it to be explained within the standard model. This predicts an increasing flux density for the forward shock component until $t \sim 4 \times 10^6$ s, inconsistent with the observed decay of the optical emission from $t \sim 10^4$ s. A highly magnetized fireball is also ruled out due to unrealistic microphysic parameters and predicted light-curve behaviour that is not observed. We conclude that a long-lived central engine with a finely tuned energy injection rate and a sudden cessation of the injection is required to create the observed light curves, consistent with the same conditions that are invoked to explain the plateau phase of canonical X-ray light curves of γ-ray bursts.

Key words: gamma-rays: bursts.

1 INTRODUCTION

The temporal shape of the prompt emission of γ-ray bursts (GRBs) can show a variety of profiles: from narrow and symmetric to wide and asymmetric pulses. In some cases, a less energetic precursor is also detected, and in other cases a few overlapping pulses can take place for the entire duration of the γ-ray emission. It is true that many of those pulses (overlapping or single) detected for long-duration GRBs can be described by the superposition of 'fast rise exponential decay' (FRED) profiles, one for each pulse. Moreover, several GRBs display only a single-shot FRED-like emission over the background in the γ-ray passband that can be easily described by a simple Norris exponential model (Norris et al. 1996). In the context of the standard fireball model (Rees & Mészáros 1992), one may expect such GRBs to exhibit comparably simple behaviour in their afterglows at other wavelengths, and therefore be ideal test beds for the model. For full temporal and spectral coverage, the predicted properties of the multiwavelength light curves have well-predicted shapes, depending on the relative contribution of the different components.

In the X-ray band, the temporal decay of many GRBs observed by *Swift* is well described by a canonical 'steep-shallow-steep' decay

⋆E-mail: axm@astro.livjm.ac.uk

(Tagliaferri et al. 2005; Nousek et al. 2006; Zhang et al. 2006), with superposed flares observed in ∼50 per cent of bursts (O'Brien et al. 2006; Chincarini et al. 2007; Falcone et al. 2007). The initial steep decay is interpreted as the result of the high-latitude emission or as the contribution of the reverse shock (RS) emission (e.g. Panaitescu & Kumar 2004; Zhang et al. 2006), the shallow phase is consistent with long-lasting central energy activity (Zhang et al. 2006), and the late steep decay is evidence of decaying forward shock (FS) emission (i.e. the standard X-ray afterglow phase).

In the optical band, observed light curves are expected to show a variety of shapes depending on the relative contribution of the FS and RS emission (Kobayashi & Zhang 2003; Zhang, Kobayashi & Meszaros 2003) and the starting time of the observations. In particular, if the optical observations start when the RS contribution still dominates or when the central engine is still active, the detected temporal decay deviates from a simple power law (see fig. 1 in Melandri et al. 2008). Melandri et al. (2008) investigated the behaviour of the early decay phase in the optical and X-ray bands for 24 GRBs and classified them into four self-consistent groups based on the relative shapes observed in the two bands. Although 14 of the GRBs were well described by the standard model, the remaining 10 required adaptations such as ambient density gradients or energy injections from long-lived central engines. In some cases, even these modifications were unable to fully explain the light-curve properties.

GRB 070419A was particularly problematic, despite a simple FRED γ-ray profile. In this paper, we present a comprehensive multiwavelength temporal and spectral study of GRB 070419A, including published and unpublished data from infrared (IR) to γ-ray bands, and use this extensive data set to challenge the standard model.

Throughout, we use the following conventions: the power-law flux density is given as $F(\nu, t) \propto t^{-\alpha}\ \nu^{-\beta}$, where α is the temporal decay index and β is the spectral slope; we assume a standard cosmology with $H_0 = 70\,\mathrm{km\,s^{-1}\,Mpc^{-1}}$, $\Omega_m = 0.3$ and $\Omega_\Lambda = 0.7$; and all uncertainties are quoted at the 1σ confidence level (cl), unless stated otherwise.

2 OBSERVATIONS

2.1 *Swift*/BAT data

On 2007 April 19 at 09:59:26 UT, the Burst Alert Telescope (BAT; Barthelmy et al. 2005) triggered on GRB 070419A (Stamatikos et al. 2007a), a dim long GRB with a duration of $T_{90} \approx 110$ s. The γ-ray emission observed by BAT is a single-shot FRED light curve, with a total duration of a few hundred seconds. This event displayed an average γ-ray fluence ($\sim 5 \times 10^{-7}\,\mathrm{erg\,cm^{-2}}$) and a peak photon flux lying at the low end of the distribution of *Swift* GRBs (Sakamoto et al. 2008). The redshift of the burst ($z = 0.97$; Cenko et al. 2007) resulted in an isotropic energy estimate of $\sim 1.6 \times 10^{51}$ erg in the 15–150 keV observed bandpass (Stamatikos et al. 2007c).

2.2 *Swift*/XRT data

Follow-up observations of the BAT error circle were performed with the X-ray Telescope (XRT; Burrows et al. 2005) starting about 113 s after the BAT trigger. A bright, uncatalogued, fading source was detected at $\alpha(\mathrm{J2000}) = 12^h10^m58.80^s$, $\delta(\mathrm{J2000}) = +39^\circ\,55'\,32.4''$ (Perri et al. 2007) with an uncertainty of 2.2 arcsec. The light curve showed a rapid decay at early times followed (after 10^3 s) by a power-law decline with $\alpha = 1.2 \pm 0.2$. The X-ray spectrum is well fitted by an absorbed power law with a photon index $\Gamma_X = 2.46 \pm 0.09$ and $N_\mathrm{H} = (1.9 \pm 0.2) \times 10^{21}\,\mathrm{cm^{-2}}$ (Stamatikos et al. 2007c).

Table 1. Log of the optical observations.

Telescope	Filters	$\Delta t_{\mathrm{start}}$ (min)	Δt_{end} (min)	Reference
Super-LOTIS	*R*	3.43	35.46	This work
KAIT	*VRI*	5.24	57.66	This work
P60	Ri'	5.87	92.35	Cenko et al. (2009)
Kuiper	*VR*	27.68	97.68	This work
FTN	BRi'	39.43	101.46	This work
Kiso	*BR*	51.05	112.24	This work
Lulin	*R*	112.75	236.32	This work
Maidanak	*R*	352.80	352.80	This work
KPNO 4-m	*R*	1036.97	1036.97	This work
LBT	r'	5328.00	44352.00	Dai et al. (2008)

$\Delta t_{\mathrm{start}}$ and Δt_{end} refer to the first and last photometric measurement acquired with the corresponding telescope. A complete list of all the photometric points presented on this work is reported in Table 2.

2.3 Optical data

The afterglow of GRB 070419A was followed in the optical band from about 3 min and continued up to ∼18 hr after the burst event. Late-time observations were acquired with the 8.4-m Large Binocular Telescope (LBT) in the SDSS-*r* filter and showed a bump in the light curve (Dai et al. 2008), compatible with a supernova bump (see Section 4.3 for a more detailed discussion of the possible supernova contribution). A log of the observations is given in Table 1, where we report the starting and ending time of the observations with each facility.

We collected, cross-calibrated and analysed all the available optical data acquired by ground-based telescopes for this event. We calibrated the optical data using a common set of selected catalogued stars present in the field of view. SDSS pre-burst observation (Cool et al. 2007) has been used for r' and i' filters, USNO-B1 $R2$ and $B2$ magnitudes for *R* and *B* filters, respectively, and Nomad *V* magnitudes for the *V* filter. LBT r' magnitudes are reported in the *R* band applying an average colour term of $\langle R - r' \rangle \approx -0.31$ mag, estimated from several field stars. In the same way, KAIT *I*-band magnitudes are given in the i' band assuming an average colour term of $\langle I - i' \rangle \approx -0.93$ mag.

Next, the calibrated magnitudes were corrected for the Galactic absorption along the line of sight ($E_{B-V} = 0.028$ mag; Schlegel, Finkbeiner & Davis 1998); the estimated extinctions in the different filters are $A_B = 0.12$ mag, $A_V = 0.09$ mag, $A_R = 0.07$ mag and $A_i' = 0.05$ mag. Corrected magnitudes were then converted into flux densities, F_ν (mJy), following Fukugita et al. (1996). Results are summarized in Table 2.

The optical afterglow of GRB 070419A was also detected by the *Swift*/Ultra-Violet and Optical Telescope (UVOT; Roming et al. 2005). Observations began ∼115 s after the event. The best position for the optical afterglow is measured in the KAIT images at $\alpha(\mathrm{J2000}) = 12^h10^m58.82^s$, $\delta(J2000) = +39^\circ\,55'33.92''$ (Chornock, Li & Fillipenko 2007). Deriving accurate photometry of the afterglow was difficult, due to the presence of a diffraction spike from a mag 7 star in the field of view. A clear detection was possible in the *V* band, while only a 3σ upper limits were estimated for the *B* and *U* filters (Stamatikos et al. 2007c). UVOT-*V* magnitudes are plotted together with all of the ground-based optical data (Fig. 7 in Section 3.5), but no cross-calibration between UVOT and other optical data was performed. Thus, we cannot exclude the presence

Table 2. Optical and IR calibrated magnitudes for the afterglow of GRB 070419A.

Filter	Telescope	Δt (min)	Exp. time (min)	Magnitude	F_ν (mJy)	Filter	Telescope	Δt (min)	Exp. time (min)	Magnitude	F_ν (mJy)
R	S-Lotis	3.436	2.5	19.60 ± 0.21	0.0476 ± 0.0092	*B*	FTN	47.97	1.67	20.86 ± 0.30	0.0205 ± 0.0057
R	S-Lotis	3.925	2.0	19.75 ± 0.23	0.0415 ± 0.0088	*B*	FTN	56.25	2.0	21.62 ± 0.35	0.0102 ± 0.0033
R	S-Lotis	7.597	1.0	18.45 ± 0.12	0.1375 ± 0.0152	*B*	FTN	65.13	3.0	21.69 ± 0.29	0.0095 ± 0.0025
R	S-Lotis	8.718	1.0	18.65 ± 0.12	0.1143 ± 0.0126	*B*	FTN	80.09	5.0	21.90 ± 0.23	0.0078 ± 0.0016
R	S-Lotis	10.889	2.0	18.76 ± 0.11	0.1033 ± 0.0104	*B*	FTN	96.90	4.0	22.17 ± 0.30	0.0061 ± 0.0017
R	S-Lotis	13.062	2.0	18.84 ± 0.11	0.0959 ± 0.0097	*B*	Kiso	58.78	5.0	21.80 ± 0.28	0.0086 ± 0.0022
R	S-Lotis	15.968	4.0	18.90 ± 0.08	0.0908 ± 0.0067	*B*	Kiso	74.18	5.0	21.50 ± 0.24	0.0114 ± 0.0025
R	S-Lotis	20.428	4.0	19.02 ± 0.08	0.0813 ± 0.0060	*B*	Kiso	89.41	5.0	22.20 ± 0.48	0.0059 ± 0.0027
R	S-Lotis	24.886	4.0	19.14 ± 0.14	0.0728 ± 0.0094	*B*	Kiso	104.60	5.0	22.49 ± 0.48	0.0045 ± 0.0021
R	S-Lotis	29.677	5.0	19.27 ± 0.10	0.0646 ± 0.0059						
R	S-Lotis	35.468	5.0	19.58 ± 0.13	0.0485 ± 0.0058	*V*	KAIT	5.245	2.0	19.811 ± 0.55	0.0470 ± 0.0248
R	KAIT	3.665	0.333	20.45 ± 0.88	0.0218 ± 0.0196	*V*	Kuiper	36.553	1.0	19.961 ± 0.11	0.0410 ± 0.0041
R	KAIT	6.208	0.75	19.19 ± 0.17	0.0695 ± 0.0109	*V*	Kuiper	38.388	1.0	19.857 ± 0.11	0.0451 ± 0.0045
R	KAIT	9.733	1.0	18.59 ± 0.08	0.1208 ± 0.0089	*V*	Kuiper	40.122	1.0	20.112 ± 0.12	0.0356 ± 0.0039
R	KAIT	21.65	1.0	19.07 ± 0.14	0.0776 ± 0.0100	*V*	Kuiper	41.858	1.0	20.144 ± 0.12	0.0346 ± 0.0038
R	KAIT	24.00	1.0	19.29 ± 0.18	0.0634 ± 0.0105	*V*	Kuiper	43.597	1.0	20.237 ± 0.13	0.0318 ± 0.0038
R	KAIT	26.40	1.0	19.26 ± 0.18	0.0652 ± 0.0108	*V*	Kuiper	45.336	1.0	20.141 ± 0.12	0.0347 ± 0.0038
R	KAIT	30.572	3.0	19.57 ± 0.22	0.0490 ± 0.0099	*V*	Kuiper	47.075	1.0	19.990 ± 0.11	0.0399 ± 0.0040
R	KAIT	36.483	2.0	19.97 ± 0.25	0.0339 ± 0.0078	*V*	Kuiper	48.826	1.0	20.009 ± 0.11	0.0392 ± 0.0039
R	KAIT	41.173	5.0	20.15 ± 0.21	0.0287 ± 0.0055	*V*	Kuiper	50.566	1.0	20.182 ± 0.13	0.0334 ± 0.0040
R	KAIT	47.653	6.0	20.57 ± 0.30	0.0195 ± 0.0054	*V*	Kuiper	52.315	1.0	19.956 ± 0.11	0.0412 ± 0.0041
R	KAIT	57.661	7.0	20.71 ± 0.33	0.0171 ± 0.0053	*V*	Kuiper	54.054	1.0	20.502 ± 0.17	0.0249 ± 0.0039
R	Kuiper	27.681	1.0	19.54 ± 0.07	0.0503 ± 0.0032	*V*	Kuiper	55.790	1.0	20.433 ± 0.16	0.0265 ± 0.0039
R	Kuiper	29.420	1.0	19.50 ± 0.07	0.0522 ± 0.0033	*V*	Kuiper	57.524	1.0	20.774 ± 0.21	0.0194 ± 0.0037
R	Kuiper	31.148	1.0	19.65 ± 0.08	0.0455 ± 0.0033	*V*	Kuiper	59.257	1.0	20.387 ± 0.15	0.0277 ± 0.0038
R	Kuiper	32.890	1.0	19.60 ± 0.07	0.0477 ± 0.0030	*V*	Kuiper	97.687	12.0	21.663 ± 0.30	0.0085 ± 0.0024
R	Kuiper	64.489	4.0	20.81 ± 0.10	0.0156 ± 0.0014						
R	Kuiper	69.23	4.0	20.83 ± 0.10	0.0153 ± 0.0014	*I*	KAIT	7.695	1.0	19.56 ± 0.45	0.0571 ± 0.0243
R	Kuiper	73.96	4.0	20.95 ± 0.10	0.0137 ± 0.0012	*I*	KAIT	8.500	1.0	18.84 ± 0.25	0.1109 ± 0.0257
R	Kuiper	78.71	4.0	21.03 ± 0.11	0.0128 ± 0.0012	*I*	KAIT	11.05	1.0	18.50 ± 0.18	0.1517 ± 0.0252
R	Kuiper	83.46	4.0	21.26 ± 0.18	0.0103 ± 0.0017	*I*	KAIT	13.40	1.0	18.59 ± 0.22	0.1397 ± 0.0285
R	Kuiper	88.751	4.0	21.13 ± 0.12	0.0116 ± 0.0013	*I*	KAIT	16.44	2.0	18.75 ± 0.11	0.1205 ± 0.0122
R	FTN	39.430	1.0	20.20 ± 0.24	0.0274 ± 0.0061	*I*	KAIT	22.32	3.0	18.99 ± 0.12	0.0966 ± 0.0107
R	FTN	47.384	0.5	20.37 ± 0.16	0.0234 ± 0.0034	*I*	KAIT	31.77	5.0	20.18 ± 0.48	0.0323 ± 0.0147
R	FTN	51.914	1.0	20.40 ± 0.16	0.0228 ± 0.0033	i'	FTN	46.644	0.667	20.73 ± 0.32	0.0194 ± 0.0058
R	FTN	58.809	2.0	20.46 ± 0.12	0.0216 ± 0.0023	i'	FTN	53.698	1.0	20.58 ± 0.17	0.0223 ± 0.0035
R	FTN	68.706	3.0	20.92 ± 0.15	0.0141 ± 0.0019	i'	FTN	60.615	2.0	20.90 ± 0.16	0.0166 ± 0.0024
R	FTN	78.623	2.0	21.10 ± 0.20	0.0119 ± 0.0022	i'	FTN	72.505	3.0	20.96 ± 0.14	0.0157 ± 0.0020
R	FTN	88.642	3.0	21.30 ± 0.21	0.0099 ± 0.0019	i'	FTN	81.405	2.0	20.96 ± 0.16	0.0157 ± 0.0023
R	FTN	101.46	4.0	21.15 ± 0.15	0.0114 ± 0.0015	i'	FTN	92.399	3.0	21.58 ± 0.30	0.0089 ± 0.0024
R	Lulin	112.75	10.0	21.26 ± 0.17	0.0103 ± 0.0016						
R	Lulin	125.31	15.0	21.70 ± 0.14	0.0068 ± 0.0009	*J*	UKIRT	39.24	3.0	18.27 ± 0.08	0.0802 ± 0.0059
R	Lulin	236.32	30.0	22.43 ± 0.17	0.0035 ± 0.0005	*J*	UKIRT	48.84	3.0	18.56 ± 0.09	0.0614 ± 0.0051
R	Kiso	51.05	5.0	20.13 ± 0.11	0.0292 ± 0.0029						
R	Kiso	66.65	5.0	20.75 ± 0.20	0.0165 ± 0.0030	*H*	UKIRT	44.04	3.0	17.83 ± 0.13	0.0766 ± 0.0092
R	Kiso	81.88	5.0	20.90 ± 0.23	0.0144 ± 0.0030						
R	Kiso	112.24	15.0	21.66 ± 0.34	0.0071 ± 0.0022	*K*	UKIRT	53.76	3.0	17.26 ± 0.18	0.0838 ± 0.0139
R	Maidanak	352.8	55.0	22.45 ± 0.32	0.0034 ± 0.0010	*K*	UKIRT	99.90	15.0	18.30 ± 0.18	0.0321 ± 0.0053
R	KPNO 4-m	1036.97	5.0	23.37 ± 0.20	0.0014 ± 0.0003						

Magnitudes are not corrected for Galactic absorption. P60 (Cenko et al. 2009) and LBT (Dai et al. 2008) magnitudes are not reported in this table, but they are plotted in Fig. 9. KAIT-*I* magnitudes have been calibrated against SDSS-i' catalogued magnitudes. Flux densities (F_ν) have been estimated from extinction-corrected magnitudes.

of a large offset between UVOT magnitudes and calibrated ground-based photometry.

3 RESULTS

We have undertaken a complete temporal and spectral analysis of the available *Swift* data. In this section, we report the results of our γ-ray/X-ray/optical analysis.

3.1 γ-rays

3.1.1 γ-ray light curve

As observed by BAT, the γ-ray behaviour of GRB 070419A is a single FRED light curve, lasting a few hundred seconds. It can be easily fit with a Norris simple exponential model (peakedness fixed to 1):

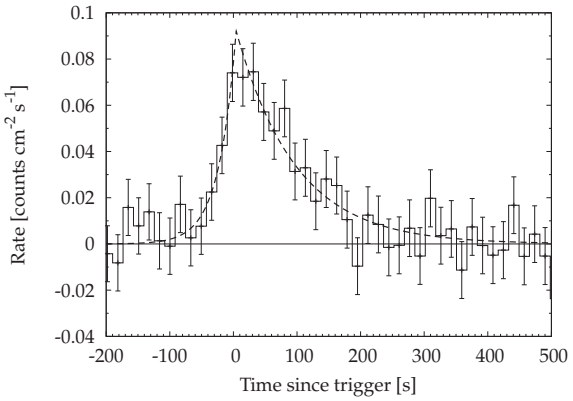

Figure 1. The BAT light curve. There is significant emission above the background up to $t \approx 300$ s. The dashed line represents the best fit of the light curve with the Norris profile.

$$F(t) = N^{\rm BAT} \times e^{-|t-t_{\rm peak}|/t_{\rm rise}} \quad t < t_{\rm peak}$$
$$= N^{\rm BAT} \times e^{-(t-t_{\rm peak})/t_{\rm decay}} \quad t > t_{\rm peak}. \qquad (1)$$

The parameters of the best fit are $t^{\rm BAT}_{\rm peak} = 4.4 \pm 3.4$, $t^{\rm BAT}_{\rm rise} = 27.3 \pm 5.6$ and $t^{\rm BAT}_{\rm decay} = 93.0 \pm 11.0$ s (χ^2/d.o.f. = 0.49). The BAT light curve visible in Fig. 1 shows significant emission above the background up to 300 s after the burst onset time. In the same figure, we show the result of the fit of the light curve done in the interval −100 to 300 s.

3.1.2 γ-ray spectral analysis

We independently analysed BAT data with the standard BAT pipeline (Krimm et al. 2004). Using the ftool 'battblocks' (v1.7) we determined a value of $T_{90} = 112 \pm 2$ s (going from −26 to +86 s). Fitting the 15–150 keV spectrum with a single power law, integrated over the T_{90} interval, gives $\Gamma_\gamma = 2.4 \pm 0.3$, fluence $f = 5.1 \pm 0.8 \times 10^{-7}$ erg cm^{-2} and a corresponding peak photon flux of 0.14 ± 0.03 ph cm^{-2} s^{-1}. All of these results are in agreement with the BAT team's published values (Stamatikos et al. 2007b,c).

3.2 X-rays

3.2.1 X-ray light curve

From our independent analysis of the XRT data, we find that the light curve in the X-ray band can be fitted by an exponential plus power-law model,

$$F(t) = N^{\rm XRT}_{\rm exp} \times e^{-(t-t_0)/\tau} + N^{\rm XRT}_{\rm pl} \times t^{-\alpha_X}, \qquad (2)$$

with best-fitting parameters (uncertainties are 90 per cent cl) $t_0 = 0.0$ s (fixed, as insensitive parameter), $\tau = (71.9 \pm 2.4)$ s and $\alpha_X = 1.27^{-0.12}_{+0.18}$. The result of the fit can be seen in Fig. 2, where the two components of the fit are shown separately. These values are in good agreement with those found by Stamatikos et al. (2007c). However, the χ^2 per degree of freedom (d.o.f.) of this fit is not acceptable (χ^2/d.o.f. = 190/127 ≈ 1.5).

A more complex model (exponential with peakedness free to vary, plus two power laws) gives a satisfactory result. The justification for a more complex model is the unacceptable χ^2 of the previous fit, due to bad residuals of the early-time X-ray data. The best-fitting parameters are $N^{\rm XRT}_{\rm exp} = 32.1^{-7.5}_{+13.4}$ counts s^{-1}, $t_0 = 0.0$ s (fixed), $\tau = 259^{-18}_{+13}$ s, peakedness $= 5.6^{-1.6}_{+2.2}$, $N^{\rm XRT}_{\rm pl1} = 14.96^{-5.58}_{+9.53} \times 10^7$ counts s^{-1}, $N^{\rm XRT}_{\rm pl2} = 1.6 \pm 0.7$ counts s^{-1}, $\alpha_{\rm X,1} = 3.0 \pm 0.1$ and $\alpha_{X,2} = 0.65^{-0.39}_{+0.35}$. With this more complex model, the χ^2 is now acceptable (χ^2/d.o.f. = 137/124 ≈ 1.1). Evidently, the improvement in the total χ^2 is too large (53) compared with the change in the d.o.f. (3), when moving from the first to the second model. The P-value associated with this change in the χ^2 with 3 d.o.f. is 2×10^{-11}, so completely negligible, in agreement with what one would obtain with an F-test. However, it should be noted that the goodness of the fit in this case is related to the sparse data coverage at very late times.

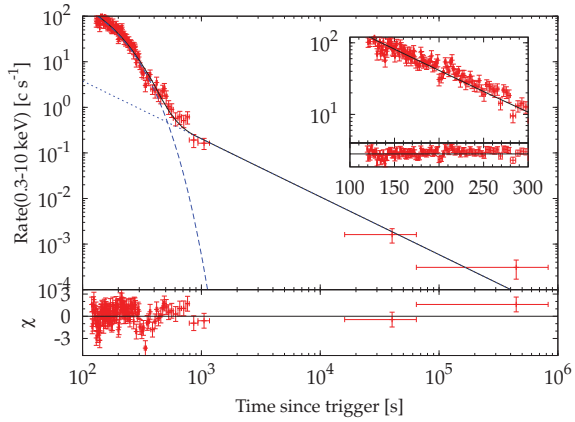

Figure 2. The XRT light curve, fitted using the exponential plus single power-law model as explained in the text. The two components of the model are shown separately. In the inset, the fit of the first 300 s of data with the exponential function is shown together with the residuals of the fit.

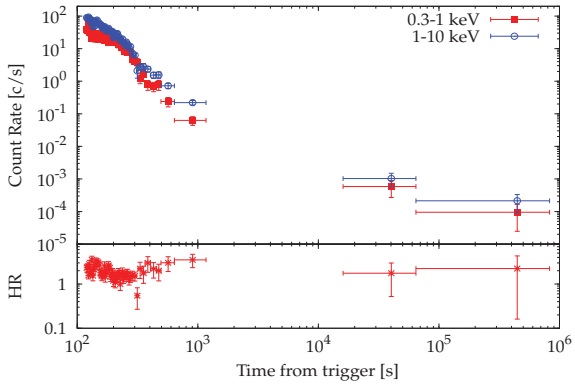

Figure 3. HR and X-ray light curve in two different bands. At early times, a spectral softening of the emission is visible over the first 200 s of data.

In Fig. 3, the X-ray light curve extracted in two separate bands (0.3–1 keV and 1–10 keV) is shown, together with the hardness ratio (HR; hard/soft, lower panel) in the X-ray band. At early times (between ∼100 and ∼300 s), the X-ray emission softened, then hardened up to ∼1000 s when the HR became roughly constant up to the end of the observations.

3.2.2 X-ray spectral analysis

In Fig. 4, the total windowed timing (WT) 0.3–10 keV spectrum (left-hand panel) and the total photon counting (PC) spectrum (right-hand panel) are shown. The adopted model is an absorbed power law. The Galactic absorption is taken into account separately and the intrinsic $N_{\rm H}$ is given in the GRB rest frame. All uncertainties are at the 90 per cent cl.

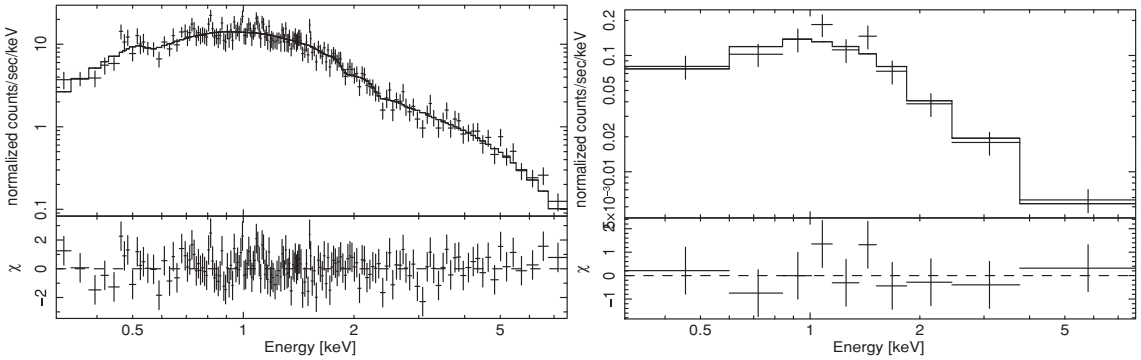

Figure 4. Left-hand panel: XRT WT spectrum. Right-hand panel: XRT PC spectrum.

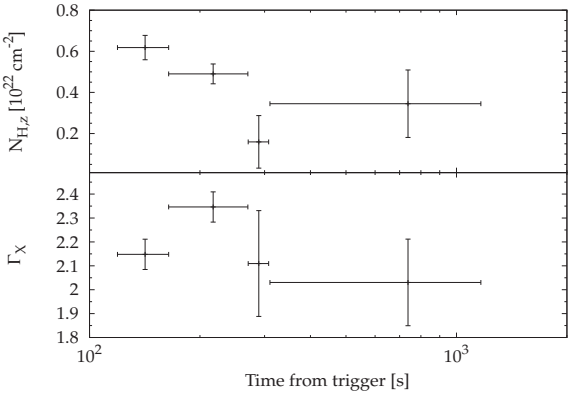

Figure 5. Intrinsic $N_{\rm H}$ and photon index as a function of time. Error bars shown are 1σ.

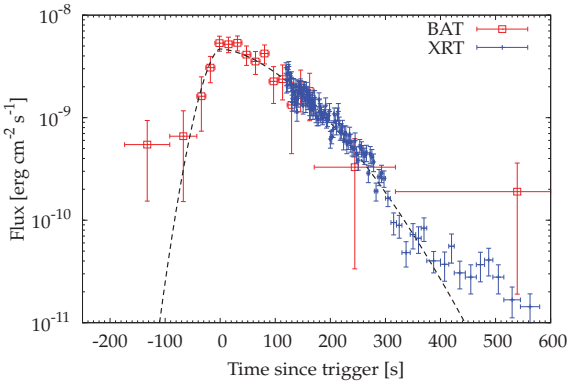

Figure 6. The joint BAT–XRT light curve can be fitted with the same Norris profile used for the BAT emission. See Section 3.3 for details.

The parameters of the fit for the WT spectrum (119–309 s) are $N_{\rm H(Gal)} = 2.4 \times 10^{20}\,{\rm cm}^{-2}$ (fixed), $N_{\rm H,z} = (5.1 \pm 0.6) \times 10^{21}\,{\rm cm}^{-2}$ and $\Gamma_X = 2.2 \pm 0.1$ (χ^2/d.o.f. = 142/161). The parameters of the fit for the PC spectrum (310–1165 s) are $N_{\rm H(Gal)} = 2.4 \times 10^{20}\,{\rm cm}^{-2}$ (fixed), $N_{\rm H,z} = 3.4^{-2.5}_{+3.4} \times 10^{21}\,{\rm cm}^{-2}$ and $\Gamma_X = 2.0 \pm 0.3$ (χ^2/d.o.f. = 4.8/7).

3.2.3 X-ray temporally resolved analysis

We extracted the XRT spectra in four separate time intervals each collecting 2000 source photons. In Fig. 5, we plot the $N_{\rm H}$ (intrinsic) and the photon index as a function of time. Clearly, as also shown in Fig. 3, there is marginal evidence for a hard-soft-hard trend in the photon index evolution; the same holds for the $N_{\rm H}$ evolution.

3.3 Combined γ/X-ray analysis

We calculated the flux in the 0.3–10 keV band after removing the $N_{\rm H}$ at low energies, both Galactic and intrinsic. Then we extrapolated it into the BAT 15–150 keV band taking into account the $\Gamma = 2.2$ unbroken power-law spectrum between XRT and BAT. The result is shown in Fig. 6, in which the initial exponential X-ray decay perfectly matches the decay of the FRED prompt emission seen by BAT. In this case, we allowed the peakedness of the Norris profile free to vary. The best fit shown is obtained by fitting both fluxes together (90 per cent cl) with $t_{\rm peak}^{\rm BAT+XRT} = 0 \pm 15$s, $t_{\rm rise}^{\rm BAT+XRT} = 36^{-24}_{+30}$s, $t_{\rm decay}^{\rm BAT+XRT} = 147^{-17}_{+20}$s and peakedness $= 1.64^{-0.16}_{+0.15}$(χ^2/d.o.f. = 163/128 $\approx$ 1.3). The fit was done on the points earlier than $t =$ 400 s, after which the power law takes over (not shown in this plot). It is clear that the initial steep decay seen in the X-ray band is just the tail of the exponential (single shot) decay observed in the γ-ray band, corresponding to the tail of the prompt emission.

3.4 The choice of t_0

The decay index of early afterglows is very sensitive to the choice of t_0. Correctly choosing t_0 is essential to derive the right index as well as to understand the emission process (Piro et al. 2005; Tagliaferri et al. 2005; Quimby et al. 2006). In the previous section, t_0 is set at the GRB trigger time, and it is almost at the peak of the prompt emission. If the emission is due to an internal shock or external shock, t_0 should be set before the peak (Lazzati & Begelman 2006; Kobayashi & Zhang 2007).

We can see how the choice of t_0 affects the decay index as follows (e.g. Yamazaki 2009). Let t be the time since the GRB trigger; the peak is located at $t = 0$ s on this time-scale. Next, assuming that the temporal decay right after the peak is actually described by a power law with another time ($T = t + t_0$), where the interval between the time $T = 0$ and $T = 0$ is assumed to be exactly t_0, we get

$$f \propto T^{-\alpha} \propto (t + t_0)^{-\alpha}. \quad (3)$$

Doing this, one finds that the flux f is constant if $t \ll t_0$, while it is described by a power law $f \propto t^{-\alpha}$ if $t \gg t_0$.

Although we have fitted the early BAT–XRT data with an exponential function, it might be possible to fit the same data by a single power law with a different value of t_0. We tested this possibility by re-examining the data assuming different values for t_0. The decay indices right after the peak are $\alpha = 2.1 \pm 0.13$ if $t_0 = 100$ s, $\alpha = 3.2 \pm 0.2$ if $t_0 = 200$ s and $\alpha = 4.2 \pm 0.3$ if $t_0 = 300$ s.

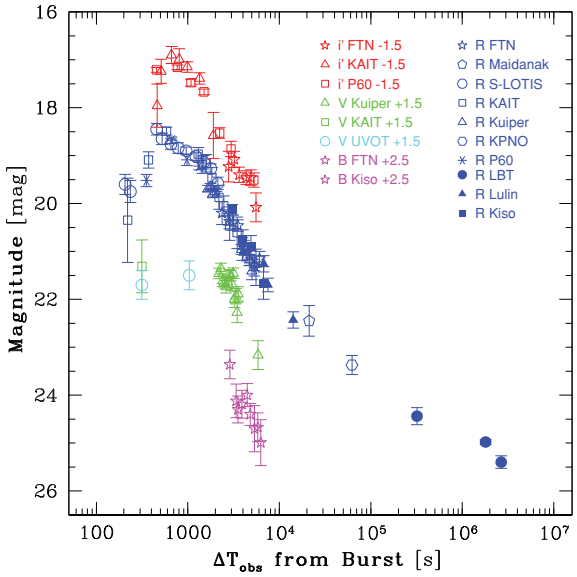

Figure 7. Observed optical light curves (*BVRi'*) for the afterglow of GRB 070419A.

In all the cases, the light curves still have a clear break around the penultimate BAT point (corresponding to $T \approx t_0 + 250$ s, for any chosen value of t_0). With an even larger t_0, it is possible to describe the light curve roughly with a single power law. However, the best-fitting value of α is already very high with $t_0 = 300$ s and it would be even higher for a larger t_0. The upper limit on the decay index is given by $\alpha = 2 + \beta$ (the high-latitude emission), where β is the spectral index. The best-fitting value for $t_0 = 300$ s ($\alpha = 4.2 \pm 0.3$) is already greater than this upper limit. Furthermore, after the break, the decay is even steeper ($\alpha = 6.8 \pm 0.8$ or higher for correspondingly larger values of t_0). Thus, the post-break index is steeper than the limit from the high-latitude emission.

The early BAT–XRT light curve is described neither by the emission from an external shock nor by that from a single internal shock. The very steep decay between $t = 250$ and 300 s indicates that the central engine is active at least for ∼250 s, and that the early part ($t < 250$ s) should be the result of the superposition of many pulses (internal shocks). Late-afterglow modelling is insensitive to the choice of t_0. In the rest of the paper (discussion on intermediate/late-time afterglow), we assume $t_0 = 0$ s.

3.5 Optical light curve

Fig. 7 shows the optical light curve. Even if the light curve is well sampled only in the *R* band, the general behaviour is seen in all the other optical bands. The top panel of Fig. 8 is a linear-log plot of the γ-ray/X-ray/optical light curves for an immediate comparison with Fig. 6. In the bottom panel of the same figure (log–log scale), it is possible to appreciate how the peak in the optical band coincides with the deviation in the X-ray band from the exponential tail.

In Fig. 9, we show the simple fit of the *R*-band light curve with a series of single power-law segments. Each segment is shown together with the sum of the two components at late times. The value of the decay index of each power law is reported in Table 3, together with the time intervals over which the data have been fitted by the correspondent component. The χ^2/d.o.f. of the late-time fit $f(x)$ (after 10^3 s), consisting of the two components f_3 and f_4, is $37/41 = 0.91$.

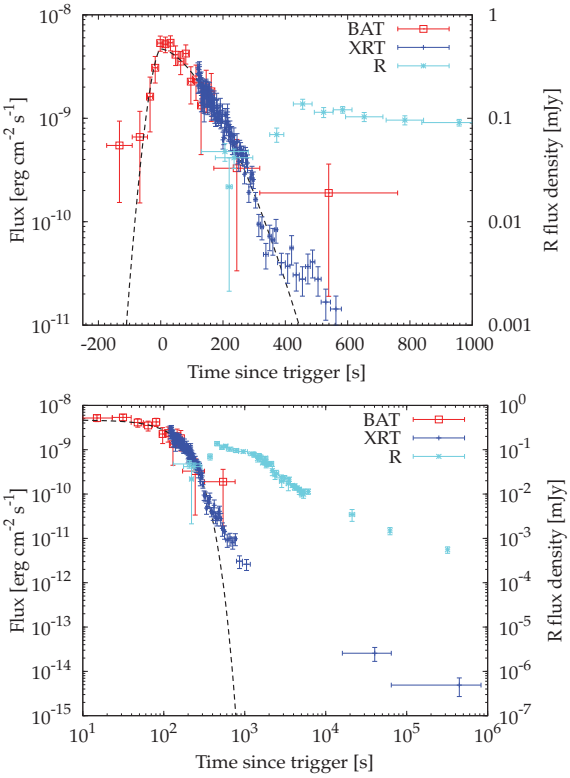

Figure 8. Top panel: γ-ray/X-ray/optical light curves on a linear-log scale. Same as in Fig. 6 for the joint BAT–XRT light curve. We overplot the optical flux in the *R* band. Bottom panel: γ-ray/X-ray/optical light curves on a log–log scale. In this case, we excluded from the plot the initial fluxes in the γ-ray (at negative times) and show the late-time optical and X-ray behaviours.

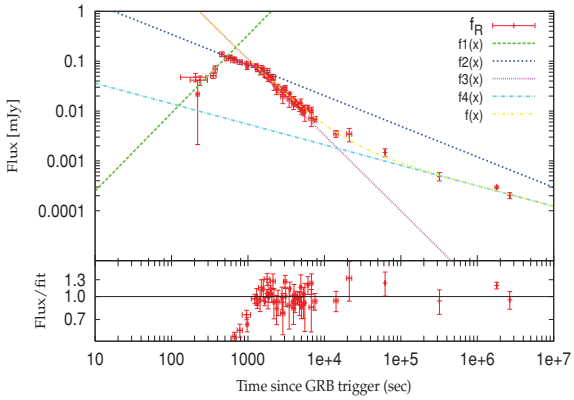

Figure 9. *R*-band optical light curve best fit. The fit $f(x)$ is the sum of two power laws ($f3$, $f4$) for which the parameters are reported in Table 3. The lower panel shows the residuals of the fit for the last two components.

3.6 Infrared data and spectral energy distribution

The fading afterglow of GRB 070419A was detected in the IR bands thanks to the United Kingdom Infrared Telescope (UKIRT). Observations started about 40 min after the event and were performed with *JHK* filters (Rol, Tanvir & Kerr 2007). The calibrated IR magnitudes (with respect to the 2MASS catalogue) are reported in Table 2. As for the optical band, IR magnitudes have been corrected for the estimated extinction ($A_J = 0.025$ mag, $A_H = 0.016$ mag, $A_K = 0.010$ mag) and then converted into flux densities. Coupling those

Table 3. Best-fitting parameters of the optical light curve.

Component	$N^{\rm opt}$ (F_j) (mJy)	α	$t_{\rm interval}$ (s)
f_1	$(6.84 \pm 2.83) \times 10^{-6}$	-1.56 ± 0.70	<460
f_2	5.81 ± 3.58	0.61 ± 0.09	$460 < t < 1500$
f_3	$(3.8 \pm 3.2) \times 10^{3}$	1.51 ± 0.12	$1500 < t < 10^4$
f_4	0.09 ± 0.19	0.41 ± 0.17	$t > 10^4$

Table 4. Observed $F_\nu(t = \Delta t)$ and extrapolated $F_\nu(t = 3000$ s) flux.

Band	Δt [s]	$F_\nu(\Delta t)$ [mJy]	$F_\nu(3000$ s) [mJy]
B	2878	0.0205 ± 0.0057	0.0103 ± 0.0040
V	2930	0.0392 ± 0.0039	0.0306 ± 0.0040
R	3063	0.0292 ± 0.0029	0.0238 ± 0.0050
i'	2799	0.0194 ± 0.0058	0.0230 ± 0.0045
J	2930	0.0614 ± 0.0051	0.0059 ± 0.0050
H	2642	0.0766 ± 0.0092	0.0065 ± 0.0090
K	3225	0.0838 ± 0.0014	0.0916 ± 0.0014
X-ray		*	$6.0 \pm 3.0 \times 10^{-5}$

*Due to the sparse coverage in the X-ray band after $\sim 10^3$ s, the extrapolation of the X-ray flux at $t = 3000$ s has been done taking into account the two possible fits for the late-time behaviour as described in Section 3.2.1.

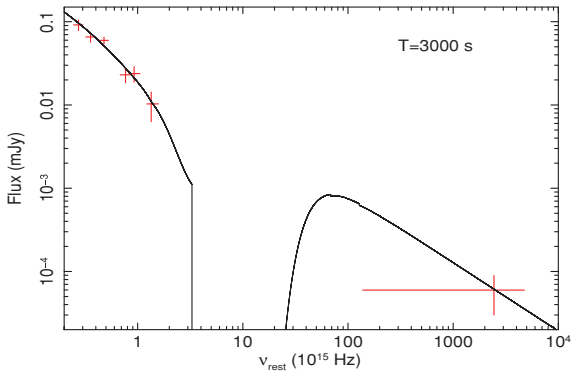

Figure 10. SED fit at $t = 3000$ s after the burst event.

data with optical and X-ray data, we have constructed a spectral energy distribution (SED) extrapolating/interpolating the observations at a common time, chosen to be $t_{\rm SED} = 3000$ s $= 50$ min after the burst. In doing this, we excluded the estimate of the flux in the *V* band, for which the calibration of the optical data is uncertain and therefore the inferred value for the flux density is not accurate. The extrapolated fluxes for all the filters are reported in Table 4.

The SED, showed in Fig. 10, is well fitted by a simple optically absorbed power law. The absorption in the X-ray band has been fixed to a negligible value because it cannot be determined by the fit with a single X-ray point. The assumed extinction profile is the Small Magellanic Cloud profile (Pei 1992). The best-fitting values in the rest frame of the GRB ($z = 0.97$) are $\beta_{OX} = 0.82^{-0.07}_{+0.16}$ and $A_V = 0.37 \pm 0.19$ mag.

4 DISCUSSION

4.1 X-ray emission

From the analysis of the high-energy data of GRB 070419A, it seems clear that the emission can be simply explained by a central engine still active up to at least 250 s, very likely up to 10^3 s (see Fig. 2). After that time, the FS emission takes over and the X-ray light curve can be explained by a simple power-law decay (or a slightly complex two-component model).

4.2 Optical emission

Clearly, the optical light curve (Fig. 7) is too complex to be explained with the standard FS model. In general, optical brightening could be due to the enhancement in the ambient density. Since the luminosity above the cooling frequency is insensitive to the ambient density, if the X-ray band is located above the cooling frequency, the lack of a corresponding peak in the X-ray light curve would be naturally explained. However, the features in the optical light curve are too sharp to be explained by the density enhancement model (Nakar & Granot 2007). Another mechanism should be responsible for the production of the observed optical features.

A possible mechanism is RS emission, which dominates in the optical band at early times. Although the decay behaviour of $\sim t^{-2}$ is well known for the RS emission, the initial decay could be as shallow as $t^{-0.5}$ if the typical frequency is above the optical band ($\nu_{\rm opt} < \nu_{\rm m,r} < \nu_{\rm c,r}$) at the RS crossing time (Sari & Piran 1999; Kobayashi 2000). Since the observed index ($\alpha = 0.61 \pm 0.09$) is consistent with the expected value, we test this possibility in detail.

Assuming that the optical peak ($t_{\rm peak} \approx 450$ s) gives the fireball deceleration time, we can estimate the initial Lorentz factor of the fireball as $\Gamma \approx 350\, n^{-1/8}\, ((1+z)/1.97)^{3/8}\, (T/450\,{\rm s})^{-3/8}\, (E/(2 \times 10^{51}\,{\rm erg}))^{1/8}$. If the break in the optical light curve around 1500 s is due to the passage of the typical frequency of the RS, $\nu_{m,r} \propto t^{-54/35}$, through the optical band (Kobayashi 2000), $\nu_{m,r}$ should be around 3×10^{15} Hz at $t = t_{\rm peak}$. The typical frequency of the FS, $\nu_{m,f} = \Gamma^2\, \nu_{m,r}$, should be about 4×10^{20} Hz at the peak time (e.g. Kobayashi & Zhang 2003). We expect that the FS emission in the optical band should increase as $t^{1/2}$ in the interstellar medium (or $t^{-1/4}$ in the wind ambient) until $t \approx 4 \times 10^6$ s when $\nu_{m,f} \propto t^{-3/2}$ passes through the optical band. Since the observed optical luminosity already decreases as $t^{-0.4}$ or steeper around 10^4 s, this is not consistent.

If the fireball is magnetized, the $\nu_{m,f}$ could be smaller by a factor of $R_{\rm B}^{-1/2}$, where $R_{\rm B}$ is the ratio of the microscopic parameters in the two shock regions (we use the same notation as Gomboc et al. 2008; $R_{\rm B} = \varepsilon_{\rm B,r}/\varepsilon_{\rm B,f}$). The passage time of $\nu_{m,f}$ through the optical band scales as $R_{\rm B}^{1/3}$. In order to get a FS peak time two orders of magnitude smaller, a very large $R_{\rm B} \approx 10^6$ is needed. With this value of $R_{\rm B}$, the luminosity ratio between the RS and FS peaks is about $\Gamma\, R_{\rm B}^{1/2} \approx 4 \times 10^5$. In the observational data, the RS component is only a few times brighter than the FS component. The introduction of magnetization cannot fix the problem with the FS peak. If we stick with the RS model, the typical frequency of the RS emission ($\nu_{m,r}$) should be well below the optical band at the shock crossing time. The initial shallow decay ($t^{-0.5}$) in the optical might be explained with energy injection to the fireball ejecta (refreshed shocks). We cannot rule out this possibility, but the energy injection rate should be tuned very carefully in order to reproduce the observed power-law decay, and moreover we would need to assume a sharp cessation of the injection to get the clear break.

The shallow decay phase observed between 450 and 1500 s, still described by a power law, and the very sharp transitions from one power law to another in the optical light curve are puzzling features for any model. One possible explanation of the observed features in the optical light curve is the assumption of a finely tuned long-lived

central engine. This condition is indeed necessary to explain the plateau phase observed in the canonical X-ray light curves of many GRBs.

4.3 Supernova/host-galaxy contribution

As discussed above, the optical light curve continues to decay to late times with an unusually shallow gradient. Late-time observations consist of LBT detections in the SDSS-r filter, the first ($t \approx 3.2 \times 10^5$ s) and third ($t \approx 2.6 \times 10^6$ s) of which are consistent with the shallow decay of the afterglow emission. At $t \approx 1.8 \times 10^6$ s, a small excess above the underlying power law is observed (see Fig. 7). This feature has been attributed to a possible supernova component (Dai et al. 2008), but interpretation of the late-time data is critically dependent on the model of the underlying afterglow. Given the faintness of the emission at these late times ($r' \approx 25.7$ mag), which is not atypical for GRB host-galaxy magnitudes at this redshift (Ovaldsen et al. 2007; Wainwright et al. 2007), future deep optical imaging of the GRB location would confirm whether a host-galaxy contribution is present or the light has continued to decline below detection limits.

5 CONCLUSIONS

(i) The γ-ray profile of GRB 070419A consists of a single shot (FRED) a few hundred seconds long. The γ-ray fluence ($\sim 5 \times 10^{-7}$ erg cm^{-2}) has an average value for the *Swift* GRB population, but the peak photon flux puts this event at the low end of that distribution among *Swift* GRBs (Sakamoto et al. 2008).

(ii) The XRT 0.3–10 keV data show the presence of some intrinsic (rest-frame) absorption, and there is weak evidence for an evolution of both $N_{\rm H}$ and the photon index (mean value of $\Gamma_X \sim 2.2$) with time.

(iii) The XRT–BAT fluxes, derived in the 15–150 keV band after removing the absorption in XRT curves, show that the initial steep X-ray decay is just the decay of the FRED, modelled with a Norris profile (Norris et al. 1996). The early BAT–XRT light curve is due to internal shocks or other processes related to prolonged central engine activity up to at least 250 s.

(iv) After 400–500 s, the late-time X-ray power law begins to emerge, with index $\alpha_X \approx 1.2 \pm 0.2$ (or $\alpha_{X,2} \approx 0.7$ in the case of the more complex fit model with two power laws). This behaviour seems to be supported by the optical light curve that shows a peak roughly at the same time ($t_{\rm peak} \approx 450$ s).

(v) We tried to explain the behaviour of the optical light curve in the context of the standard fireball model. However, the simple and natural explanation (FS plus RS components) does not work. The magnetization of the ejecta could affect the FS peak time significantly, but the effect is negligible and not in agreement with the observations. Another possibility to explain the optical behaviour is to argue for the existence of a significant density enhancement in the ambient medium. The luminosity below the cooling frequency is proportional to $\rho^{1/2}$. If a blast wave hits a density enhancement of several tens or hundreds, the bump in the optical at $\sim$450 s could be explained. However, the observed peak feature might be too sharp for this model.

(vi) We cannot rule out the possibility of a finely tuned central engine for GRB 070419A. The optical light curve would not be easily reproduced without assuming a particular energy injection rate and a sudden cessation of the injection in order to create the observed optical features.

(vii) From our detailed multiwavelength analysis, we can conclude that GRB 070419A is not explained in the context of the simple standard fireball model. Assuming energy injection or a tail component following the fireball, or even a more complex emission picture, the RS model might explain the observations, but this scenario would result in a rather ad hoc explanation only for this particular event.

ACKNOWLEDGMENTS

AM acknowledges funding from the Particle Physics and Astronomy Research Council (PPARC). CGM is grateful for financial support from the Royal Society and Research Councils UK. AVF's group is supported by US National Science Foundation (NSF) grant AST–0607485, Gary and Cynthia Bengier and the TABASGO Foundation. The Liverpool Telescope is operated by Liverpool John Moores University at the Observatorio del Roque de los Muchachos of the Instituto de Astrofisica de Canarias. The Faulkes Telescopes, now owned by Las Cumbres Observatory, are operated with support from the Dill Faulkes Educational Trust. KAIT and its ongoing operation were made possible by donations from Sun Microsystems, Inc., the Hewlett-Packard Company, AutoScope Corporation, Lick Observatory, the NSF, the University of California, the Sylvia & Jim Katzman Foundation and the TABASGO Foundation. We thank R. Chornock for initial discussions of the KAIT data on the optical afterglow of GRB 070419A. This work made use of data supplied by the UK *Swift* Science Data Centre at the University of Leicester.

REFERENCES

Barthelmy S. D. et al., 2005, Space Sci. Rev., 120, 143
Burrows D. N. et al., 2005, Sci, 309, 1833
Cenko S. B., Gezari S., Small T., Fox D. B., Chornock R., 2007, GCN Circ. 6322
Cenko S. B. et al., 2009, ApJ, 693, 1484
Chincarini G. et al., 2007, ApJ, 671, 1903
Chornock R., Li W., Filippenko A. V., 2007, GCN Circ. 6304
Cool J. et al., 2007, GCN Circ. 6318
Dai X. et al., 2008, ApJ, 682, L77
Falcone A. D. et al., 2007, ApJ, 671, 1921
Fukugita M., Ichikawa T., Gunn J. E., Doi M., Shimasaku K., Schneider D. P., 1996, AJ, 111, 1748
Gomboc A. et al., 2008, ApJ, 687, 443
Kobashi S., 2000, ApJ, 545, 807
Kobayashi S., Zhang B., 2003, ApJ, 582, L75
Kobayashi S., Zhang B., 2007, ApJ, 655, 973
Krimm H. A. et al., 2004, in Fenimore E., Galassi M., eds, AIP Conf. Proc. Vol. 727, Gamma-Ray Burst: 30 Years of Discovery. Am. Inst. Phys., New York, p. 659
Lazzati D., Begelman M. C., 2006, ApJ, 641, 972
Melandri A. et al., 2008, ApJ, 686, 1209
Nakar E., Granot J., 2007, MNRAS, 380, 1744
Norris J. P., Nemiroff R. J., Bonnell J. T., Scargle J. D., Kouveliotou C., Paciesas W. S., Meegan C. A., Fishman G. J., 1996, ApJ, 459, 393
Nousek J. A. et al., 2006, ApJ, 642, 389
O'Brien P. T. et al., 2006, ApJ, 647, 1213
Ovaldsen J.-E. et al., 2007, ApJ, 662, 294
Panaitescu A., Kumar P., 2004, MNRAS, 353, 511
Pei Y. C., 1992, ApJ, 395, 130
Perri M., Stratta G., Evans P. A., Goad M. R., Burrows D. N., Stamatikos M., 2007, GCN Circ. 6333
Piro L. et al., 2005, ApJ, 623, 314
Quimby R. M. et al., 2006, ApJ, 640, 402

Rees M. J., Mészáros P., 1992, MNRAS, 258, 41
Rol E., Tanvir N., Kerr T., 2007, GCN Circ. 6309
Roming P. W. A. et al., 2005, Space Sci. Rev., 120, 95
Sari R., Piran T., 1999, ApJ, 520, 641
Sakamoto T. et al., 2008, ApJS, 175, 179
Schlegel D., Finkbeiner D. P., Davis M., 1998, ApJ, 500, 525
Stamatikos M. et al., 2007a, GCN Circ. 6302
Stamatikos M. et al., 2007b, GCN Circ. 6326
Stamatikos M., Parsons A., Perri M., Landsman W., Barthelmy S. D., Burrows D. N., Roming P., Gehrels N., 2007c, GCN Rep. 47.1
Tagliaferri G. et al., 2005, Nat, 436, 985
Wainwright C., Berger E., Penprase B. E., 2007, ApJ, 657, 367
Yamazaki R., 2009, ApJ, 690, 118
Zhang B., Kobayashi S., Meszaros P., 2003, ApJ, 595, 950
Zhang B. et al., 2006, ApJ, 642, 354

This paper has been typeset from a TEX/LATEX file prepared by the author.

Follow-up observations of bright core-collapse supernovae
核塌縮超新星後續光變觀測

Li-Ching Huang, Ting-Wan Chen and Wing-Huen Ip
Institute of Astronomy, NCU

There are two main mechanisms of supernova, white dwarves accretion mass from the companion stars in the binary systems and the end of massive star lives, core-collapse. Those supernovae from white dwarves are classified as type Ia supernovae, and those from the massive stars are type Ib/c or type II supernovae.Type IIn supernovae is a rarely type of supernovae, i.e., only 3% of the total supernovae. It is a kind of supernovae with dense circumstellar matter (CSM) during expansion of the supernova ejecta. Dense CSM absorbs the momentum and drains the kinetic energy from the blast wave. When the shock wave hits the material around the supernova and excites them, we can then observe the emission lines in the spectra. The higher mass-loss rates or slower wind speeds make more luminous SNe IIn.

We chose a bright type IIn supernova, SN 2008ip, to follow-up. SN 2008ip was discovered on 2008/12/31 (CBET 1641) with magnitude = 15.7 (unfiltered) by Takao Kobayashi. It is located at R.A. = 12h57m50s.20, Dec. = +36°22'33".5, 30" east and 18" north of the center of its host galaxy NGC4846, with z= 0.015124. It reached the brightest magnitude on 2009/1/1, with magnitude= 15.5 (unfiltered). z=0.15124.

To observe SN 2008ip, we use SLT and LOT in B, V, R, I four bands. From 2009.01.06 to 2009.02.15, it was bright enough to observe by SLT. We observed it every 7 days if it was a good weather, and we had observed nine times during these day. After 2009.02.24, SN 2008ip was too dim to observed by SLT, so we LOT to continue the observation. From 2009.02.24 to 2009.07.20, we had observed fifteen times. We got the images of SN 2008ip from age = 6 days to 201 days by SLT and LOT.

We compare the light curves of SN 2008ip with other type IIn supernovae, SN 1988Z, SN 1995G and SN 2006tf, and found that because there is no an unified model, type IIn supernovae can not be standard candles. Second, the smaller magnitude decay in R band and I band of SN 2008ip may be caused by the interaction with circumstellar matter on the galaxy arm. Also, SN 2008ip was dimer than SN 2006tf in absolute magnitudes. This means that the progenitor of it might have lower mass than SN 2006tf.

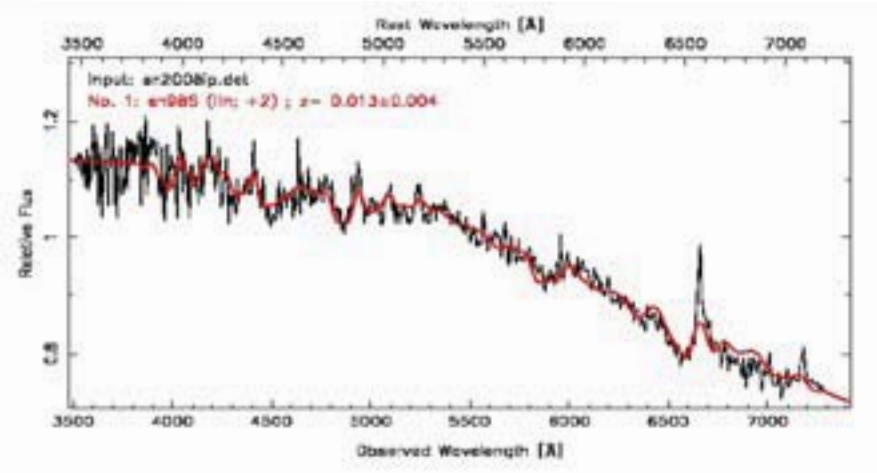

Fig. 1 The spectrum of SN 2008ip. It can be found narrow Hα emission line at λ=6563Å in SN 2008ip spectrum, so we can identify that it is a type IIn supernova. (CfA spectrum, http://www.cfa.harvard.edu/ssn2008ip.jpg

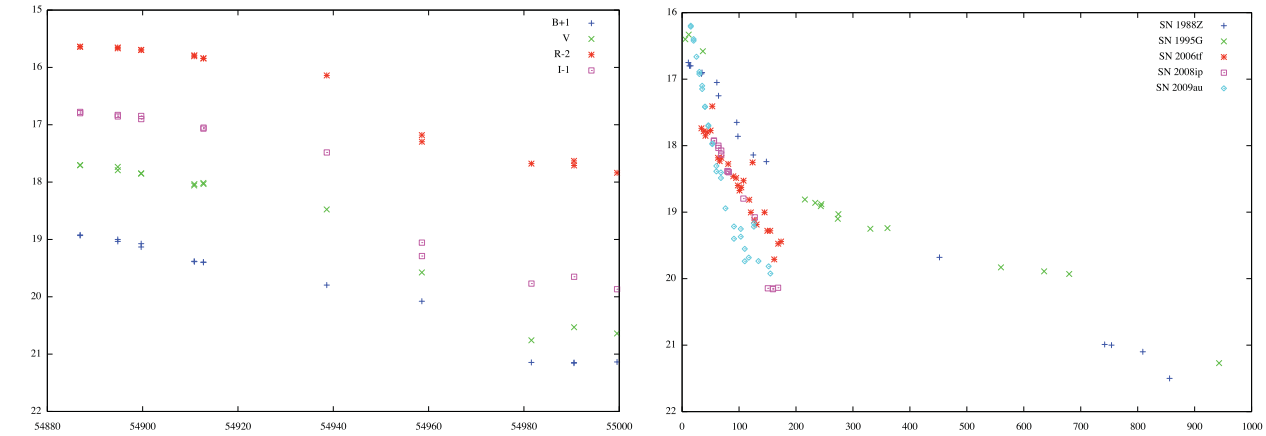

Fig. 2 (Right) The light curves of SN 2008ip. (Left) The light curves of five type IIn supernovae, SN 2008ip, SN 2009au, SN 1988Z, SN 1995G and SN 2006tf, in B band.

Weighting the Jovian Trojans: Searching for the possible binary Trojans

Lin, Hsing-Wen 林省文, Institute of Astronomy, NCU 中央大學天文所

In 2009B we performed sparse-sampled (Mann et al. 2007) photometric survey for about 60 known L4 Jovian Trojans with LOT, and tried to identify the possible binary Trojans. The goals of this project are: 1. to derive the bulk densities of the Trojans, and 2. to calculate the binary fraction. This two observable properties will shed new light on the origin of Jovian Trojans and improve our knowledge of Solar system formation and planetary migration.

A fully automatic image processing pipeline have been produced to present the differential photometry and photometric range of the asteroids. The preliminary result shows the photometric range distribution of L4 Trojans might be different with distribution of L5 Trojans. Also, we select two possible binary candidates from these data set.

Figure 1 shows the relationship between absolute magnitude and photometric range. The L5 data and some L4 data are from Mann et al (2007). It does not show any special feature, the photometric range is not the function of Absolute magnitude for Jovian Trojan in 8<H<13.

Figure 2 are the histograms of the photometric range. L4 and L5 seem have different distribution. This result may point out the different origin of L4 and L5 Jovian Trojans, but it is still unsure.

Figure 1

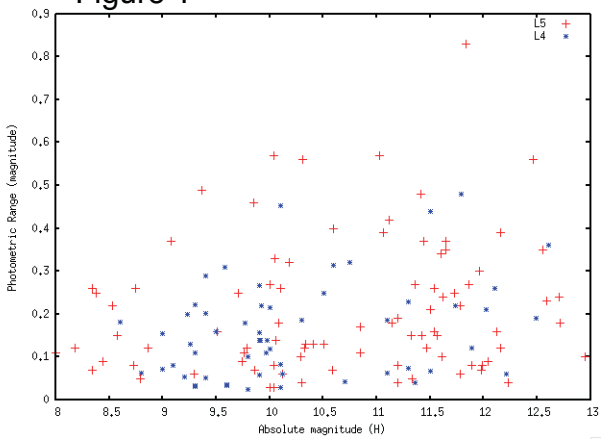

Figure 2

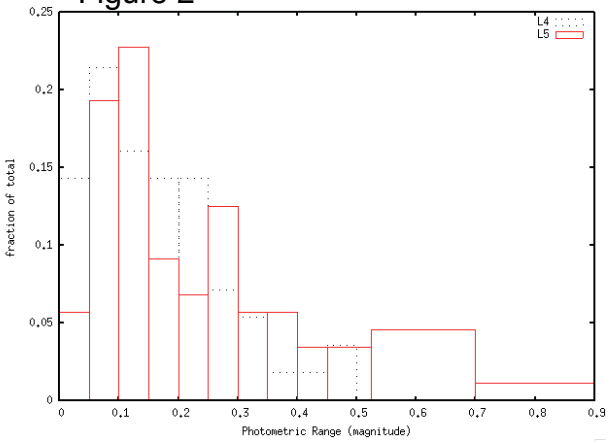

The 2009B observation also identify some possible binary systems. All of them have large photometry range. Figure 3 shows the lightcurves of one of the candidate.

Figure 3

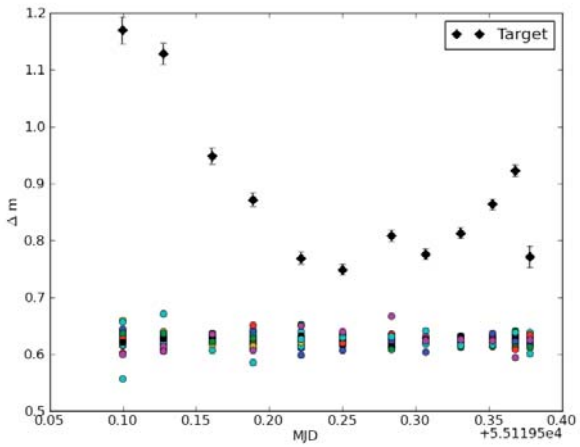

Limiting Magnitudes and Sky Background Brightness Measurements at Lulin Observatory

Lin, Chien-Cheng, Yang, Ting-Chang, Daisuke Kinoshita, Chow-Choong Ngeow

Institute of Astronomy, NCU, Taiwan

m949006@astro.ncu.edu.tw

ABSTRACT

The Lulin One-meter Telescope at Lulin Observatory in Taiwan is going to be used for the follow-up observations for the Pan-STARRS sky surveys. In order to evaluate the performance of the CCD photometric system and the characteristics and quality of the site, we have obtained the data of photometric standards as well as calibration data on 01 August, 2009. We report the results of our analysis of the sky background brightnesses and limiting magnitudes in B, V, R, I bands. The limiting magnitude derived from magnitude differences is useful for follow-up observations. This method will be used for next observation run with SDSS filters.

Subject headings: photometry, limiting magnitude, sky background brightness

1. Introduction

Institute of Astronomy at National Central University (IANCU) is participating the Pan-STARRS[1](PS1) Science Consortium, and will be able to access the data of PS1 sky surveys. In order to achieve our scientific goals, immediate and intensive follow-up observations are necessary. The Lulin Observatory (Longitude = $120°52'25''E$, Latitude = $23°28'7''N$ and at a height of 2862 m above sea level) is one of the best-placed sites in Taiwan for following up the PS1 sky survey. Because of its location, there is no other observatory join PS1 project between Hawaii and Europe. Besides, the latitude of Lulin observatory is also comparable to Hawaii.

Before scientific follow-up observations begin, it is extremely important to evaluate and calibrate the instrument of the observatory. The performance and characteristics of the imaging camera, which currently installed at LOT(Lulin One-meter Telescope), was done by Kinoshita et al. (2005); however, we have replaced a set of broadband filters in 2007. Moreover, a new set of SDSS like filters[2], g′-, r′-, i′- , z′-band, will be installed soon. Thus, we need to characterize the new photometric system, by measuring the limiting magnitude, as well as the sky background brightness of the site, for the future follow-up observations.

[1]http://pan-starrs.ifa.hawaii.edu/public/

[2]http://www.sdss.org/dr7/instruments/imager/index.html#filters

2. Observation and Data Reduction

Photometric standard star field PG2213-006 (RA= $22^{\rm h}16^{\rm m}23^{\rm s}$, Dec. $= -00°21'41''$) was observed with LOT using Bessell B, V, R, I band filters (Yang and Lin 2006) on 01 August, 2009. PI1300B CCD camera was used(1300 × 1340 pixels, plate scale $0\farcs52$ pixel^{-1}, $\sim 11\farcm0 \times 11\farcm0$ field of view). The CCD has a readout noise of 4.6 ± 0.5 e^- and a gain of 1.95 ± 0.02 e^-/ADU(Huang et al. 2008). Flat-field exposures were obtained on the twilight sky. The seeing condition within this run of observation varied between $1\farcs8$ and $2\farcs3$, because of thin clouds sometimes appeared during observation, which is slightly higher than the average seeing at Lulin Observatory of $1\farcs59$ (Lin 2007).

There were 16 exposures of PG2213-006 in total. Pairs of two consecutive exposures were taken in B, V, R, I bands. Our observational strategy is suitable for calculating limiting magnitudes. The journal of observations is summarized in Table 1. The standard data reduction routines, including bias and dark current subtraction and flat-field correction, were done in IRAF(Image Reduction and Analysis Facility, provided and maintained by NOAO)(Tody 1986, 1993).

3. Photometric Calibration

We detected the point sources using "`source extractor`"[3](Bertin and Arnout 1996) and measured their positions and instrumental magnitudes that the magnitudes were derived from aperture photometry. Then, we used the "`imwcs`" task of WCSTools[4] together with the USNO-B1.0 catalog (Monet et al. 2003) to convert the image coordinate system into world coordinate system. In order to compare our results of photometry with other instruments, we need to calibrate the magnitudes from instrumental system into the standard system. According to our observation schedule, half an hour interval and only one field observation, we could not have enough airmass information of different zenith distances to estimate the extinction coefficients. We, therefore, ignored the extinction

[3]http://sextractor.sourceforge.net/

[4]http://tdc-www.harvard.edu/software/wcstools/

Table 1. Journal of Photometric Observations of PG2213-006 FOV,

Observation Date	Filter	Airmass	Exposure Times [sec]	Seeing[arcsec]
2009 August 1	B	1.259/1.297	40×2/320×2	2.3/2.0
2009 August 1	V	1.267/1.338	20×2/160×2	2.1/1.9
2009 August 1	R	1.274/1.364	10×2/80×2	2.0/1.8
2009 August 1	I	1.280/1.386	20×2/160×2	1.8/2.0

coefficient term and color term of the transformation equations. We defined simple transformation equations for the conversions,

$$B_{\rm std} = B_{\rm inst} + \triangle_B, \quad (1)$$
$$V_{\rm std} = V_{\rm inst} + \triangle_V, \quad (2)$$
$$R_{\rm std} = R_{\rm inst} + \triangle_R, \quad (3)$$
$$I_{\rm std} = I_{\rm inst} + \triangle_I, \quad (4)$$

where $B_{\rm std}, V_{\rm std}, R_{\rm std}, I_{\rm std}$ are the standard magnitudes, $B_{\rm inst}, V_{\rm inst}, R_{\rm inst}, I_{\rm inst}$ are the instrumental magnitudes, and $\triangle_B \sim 22.78, \triangle_V \sim 22.48, \triangle_R \sim 22.59, \triangle_I \sim 21.83$ are relative zero points. Seven standard stars provided by Landolt (2009) were used to calibrate the instrumental magnitudes.

4. Sky Background Brightness

We used the data taken on 01 August, 2009 to measure the sky background brightness. The moon phase was 10.1. During the observation, the moon was below the horizon, and the angular separations between the moon and our target field was 72 degrees. `Source extractor` was used to obtain the mean background values in each bands. Using equations 1 to 4, we derived the magnitudes of sky background brightness in the standard system. The sky background brightness in B, V, R, I bands are $B = 21.38 \pm 0.41$, $V = 20.14 \pm 0.26$, $R = 20.06 \pm 0.24$, and $I = 18.92 \pm 0.20$ mag arcsec^{-2}, respectively. Since we had narrow range of airmass ~ 1.30 in each bands, we ignored the airmass coefficients and color terms while we evaluated the transformation equations. The error of the magnitudes are believed to be lower limits on the actual uncertainties. Compared to Kinoshita et al. (2005), $B = 22.0, V = 21.3, R = 20.9$, and $I = 19.5$, we believe our estimation of sky background brightness brighter than before might be due to the moon in the west and the light pollution from nearby cities.

5. Limiting Magnitudes

The detection limit of the images can be estimated and/or measured in several ways: (1)Maximum number of stars in histogram (Gwyn 2008), (2)Magnitudes versus error of magnitudes (Gwyn 2008), (3)Magnitude differences between two images (Ito 1998). The first method is very simple. The peak value of the histogram, where the number of stars start to turn over, is a rough measure of the detection limit of the image. Figure 1 shows the number of stars with histogram. However, the stars are not enough for its completeness. Therefore, we will not use this method for calculating the limiting magnitudes.

Figure 2 shows standard magnitude against magnitude errors using the second method, a 10-sigma detection corresponds to a signal-to-noise ratio (S/N) of 10 and approximate to a magnitude error of 0.1 magnitudes. The magnitude error of stars were returned from `source extractor`. To

evaluate the limiting magnitudes from Figure 2, we used a third-order polynomial function to fit these data.

Figure 3 to 6 demonstrate the third method which is standard magnitudes against magnitude differences from pairs of two consecutive exposures in B, V, R, I bands. We divided the total number of stars into seven bins from brightest to faintest stars for short exposure (upper panel) and ten bins for long exposure (lower panel), and error bars indicated the standard deviation in each bin. Each bin has the same number of stars. We estimated the limiting magnitude if the error of bins is larger than the error of magnitude difference 0.14mag, considering m_{1err} or m_{2err} equals to 0.1 magnitude or, approximately, S/N=10. The error of magnitude difference can be derived from the following equation,

$$(m_1 - m_2)_{err} = \sqrt{m_{1err}^2 + m_{2err}^2} \tag{5}$$

where m_{1err}, m_{2err} are error of the measurements, and $m1, m2$ are standard magnitudes for pairs of two consecutive exposures. If m_{1err} and m_{2err} are about the same and assuming that the correlation between m_1 and m_2 is negligible. Then $(m_1 - m_2)_{err}$ will approximate to $\sqrt{2}m_{1err}$ or $\sqrt{2}m_{2err}$. The results for the thrid method are given in Table 2.

6. Discussion and Summary

One night observation data, 01, August 2009, was used to perform the analysis of sky brightness and limiting magnitudes for PI1300B CCD installed at LOT. We derived simple transformation equations without considering the extinction coefficient and the color terms. The sky background brightness brighter than five years ago might be due to not only moon light effect but also the light pollution from nearby cities.

When comparing with method 1, 2 and 3, we found that the results are slightly different. For method 1, it is a very rough estimate. If we want to determine limiting magnitudes accurately, we need to have enough stars for the completeness. Then we can estimate the limiting magnitudes by assuming a power law function to fit the histogram. However, it is not a proper method according to our observation strategy. For method 2, one needs to assume a polynomial function model to fit the data of magnitude versus magnitude errors. In addition, magnitude error of stars will be different depend on how one gets the star magnitudes. Therefor, there are too many uncertainties of the assumptions for us using this method. For method 3, we do not need to assume any models or functions to fit the data of magnitude versus magnitude differences. It is much convenience of the limiting magnitude estimation. And the other advantage of method 3 is that we can ignore the systematic changes of observing conditions during the acquisitions of pairs of images since we observed two images within very short time intervals. We will adopt the limiting magnitudes estimated from magnitudes versus magnitude differences as our final results. And this method will be used for SDSS filters when they are installed as well.

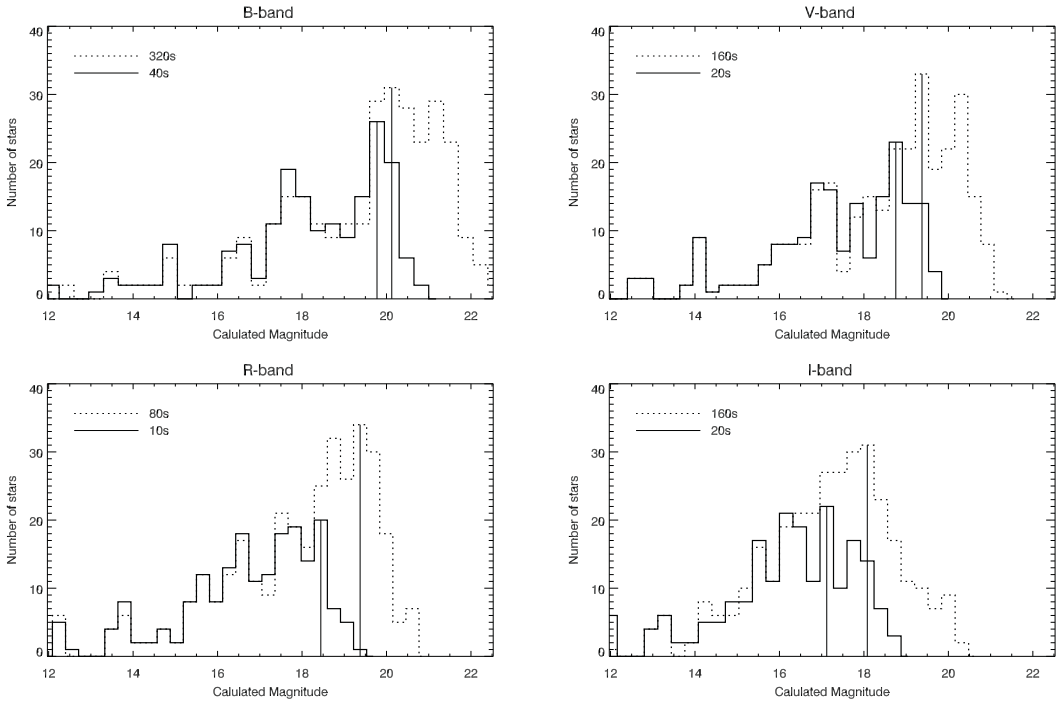

Fig. 1.—: Number of stars count in histogram for $BVRI$ bands. The dashed and solid lines are for the long exposure and short exposure, respectively. Vertical solid straight lines indicate the maximum star counts related the limiting magnitudes.

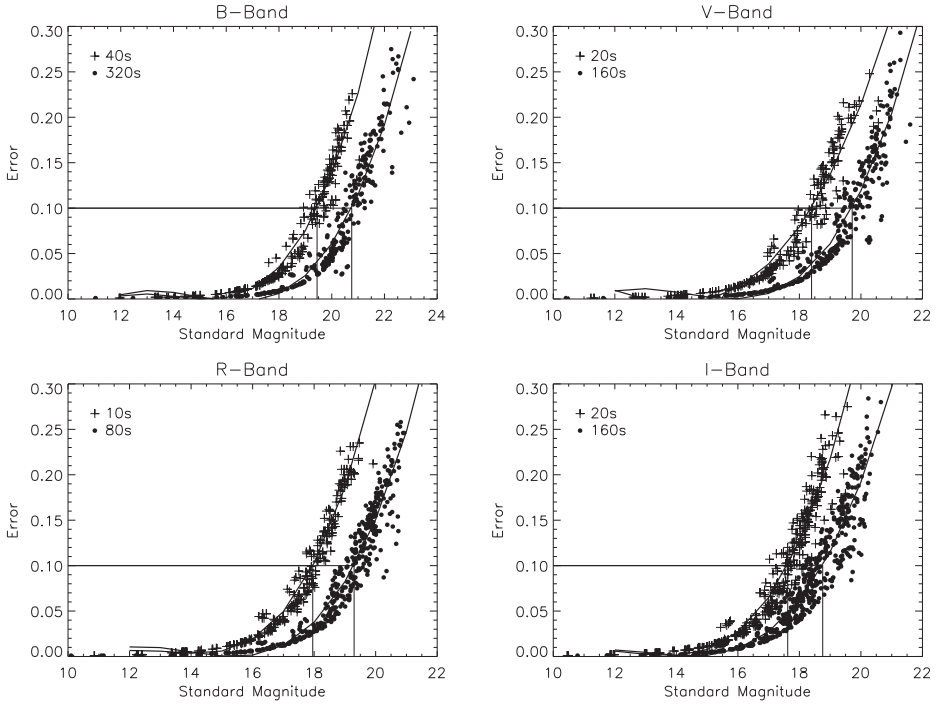

Fig. 2.—: Standard magnitude using transformation equations given in equation (1) to (4) versus magnitude errors in $BVRI$ bands. Crosses are short exposure time with 40, 20, 10, 20 seconds for BVRI band, respectively, while fill circles are long exposure time with 320, 160, 80, 160 seconds, respectively. The solid curves are fitted results to these data.

Acknowledgement : We would like to thank the staff in Lulin Observatory for the logistics. Chien-Cheng, Lin would like to thank Prof. Wen-Ping, Chen's for helpful discussions and comments.

REFERENCES

Bertin, E. and Arnouts, S. 1996, A&A Supplement 317, 393

Gwyn, Stephen D. J. 2008, PASP, 120, 212

Huang, H.F. , Kinoshita, D., and Shih, C.Y. 2008, JTAM Vol. 6, p. 18.

Ito, N. 1998, Report of Kiso Observatory, http://www.ioa.s.u-tokyo.ac.jp/kisohp/INSTRUMENTS/2kccd/reports/981126.ps

Kinoshita, D., Chen, C. W., Lin, H. C., Lin, Z. Y., Huang, K. Y., Chang, Y., and Chen, W. P. 2005, Chin. J. Astron. Astrophys., 5, L315

Landolt, A. U. 2009, AJ, 137, 4186

Lin, H.C. 2007, Annual Report of Lulin Observatory, edited by Chang, M.S., p. 72.

Massey, P. 1990, NOAO Newsletter, March, p. 16.

Monet, D., et al. 2003, AJ, 125, 984

Tody, D. 1986, in Proc. SPIE Instrumentation in Astronomy VI, ed. D.L. Crawford, 627, 733

Tody, D. 1993, in Astronomical Data Analysis Software and Systems II, A.S.P. Conference Ser., Vol 52, eds. R.J. Hanisch, R.J.V. Brissenden, & J. Barnes, 173.

Yang, T.C. and Lin, H.C. 2006, Annual Report of Lulin Observatory, edited by Chang, M.S., p. 67.

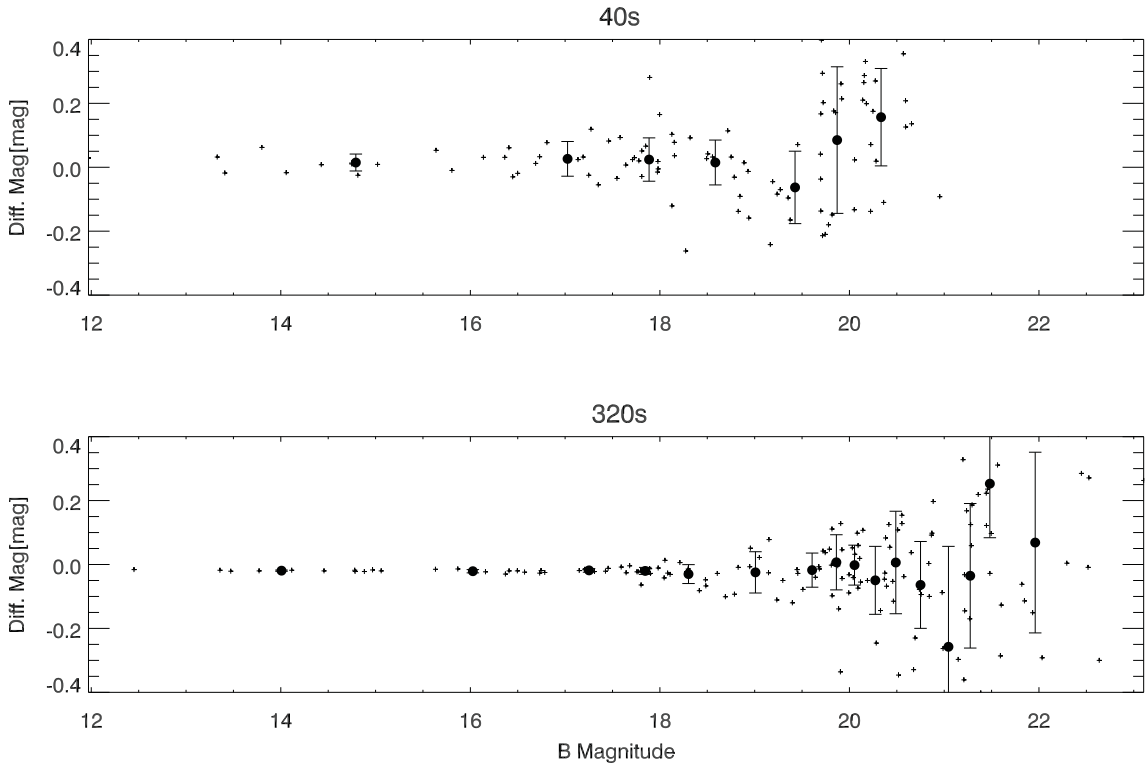

Fig. 3.—: Standard B-band magnitudes against difference magnitudes using two adjacent images. The panel on top is for short exposure images, and bottom panel is for long exposure images. Solid circles are averages in each bins.

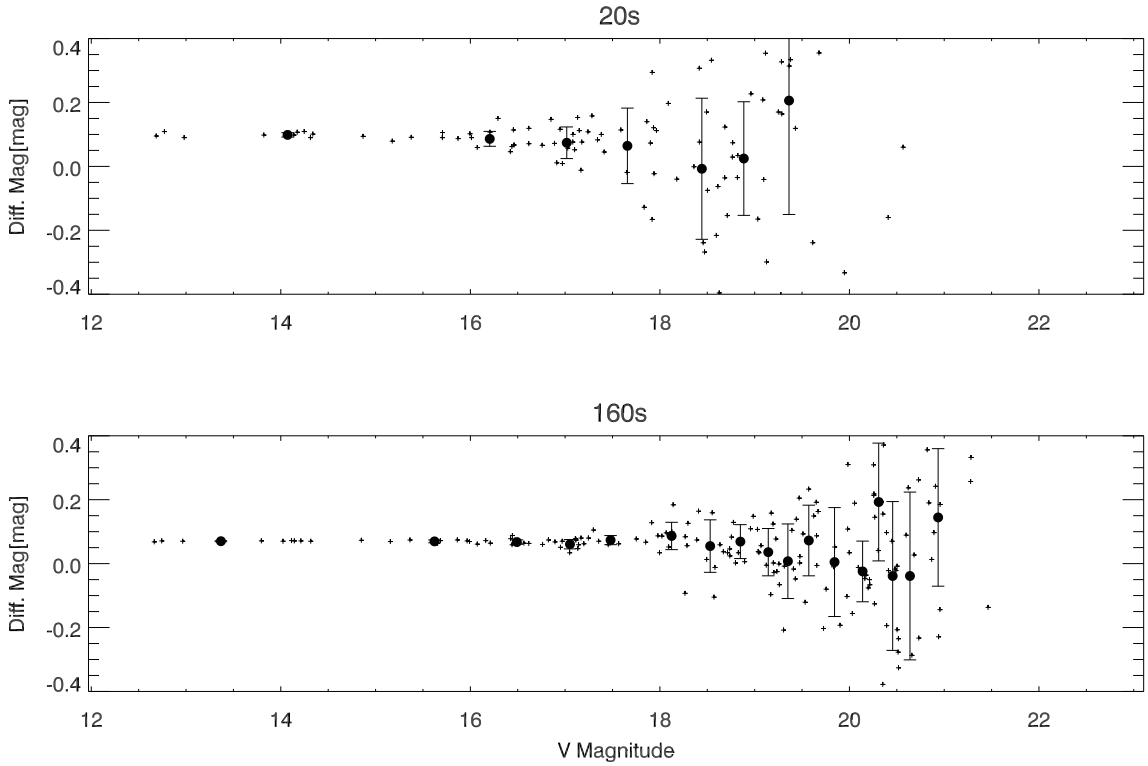

Fig. 4.—: Sampe as Figure 3, but for V-band.

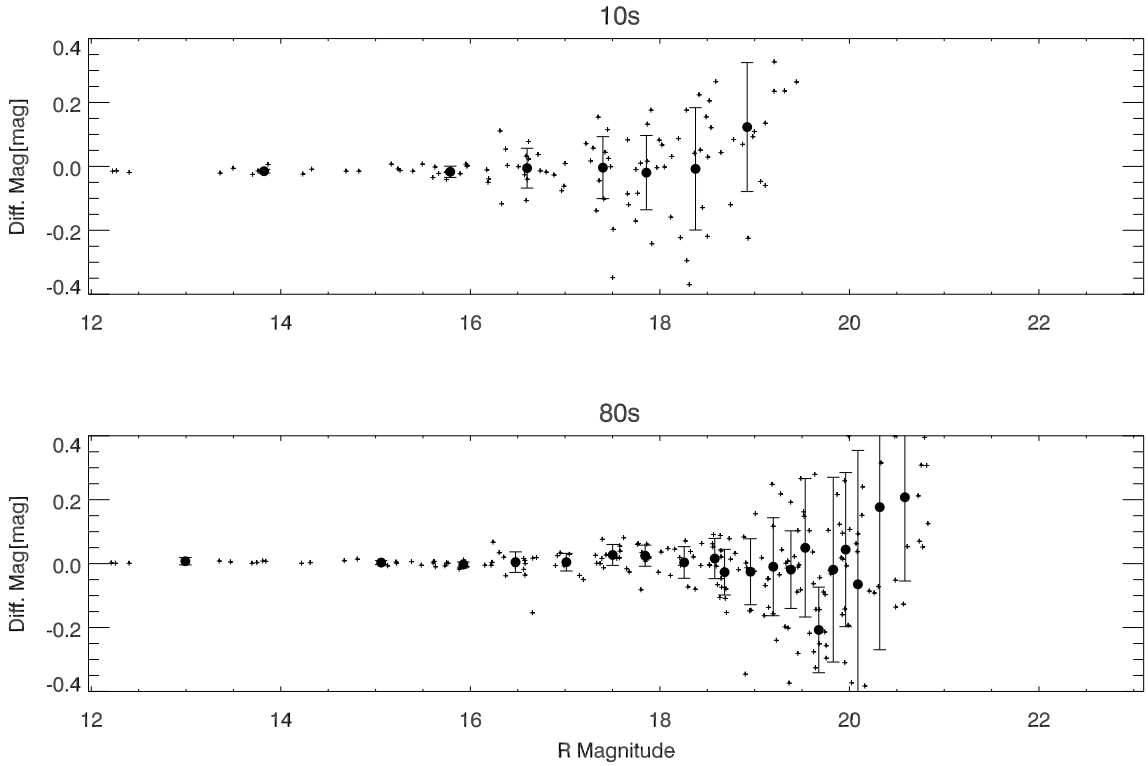

Fig. 5.—: Sampe as Figure 3, but for R-band.

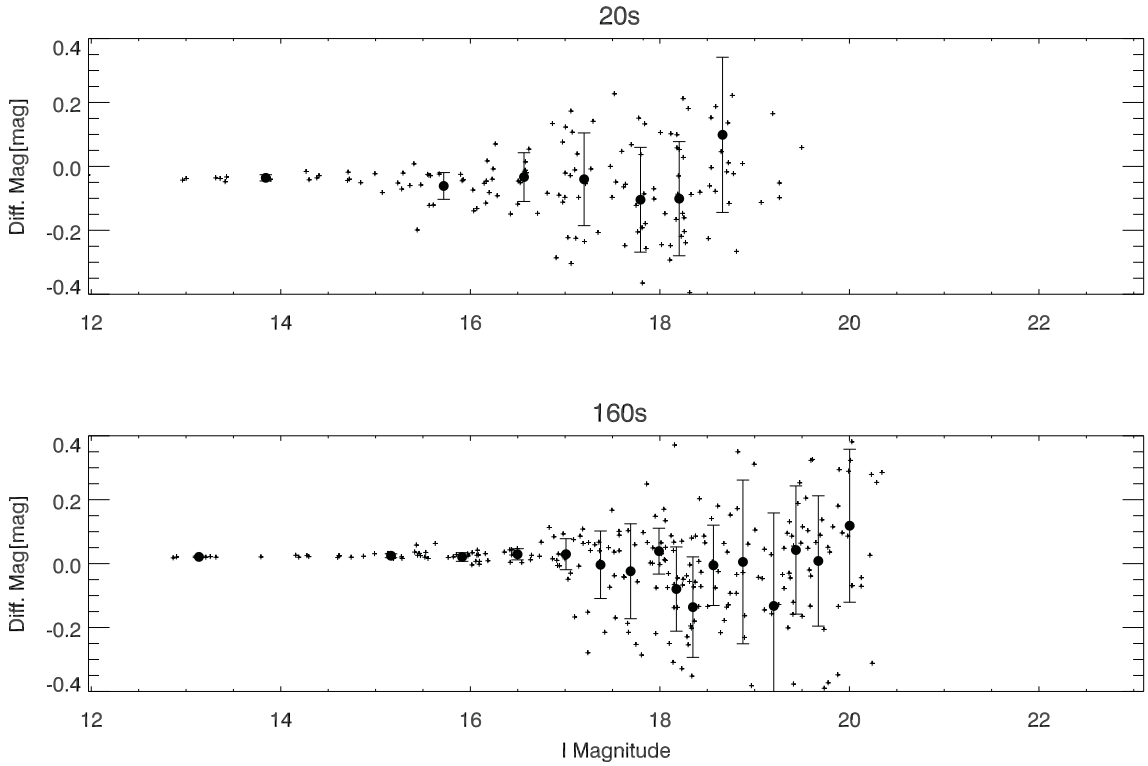

Fig. 6.—: Sampe as Figure 3, but for I-band.

Table 2. Comparison of limiting magnitudes from the three methods mentioned in text.

Filter	Exposure Times [sec]	Number of Stars[a]	Method 1[b]	Method 2[c] S/N=10	Method 3[d] S/N=10
B	40	111	19.7mag	19.4mag	19.6mag
B	320	187	21.1mag	20.8mag	20.4mag
V	20	109	18.7mag	18.4mag	18.3mag
V	160	194	20.1mag	19.7mag	19.8mag
R	10	126	18.3mag	18.0mag	17.9mag
R	80	239	19.7mag	19.3mag	19.6mag
I	20	167	18.0mag	17.6mag	17.4mag
I	160	295	18.4mag	18.8mag	18.4mag

[a]Total number of stars in the field of view

[b]Maximum number of stars in the histogram

[c]Magnitudes versus error of magnitudes

[d]Differential magnitudes.

The Infuences of the Different CCD Thicknesses and Cooling Temperature on the Liniting Magnitude

Ru-Huei Huang, Kinoshita Daisuke, Ching-Huag Wu, I-Cheng Shen, Tse-Chuan Chen, Yuji Urata
Graduate Institude of Astronomy, National Central University

CCD (Charge Couple Device) is the most popular detector which is used in astronomical observations. The advantages include low noise, good linearity, high quantum efficiency, and high dynamic range. The limiting magnitude of the instrument is an important index for observation planning. It is essential for efficient execution of observations to know the limiting magnitude prior to the observation.

We focus on two properties of the CCD. One is the cooling temperature of the CCD, and the other is thickness of the depletion layer. The amounts of lower readout noise and dark current strongly depends on the cooling temperature. We could expect significant decrease of the noise at lower CCD operating temperature. There are two common problems for the conventional thinned CCDs. One is that the quantum efficiency (QE) at longer wavelength region is very poor (~ 10% at λ = 900nm ~ 1000nm). The other is the fringe pattern at longer wavelength region is serious and causes larger photometric errors. The thicker deep depletion and fully depleted CCDs achieve higher QE and less fringe pattern.

We have four CCD cameras. Table 1 lists the specifications of the cameras. The PI1300 and Andor936 CCD cameras are for 1-m telescope and SI1100 and NCU-cam CCD cameras are for upcoming 2-m telescope. The specifications and operation conditions of the instrument influence the limiting magnitude.

Before the actual observations, we can use the theoretical calculations to inspect the observational results whether is reliable. Therefore, We use CCD Equation （ Massey 1990 ） as Eq. (1) to estimate limiting magnitude.

$$\frac{S}{N}=\frac{Nt}{\sqrt{Nt+n_{pix}\left(N_S t+N_D t+N_R^2\right)}} \qquad (1)$$

S/N is signal-to-noise ratio, N is the count rate in electrons per second, N_S is the total number of photons per pixel from the background or sky, N_D is the total number of dark current electrons per pixel, N_R is the total number of electrons per pixel resulting from the readout noise, n_{pix} is pixel number within an aperture area, and t is the CCD integration time. We assume signal-to-noise ratio

of 10 within an integration time of 300 sec to calculate limiting magnitude. The calculated limiting magnitudes for Bessel UBVRI bands and SDSS g',r',i',z' bands.

Here report preliminary the results of our calculations. The results show that PI1300 camera seems to have fainter limiting magnitude, it might be because of some specifications and operation conditions is not reliable. However, it is extremely important to measure the dependency of the cooling temperature and depletion layerthickness on the limiting magnitude quantitatively. Therefore, we will use our new cameras to perform a series of observations in 2010A semester. After analyze the observational results, we will make the comparison and the discussion for the theoretical and the actual difference.

Table 1. The specifications of the four cameras. Top is operating temperature of the CCD. The dark current (electron/pixel/sec) and the readout noise (electron/pixel/sec) are derived from previous work (Kinoshita et al. 2005).

	PI1300	Andor936	SI1100	NCU-cam
Pixel number	1340 X 1300	2048 X 2048	2048 X 4096	2048 X 4096
Pixel size	20μm X 20μm	13.5μm X 13.5μm	15μm X 15μm	15μm X 15μm
Thickness	15μm	15μm	40μm	200μm
Dark current	0.064	0.007	0.0001	0.001
Readout noise	4	4	3	5
T_{op}	-50°C	-70°C	-100°C	-100°C

Table 2. Calculated limiting magnitudes for four CCD cameras.

	U	V	B	R	I	g'	r'	i'	z'
PI1300	19.8	21.7	21.2	21.0	20.0	19.1	19.2	19.5	19.2
Andor936	19.3	21.7	21.2	21.0	20.0	19.1	19.2	19.5	19.3
SI1100	19.5	21.6	21.1	21.0	20.1	19.1	19.4	19.5	19.4
NCU-cam	19.6	21.7	21.2	21.0	20.0	19.0	19.2	19.5	19.5

Figs. Those figures plot integration time versus calculated magnitude for Bessel UBVRI bands

and SDSS g',r',i',z' bands.

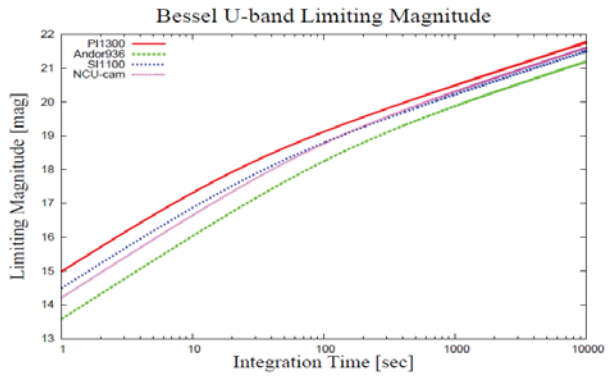

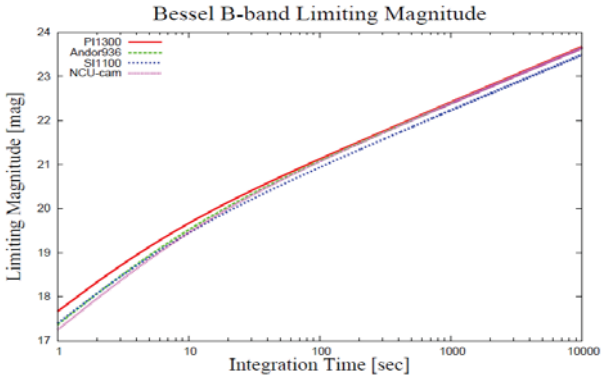

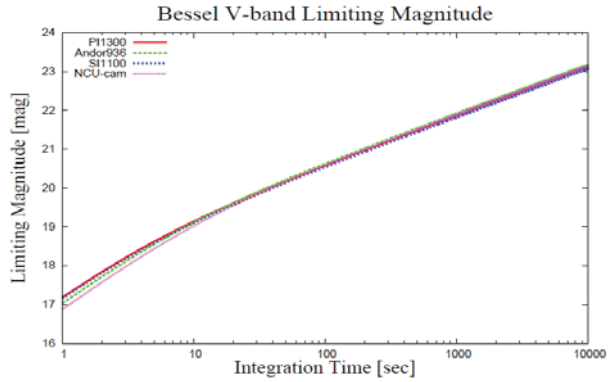

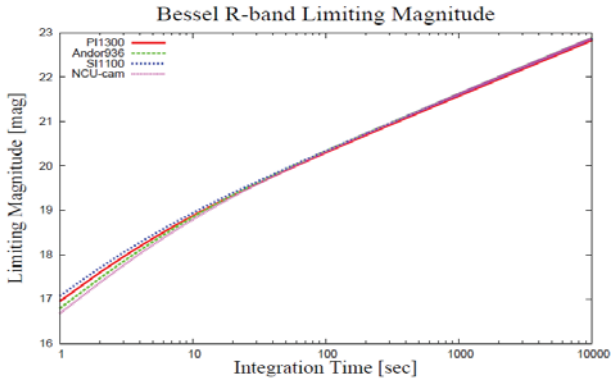

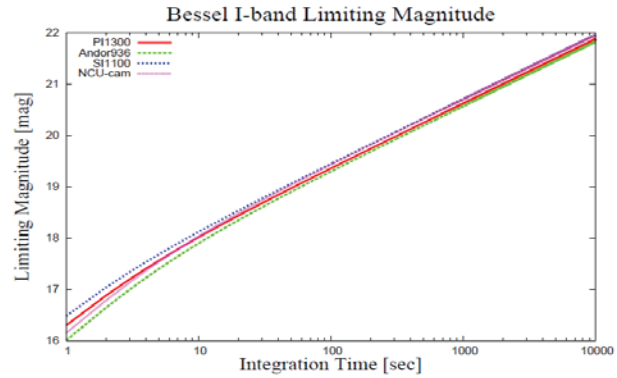

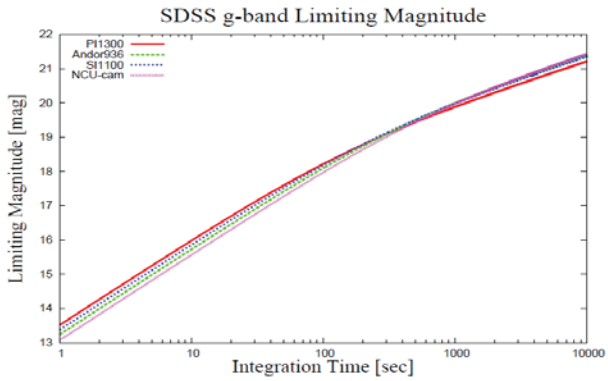

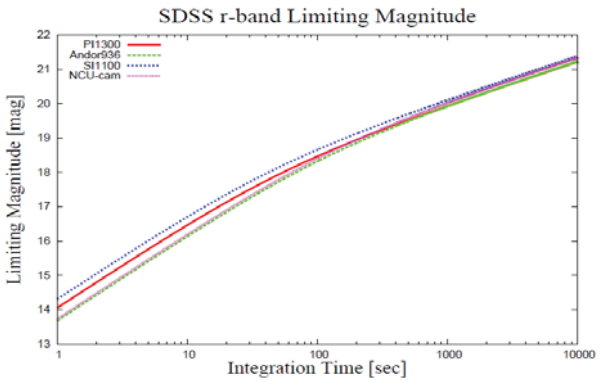

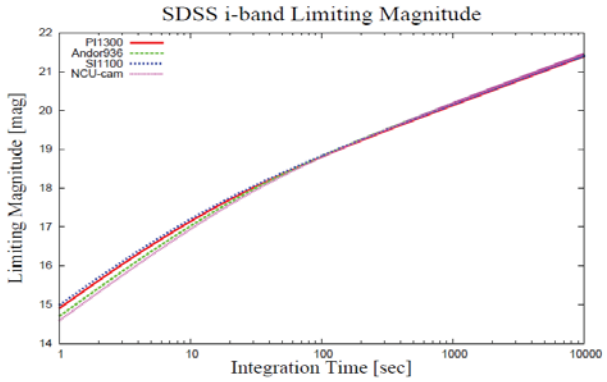

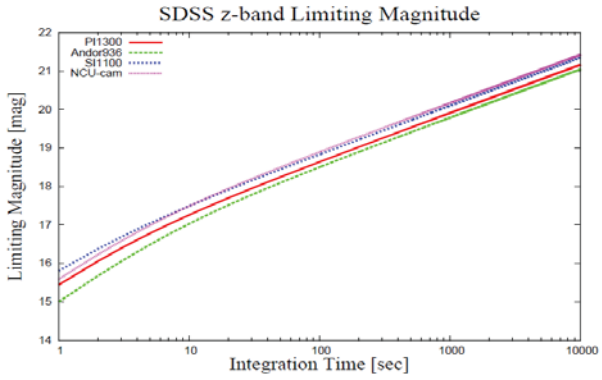

An Overview of Lulin Sky Survey

Quanzhi Ye
Department of Atmospheric Science, Sun Yat-sen University, Guangzhou, China (mainland)

ABSTRACT

A three-year survey program of small solar system bodies was carried out with the 0.41-m Ritchey-Chretien telescope at Lulin Observatory in Taiwan from 2006-2009, the program is performed remotely from mainland China with self-developed robotic software and was aimed at detecting new minor planets and comets, as well as improving the orbits of known minor planets and comets. Photometric studies of a few selected unusual minor planets have also been conducted. During the three-year study, a total of 781 new objects were discovered, including C/2007 N3 (Lulin) and three fragments of 73P/Schwassmann-Wachmann. A total of 80,934 astrometric observations were reported to the Minor Planet Center, with an internal error below 0.5". As the observatory is located at a longitude where there are few other minor planet observers, the program also provided immediate confirmation for a number of newly-discovered near-Earth asteroids. The possibility of detecting transients (such as supernovas or long-period variable stars) using the data is also explored.

CCD LIGHTCURVE ANALYSIS OF (53430) 1999 TY16

Quanzhi Ye
Department of Atmospheric Science, Sun Yat-sen University, Guangzhou, China (mainland)
tom6740@gmail.com

Liaoshan Shi
School of Physics and Engineering, Sun Yat-sen University, Guangzhou, China (mainland)

Hung-Chin Lin
Graduate Institute of Astronomy, National Central University, Chung-li, Taiwan

(Received: 2009 Apr. 4 Revised:)

Photometric observations of high-inclination near-Earth asteroid (53430) 1999 TY16 were obtained in the course of Lulin Sky Survey (LUSS) in late 2008. These data allowed determination of the rotation period to be 9.582 ± 0.001 h.

High inclination near-Earth asteroid (53430) 1999 TY16 was discovered by LINEAR program on 1999 October 13 (Williams, 1999) and no photometric result had been published before this work. From 2008 November 14 to December 3, six nights of data were obtained using Lulin Observatory's 0.41-m Ritchey-Chretien telescope equipped with a 4-mega pixel back-illuminated CCD. The data were measured with Raab's *Astrometrica* and Warner's *MPO Canopus* and were internally calibrated with Warner's UCAC-2MASS system (Warner, 2007). The observations clearly yielded a period of 9.582 ± 0.001 h (Figure 1) with the magnitude amplitude to be 0.8 mag.

BVRI observations were also obtained on November 21 and 30, but reduction to a standard system was not possible due to an insufficient number of standard stars in the image and poor photometric conditions.

Acknowledgements

We would like to thank Brian D. Warner for his review of the manuscript. We would like to thank Hsiang-Yao Hsiao and Chi Sheng Lin for their assistance on obtaining the observations. This work is supported by a 2007 Gene Shoemaker NEO Grant from the Planetary Society. The 0.41-m Ritchey-Chretien telescope is operated with support from the Graduate Institute of Astronomy, National Central University.

Reference

Warner, B. W. (2007). "Initial Results from a Dedicated H-G Project", *Minor Planet Bulletin* **34**, 113-119.

Williams, G. V. (1999). "1999 TY16" *MPEC* 1999-U07.

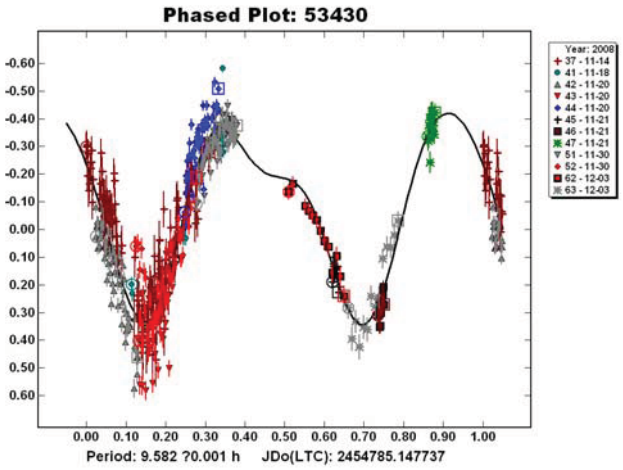

PHOTOMETRIC OBSERVATIONS AND LIGHTCURVE ANALYSIS OF NEAR-EARTH ASTEROIDS (136849) 1998 CS1, 2006 SZ217 AND 2008 UE7

Quanzhi Ye
Department of Atmospheric Science, Sun Yat-sen University, Guangzhou, China (mainland)
tom6740@gmail.com

Liaoshan Shi
School of Physics and Engineering, Sun Yat-sen University, Guangzhou, China (mainland)

Wentao Xu
School of Physics and Technology, Wuhan University, Wuhan, China (mainland)

Hung-Chin Lin
Graduate Institute of Astronomy, National Central University, Chung-li, Taiwan

Junfeng Zhang
Department of Atmospheric Science, Sun Yat-sen University, Guangzhou, China (mainland)

(Received: Revised:)

Near-Earth Asteroids (NEAs) (136849) 1998 CS1, 2006 SZ217 and 2008 UE7 were observed photometrically in the course of Lulin Sky Survey (LUSS) in December 2008 and January 2009, the rotation periods and lightcurve amplitudes for these three asteroids have been determined as 4.150 ± 0.001 h and 0.11 mag for (136849) 1998 CS1, 3.2474 ± 0.0001 h and 0.10 mag for 2006 SZ217, and 3.25146 ± 0.00001 h and 0.13 mag for 2008 UE7.

Photometric studies of three near-Earth asteroids (NEAs) were carried out in December 2008 and January 2009 in the course of Lulin Sky Survey (LUSS). LUSS was equipped with a 0.41-m Ritchey-Chretien telescope operating at F/6.25 and a back-illuminated Apogee U42 CCD. It was mainly aimed at gaining astrometric observations of asteroids and comets, but photometric studies were performed occasionary and were mostly focus at unusual asteroids such as NEAs or asteroids with large eccentricity. CCD images were reduced and calibrated remotely by the automatic pipeline *INT* (Ye, 2008) and then were transferred to a local computer. The brightness variations of asteroids were determined by differential photometry using *MPO Canopus* while the astrometric data was measured by *MPT* (Ye, 2008). The observing procedure and result for each asteroid is described below.

(136849) 1998 CS1 was discovered by Beijing Schmidt CCD Asteroid Program (SCAP) on 1998 Feburary 9 (Tichy et al., 1998) and is classified as a Potentially Hazardous Asteroid (PHA). No photometric result has been published before this work. From 2009 January 8 to 11, three nights of data were successfully obtained, and a period of 4.150 ± 0.001 h can be yielded, the lightcurve figure is shown as Figure 1. However, an internally calibration was failed to done due to insufficient available comparison stars and we noticed that the curves of different nights do not fitted with each other very well, the possibilities of a period of 5.54 h or a much longer one, although not significant, cannot be ruled out. We have attempted to get more images in January 14-17 but were failed due to bad weather and technical problem. Further observations are recommended for this target.

2006 SZ217 was discovered by the Spacewatch program on 2006 September 30 (Bressi et al., 2006), no photometric result has been published before this work. Five nights of data was taken on December 6 to 15, but most of them were suffering from heavy moonlight and errors were as large as +/-0.1 mag for some images. However, a period of 3.2474 ± 0.0001 h can still be yielded with some confidence. The lightcurve figure is

shown as Figure 2.

2008 UE7 was discovered by LINEAR program on 2008 October 26 (Young et al., 2008) and is classified as a PHA, no photometric result has been reported yet. In this work, we obtained in total of five nights of data from December 1 to 7 and the data quality is decent. Based on the data, we are able to find found a period of 3.25146 ± 0.00001 h.

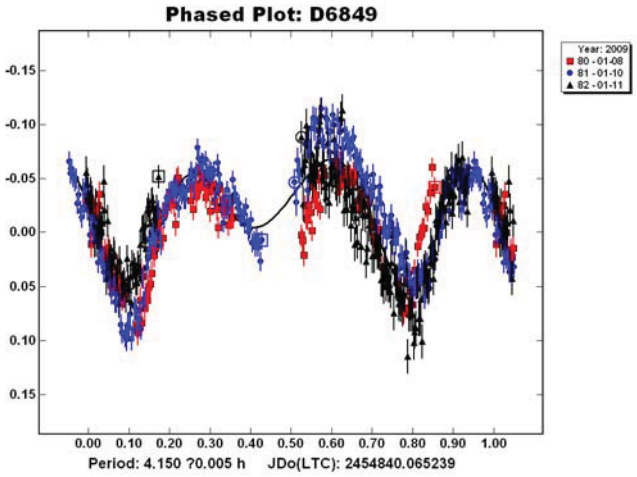

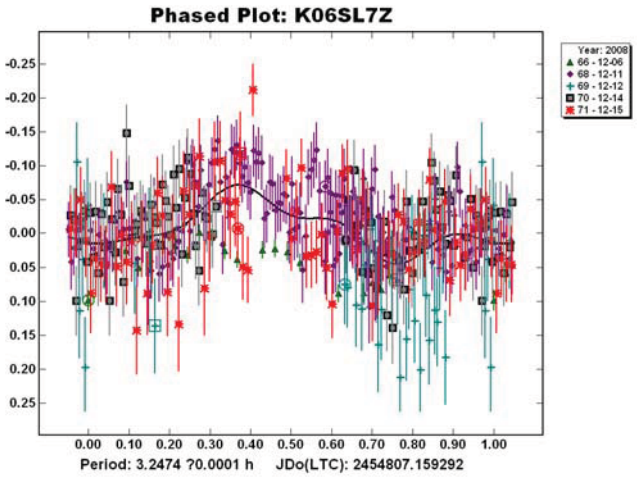

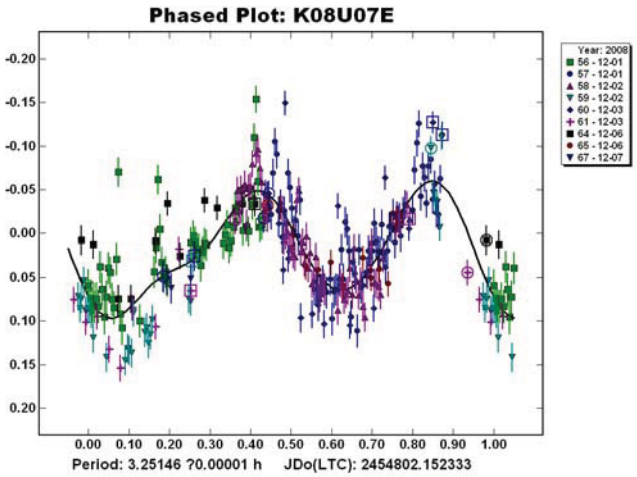

Acknowledgements

We would like to thank Hsiang-Yao Hsiao and Chi Sheng Lin for their assistance on obtaining the observations, and Atmospheric Laboratory of Sun Yat-sen University for assistance on the research. This work is supported by a 2007 Gene Shoemaker NEO Grant from the Planetary Society. The 0.41-m Ritchey-Chretien telescope is operated with support from the Graduate Institute of Astronomy, National Central University.

Reference

Bressi, T. H., Read, M. T., Tubbiolo, A. F., Hug, G., Tibbets, D., McGaha, J. E., Kowalski, R. A., Beshore, E. C., Christensen, E. J., Garradd, G. J., Gibbs, A. R., Grauer, A. D., Hill, R. E., Larson, S. M., McNaught, R. H., Birtwhistle, P., Spahr, T. B. (2006). "2006 SZ217" *MPEC* 2006-T01.

Tichy, M., Moravec, Z., Tesi, L., Boattini, A., Forti, G., Zhu, J., Chen, Y. J., Zheng, Z. Y., Li, X. Y., Nakamura, A., Williams, G. V. (1998). "1998 CS1" *MPEC* 1998-C27.

Ye, Q.-z., Lin, H.-C., Lin, C. S., Shih, C.-y. (2008). "Lulin Sky Survey", *Lulin Observatory Annual Report* **5**, 58.

Young, J., Bezpalko, M., Torres, D., Kracke, R., Spitz, G., Kistler, J., Stuart, J., Scruggs, S., Ryan, W. H., Birtwhistle, P., Spahr, T. B. (2008). "2008 UE7" *MPEC* 2008-U72.

The Astrophysical Journal, 691:L13–L19, 2009 January 20 doi:10.1088/0004-637X/691/1/L13

THE JUNE 2008 FLARE OF MARKARIAN 421 FROM OPTICAL TO TeV ENERGIES

I. Donnarumma[1], V. Vittorini[1,2], S. Vercellone[3], E. Del Monte[1], M. Feroci[1], F. D'Ammando[1,2], L. Pacciani[1], A. W. Chen[3,4], M. Tavani[1,2], A. Bulgarelli[5], A. Giuliani[3], F. Longo[6], G. Pucella[1], A. Argan[1], G. Barbiellini[6], F. Boffelli[7], P. Caraveo[3], P. W. Cattaneo[7], V. Cocco[1], E. Costa[1], G. De Paris[1], G. Di Cocco[5], Y. Evangelista[1], M. Fiorini[3], T. Froysland[2,4], M. Frutti[1], F. Fuschino[5], M. Galli[8], F. Gianotti[5], C. Labanti[5], I. Lapshov[1], F. Lazzarotto[1], P. Lipari[9], M. Marisaldi[5], M. Mastropietro[10], S. Mereghetti[3], E. Morelli[5], A. Morselli[11], A. Pellizzoni[3], F. Perotti[3], P. Picozza[11], G. Porrovecchio[1], M. Prest[12], M. Rapisarda[13], A. Rappoldi[7], A. Rubini[1], P. Soffitta[1], M. Trifoglio[5], A. Trois[1], E. Vallazza[6], A. Zambra[3], D. Zanello[9], C. Pittori[14], P. Santolamazza[14], F. Verrecchia[14], P. Giommi[14], S. Colafrancesco[14], L. Salotti[15] (The AGILE Team), M. Villata[16], C. M. Raiteri[16], W. P. Chen[17], N. V. Efimova[18], B. Jordan[19], T. S. Konstantinova[18], E. Koptelova[17], O. M. Kurtanidze[20,21,22], V. M. Larionov[18,23], J. A. Ros[24], A. C. Sadun[25] (The GASP-WEBT Team), H. Anderhub[26], L. A. Antonelli[27], P. Antoranz[28], M. Backes[29], C. Baixeras[30], S. Balestra[28], J. A. Barrio[28], H. Bartko[31], D. Bastieri[32], J. Becerra González[33], J. K. Becker[29], W. Bednarek[34], K. Berger[34], E. Bernardini[35], A. Biland[26], R. K. Bock[31,32], G. Bonnoli[36], P. Bordas[37], D. Borla Tridon[31], V. Bosch-Ramon[37], T. Bretz[38], I. Britvitch[26], M. Camara[28], E. Carmona[31], A. Chilingarian[40], S. Commichau[26], J. L. Contreras[28], J. Cortina[39], M. T. Costado[33,41], S. Covino[27], V. Curtef[29], F. Dazzi[32], A. De Angelis[42], E. De Cea del Pozo[43], R. de los Reyes[28], B. De Lotto[42], M. De Maria[42], F. De Sabata[42], C. Delgado Mendez[33], A. Dominguez[44], D. Dorner[26], M. Doro[32], D. Elsaesser[38], M. Errando[39], D. Ferenc[45], E. Fernández[39], R. Firpo[39], M. V. Fonseca[28], L. Font[30], N. Galante[31], R. J. García López[33,41], M. Garczarczyk[39], M. Gaug[33], F. Goebel[31,77], D. Hadasch[30], M. Hayashida[31], A. Herrero[33,41], D. Höhne-Mönch[38], J. Hose[31], C. C. Hsu[31], S. Huber[38], T. Jogler[31], D. Kranich[26], A. La Barbera[27], A. Laille[45], E. Leonardo[36], E. Lindfors[46], S. Lombardi[32], M. López[32], E. Lorenz[26,31], P. Majumdar[35], G. Maneva[47], N. Mankuzhiyil[42], K. Mannheim[38], L. Maraschi[27], M. Mariotti[32], M. Martínez[39], D. Mazin[39], M. Meucci[36], M. Meyer[38], J. M. Miranda[28], R. Mirzoyan[31], J. Moldón[37], M. Moles[44], A. Moralejo[39], D. Nieto[28], K. Nilsson[46], J. Ninkovic[31], I. Oya[28], R. Paoletti[36], J. M. Paredes[37], M. Pasanen[46], D. Pascoli[32], F. Pauss[26], R. G. Pegna[36], M. A. Perez-Torres[44], M. Persic[42,48], L. Peruzzo[32], F. Prada[44], E. Prandini[32], N. Puchades[39], A. Raymers[40], W. Rhode[29], M. Ribó[37], J. Rico[49,39], M. Rissi[26], A. Robert[30], S. Rügamer[38], A. Saggion[32], T. Y. Saito[31], M. Salvati[27], M. Sanchez-Conde[44], P. Sartori[32], K. Satalecka[35], V. Scalzotto[32], V. Scapin[42], T. Schweizer[31], M. Shayduk[31], K. Shinozaki[31], S. N. Shore[50], N. Sidro[39], A. Sierpowska-Bartosik[43], A. Sillanpää[46], J. Sitarek[31,34], D. Sobczynska[34], F. Spanier[38], A. Stamerra[36], L. S. Stark[26], L. Takalo[46], F. Tavecchio[27], P. Temnikov[47], D. Tescaro[39], M. Teshima[31], M. Tluczykont[35], D. F. Torres[49,43], N. Turini[36], H. Vankov[47], A. Venturini[32], V. Vitale[42], R. M. Wagner[31], W. Wittek[31], V. Zabalza[37], F. Zandanel[44], R. Zanin[39], J. Zapatero[30] (The MAGIC Collaboration), V. Acciari[51,52], E. Aliu[53], T. Arlen[54], M. Beilicke[55], W. Benbow[51], S. M. Bradbury[56], J. H. Buckley[55], V. Bugaev[55], Y. Butt[57], K. Byrum[58], A. Cannon[59], A. Cesarini[60], Y. C. Chow[54], L. Ciupik[61], P. Cogan[62], P. Colin[63], W. Cui[64], M. K. Daniel[56], R. Dickherber[55], C. Duke[65], T. Ergin[57], S. J. Fegan[54], J. P. Finley[64], G. Finnegan[63], P. Fortin[66], A. Furniss[67], D. Gall[64], G. H. Gillanders[60], R. Guenette[62], G. Gyuk[61], J. Grube[56,59], D. Hanna[62], J. Holder[53], D. Horan[58,76], C. M. Hui[63], T. Brian Humensky[68], A. Imran[69], P. Kaaret[70], N. Karlsson[61], M. Kertzman[71], D. Kieda[63], J. Kildea[51], A. Konopelko[72], H. Krawczynski[55], F. Krennrich[69], M. J. Lang[60], S. LeBohec[63], G. Maier[62], A. McCann[62], M. McCutcheon[62], A. Milovanovic[56], P. Moriarty[52], T. Nagai[69], R. A. Ong[54], A. N. Otte[67], D. Pandel[70], J. S. Perkins[53], A. Pichel[73], M. Pohl[69], K. Ragan[64], L. C. Reyes[74], P. T. Reynolds[75], E. Roache[51], H. J. Rose[56], M. Schroedter[69], G. H. Sembroski[64], A. W. Smith[58], D. Steele[61], S. P. Swordy[68], M. Theiling[51], J. A. Toner[60], L. Valcarcel[62], A. Varlotta[64], S. P. Wakely[68], J. E. Ward[59], T. C. Weekes[51], A. Weinstein[54], D. A. Williams[67], S. Wissel[68], M. Wood[54], and B. Zitzer[64] (The VERITAS Collaboration)

[1] INAF/IASF-Roma, I-00133 Roma, Italy; immacolata.donnarumma@iasf-roma.inaf.it
[2] Dipartimento di Fisica, Università Tor Vergata, I-00133 Roma, Italy
[3] INAF/IASF-Milano, I-20133 Milano, Italy
[4] CIFS-Torino, I-10133 Torino, Italy
[5] INAF/IASF-Bologna, I-40129 Bologna, Italy
[6] Dipartimento Fisica and INFN Trieste, I-34127 Trieste, Italy
[7] INFN-Pavia, I-27100 Pavia, Italy
[8] ENEA-Bologna, I-40129 Bologna, Italy
[9] INFN-Roma La Sapienza, I-00185 Roma, Italy
[10] CNR-IMIP, Roma, Italy
[11] INFN-Roma Tor Vergata, I-00133 Roma, Italy
[12] Dipartimento di Fisica, Università Dell'Insubria, I-22100 Como, Italy
[13] ENEA Frascati, I-00044 Frascati (Roma), Italy
[14] ASI Science Data Center, I-00044 Frascati (Roma), Italy
[15] Agenzia Spaziale Italiana, I-00198 Roma, Italy
[16] INAF, Osservatorio Astronomico di Torino, Italy; villata@oato.inaf.it, raiteri@oato.inaf.it
[17] Institute of Astronomy, National Central University, Taiwan
[18] Astronomical Institute, St. Petersburg State University, Russia
[19] School of Cosmic Physics, Dublin Institute For Advanced Studies, Republic of Ireland
[20] Abastumani Astrophysical Observatory, Georgia
[21] Astrophysikalisches Institut Potsdam, Germany

[22] Landessternwarte Heidelberg-Königstuhl, Germany
[23] Pulkovo Observatory, St. Petersburg, Russia
[24] Agrupació Astronòmica de Sabadell, Spain
[25] Department of Physics, University of Colorado at Denver, CO, USA
[26] ETH Zurich, CH-8093, Switzerland
[27] INAF National Institute for Astrophysics, I-00136 Rome, Italy
[28] Universidad Complutense, E-28040 Madrid, Spain
[29] Technische Universität Dortmund, D-44221 Dortmund, Germany
[30] Universitat Autònoma de Barcelona, E-08193 Bellaterra, Spain
[31] Max-Planck-Institut für Physik, D-80805 München, Germany; robert.wagner@mpp.mpg.de, cchsu@mpp.mpg.de
[32] Università di Padova and INFN, I-35131 Padova, Italy
[33] Instituto de Astrofísica de Canarias, E-38200 La Laguna, Tenerife, Spain
[34] University of Łódź, PL-90236 Lodz, Poland
[35] Deutsches Elektronen-Synchrotron (DESY), D-15738 Zeuthen, Germany; satalk@ifh.de
[36] Università di Siena and INFN Pisa, I-53100 Siena Italy
[37] Universitat de Barcelona (ICC/IEEC), E-08028 Barcelona, Spain
[38] Universität Würzburg, D-97074 Würzburg, Germany
[39] IFAE, Edifici Cn., Campus UAB, E-08193 Bellaterra, Spain
[40] Yerevan Physics Institute, AM-375036 Yerevan, Armenia
[41] Departamento de Astrofisica, Universidad, E-38206 La Laguna, Tenerife, Spain
[42] Università di Udine and INFN Trieste, I-33100 Udine Italy
[43] Institut de Cienciès de l'Espai (IEEC-CSIC), E-08193 Bellaterra, Spain
[44] Instituto de Astrofísica de Andalucia (CSIC), E-18080 Granada, Spain
[45] University of California, Davis, CA-95616-8677, USA
[46] Tuorla Observatory, Turku University, FI-21500 Piikkiö, Finland
[47] Institute for Nuclear Research and Nuclear Energy, BG-1784 Sofia, Bulgaria
[48] INAF/Osservatorio Astronomico and INFN, I-34143 Trieste, Italy
[49] ICREA, E-08010 Barcelona, Spain
[50] Università di Pisa, and INFN Pisa, I-56126 Pisa, Italy
[51] Fred Lawrence Whipple Observatory, Harvard-Smithsonian Center for Astrophysics, Amado, AZ 85645, USA
[52] Department of Life and Physical Sciences, Galway-Mayo Institute of Technology, Dublin Road, Galway, Republic of Ireland
[53] Department of Physics and Astronomy and the Bartol Research Institute, University of Delaware, Newark, DE 19716, USA
[54] Department of Physics and Astronomy, University of California, Los Angeles, CA 90095, USA
[55] Department of Physics, Washington University, St. Louis, MO 63130, USA
[56] School of Physics and Astronomy, University of Leeds, Leeds LS2 9JT, UK; jeffrey.grube@ucd.ie
[57] Harvard-Smithsonian Center for Astrophysics, 60 Garden Street, Cambridge, MA 02138, USA
[58] Argonne National Laboratory, 9700 S. Cass Avenue, Argonne, IL 60439, USA
[59] School of Physics, University College Dublin, Belfield, Dublin 4, Republic of Ireland
[60] School of Physics, National University of Ireland, Galway, Republic of Ireland
[61] Astronomy Department, Adler Planetarium and Astronomy Museum, Chicago, IL 60605, USA
[62] Physics Department, McGill University, Montreal, QC H3A 2T8, Canada
[63] Physics Department, University of Utah, Salt Lake City, UT 84112, USA
[64] Department of Physics, Purdue University, West Lafayette, IN 47907, USA
[65] Department of Physics, Grinnell College, Grinnell, IA 50112-1690, USA
[66] Department of Physics and Astronomy, Barnard College, Columbia University, NY 10027, USA
[67] Santa Cruz Institute for Particle Physics and Department of Physics, University of California, Santa Cruz, CA 95064, USA
[68] Enrico Fermi Institute, University of Chicago, Chicago, IL 60637, USA
[69] Department of Physics and Astronomy, Iowa State University, Ames, IA 50011, USA
[70] Department of Physics and Astronomy, University of Iowa, Van Allen Hall, Iowa City, IA 52242, USA
[71] Department of Physics and Astronomy, DePauw University, Greencastle, IN 46135-0037, USA
[72] Department of Physics, Pittsburg State University, 1701 South Broadway, Pittsburg, KS 66762, USA
[73] Casilla de Correo 67, Sucursal 28, (C1428ZAA) Ciudad Autònoma de Buenos Aires, Argentina
[74] Kavli Institute for Cosmological Physiscs, University of Chicago, Chicago, IL 60637, USA
[75] Department of Applied Physics and Instumentation, Cork Institute of Technology, Bishopstown, Cork, Republic of Ireland
[76] Laboratoire Leprince-Ringuet, Ecole Polytechnique, CNRS/IN2P3, F-91128, Palaiseau, France
Received 2008 October 15; accepted 2008 December 4; published 2008 December 29

ABSTRACT

We present optical, X-ray, high-energy ($\lessapprox$ 30 GeV) and very high energy ($\gtrapprox$ 100 GeV; VHE) observations of the high-frequency peaked blazar Mrk 421 taken between 2008 May 24 and June 23. A high-energy γ-ray signal was detected by *AGILE* with $\sqrt{TS} = 4.5$ between June 9 and 15, with $F(E > 100\ \mathrm{MeV}) = 42^{+14}_{-12} \times 10^{-8}$ photons cm^{-2} s^{-1}. This flaring state is brighter than the average flux observed by EGRET by a factor of ∼3, but still consistent with the highest EGRET flux. In hard X-rays (20–60 keV) SuperAGILE resolved a five-day flare (June 9–15) peaking at ∼55 mCrab. SuperAGILE, *RXTE*/ASM and *Swift*/BAT data show a correlated flaring structure between soft and hard X-rays. Hints of the same flaring behavior are also detected in the simultaneous optical data provided by the GASP-WEBT. A *Swift*/XRT observation near the flaring maximum revealed the highest 2–10 keV flux ever observed from this source, of 2.6×10^{-9} erg cm^{-2} s^{-1} (i.e. > 100 mCrab). A peak synchrotron energy of ∼3 keV was derived, higher than typical values of ∼0.5–1 keV. VHE observations with MAGIC and VERITAS between June 6 and 8 showed the flux peaking in a bright state, well correlated with the X-rays. This extraordinary set of simultaneous data, covering a 12-decade spectral range, allowed for a deep

analysis of the spectral energy distribution as well as of correlated light curves. The γ-ray flare can be interpreted within the framework of the synchrotron self-Compton model in terms of a rapid acceleration of leptons in the jet.

Key words: BL Lacertae objects: individual (Mrk 421) – gamma rays: observations – galaxies: jets – radiation mechanisms: non-thermal – X-rays: galaxies

1. INTRODUCTION

Mrk 421 is a nearby blazar ($z = 0.031$) and one of the brightest BL Lac objects given its distance of 134.1 Mpc ($H_0 = 71$ km s^{-1} Mpc^{-1}, $\Omega_m = 0.27, \Omega_\lambda = 0.73$). It was observed in γ-rays by EGRET (Lin et al. 1992), and it was the first extragalactic object detected at $E > 500$ GeV (Punch et al. 1992). It belongs to the class of high-energy peaked BL Lac objects (HBLs) (Padovani & Giommi 1995), i.e. radio-loud active galactic nuclei with high radio and optical polarization. Its spectral energy distribution (SED) is double humped with a first peak usually in the soft-to-medium X-ray range, and a second one at GeV–TeV energies (Sambruna et al. 1996; Fossati et al. 1998). The first hump is commonly interpreted as due to synchrotron radiation from high-energy electrons in a relativistic jet, while the origin of the second peak is still uncertain. In the leptonic scenario, it is interpreted as inverse Compton (IC) scattering of the synchrotron (synchrotron self-Compton, SSC) or external photons (external Compton, EC) by the same population of relativistic electrons. The observed correlated variability between X-rays and TeV γ-rays (Maraschi et al. 1999; Fossati et al. 2008, Wagner 2008) is well explained in the SSC framework (Ghisellini et al. 1998), whereas the EC scenario is unlikely to apply in HBLs, due to the low density of ambient photons. Alternatively, hadronic models invoke proton-initiated cascades and/or proton–synchrotron emission (Aharonian 2000, Mücke et al. 2003).

Leptonic and hadronic scenarios for HBLs predict different properties of the γ-ray emission in relation to emissions in other energy bands. Specifically, the hadronic models (as opposed to the SSC ones) predict a flatter slope of the $\sim$ 100 MeV IC emission than that of the synchrotron emission in the optical, UV energy bands. γ-ray observations of flaring BL Lac objects and simultaneous multiwavelength data are, thus, the keys to investigating these two scenarios.

A hard X-ray flare of Mrk 421 was detected by SuperAGILE on 2008 June 10 (Costa et al. 2008). This detection was later followed by a detection in γ-rays (Pittori et al. 2008) by the *AGILE*/GRID (gamma-ray imaging detector) and prompted a target of opportunity (ToO) observation by *Swift*/XRT, complementing the ongoing multifrequency observing campaign of Mrk 421 with WEBT (optical), MAGIC and VERITAS (TeV). We report on the observations and the analysis of these data, complemented by the publicly available data from *RXTE*/ASM (2–12 keV) and *Swift*/BAT (15–50 keV), and discuss the spectral energy distribution of the source during this bright γ-ray flare.

2. OBSERVATIONS AND RESULTS

2.1. AGILE Observations

AGILE (Tavani et al. 2008) is a small mission of the Italian Space Agency for the exploration of the γ-ray sky, operating in a low Earth orbit since 2007 April 23. The *AGILE* composite payload allows for simultaneous observations in the energy ranges 30 MeV–30 GeV and 20–60 keV over a very wide field of view (FOV) by means of GRID and the hard X-ray imager SuperAGILE, respectively. Mrk 421 was observed for five days, between 2008 June 9 17:02 UT and 2008 June 15 02:17 UT.

2.1.1. Hard X-Ray Observations

On 2008 June 10, SuperAGILE detected enhanced hard X-ray emission from Mrk 421. The measured flux in 20–60 keV was found to be above 30 mCrab (24 hr average), almost an order of magnitude larger than its typical flux in quiescence. The source was at $\sim$ (0, 20) degrees in the orthogonal SuperAGILE reference frame (Feroci et al. 2007), thus exposing an effective area $\sim$ 55% of the full on-axis value. In the following days, the flux increased up to about 55 mCrab. The five-day 20–60 keV SuperAGILE light curve is shown in Figure 1(c). Using the publicly available light curves for this source from the BAT experiment[78] in the 15–50 keV energy range (near the SuperAGILE bandpass), we calculated daily averages of the sparse observations. This allowed us to obtain good coverage also before and after the *AGILE* observation (black squares in Figure 1(c)), revealing that SuperAGILE indeed observed the maximum brightness of this hard X-ray flare. Both SuperAGILE and BAT count rates were converted to physical units by assuming a Crab-like spectrum.

SuperAGILE photon-by-photon data allow extraction of a time-averaged energy spectrum from the mask-convolved data. Given the lack of substantial spectral variability in the SuperAGILE/ASM hardness ratio (Figure 1(e)), we accumulated the average energy spectrum from the data of the last four days of the observations, when the source flux varied between 35 and 55 mCrab, for a total net source exposure of $\sim$140 ks. Despite poor statistics, this four-point energy spectrum is able to reasonably constrain the photon index of a simple power law, $\Gamma = 2.43^{+0.69}_{-0.64}$ ($\chi^2_{\rm dof} = 0.8$, 2 dof). The average flux is $F(20\text{–}60\ \text{keV}) = (4.90 \pm 0.54) \times 10^{-10}$ erg cm^{-2} s^{-1} ($(9.8 \pm 1.1) \times 10^{-3}$ photons cm^{-2} s^{-1}).

2.1.2. Gamma-Ray Observations

The GRID data were analyzed using the *AGILE* standard pipeline (Vercellone et al. 2008), with a bin size of $0.^\circ25 \times 0.^\circ25$. Only events flagged as γ-rays and not recorded while the satellite crossed the South Atlantic Anomaly were accepted. We also rejected all events with reconstructed direction within 10° from the Earth limb, thus, reducing contamination from Earth's γ-ray albedo.

Mrk 421, observed $\sim 20^\circ$ off-axis with respect to the boresight, was not detected on daily time scales, implying a daily-averaged flux smaller than $\sim 100 \times 10^{-8}$ photons cm^{-2} s^{-1}, similar to what observed by EGRET (Hartman et al. 1999). A 4.5 σ significance in the range of 100 MeV–10 GeV resulted from an integration over the whole five-day period (net exposure $\sim$ 260 ks). The measured flux is $\left(42^{+14}_{-12}\right) \times 10^{-8}$ photons

[77] Deceased.

[78] http://swift.gsfc.nasa.gov/docs/swift/results/transients/weak/Mrk421/

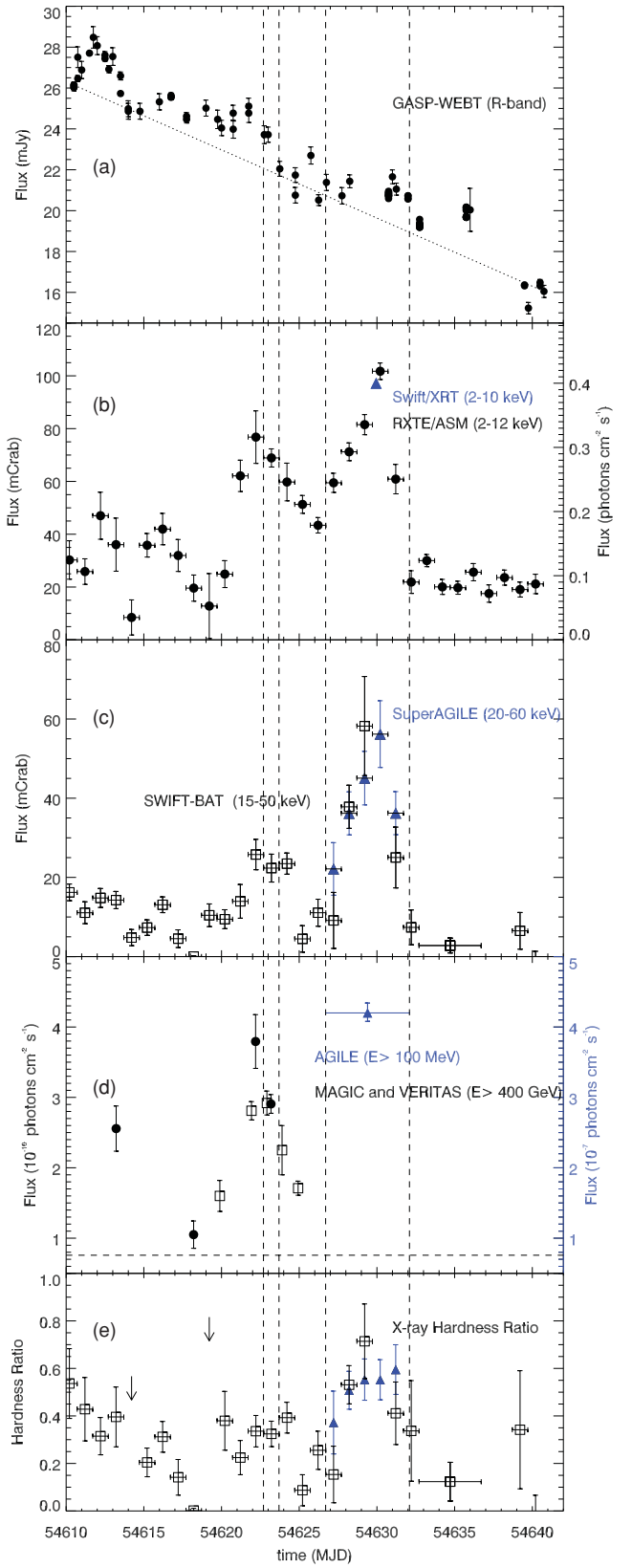

Figure 1. (a) *R*-band optical light curve from GASP-WEBT (May 24–June 23); (b) ASM (2–12 keV) light curve (bin size is one day) and XRT (2–10 keV) flux (blue triangle); (c) SuperAGILE (20–60 keV, blue triangles; 1 Crab = 0.2 ph cm^{-2} s^{-1}) and BAT (15–50 keV, empty black squares; 1 Crab = 0.29 ph cm^{-2} s^{-1}); (d) MAGIC and VERITAS (>400 GeV, empty black squares and black circles, respectively), the Crab flux > 400 GeV (horizontal dashed line), AGILE (> 100 MeV, blue triangle); (e) hardness ratio computed using the SuperAGILE (or BAT) and ASM data for each day. The dashed vertical lines mark periods 1 and 2 (see the text for details).

cm^{-2} s^{-1}, about ∼3 times higher than the average flux detected by EGRET (∼ 13×10^{-8}, Hartman et al. 1999) and ∼1.5 times higher than, but still consistent with the highest flux $(27 \pm 7) \times 10^{-8}$ photons cm^{-2} s^{-1} observed during the Viewing Period 326. The short duration of the *AGILE* observation did not allow us to follow the possible decay of the γ-ray emission. Due to the relative faintness of the source and the short exposure, the GRID data do not allow us to extract a reliable energy spectrum.

2.2. The Soft X-Ray Band

2.2.1. Swift XRT

Following the SuperAGILE detection, on 2008 June 12 we triggered a ToO observation with the *Swift*/XRT that promptly observed the source for 5 ks between 2008 June 12 19:33:20 UT (MJD 54629.8) and June 13 at 01:57:37 UT (MJD 54630.1).

The XRT data were processed using the standard procedure (`xrtpipeline` v0.12.0) developed at the ASI Science Data Center and distributed by the NASA/HEASARC. Observations were taken in Window Timing mode at a count rate of 120–150 counts s^{-1}. We selected XRT grades 0–2 (Burrows et al. 2005) and extracted the WT data in a rectangular 40 × 20 pixel region centered on the source. The background was also extracted within a box (40 × 20 pixel), far from background sources.

Due to calibration uncertainties, we restricted our spectral fit to the energy range 0.7–9.0 keV and added a 3% systematics to the model (Cusumano et al. 2006). The XRT spectral data are well described by an absorbed log-parabolic model. A joint fit of the XRT and SuperAGILE spectral data using the four-day average spectrum described in Section 2.1.1. used the log-parabolic model with Galactic absorption ($N_{\rm H}^{\rm Gal} = 1.61 \times 10^{20}$ cm^{-2}; Lockman & Savage 1995), defined as

$$F(E) = K E^{-a-b\log(E)} \text{ photons cm}^{-2}\text{ s}^{-1},$$

where a is the photon index at 1 keV, and b is the curvature parameter (Massaro et al. 2004; Massaro et al. 2008; Tramacere et al. 2007a, 2007b). This model usually describes adequately the featureless and curved spectrum in HBLs. The joint fit provides $a = 1.65^{+0.01}_{-0.02}$, $b = 0.37^{+0.01}_{-0.005}$ ($\chi^2_{\rm dof} = 1.4$, 763 dof), which implies a peak energy $2.97^{+0.22}_{-0.18}$ keV, and predicts $F_{2-10\,\rm keV} = 2.56 \times 10^{-9}$ erg cm^{-2} s^{-1} (or 0.4 photons cm^{-2} s^{-1}) and $F_{20-60\,\rm keV} = (5.7 \pm 0.6) \times 10^{-10}$ erg cm^{-2} s^{-1} ($(1.1 \pm 0.1) \times 10^{-2}$ photons cm^{-2} s^{-1}), comparable to the standalone SuperAGILE best fit.

2.2.2. RXTE All Sky Monitor (ASM)

Given the high flux observed by *Swift*/XRT, we retrieved the public light curves provided by the all sky monitor (ASM)[79] to trace the evolution of the soft X-rays during the AGILE observation. Figure 1(b) shows the daily light curve of Mrk 421 in the energy range 2–12 keV, obtained by properly averaging the dwell-by-dwell data.

The emission at soft X-rays is well correlated with hard X-ray emission. The ASM data show that the XRT observation took place when the source was at its maximum emission at soft X-rays (MJD ∼ 54630). Comparing the relative intensity of the two flares in Figure 1, it appears that the second peak

[79] http://xte.mit.edu/asmlc/ASM.html

is significantly harder than the first one. This is also shown in Figure 1(e), where we computed the daily-averaged hardness ratio between hard (15–60 keV) and soft (2–12 keV) X-rays. The source appears to have undergone the hardest part of this double-humped flare just during the *AGILE* γ-ray detection.

2.3. Observations in the VHE γ-Rays

The four-telescope array VERITAS (Acciari et al. 2008) at the Fred Lawrence Whipple Observatory (Arizona) and the single-dish instrument MAGIC (Baixeras et al. 2004; Tescaro et al. 2007) at La Palma are imaging air Cherenkov telescopes covering an energy range from $\sim$ 100 GeV to some tens of TeV. The instruments have a typical energy resolution of $<$20% (VERITAS) and 20–30% (MAGIC), and event-by-event angular resolution of $< 0.^{\circ}14$. Wobble-mode observations (Daum et al. 1997) at an $0.^{\circ}4$ offset from the camera center were taken on five nights from 2008 June 3–8 with MAGIC at zenith angles (ZA) between 28° and 48° and on four nights (May 27, June 1, 5, 6) with VERITAS (wobble offset: $0.^{\circ}5$) at ZA between 32° and 40° during partial moonlight conditions. The total live time after applying quality selection is 2.95 and 1.17 hr with MAGIC and VERITAS, respectively. The data were analyzed using the MAGIC (Albert et al. 2008a) and VERITAS (Daniel et al. 2007; Acciari et al. 2008) standard calibration and analyses and image parameters (Hillas 1985). For VERITAS, the γ-ray direction and air shower impact parameter on the ground are reconstructed using the stereoscopic techniques in Hofmann et al. (1999) and Krawczynski et al. (2006). Any γ-ray excess is derived from the θ^2 distribution, where θ represents the angular distance between the source position in the sky and the reconstructed arrival position of the air shower. For MAGIC, θ is estimated using the DISP method (Fomin et al. 1994). For VERITAS, 99.9% of the background of cosmic rays is rejected by using selection cuts on θ^2, mean scaled width and length, and by using quality cuts of each event. The MAGIC analysis utilizes a random forest method (Albert et al. 2008b) to discriminate the dominating background of hadronic cosmic-ray events and for the energy estimation of the γ-ray events. The energy and effective area of each event are reconstructed from Monte Carlo simulations. The integral flux and energy spectrum of the source are then derived from the effective areas for nights with a significant detection. Two independent analyses of both the MAGIC and VERITAS data sets yielded consistent results. In total, a signal corresponding to a significance level of 44σ (VERITAS) and 66σ (MAGIC) is obtained by following Equation (17) of Li & Ma (1983). The combined MAGIC–VERITAS data (Figure 1(d)) show a transient peaking near MJD 54622. The VERITAS energy spectrum for June 6 is provided. A power-law fit over the energy range 0.3–5 TeV resulted in a $\chi^2_{\rm dof} = 0.7$ with a photon index $\Gamma = 2.78 \pm 0.09$. In Figure 2, we show the intrinsic γ-ray spectrum at the source reconstructed by removing attenuation effects by the extragalactic background light (Hauser & Dwek 2001) following the procedure of Raue & Mazin (2008)[80]. Fitting a power law to the intrinsic spectrum yields a photon index $\Gamma = 2.59 \pm 0.08$, which is not significantly harder than the measured spectrum due to the relatively low redshift $z = 0.031$.

2.4. Optical and UV Observations

Mrk 421 is one of the 28 γ-ray-loud blazars that are regularly monitored by the GLAST-*AGILE* Support Program (GASP; Villata et al. 2008) of the Whole Earth Blazar Telescope (WEBT)[81]. The GASP observations started in early 2007 November. The *R*-band data were calibrated according to the photometric sequence by Villata et al. (1998). A careful data analysis is warranted because the source flux is contaminated by the emission of the host galaxy and nearby objects. The flux contribution of these objects was subtracted according to Nilsson et al. (2007). Moreover, we corrected for a Galactic extinction of $A_R = 0.042$ mag. The resulting *R*-band light curve[82] during the period considered in this Letter is shown in Figure 1(a).

During the *Swift* pointing on 2008 June 12–13, the UVOT (Poole et al. 2008) instrument observed Mrk 421 in the UVW1 and UVW2 photometric bands. The UVOTSOURCE tool is used to extract counts, correct for coincidence losses, apply background subtraction, and calculate the source flux. We applied a standard 5 arcsec radius source aperture, and a 20 arcsec background region. The source fluxes are dereddened using the interstellar extinction curve in Fitzpatrick (1999).

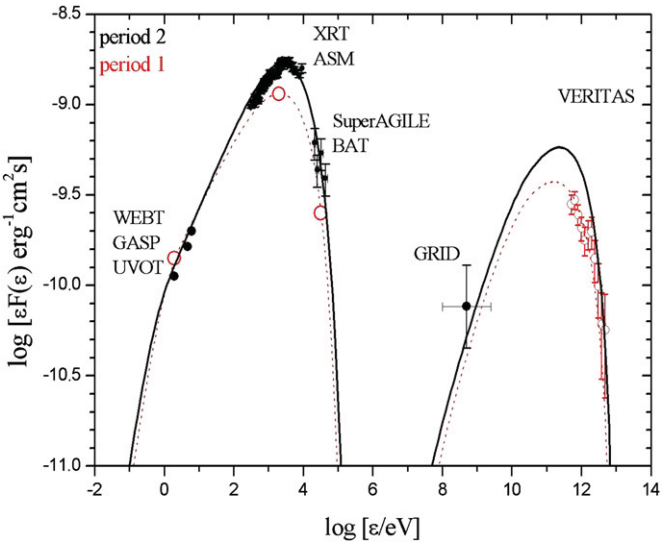

Figure 2. SEDs of Mrk 421 obtained by combining the GASP-WEBT, *Swift*/UVOT, *RXTE*/ASM, XRT, SuperAGILE, BAT, GRID and VERITAS data in period 1 and period 2 (red empty circles and black filled circles, respectively). Both are one-zone SSC models (the red dashed line for period 1 and the black solid line for period 2).

3. DISCUSSION

Mrk 421 showed very interesting broadband activity during the first half of 2008 June as derived from *AGILE* data combined with those of WEBT, *Swift*, MAGIC, and VERITAS. Using our multifrequency data, we were able to derive time-resolved SEDs (Figure 2). We distinguish two time periods: period 1: 2008 June 6, with the inclusion of optical, X-ray (XTE and BAT) and TeV data (VERITAS); and period 2: 2008 June 9–15, including optical, UV, X-rays (XRT and SuperAGILE) and gamma-ray data (*AGILE*). The source shows a very interesting time-variable broadband emission that appears to be in overall agreement with an SSC model. The optical, soft and hard X-ray bands strongly constrain the SED around the synchrotron peak, and its daily variability reveals the physical processes of Mrk 421. Possible correlated variability is shown in Figure 1 between the

[80] http://www.desy.de/~mraue/ebl/

[81] http://www.oato.inaf.it/blazars/webt see, e.g. (Villata et al. 2007; Raiteri et al. 2007).

[82] The optical data presented in this Letter are stored in the GASP-WEBT archive; for questions regarding their availability, please contact the WEBT President Massimo Villata at villata@oato.inaf.it.

Table 1
SSC Model Parameters

Parameter	Period 1	Period 2
γ_b	$3.6 \cdot 10^5$	$4.2 \cdot 10^5$
$\gamma_{\max}$	$1.3 \cdot 10^6$	$1.3 \cdot 10^6$
p_1	2.22	2.1
p_2	4.5	5
B (G)	0.1	0.1
K (cm^{-3})	$4 \cdot 10^{-4}$	$6 \cdot 10^{-4}$
δ	20	20
$\theta[^\circ]$	2	2

optical (an overall decreasing trend with superimposed spikes of emission), the X-rays (several emission peaks lasting few days), and the high-energy parts of the spectrum. Based on the physical constraints obtained for the synchrotron peak, we can model both the HE and VHE γ-ray emission. The data collection and broadband SED extend over 12 decades in energy. Taking advantage of the overlapping MAGIC and VERITAS observations, we present a combined VHE light curve using the current generation of northern imaging air Cherenkov systems.

We first model the synchrotron peak of emission using period 1 optical, soft and hard X-ray data. The short time variability (Figure 1) constrains the size of the emitting region to $R < cT\delta \sim 5 \times 10^{16}(\delta/20)$ cm. Hence, we consider a one-zone SSC model (Tavecchio et al. 1998) based on a blob of comoving size $R = 4 \times 10^{16}$ cm, with a relativistic Doppler factor $\delta = 20$ and characterized by nonthermal comoving electron energy distribution function described by a double power-law

$$n_e(\gamma) = \frac{K\gamma_b^{-1}}{(\gamma/\gamma_b)^{p_1} + (\gamma/\gamma_b)^{p_2}}, \quad (1)$$

where the comoving Lorentz factor (γ) varies in the range $\gamma_{\min} = 4 \times 10^3 < \gamma < \gamma_{\max} = 1.3 \times 10^6$, the normalization (density) constant $K = 4 \times 10^{-4}$ cm^{-3}, and the break energy $\gamma_b = 3.6 \times 10^5$ and with $p_1 = 2.22$, $p_2 = 4.5$, the low-energy and high-energy power-law indices, respectively (see Table 1). With these parameters, we found that the data for period 1 are best fitted with a comoving magnetic field $B = 0.1$ G.

Variability may be caused by several factors. We consider two cases: (A) hardening/softening of the electron energy distribution function caused by particle acceleration processes; (B) increase/decrease of the comoving particle density, as a consequence of additional particle injection/loss by shock processes.

We expect TeV variability to be comparable with the X-ray one if case (A) applies: this is because the emission is in the Klein–Nishina regime. Alternatively, for case (B), we expect the TeV relative variability ($\Delta F/F$) to be a factor of 2 greater than that of the X-ray flux variability.

Our *AGILE*, MAGIC, and VERITAS data appear to support case (A). We compare the SEDs for periods 1 and 2, to better assess the spectral evolution. In Figure 2, we show our optimized modeling of the time-resolved synchrotron peak and consequent SSC high-energy emission for period 1 as well as for 2008 June 12–13 of period 2. In the last case, the adopted model parameters are $p_1 = 2.1$, $p_2 = 5$, $\gamma_b = 4.2 \times 10^5$, $K = 6 \times 10^{-4}$ cm^{-3}. Our model predicts an even larger TeV flux for period 2 (no TeV observations exist, however) than detected in period 1.

A detailed discussion of the complex optical versus X-ray variability of Mrk 421 as shown in Figure 1 will be presented elsewhere. We note here a few remarkable points. The optical light curve shows variations of the order of 10% on a timescale of a few days, superimposed on a long decay during the entire period. Individual soft and hard X-ray peaks result in increased fluxes by a factor of ∼2.5 and ∼5, respectively: no long-term decay appears. This different behavior of the X-ray radiation and the bulk of the optical emission may, interestingly, suggest more complex scenarios than (A) and (B): optical and X radiation come from two different jet regions, each one characterized by its own variability. A possible scenario is one in which the inner jet region would produce the X-rays, and it would be at least partially transparent to the optical radiation. In contrast, the outer region can only produce lower-frequency emission. The signature of the X-ray events visible in the optical light curve would come from the inner region and would be diluted by the optical radiation emitted from the outer region (see Villata & Raiteri 1999 for the case of Mrk 501; Villata et al. 2004).

Interestingly, the 2–10 keV flux measured by XRT on June 12–13, $\sim 2.6 \times 10^{-9}$ erg cm^{-2} s^{-1}, is higher than all previous observations ($< 2 \times 10^{-9}$ erg cm^{-2} s^{-1}; Fossati et al. 2008; Lichti et al. 2008). A joint analysis of the XRT and SuperAGILE data, covering the range from 0.7 to 60 keV, provides a best-fit spectral model consistent with a log-parabolic shape, with parameters implying a peak energy ∼3 keV, in good agreement with the steeper positive correlation between the peak energy and the maximum of the SED found by Tramacere et al. (2007a) (see their Figure 3), although our value of the peak energy shows a significant shift with respect to typical values of 0.5–1 keV for this source.

We conclude our analysis of the broadband variable emission from Mrk 421 by emphasizing that our multitelescope/instrument data show a very interesting variability that provides support for an SSC model of the source. The γ-ray emission detected by *AGILE* during period 2 and the TeV emission detected during period 1 can be successfully modeled from the characteristics of the corresponding synchrotron peaks.

AGILE is a mission of ASI, with co-participation of INAF and INFN. This work was partially supported by ASI grants I/R/045/04, I/089/06/0, I/011/07/0 and by the Italian Ministry of University and Research (PRIN 2005025417), (ASDC) I/024/05/1. The MAGIC collaboration thanks the Instituto de Astrofísica de Canarias for the excellent working conditions at the Observatorio del Roque de Los Muchachos in La Palma and support by the German BMBF and MPG, the Italian INFN and Spanish MCINN is acknowledged. This work was supported by ETH Research Grant TH 34/043, by the Polish MNiSzW Grant N N203 390834, the YIP of the Helmholtz Gemeinschaft, the grant of Georgian National Science Foundation GNSF/ST07/4-180. E.K. acknowledges financial support from the NCS grant No. 96-2811-M-008-058. The VERITAS collaboration is supported by grants from the U.S. Department of Energy, the National Science Foundation, and the Smithsonian Institution, by NSERC in Canada, Science Foundation Ireland, and PPARC in the UK. We acknowledge the technical support staff at the FLWO. We also acknowledge the *Swift* Team for carrying out the ToO observation.

REFERENCES

Acciari, V. A., et al. (VERITAS Collaboration) 2008, ApJ, 679, 1427
Aharonian, F. A. 2000, NewA, 5, 377
Albert, et al. (MAGIC Collaboration) 2008a, ApJ, 674, 1037
Albert, et al. (MAGIC Collaboration) 2008b, Nucl. Instrum. Methods A, 588, 424

Baixeras, C., et al. 2004, Nucl. Instrum. Methods A, 518, 188
Burrows, D. N., et al. 2005, Space Sci. Rev., 120, 165
Costa, E., et al. 2008, ATEL, 1574, 1
Cusumano, G. in Proc. *Swift* and GRBs: Unveiling the Relativistic Universe, June 5–9, 2006, Venice (Italy)
Daniel, M. K., et al. 2007, Proc. 30th ICRC Merida, Mexico, 283
Daum, A., et al. (HEGRA Collaboration) 1997, Astropart. Phys., 8, 1
Feroci, M., et al. 2007, Nucl. Instrum. Methods Phys. Res. A, 581, 728
Fitzpatrick, E. 1999, PASP, 111, 63
Fomin, V. P., et al. 1994, Astropart. Phys., 2, 137
Fossati, G., et al. 1998, MNRAS, 299, 433
Fossati, G., et al. 2008, ApJ, 677, 906
Ghisellini, G., et al. 1998, MNRAS, 301, 451
Hartman, R. C., et al. 1999, ApJS, 123, 79
Hauser, M. G., & Dwek, E. 2001, ARA&A, 39, 249
Hillas, A. M. 1985, in Proc. 19th ICRC, La Jolla, USA, 3, 445
Hofmann, W., et al. 1999, Astropart. Phys., 12, 135
Krawczynski, H., et al. 2006, Astropart. Phys., 25, 380
Lichti, G. G., et al. 2008, A&A, 486, 721
Lin, Y. C., et al. 1992, ApJ, 401, 61
Lockman, F. J., & Savage, B. D. 1995, ApJS, 97, 1
Li, T.-P., & Ma, Y.-Q. 1983, ApJ, 272, 317
Maraschi, L., et al. 1999, ApJ, 526L, 81M
Massaro, E., et al. 2004, A&A, 422, 103
Massaro, F., Tramacere, A., Cavaliere, A., Perri, M., & Giommi, P. 2008, A&A, 478, 395
Mücke, A., et al. 2003, Astropart. Phys., 18, 593
Nilsson, K., et al. 2007, A&A, 475, 199
Padovani, P., & Giommi, P. 1995, ApJ, 444, 567
Pittori, C., et al. 2008, ATEL, 1583, 1
Poole, T. S., et al. 2008, MNRAS, 383, 627
Punch, M., et al. 1992, Nature, 358, 477
Raiteri, C. M., et al. 2007, A&A, 473, 819
Raue, M., & Mazin, D. 2008, Int. J. Mod. Phys. D, 17, 1515
Sambruna, R. M., Maraschi, L., & Urry, C. 1996, ApJ, 463, 444
Tavani, et al. 2008, arXiv:0807.4254v1
Tavecchio, F., et al. 1998, ApJ, 509, 608
Tescaro, D., et al. (MAGIC Collaboration) 2007, in Proc. 30th ICRC, Merida, Mexico (arXiv:0709.1410)
Tramacere, A., et al. 2007a, A&A, 466, 521T
Tramacere, A., et al. 2007b, A&A, 467, 501T
Vercellone, S., et al. 2008, ApJ, 676, 13
Villata, M., & Raiteri, C. M. 1999, A&A, 347, 30
Villata, M., et al. 1998, A&AS, 130, 305
Villata, M., et al. 2004, A&A, 421, 103
Villata, M., et al. 2007, A&A, 464, L5
Villata, M., et al. 2008, A&A, 481, L79
Wagner, R. M. 2008, PoS (BLAZARS2008), 63, 013 (arXiv:0809.2483)

The Astrophysical Journal, 693:564–585, 2009 March 1 doi:10.1088/0004-637X/693/1/564

2006 WHOLE EARTH TELESCOPE OBSERVATIONS OF GD358: A NEW LOOK AT THE PROTOTYPE DBV

J. L. Provencal[1,2], M. H. Montgomery[2,3], A. Kanaan[4], H. L. Shipman[1], D. Childers[5], A. Baran[6], S. O. Kepler[7], M. Reed[8], A. Zhou[8], J. Eggen[8], T. K. Watson[9], D. E. Winget[3], S. E. Thompson[1,2], B. Riaz[1], A. Nitta[10], S. J. Kleinman[10], R. Crowe[11], J. Slivkoff[11], P. Sherard[11], N. Purves[11], P. Binder[11], R. Knight[11], S. -L. Kim[12], Wen-Ping Chen[13], M. Yang[13], H. C. Lin[13], C. C. Lin[13], C. W. Chen[13], X. J. Jiang[14], A. V. Sergeev[15], D. Mkrtichian[16,17], M. Andreev[15], R. Janulis[18], M. Siwak[19], S. Zola[6,19], D. Koziel[19], G. Stachowski[6], M. Paparo[20], Zs. Bognar[20], G. Handler[21], D. Lorenz[21], B. Steininger[21], P. Beck[21], T. Nagel[22], D. Kusterer[22], A. Hoffman[22], E. Reiff[22], R. Kowalski[22], G. Vauclair[23], S. Charpinet[23], M. Chevreton[24], J. E. Solheim[25], E. Pakstiene[26], L. Fraga[4], and J. Dalessio[1,2]

[1] University of Delaware, Department of Physics and Astronomy, Newark, DE 19716, USA; jlp@udel.edu
[2] Delaware Asteroseismic Research Center, Mt. Cuba Observatory, Greenville, DE 19807, USA
[3] Department of Astronomy, University of Texas, Austin, TX-78712, USA; mikemon@rocky.as.utexas.edu
[4] Departamento de Física Universidade Federal de Santa Catarina, C.P. 476, 88040-900, Florianópolis, SC, Brazil; ankanaan@gmail.com
[5] Department of Math and Science, Delaware County Community College, 901 S. Media Rd, Media, PA-19063, USA; dpc@udel.edu
[6] Mount Suhora Observatory, Cracow Pedagogical University, Ul. Podchorazych 2, 30-084 Krakow, Poland; zola@astro1.as.ap.krakow.pl
[7] Instituto de Fíisica UFRGS, C.P. 10501, 91501-970 Porto Alegre, RS, Brazil; kepler@if.ufrgs.br
[8] Missouri State University and Baker Observatory, 901S. National, Springfield, MO 65897, USA; MikeReed@missouristate.edu
[9] Southwestern University, Georgetown, TX, USA; tkw@southwestern.edu
[10] Gemini Observatory, Northern Operations Center, 670 North A'ohoku Place, Hilo, HI 96720, USA; atsuko.nittakleinman@gmail.com
[11] University of Hawaii, Hilo, HI 96720, USA; rcrowe@hubble.uhh.hawaii.edu
[12] Korea Astronomy and Space Science Institute, Daejeon 305-348, Korea; slkim@kasi.re.kr
[13] Lulin Observatory, National Central University, Taiwan; wchen@astro.ncu.edu.tw
[14] National Astronomical Observatories, Academy of Sciences, Beijing 100012, People's Republic of China; xjjiang@bao.ac.cn
[15] Ukrainian National Academy of Sciences, Main Astronomical Observatory, Golosiiv, Kiev 022 252650, Ukraine; sergeev@terskol.com
[16] Astronomical Observatory, Odessa National University, Shevchenko Park, Odessa 65014, Ukraine; david@arcsec.sejong.ac.kr
[17] Astrophysical Research Center for the Structure and Evolution of the Cosmos, Sejong University, Seoul 143-747, Korea, davidm@sejong.ac.kr
[18] Institute of Theoretical Physics and Astronomy, Vilnius University, Vilnius, Lithuania; jr@itpa.lt
[19] Astronomical Observatory, Jagiellonian University, ul. Orla 171, 30-244 Cracow, Poland
[20] Konkoly Observatory, P.O. Box 67, H-1525 Budapest XII, Hungary; paparo@konkoly.hu
[21] Institut für Astronomie Universität Wien, Türkenschanzstrasse 17, 1180, Austria; handler@astro.univie.ac.at
[22] Institut für Astronomie und Astrophysik, Universiät Tübingen, Sand 1, 72076 Tübingen, Germany; nagel@astro.uni-tuebingen.de
[23] Laboratoire d'Astrophysique de Toulouse-Tarbes, Université de Toulouse, CNRS, 14 avenue Edouard Belin, F314000 Toulouse, France; gerardv@srvdec.obs-mip.fr
[24] Observatoire de Paris, LESIA, 92195 Meudon, France
[25] Institute of Theoretical Astrophysics, University of Oslo, P.O. Box 1029, Oslo, Norway; janerik@phys.uit.no
[26] Institute of Theoretical Physics and Astronomy, Astronomical Observatory, Gostauto 12, Vilnius LT 2600, Lithuania; erika@itpa.lt

Received 2008 August 19; accepted 2008 November 4; published 2009 March 2

ABSTRACT

We report on the analysis of 436.1 hr of nearly continuous high-speed photometry on the pulsating DB white dwarf GD358 acquired with the Whole Earth Telescope (WET) during the 2006 international observing run, designated XCOV25. The Fourier transform (FT) of the light curve contains power between 1000 and 4000 μHz, with the dominant peak at 1234 μHz. We find 27 independent frequencies distributed in 10 modes, as well as numerous combination frequencies. Our discussion focuses on a new asteroseismological analysis of GD358, incorporating the 2006 data set and drawing on 24 years of archival observations. Our results reveal that, while the general frequency locations of the identified modes are consistent throughout the years, the multiplet structure is complex and cannot be interpreted simply as $l = 1$ modes in the limit of slow rotation. The high-k multiplets exhibit significant variability in structure, amplitude and frequency. Any identification of the m components for the high-k multiplets is highly suspect. The $k = 9$ and 8 modes typically do show triplet structure more consistent with theoretical expectations. The frequencies and amplitudes exhibit some variability, but much less than the high-k modes. Analysis of the $k = 9$ and 8 multiplet splittings from 1990 to 2008 reveal a long-term change in multiplet splittings coinciding with the 1996 *sforzando* event, where GD358 dramatically altered its pulsation characteristics on a timescale of hours. We explore potential implications, including the possible connections between convection and/or magnetic fields and pulsations. We suggest future investigations, including theoretical investigations of the relationship between magnetic fields, pulsation, growth rates, and convection.

Key words: stars: evolution – stars: individual (GD358) – stars: oscillations – white dwarfs

1. INTRODUCTION

Asteroseismology of stellar remnants is traditionally the study of the interior structure of pulsating white dwarfs and subdwarfs as revealed by global stellar oscillations. The oscillations allow a view beneath the photosphere, and contain information about basic physical parameters, such as mass, rotation rate, internal transition profiles, and compositional structure. This information (see, for example, Nather et al. 1990; Winget et al. 1991; Winget et al. 1994; Kepler et al. 2000; Kanaan et al. 2005) provides important constraints on fields ranging from stellar formation and evolution, chemical evolution in our galaxy, the age of the galactic disk, the physics of Type Ia supernovae, and neutrino physics (Winget et al. 2004).

Asteroseismology is now expanding its focus to attack problems that at first consideration may not seem best suited for the technique. Convection remains one of the largest sources of theoretical uncertainty in our understanding of stars. This lack of understanding leads to considerable systematic uncertainties in such important quantities as the ages of massive stars where convective overshooting is important (Di Mauro et al. 2003) and the temperatures and cooling ages of white dwarfs (Prada et al. 2002; Wood 1992). One important early result from the Canadian asteroseismology mission Microvariability and Oscillations of Stars (*MOST*) is the difficulty in detecting predicted oscillations in Procyon A, implying possibly serious incompleteness in our understanding of stars even slightly different from the Sun (Matthews et al. 2004; Marchenko 2008).

Montgomery (2005) shows how precise observations of variable star light curves can be used to characterize the convection zone in a pulsating star. Montgomery bases his approach on important analytical (Goldreich & Wu 1999; Wu 2001) and numerical precursor calculations (Brickhill 1992). The method is based on three assumptions: (1) the flux perturbations are sinusoidal below the convection zone, (2) the convection zone is so thin that local angular variations of the nonradial pulsations may be ignored, i.e., we treat the pulsations locally as if they were radial, and (3) the convective turnover time is short compared with the pulsation timescale, so the convection zone can be assumed to respond instantaneously. Using high signal-to-noise light curves to model nonlinear effects, this approach can observationally determine the convective time scale τ_0, a temperature dependence parameter N, and, together with an independent $T_{\rm eff}$ determination, the classical convective efficiency parameter (the mixing length ratio) α.

Montgomery (2005) applies this theoretical construct to two large amplitude, monoperiodic white dwarf variables where it is possible to fold long light curves to obtain high signal-to-noise pulse shapes. The test candidates are a hydrogen atmosphere DAV (G29−38) and a helium atmosphere DBV (PG1351+489). G29−38 is a well-studied DAV known for the complexity of its pulsations (Kleinman et al. 1998). However, G29−38 was nearly monoperiodic during the 1988 Whole Earth Telescope (WET) campaign (Winget et al. 1990). PG1351+489 is dominated by a single mode and its harmonics, and was WET target in 1995 (Alves et al. 2003). Using folded light curves, Montgomery (2005) obtained results for these two stars which are consistent with mixing length theory (MLT) and other calculations of convective transport.

This significant theoretical advance offers the first empirical determination of convection parameters in stars other than the Sun. However, a result from one star in each white dwarf instability strip provides an insufficient basis for global statements about the nature of the convection zones for all white dwarfs. The next logical step is to map a population spanning a range of temperatures and masses across each instability strip, enabling us to determine the depth of their convection zones as a function of $T_{\rm eff}$ and log g.

PG1351+489 and G29−38 are examples of relatively rare, large amplitude, monoperiodic pulsators where it is possible to fold long light curves to obtain a high signal-to-noise pulse shapes. Simulations by Montgomery (2006) show that this approach is not sufficient for the more common pulsators demonstrating variable complexity in their pulsation spectra. In these cases, we require at least 5 hr of very high signal-to-noise photometry (S/N $\approx$ 1000) coupled with accurate real time frequency, amplitude, and phase information for the pulsations present in the high S/N light curve. The frequency, amplitude, and phase information, provided by a long timebase, multisite observing run, is used to fit the high S/N light curve and extract the convection parameters. The criteria for such a candidate star include nonlinear pulsations, a fairly bright target, and prior knowledge of the l and m values of the pulsations. The bright ($m_{\rm v}$ = 13.5) DB GD358 fits these criteria. GD358 is the best studied DB pulsator, and the only DB with existing, detailed asteroseismology (Winget et al. 1994, hereafter W94; Bradley & Winget 1994; Kepler et al. 2003, hereafter K03; Metcalfe et al. 2003).

In cooperation with the Delaware Asteroseismic Research Center (Provencal et al. 2005), we organized a WET run in May of 2006 (XCOV25) with GD358 as the prime target for Montgomery's light curve fitting technique. Our purpose was twofold: (1) obtain at least 5 hr of S/N $\approx$ 1000 photometry and (2) accurately identify the frequencies, amplitudes and phases present in GD358's current pulsation spectrum. The 2006 XCOV25 data set contains $\approx$436 hr of observations, with $\approx$29 hr of high S/N photometry. While GD358 is the best studied DB pulsator, the star's behavior is by no means well understood. The 2006 data set contains a great deal of interesting information on GD358's pulsational behavior. Before we can proceed with detailed lightcurve fitting, we must thoroughly understand the data set, examine GD358's pulsation spectrum, and extract accurate frequency, amplitude, and phase information. In the following, we will present an overview of the data set and reduction procedures. Our discussion will expand the existing asteroseismological analysis of GD358, exploring the 2006 XCOV25 identified modes, combination frequencies, and multiplet structure. We will compare our results with previous observations and examine the complexity and evolution of GD358's pulsations over time. Our investigation will lead us to consider connections between GD358's pulsations, its convection zone, and a possible surface magnetic field. The remarkable event that occurred in 1996 August (K03) will play an important role in this discussion. Finally, we present implications for our understanding of GD358's physical properties and suggest future investigations.

2. OBSERVATIONS AND DATA REDUCTION

GD358 (V777 Her), the brightest ($m_{\rm v}$ = 13.7) and best studied helium atmosphere white dwarf pulsator, was the target of the 25th Whole Earth Telescope (WET) run (XCOV25), the first sponsored by the Delaware Asteroseismic Research Center (DARC). The observations span 2006 May 12 to June 16, with the densest coverage between May 19 and May 31. Nineteen observatories distributed around the globe contributed a total of 88 individual runs (Table 1). The final XCOV25 light curve contains 436.1 hr of high speed photometry.

A goal of any WET run is to minimize data artifacts by obtaining as uniform a data set as possible (Nather et al. 1990). Early WET runs (e.g., Winget et al. 1991) comprised mainly 3-channel blue-sensitive photomultiplier tube (PMT) photometers that monitored the target variable, a comparison star, and sky brightness. CCDs now bring improved sensitivity and better sky measurements, but individual CCDs have distinct effective bandpasses resulting in different measured amplitudes from different observing sites. Recent WET runs (examples include Kanaan et al. 2005 and Vuckovic et al. 2006) comprise a mixture of CCD and PMT observations, and XCOV25 is no exception. CCDs were employed at sixteen observatories, and 3-channel PMT photometers at the remaining three sites. We attempt to minimize bandpass issues by using CCDs with similar detectors

Table 1
Journal of 2006 XCOV25 Observations

Run Name	Telescope	Instrument	Date	Length (hr)
konk20060512	Konkoly 1.0 m	CCD	2006 May 12	6.8
konk20060515	Konkoly 1.0 m	CCD	2006 May 15	6.3
mole20060515	Moletai 1.65 m	PMT	2006 May 15	1.3
mole20060517	Moletai 1.65 m	PMT	2006 May 17	3.5
konk20060517	Konkoly 1.0 m	CCD	2006 May 17	5.3
cuba20060517	Mt. Cuba 0.6 m	CCD	2006 May 18	5.4
kpno20060518	KPNO 2.1 m	CCD	2006 May 18	7.0
ctio20060518	CTIO 0.9 m	CCD	2006 May 19	4.4
kpno20060519	KPNO 2.1 m	CCD	2006 May 19	7.3
hawa20060518	Hawaii 0.6 m	CCD	2006 May 19	2.2
luln20060519	Lulin 1.0 m	CCD	2006 May 19	5.0
cuba20060519	Mt. Cuba 0.6 m	CCD	2006 May 20	2.5
ctio20060519	CTIO 0.9 m	CCD	2006 May 20	2.1
kpno20060520	KPNO 2.1 m	CCD	2006 May 20	7.6
hawa20060519	Hawaii 0.6 m	CCD	2006 May 20	1.7
ters20060520	Peak Terskol 2.0 m	CCD	2006 May 20	5.8
cuba20060520	Mt. Cuba 0.6 m	CCD	2006 May 21	7.1
kpno20060521	KPNO 2.1 m	CCD	2006 May 21	7.3
ctio20060520	CTIO 0.9 m	CCD	2006 May 21	0.7
hawa20060520	Hawaii 0.6 m	CCD	2006 May 21	3.5
ters20060521	Peak Terskol 2.0 m	CCD	2006 May 21	6.0
tueb20060521	Tuebingen 0.8 m	CCD	2006 May 21	6.6
lapa20060521	La Palma WHT 4.2 m	CCD	2006 May 22	0.9
cuba20060521	Mt. Cuba 0.6 m	CCD	2006 May 22	4.4
ctio20060521	CTIO 0.9 m	CCD	2006 May 22	4.5
kpno20060522	KPNO 2.1 m	CCD	2006 May 22	1.0
cuba20060521	Mt. Cuba 0.6 m	CCD	2006 May 22	1.7
hawa20060521	Hawaii 0.6 m	CCD	2006 May 22	7.8
luln20060522	Lulin 1.0 m	CCD	2006 May 22	4.5
konk20060522	Konkoly 1.0 m	CCD	2006 May 22	4.2
ters20060522	Peak Terskol 2.0 m	CCD	2006 May 22	1.3
mcdo20060523	McDonald 2.1 m	CCD	2006 May 23	7.4
kpno20060523	KPNO 2.1 m	CCD	2006 May 23	2.9
hawa20060522	Hawaii 0.6 m	CCD	2006 May 23	6.6
boao20060523	BOAO 1.8 m	CCD	2006 May 23	7.1
mcdo20060524	McDonald 2.1 m	CCD	2006 May 24	7.2
cuba20060523	Mt. Cuba 0.6 m	CCD	2006 May 24	4.0
hawa20060523	Hawaii 0.6 m	CCD	2006 May 24	3.7
boao20060524	BOAO 1.8 m	CCD	2006 May 24	6.7
ters20060524	Peak Terskol 2.0 m	CCD	2006 May 24	6.1
haut20060524	OHP 1.93 m	PMT	2006 May 24	2.3
mcdo20060525	McDonald 2.1 m	CCD	2006 May 25	6.4
hawa20060524	Hawaii 0.6 m	CCD	2006 May 25	5.7
ters20060525	Peak Terskol 2.0 m	CCD	2006 May 25	7.1
haut20060525	OHP 1.93 m	PMT	2006 May 25	4.2
ctio20060525	CTIO 0.9 m	CCD	2006 May 26	4.0
hawa20060525	Hawaii 0.6 m	CCD	2006 May 26	8.8
haut20060526	OHP 1.93 m	PMT	2006 May 26	4.0
ters20060526	Peak Terskol 2.0 m	CCD	2006 May 27	7.1
ctio20060526	CTIO 0.9 m	CCD	2006 May 27	4.3
hawa20060526	Hawaii 0.6 m	CCD	2006 May 27	9.1
chin20060527	BAO 2.16 m	PMT	2006 May 27	4.5
haut20060527	OHP 1.93 m	PMT	2006 May 27	4.6
cuba20060527	Mt. Cuba 0.6 m	CCD	2006 May 28	6.2
lna20060528	Itajuba 1.6 m	CCD	2006 May 28	3.1
mcdo20060528	McDonald 2.1 m	CCD	2006 May 28	0.7
mcdo20060528b	McDonald 2.1 m	CCD	2006 May 28	7.2
hawa20060527	Hawaii 0.6 m	CCD	2006 May 28	7.8
chin20060528	BAO 2.16 m	PMT	2006 May 28	5.2
haut20060528	OHP 1.93 m	PMT	2006 May 28	5.2
vien20060528	Vienna 1.0 m	CCD	2006 May 28	2.2
cuba20060528	Mt. Cuba 0.6 m	CCD	2006 May 29	3.4
mcdo20060529	McDonald 2.1 m	CCD	2006 May 29	8.2
cuba20060528	Mt. Cuba 0.6 m	CCD	2006 May 29	2.6
hawa20060528	Hawaii 0.6 m	CCD	2006 May 29	9.1
ters20060529	Peak Terskol 2.0 m	CCD	2006 May 29	6.0
haut20060529	OHP 1.93 m	PMT	2006 May 29	5.3
cuba20060529	Mt. Cuba 0.6 m	CCD	2006 May 30	2.7
ters20060530	Peak Terskol 2.0 m	CCD	2006 May 30	6.9
haut20060530	OHP 1.93 m	PMT	2006 May 30	4.2
hawa20060530	Hawaii 0.6 m	CCD	2006 May 31	8.7
chin20060531	BAO 2.16 m	PMT	2006 May 31	3.9
ters20060531	Peak Terskol 2.0 m	CCD	2006 May 31	7.0
nord20060606	NOT 2.7 m	CCD	2006 Jun 6	5.9
tueb20060607	Tuebingen 0.8 m	CCD	2006 Jun 7	4.2
nord20060607	NOT 2.7 m	CCD	2006 Jun 7	7.1
tueb20060608	Tuebingen 0.8 m	CCD	2006 Jun 8	4.7
nord20060608	NOT 2.7 m	CCD	2006 Jun 8	8.0
tueb20060609	Tuebingen 0.8 m	CCD	2006 Jun 9	5.4
nord20060609	NOT 2.7 m	CCD	2006 Jun 9	7.9
tueb20060610	Tuebingen 0.8 m	CCD	2006 Jun 10	5.2
tueb20060611	Tuebingen 0.8 m	CCD	2006 Jun 11	5.1
tueb20060612	Tuebingen 0.8 m	CCD	2006 Jun 12	4.5
lapa20060613	La Palma WHT 4.2 m	CCD	2006 Jun 13	1.8
tueb20060613	Tuebingen 0.8 m	CCD	2006 Jun 13	5.2
lapa20060614	La Palma WHT 4.2 m	CCD	2006 Jun 14	1.4
lapa20060615	La Palma WHT 4.2 m	CCD	2006 Jun 15	2.6
lapa20060616	La Palma WHT 4.2 m	CCD	2006 Jun 16	2.0

and equipping each CCD with a BG40 or S8612 filter to normalize wavelength response and reduce extinction effects. The bi-alkali photomultiplier tubes are blue sensitive, so no filters are required. We also made every attempt to observe the same comparison star at each site, but given plate scale differences, that is not always possible.

We employ a 10 s contiguous integration time with the PMT photometers, while the cycle time for the CCD observations, including exposure and readout times, varies for each instrument. To illustrate the extremes, the Argos camera (Nather & Mukadam 2004) at McDonald Observatory uses a frame-transfer CCD and 5 s integrations with negligible deadtime, while the camera on the CTIO 0.9m telescope operated by the SMARTS consortium uses 10 s integration and a 25 s readtime for a total cycle time of ≈35 s.

Data reduction for the PMT observations follows the prescription outlined in Nather et al. (1990) and W94. In most cases, a third channel continuously monitored sky, allowing point by point sky subtraction. For two channel observations, the telescope is occasionally moved off the target/comparison for sky observations. We examined each light curve for photometric quality, and marked and discarded "bad" points. "Bad" points are those dominated by external effects such as cosmic rays or clouds. We divided GD358's light curve by the comparison star to remove first order extinction and transparency effects. If necessary, we fit a low order polynomial to the individual light curves to remove remaining low frequency variations arising from differential color extinction. We divided by the mean light curve value and subtracted 1, resulting in a light curve with amplitude variations as fractional intensity (mmi). The unit is a linear representation of the fractional intensity of modulation (1 mmi ≈ 1 mmag). We present our Fourier transforms (FT) in units of modulation amplitude (1 mma = 1×10^{-3} ma).

XCOV25 marked an evolution of WET headquarters' role in CCD data reduction. A standard procedure for a WET run is for observers to transfer observations to headquarters for analysis

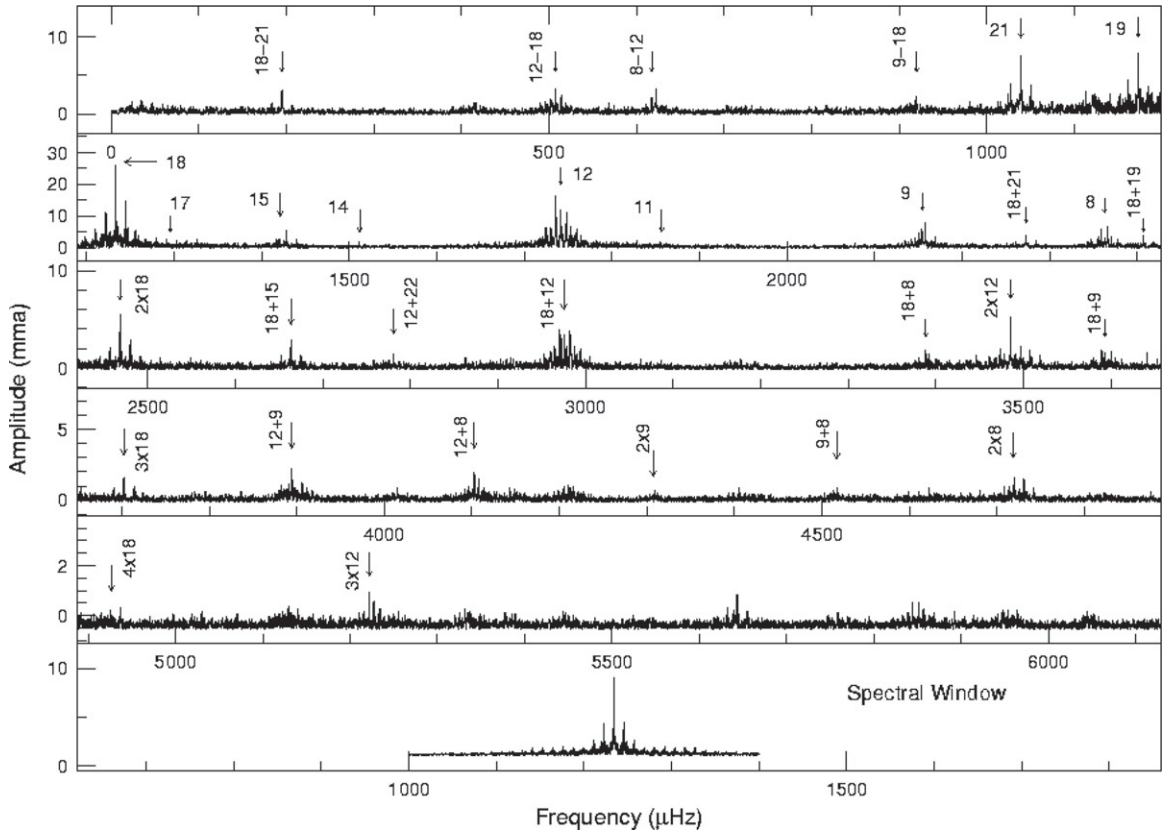

Figure 1. Fourier Transform of the 2006 GD358 photometry observations (note vertical scale in each panel). Arrows are labeled with *k* values for independent modes (single values) and first order combination frequencies. The unlabeled peaks are second and third order combinations. The spectral window is plotted in the last panel. Table 2 lists exact identifications.

at the end of each night. In the past, CCD observers completed initial reductions (bias, flat, and dark removal) at their individual sites, performed preliminary aperture photometry, and transferred the result to WET headquarters. For XCOV25, the majority of participants transferred their raw images, enabling headquarters to funnel data through a uniform reduction pipeline. The few sites unable to transfer images nightly performed preliminary reductions on site using the same procedures as those at headquarters, and sent their images at a later date.

CCD data reduction follows the pipeline described by Kanaan et al. (2002). We corrected each image for bias and dark counts, and divided by the flat-field. Aperture photometry with a range of aperture sizes was performed on each image for the target and selected comparison stars. For each individual nightly run, we chose the combination of aperture size and comparison star producing the highest signal/noise as the final light curve. Each reduced CCD light curve consists of a list of times and fractional intensities. As with the photometer observations, we examined each light curve for photometric quality and discarded "bad" points.

Finally, we combined the individual PMT and CCD light curves to produce the complete light curve for XCOV25. This last step requires detailed assessment of overlapping observations. We make two assumptions in this process: (1) our observational technique is not sensitive to periods longer than a few hours, and (2) we assume GD358 oscillates about a mean light level. These assumptions allow us to carefully identify and correct vertical offsets in overlapping segments.

This data set does contain a significant fraction of overlapping lightcurves. We experimented with the effects of overlapping data on the FT by computing FTs with (1) all data included, (2) no overlapping data, where we kept those data with higher signal-to-noise ratio, and (3) weighting the overlapping light curves by telescope aperture size. We found no significant differences between the noise levels or FTs of overlapping versus non-overlapping versus weighted data.

Despite the favorable weather enjoyed by many participating sites, there are gaps within our light curve, especially near the beginning and end of XCOV25 when fewer telescopes were on-line. These gaps produce spectral leakage in the amplitude spectrum, resulting in a pattern of alias peaks associated with each physical mode that is not of astrophysical origin. To quantify this, we sampled a single sinusoid exactly as our original data and calculated its amplitude spectrum. The "spectral window" is the pattern produced by a single frequency in our data set. The Fourier transform and spectral window of the final complete light curve are given in Figure 1.

3. FREQUENCY IDENTIFICATION

3.1. Stability

Before we can look in detail at the 2006 XCOV25 FT, we must investigate GD358's amplitude and frequency stability over the entire timebase. GD358 is known for large scale changes in amplitudes and small but not insignificant frequency variations on a variety of timescales (K03). Amplitude and/or frequency variations produce artifacts in FTs, greatly complicating any analysis. We divided the data set into three chunks spanning ≈180 hr and calculated the FT of each chunk (Figure 2). For

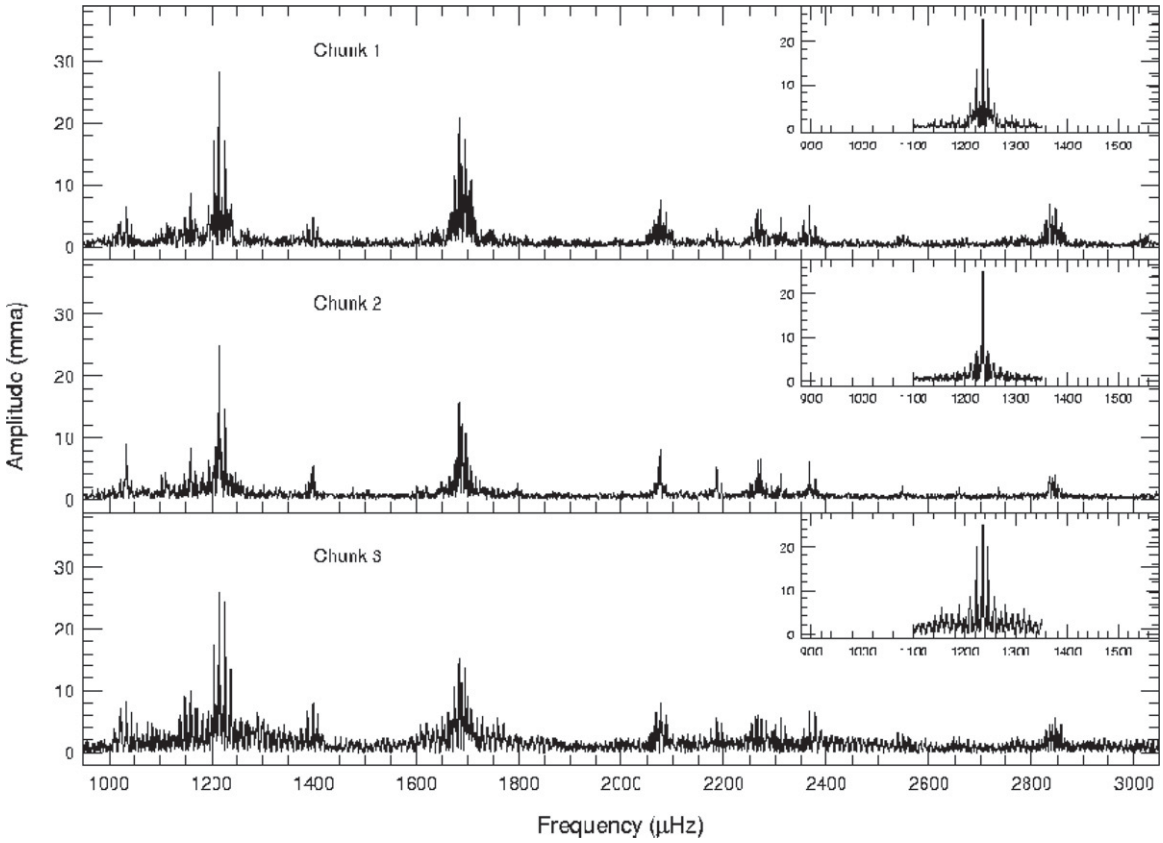

Figure 2. FTs of the 2006 data set subdivided into three chunks of ≈180 hr each. The changes in each FT can be explained as differences in the window structure/resolution for each chunk. GD358 was relatively stable over this time frame.

the dominant peak, the frequencies are consistent to within measurement error and the amplitudes remain stable to within 3σ. The differences between each FT are explained by variation in window structure and resolution from chunk to chunk. We are confident that GD358 was fairly stable over the length of XCOV25.

3.2. The 2006 Fourier Transform

To select the statistically significant peaks in the Fourier transform, we adopt the criterion that a peak have an amplitude at least 4.0 times greater than the average noise level in the given frequency range. This leads to a 99.9% probability that the peak is a real signal present in the data, and is not due to noise (Scargle 1982; Breger et al. 1993, K03, for example). Here, "noise" is defined as the average amplitude after prewhitening by the dominant frequencies in the FT, and is frequency dependent. This is a conservative estimate, as it is impossible to ensure that all of the "real" frequencies are removed when calculating the noise level. This is most certainly the case in GD358, where the FT contains myriad combination frequencies. Figure 3 displays the average amplitude, specified as the square root of the average power after prewhitening by 50 frequencies, as a function of frequency, for 2006, and previous WET runs on GD358 in 2000, 1994, and 1990.

The amplitude limit we select is very important in determining "real'signals. To confirm our uncertainty estimates, we performed several Monte Carlo simulations using the routine provided in *Period04*, software devoted to the statistical analysis of time series photometry (Lenz & Breger 2005). The Monte Carlo routine generates a set of light curves using the original times, the fitted frequencies and amplitudes, and added Gaussian noise. A least-squares fit is performed on each simulated light curve, with the distribution of fit parameters giving the uncertainties. Our Monte Carlo results are consistent with our average amplitude noise estimates (Table 2), confirming our use of the average amplitude after prewhitening.

For both Fourier analysis and multiple least squares fitting, we use the program *Period04*. The basic method involves identifying the largest amplitude resolved peak in the FT, subtracting that sinusoid from the original light curve, recomputing the FT, examining the residuals, and repeating the process. This technique is fraught with peril, especially in multiperiodic stars, where it is possible for overlapping spectral windows to conspire to produce alias amplitudes larger than real signals. Elimination of this alias issue was the driving motivation behind the development of the WET, whose goal is to obtain nearly continuous coverage over a long time baseline. Our current data set on GD 358 does contain gaps, but we have minimized the alias problem.

To illustrate the procedure we followed, let us examine the region of dominant power at 1234 μHz (Figure 4). Comparison of this region with the spectral window demonstrates that most of the signal is concentrated at 1234 μHz. We fit the data with a sine wave to determine frequency, amplitude, and phase, and subtract the result from the original light curve. The second panel of Figure 4 shows the FT prewhitened by this frequency. Careful examination reveals two residual peaks (arrows) that are clearly not components of the spectral window. We next subtract a simultaneous fit of the 1234 μHz frequency and these two additional frequencies, with the results displayed in panel 3 of Figure 4. At this point, we must proceed with extreme caution. The remaining peaks, which correspond closely with aliases in the spectral window, are significant and cannot be ignored.

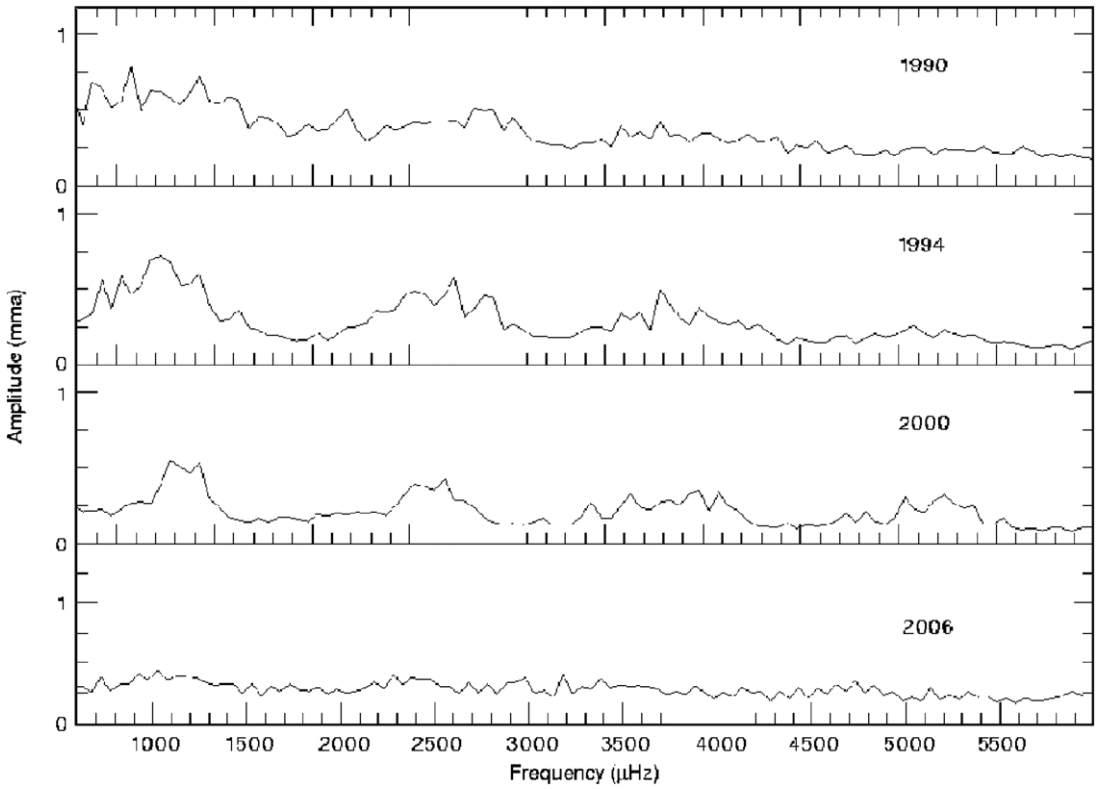

Figure 3. A comparison of the average noise from the 1990, 1994, 2000, and 2006 WET runs. Each data set was prewhitened by the 50 largest amplitude frequencies. This is a conservative estimate of the noise in each data set.

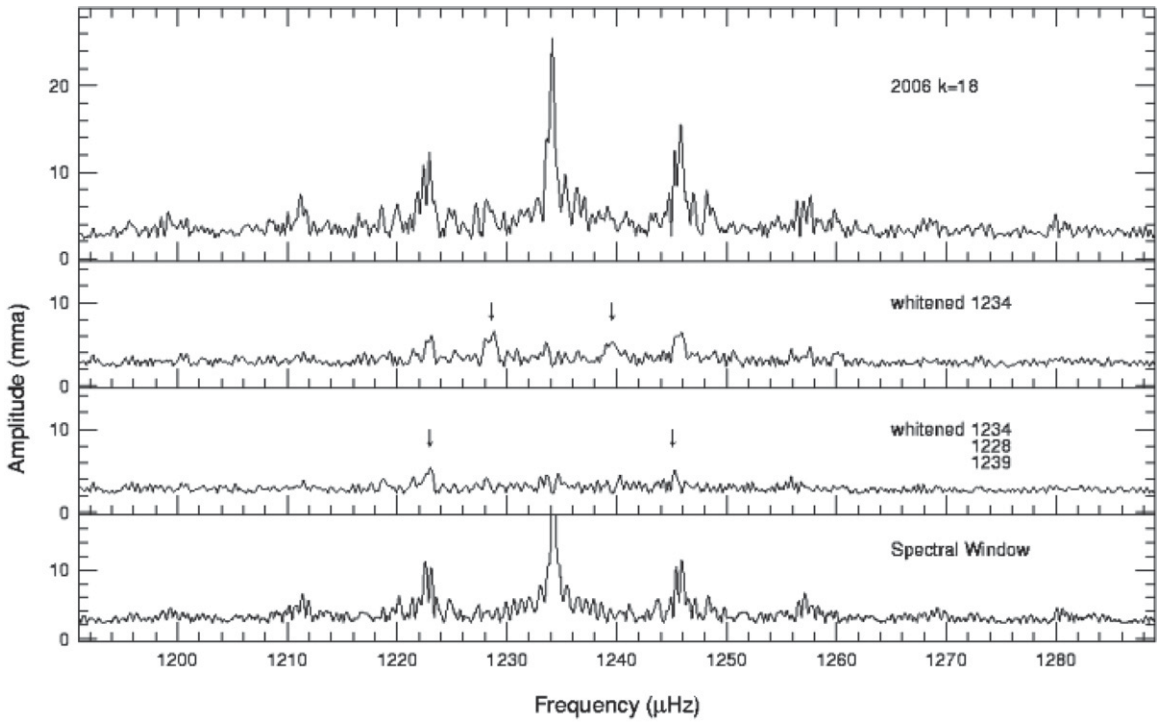

Figure 4. Demonstration of prewhitening using the dominant 1234 μHz mode in the 2006 FT. We begin with the removal of the largest amplitude resolved peak, a careful comparison of the residuals with the spectral window (last panel), and the subsequent removal of additional peaks.

We are faced with two possibilities: (1) these peaks represent real signals, and (2) amplitude modulation is present. While we have ruled out large modulations in frequency/amplitude during XCOV25, small scale amplitude modulation may be intrinsic to GD358, or artificially present in the data set. An examination of data from individual sites reveals that although the frequencies from each site are the same within the statistical uncertainties, two observatories, one using a CCD and one a

Table 2
Table of 2006 Independent Frequencies

$k(l=1)$	2006 Frequency (μHz)	Amp (mma)	S/N	MC σ_{amp} (mma)
21	1039.076 ± 0.002	7.96 ± 0.07	27	0.08
19	1173.042 ± 0.002	7.28 ± 0.07	25	0.08
18	1222.751 ± 0.001	5.0 ± 0.07	18	0.6
18	1228.792 ± 0.002	5.7 ± 0.07	19	0.07
18	1234.124 ± 0.001	24 ± 0.07	88	0.09
18	1239.540 ± 0.002	4.7 ± 0.07	18	0.07
18	1245.220 ± 0.003	4.7 ± 0.07	17	0.6
17	1295.533 ± 0.008	1.4 ± 0.08	5	0.6
15	1421.012 ± 0.008	2.8 ± 0.08	7	0.07
15	1423.942 ± 0.008	1.3 ± 0.08	6	0.07
15	1429.210 ± 0.002	5.6 ± 0.07	23	0.07
15	1434.784 ± 0.008	1.4 ± 0.07	4.4	0.06
15	1440.622 ± 0.008	1.4 ± 0.07	4.3	0.06
14	1512.010 ± 0.007	3.6 ± 0.08	8	0.07
12	1736.302 ± 0.001	17.0 ± 0.07	75	0.07
12	1737.962 ± 0.007	5.6 ± 0.07	8	0.08
12	1741.665 ± 0.001	10.9 ± 0.07	50	0.07
12	1743.738 ± 0.002	5.6 ± 0.07	8	0.07
12	1746.673 ± 0.007	1.8 ± 0.08	8	0.08
12	1749.083 ± 0.001	12.9 ± 0.07	50	0.07
11	1856.845 ± 0.009	1.4 ± 0.08	6.4	0.08
9^{-1}	2150.395 ± 0.003	4.2 ± 0.07	17	0.07
9^{0}	2154.222 ± 0.002	5.5 ± 0.07	22	0.07
9^{+1}	2158.071 ± 0.002	7.2 ± 0.07	29	0.07
8^{-1}	2359.064 ± 0.002	5.87 ± 0.07	22	0.07
8^{0}	2363.058 ± 0.007	1.82 ± 0.08	6	0.07
8^{+1}	2366.523 ± 0.002	6.54 ± 0.07	23	0.07

PMT, report consistently lower amplitudes, probably due to beating effects. Removing the suspect observations from the data set does not alter the prewhitening results for the 1234 μHz region. As an additional test, we closely examined the FTs from Figure 2. Prewhitening the 1234 μHz regions of each chunk consistently produces the same five peaks. Finally, we note that one of these peaks appears in combination with other modes (Table 3). Therefore, we believe our first possibility is most probable, all five peaks are real and are listed in Table 2.

We employed this procedure to identify frequencies satisfying our criteria of amplitudes 4σ above the average noise. The large amplitude power at 1740 μHz is particularly complex. Unlike our example at 1234 μHz, this mode contains three peaks with amplitudes over 10 mma and contains as many as nine frequencies (Figure 5). Figure 6 demonstrates the prewhitening results for modes at 2154 and 2362 μHz.

Our final identifications result from a simultaneous nonlinear least squares fit of 130 frequencies, amplitudes, and phases. We adopt the $l = 1$ mode identifications for GD358 established in W94. We emphasize, however, that k, representing the number of nodes in the radial component of displacement from the center to the stellar surface, cannot be observationally determined and may not correspond precisely to the values given here. Tables 2 lists 27 identified independent frequencies. Table 3 presents significant combination frequencies. In the interest of space, we do not list all of the combination frequencies.

Table 3
2006 Combination Frequencies

Frequency (μHz)	Combination(s) k	$f_{obs} - f_{calc}$ (μHz)	Amp (mma)	(S/N)	R_c
195.085	1234 − 21	0.04	2.7	7.7	...
507.523	1741.7 − 1234	−0.02	3.0	8.2	...
622.798	2358.1 − 1736.3	−1.0	2.8	7.5	...
920.039	9^0 − 1234	−0.06	1.9	4.5	...
2078.187	2 × 1039.1	−0.1	0.74	3.2	2.4
2273.244	1234 + 21	0.05	4.2	10.8	9.6
2407.205	1234 + 19	0.07	3.8	9.7	9.1
2462.989	1234 + 1228.8	0.07	3.7	8.2	11.4
2468.282	2 × 1234	0.034	5.1	13.1	1.8
2479.358	1234 + 1245.2	0.014	1.5	4.1	5.6
2663.369	1234 + 1429.2	0.04	2.9	7.3	9.4
2780.786	1741.7 + 1039.1	0.014	1.4	4.0	7.1
2909.416	1736.3 + 19	0.1	1.0	2.6	3.5
2964.917	1228.8 + 1736.3	−0.18	1.1	2.8	5.0
	1222.8 + 1741.7	−0.46	1.1	2.8	
2970.400	1234 + 1736.3	0.025	3.0	7.6	3.1
	1228.8 + 1741.7	−0.057			
2972.085	1234 + 1737.9	0.036	2.82	7.6	8.8
	1222.8 + 1749.1	−0.22			
2975.814	1234 + 1741.7	−0.024	3.4	8.7	5.5
	1239.5 + 1736.3	−0.039			
2977.885	1228.8 + 1749.1	0.01	1.7	4.4	11.9
	1234 + 1743.8	0.02			
2981.032	1239.5 + 1741.7	0.17	1.3	4.0	11.2
2981.947	1245.2 + 1736.3	−0.45	3.5	7.9	20.6
2983.266	1234 + 1749.1	0.057	3.1	7.9	4.66
2988.643	1239.5 + 1749.1	−0.42	1.1	3.9	9.36
3388.400	1234 + 9^0	0.052	1.5	4.0	4.75
3392.185	1234 + 2150.4	−0.013	1.7	4.4	7.35
3472.552	2 × 1736.3	−0.052	1.5	4.8	1.2
3477.939	1736.3 + 1741.7	0.06	1.7	4.5	4.0
3485.387	1741.7 + 1743.7	−0.02	5.7	16.7	11.6
	1736.3 + 1749.1	0.003	5.7	16.8	
3490.720	1741.7 + 1749.1	0.03	1.3	4.0	
3593.136	1234 + 2359.1	−0.041	1.6	4.2	4.8
3600.577	1234 + 2366.5	−0.071	1.7	4.5	4.5
3702.443	3 × 1234	0.071	2.0	5.3	
3890.607	1736.3 + 9^0	0.08	1.5	4.8	7.0
3894.392	1736.3 + 2158.1	0.016	2.7	7.7	6.8
3907.140	1749.083 + 2158.1	−0.014	1.6	5	7.7
4095.326	1736.302 + 2359.1	−0.03	1.2	4.0	5.2
4102.850	1736.302 + 2366.5	0.024	2.2	7.3	4.0
4108.130	1749.083 + 2359.1	−0.06	1.7	5.6	9.8
4209.941	2 × 1234 + 1741.7	0.028	1.3	4.8	
4308.536	2 × 9^0	−0.092	1.0	4.6	11.7
4517.044	8^0 + 9^0	−0.24	1.1	4.7	48.5
	2359.1 + 2158.1	0.13			
	2150.4 + 2366.5	−0.08			
4719.483	2 × 2359.064	−1.4	2.1	7.2	13.2
4718.268	2 × 2359.064	−0.14	1.1	4.7	
5221.734	1736.3 + 1741.7 + 1743.7	0.034	1.3	4.2	
	2 × 1736.3 + 1749.1	−0.049			
5643.452	1736.3 + 1749.1 + 2158.1	0.05	1.2	4.1	

4. GD358 IN 2006

4.1. Independent Modes

The 2006 XCOV25 data set illustrates GD358's continuing tendency for changing the distribution of amplitudes among its excited modes. Using the k identifications established in W94, we detect power at $k = 21, 19, 18, 17, 15, 14, 12, 11, 9$, and 8. The principal frequency is at 1234 μHz ($k = 18$) with an amplitude

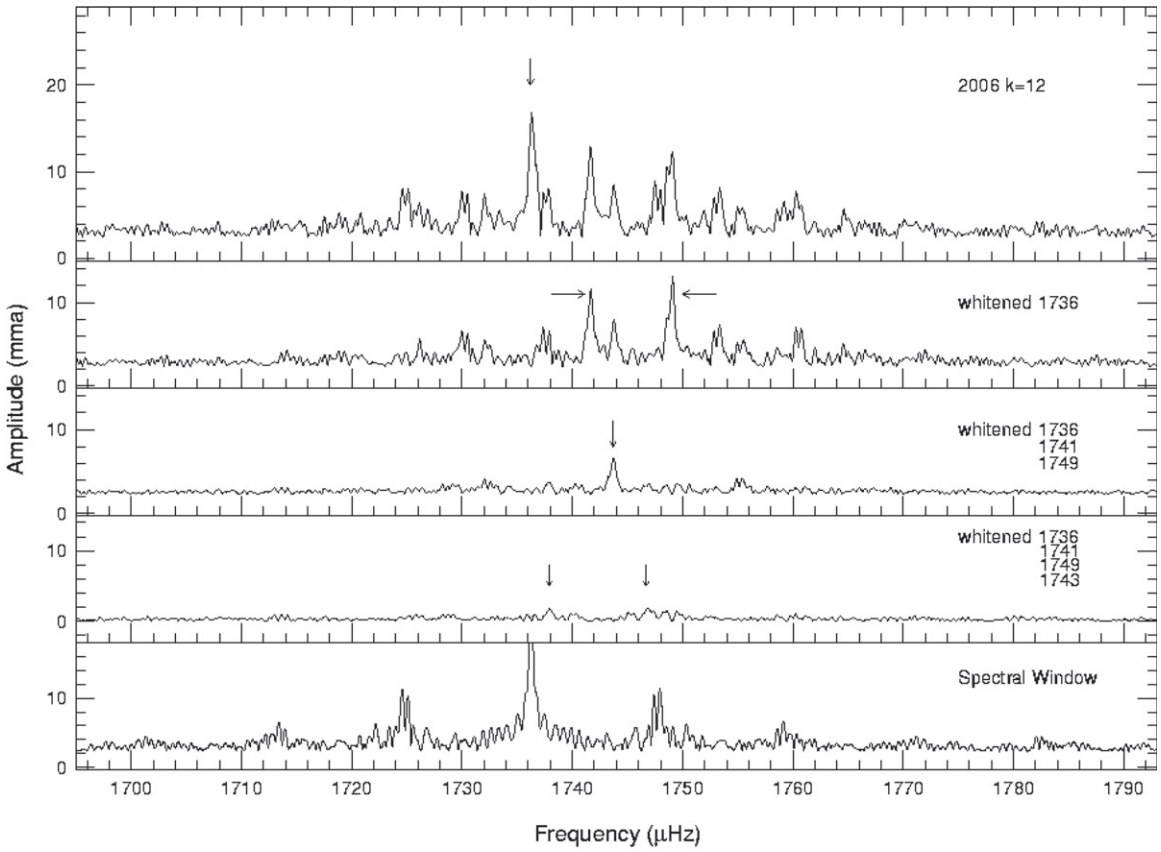

Figure 5. Prewhitening of the complex $k = 12$ mode. We find three peaks over 10 mma at 1736, 1741 and 1749 μHz, and numerous additional peaks (Table 2). This mode could contain as many as 9 components.

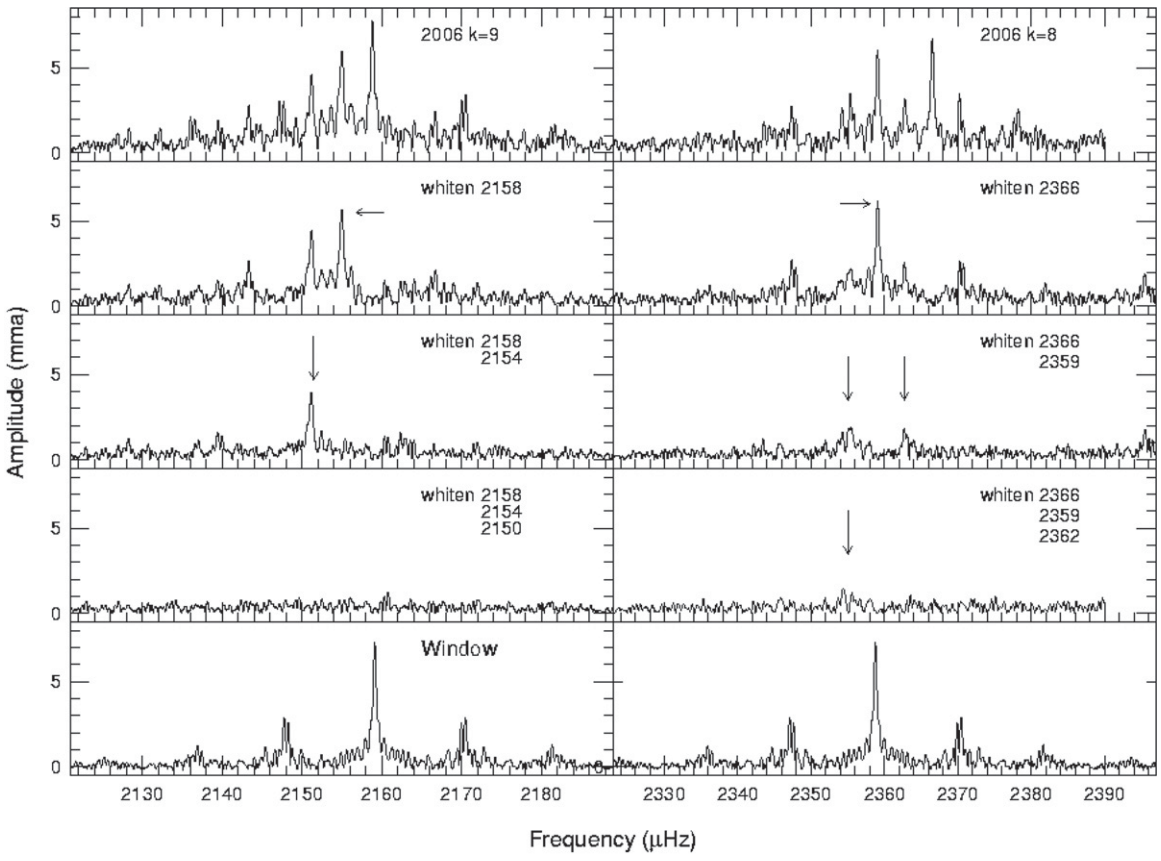

Figure 6. Prewhitening of the $k = 9$ and 8 modes. These modes are triplets consistent with previous reports of W94 and K03.

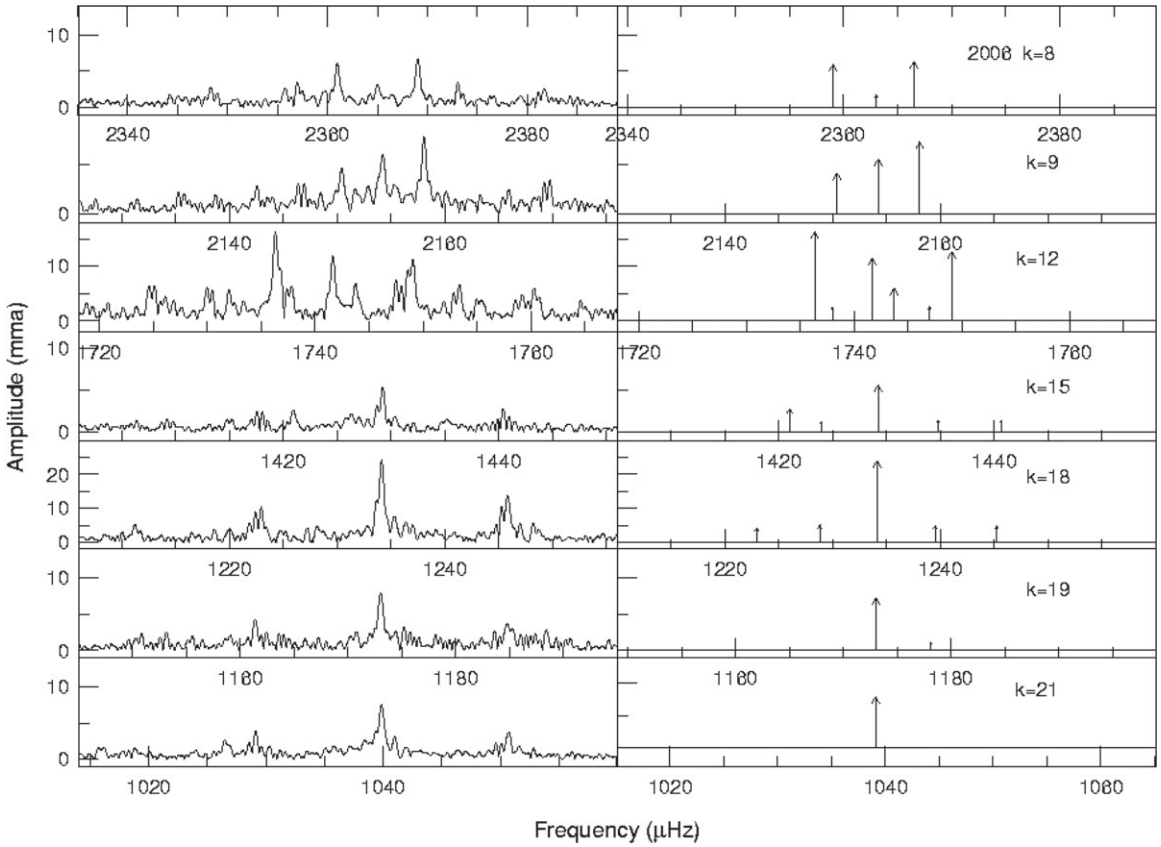

Figure 7. A "snapshot" of the 2006 largest amplitude modes and their multiplet structure. The left panels plot the observed FT, and the right panels presents the prewhitening results. The 1σ frequency errors are $\approx$0.001 μHz. Each panel spans 50 μHz. Note the changes in y scale.

of 24 mma. The previously dominant $k = 17$ and 15 modes (K03) are greatly diminished in amplitude (1.4 and 5.6 mma, respectively), and we do not detect the $k = 16$ or $k = 13$ modes reported by W94 and K03. We cannot identify the suspected $l = 2$ mode at 1255.4 μHz or $k = 7$ at 2675.5 μHz noted by K03). K03 suggest that $k = 7$ may have been excited to visibility via resonant coupling with $k = 17$ and 16. Since neither has significant amplitude in 2006 (Figure 1), it logically follows that this mode would not be detected. Perhaps the greatest surprise from XCOV25 is the appearance of prominent power at the predicted value for $k = 12$, a region of the FT previously devoid of significant peaks.

Figure 7 presents a "snapshot" of multiplet structure in the XCOV25 FT. The only modes exhibiting structure with splittings in agreement with previous observations are $k = 9$ and 8. We find average multiplet splittings of 3.83 and 3.75 μHz, respectively. The dominant $k = 18$ is a quintuplet with an average splitting of 5.6 μHz. The 5.6 μHz splitting also appears in the $k = 15$ and $k = 12$ modes. The $k = 15$ mode contains five peaks, only three of which are split by 5.6 μHz. The $k = 12$ mode could contain as many as nine components, if we relax our 4.0 σ detection criteria slightly. A possible interpretation for $k = 12$ is two, perhaps three, overlapping triplets, each with $\approx$ 5.6 μHz splitting. An $l = 2$ mode is predicted at $\approx$1745μHz, so a second possible interpretation is an overlap of $l = 1$ and $l = 2$ modes. We point out that the other high-k modes (17, 16, 14, and 13) reported by W94 to have frequency splittings of $\approx$ 6 μHz are either not detected here, or do not have sufficient amplitude to investigate multiplet structure.

Our goal for XCOV25 is the identification/confirmation of l and m values for modes in GD358's 2006 light curve. This information is required to fit our high signal-to-noise lightcurve using Montgomery's technique. However, the 2006 multiplet structure proves to be puzzling. In the limit of slow rotation, we expect each mode to be split into $2l + 1$ components. Except for $k = 9$ and $k = 8$, we do not find the distinct triplets attributable to $l = 1$. Indeed, $k = 18$ is a quintuplet at first glance suggesting $l = 2$, and $k = 15$ and 12 are both complex but lacking equal splittings. We cannot confirm the l or m designations of W94 and K03 based on multiplet structure alone. Fortunately, the identification of the spherical degree of GD358's pulsation modes as $l = 1$ does not rely solely on multiplet structure. Table 4 presents the mean period spacing for XCOV25, as well as WET runs from 1990, 1991, 1994, and 2000. The average period spacing, which is dependent on stellar mass, is 38.6 s. If GD358's modes are consecutive $l = 1$, the period spacing corresponds to a stellar mass of $\approx 0.6\ M_o$, in agreement with spectroscopic results (Beauchamp et al. 1999). If they are consecutive $l = 2$ modes, the derived stellar mass becomes $\approx 0.2\ M_o$, making GD358 one of the lowest mass field white dwarfs known and incompatible with the spectroscopic log g. In addition, the distance of 42 ± 3pc derived from GD358 models assuming $l = 1$ is consistent with the trigonometric distance of 36 ± 4pc. The distance derived derived from models assuming $l = 2$ is $\approx$75 pc (Bradley & Winget 1994). Is it possible that we have an amalgam of $l = 1$ and 2 modes? $l = 2$ modes are predicted to be quintuplets, fitting with our results for $k = 18$. However, we expect the ratio of rotational splittings between $l = 1$ and $l = 2$ to be $R_{1,2} = 0.60$ (Winget et al. 1991). Assuming

Table 4
Mean Period Spacing

Year	Time BJED	ΔP_{av} (s)
1990	2440831.772	38.60 ± 0.3
1991	2448356.716	38.39 ± 0.3
1994	2449474.998	38.67 ± 0.3
2000	2451702.402	38.77 ± 0.3
2006	2453868.311	38.77 ± 0.3

Notes. The spacing from the "period transform is given as PT, and the value from the subtracting of low- and high-k periods is "K."

$k = 8$ and 9 are $l = 1$ as indicated by their triplet structure, we expect an $l = 2$ splitting of 6.3 μHz, much larger than the observed 5.6 μHz splitting. We have no easy explanation for the 5.6 μHz splitting, and hesitate to identify $k = 18$ as an $l = 2$ mode solely on the basis of a quintuplet. The $k = 12$ and $k = 15$ modes contain the mysterious 5.6 μHz splitting, but the splittings are unequally spaced. The "best fit" pulsation models do predict $l = 2$ modes at 1250 μHz (near $k = 18$) and 1745 μHz (near $k = 12$) (Metcalfe et al. 2003). The 1250 μHz mode is not detected in this data set. Some of the complex peaks at $k = 12$ could correspond to an underlying $l = 2$ mode, but the splittings do not support this conclusion. Finally, optical and UV radial velocity variations have been used to determine the l values for several modes in GD358, including $k = 18$. Kotak et al. (2003) identified radial velocities corresponding to $k =$ 18, 17, 15, 9, and 8 in their time-resolved optical spectra. They determined that these modes all share the same l value, which is probably $l = 1$. Castanheira et al. (2005) use *HST* UV time resolved spectroscopy to determine that $k = 9$ and 8 are best explained as $l = 1$.

While we are fairly certain that the majority of GD358's modes are $l = 1$, except for $k = 9$ and 8, we cannot directly provide m identifications for the observed multiplet components or confirm the m identifications of W94 and K03. For this data set, we must resort to indirect means. In the next section, we examine the combination frequencies, and, limiting ourselves to $l = 1$, explore their potential for pinning down the multiplet m components in GD358.

4.2. Combination Frequencies

GD358's 2006 FT contains a rich distribution of combination frequencies, from differences to simple harmonics to fourth order combinations. Combinations peaks are typically observed in the FTs of large amplitude pulsators (Dolez et al. 2006; Yeates et al. 2005; Thompson et al. 2003; Handler et al. 2002, W94). Their frequencies correspond to integer multiples of a single frequency (harmonics), combinations (both sums and differences) of different components of a given multiplet, or combinations (again both sums and differences) of components of different modes (cross combinations). The general consensus on the origin of these combinations dictates that they are not independent modes, but are the result of nonlinear mixing induced by the convection zone in the outer layers of the star (Brickhill 1992; Wu 2001; Ising & Koester 2001). The convection zone varies its depth in response to the pulsations, distorting and delaying the original sinusoidal variations, and redistributing some power into combination frequencies. While combinations themselves do not provide additional direct information about the interior structure of the star, they are sensitive to mode geometry, making them potential tools for identifying l and/or m values and orientation for each mode.

Wu (2001) provides a theoretical overview of combinations and their interpretation. Handler et al. (2002) and Yeates et al. (2005) apply Wu's approach to several ZZ Ceti (DA) stars. Yeates et al. (2005) focus on the dimensionless ratio R_c first introduced by van Kerkwijk et al. (2000). The theoretical value of R_c is given as $R_c = F(\omega_i, \omega_j, \tau_{c_0}, 2\beta + \gamma)G(l, m, \theta)$. The first term, F, includes the frequencies of the parent modes (ω_i, ω_j), as well as properties inherent to the star, such as the depth of the stellar convection zone at equilibrium (τ_{c_0}) and the sensitivity of the convection zone to changes in temperature (β, γ). The second term, G, includes geometric factors such as the l and m values of the parent modes, and the inclination angle of the pulsation axis. Both Wu (2001) and Yeates et al. (2005) present theoretical predictions for various combinations of l and m values.

The observed value of R_c is defined as the ratio between the observed amplitude of a combination and the product of the observed amplitudes of its parent modes, including a correction factor incorporating the bolometric correction and an estimate for the convective exponent. The convective exponent appears in theoretical estimations of the thermal response timescale of the convection zone. From Montgomery (2008), we estimate the bolometric flux correction for GD358 to be 0.35 and the convective exponent to be 25. For harmonic combinations, this produces a corrective factor of 0.22. Cross combinations include an additional factor of 2, resulting in a correction of 0.44. With this formalism, and limiting ourselves to the previous identification of the principal modes as $l = 1$, and with the smorgasbord of combination frequencies present in GD358, it should be possible to determine m values of the parent modes, to provide limits on the inclination angle, and to further study convection in white dwarfs. However, interpretation of the combination frequencies is not as straightforward as we would hope.

The analysis of R_c for harmonic combinations is simplified by the fact that we are certain that the combination contains a single parent, and so single values for l and m. In the 2006 data set, we detect the dominant 1234 μHz mode's first, second, and third harmonics, and place upper amplitude limits of ≈ 0.3 mma on higher orders. The first harmonic, at 2468.282 μHz with an amplitude of 5.1 mma, is the 12th highest amplitude peak in the FT and the second highest amplitude combination frequency observed.

The second largest mode and most complicated multiplet in the 2006 FT is $k = 12$. Focusing on its three large amplitude components (Table 3), we find the first harmonic of 1736 μHz, near 3472 μHz with an amplitude of 1.5 mma. Interestingly, the largest peak near 3472 μHz is actually a sum of $k = 12$ components (see Table 3), not a simple harmonic, a behavior distinctly different from $k = 18$. We place an upper limit of 0.5 mma for a 1st harmonic of 1741.67 μHz, 0.6 mma for 1749.08 μHz, and upper limits of 0.3 mma for all higher orders for all other components of $k = 12$.

For the remaining modes in Table 2, we detect the first harmonic of 1039 μHz ($k = 21$) with an amplitude of 0.7 mma. For $k = 19$, 17, 15, 14, and 11, we place upper limits of 0.5 mma for their first harmonics. The 2154 μHz peak, identified as $k = 9$, $m = 0$ ($k = 9^0$) in W94, has a first harmonic with an amplitude of 1.0 mma. It is surprising that we do not detect a harmonic of the larger amplitude $k = 9^{+1}$ component. We place upper limits of 0.4 mma for harmonics of the $k = 9^{\pm 1}$ components. Finally, the 2359 μHz component of $k = 8$, identified as $k = 8^{-1}$ in W94, has a first harmonic at 4719.483 μHz (2.1 mma). We place upper limits of 0.4 mma for harmonics of the $k = 8^0$ and

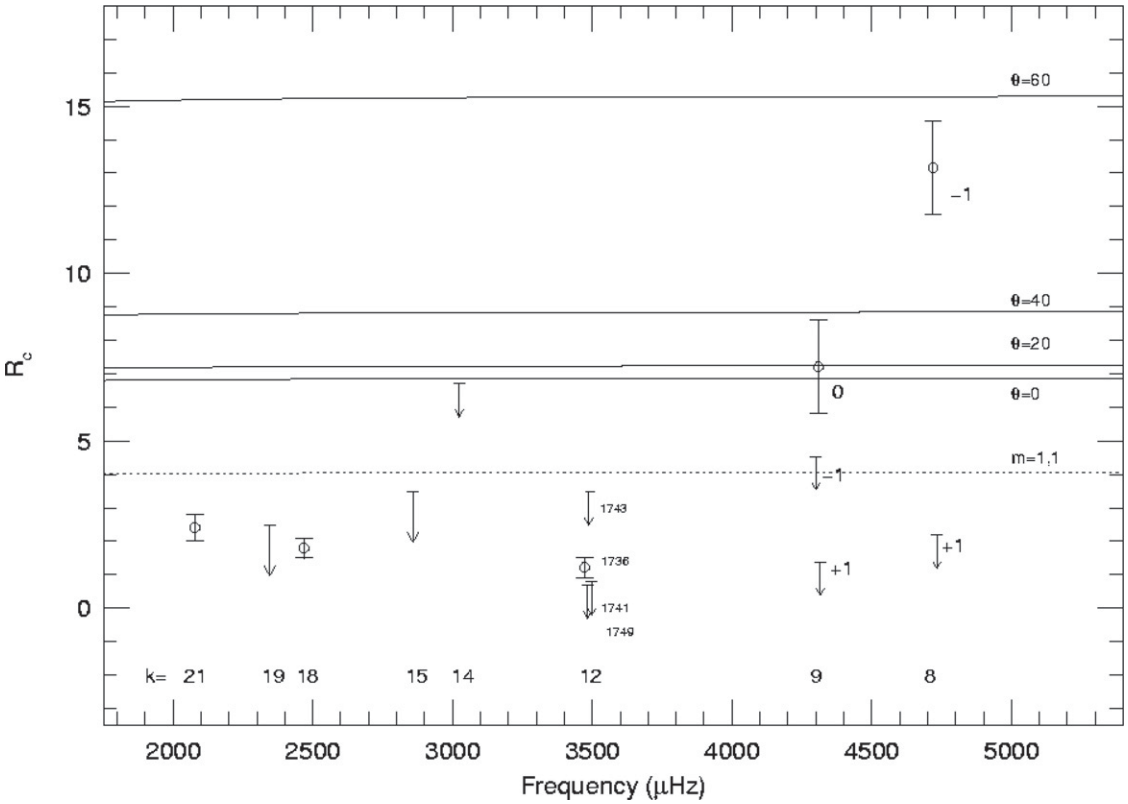

Figure 8. Observed R_c values (ratio of amplitude of the combination to the product of the parent amplitudes) for detected harmonics. The open circles denote detected harmonics with estimated errors, and the vectors plot upper limits on other harmonics. The solid lines represent theoretical values for the harmonics of $m = 0$ modes for inclinations of 0, 20, 40, and 60°. The dotted line gives the theoretical value for the harmonics of $m = 1$ and $m = -1$ modes, which do not depend on inclination. We rely on previous identifications of m values for $k = 9$ and 8.

$k = 8^{+1}$ components. We note again that the larger amplitude $k = 8^{+1}$ does not have a significant harmonic.

We begin by plotting the observed values of R_c for first order harmonics in Figure 8. If no harmonic is detected, we present upper limits. Since we do not have m identifications for most modes but we know that m must be the same for harmonic parents, we plot theoretical predictions for $l = 1$, $m = 0, 0$ combinations for inclinations of 0, 20, 40, and 60° (solid lines) and $l = 1$, $m = 1, 1$ and $m = -1, -1$ (dotted line). R_c values for $m = 1, 1$ and $m = -1, -1$ combinations do not depend on inclination. Surprisingly, the observed R_c values and upper limits for the high-k modes are lower than the theoretical predictions. We could argue that, under the theoretical assumptions of Wu (2001), the detected high-k multiplet components are not consistent with $m = 0$.

From the $k = 9$ harmonics, we find behavior closer to theoretical predictions. The $k = 9^0$ harmonic is consistent with an inclination of between 0 and 40°, while the $k = 9^{\pm 1}$ components are in the direction of theoretical predictions. However, for $k = 8$, the $k = 8^{-1}$ harmonic has a larger value of R_c than the $k = 8^{+1}$ upper limit, something that is difficult to explain using current theory and simple viewing arguments. The upper limit of R_c for $k = 8^0$ is 29, and is not shown in Figure 8.

The most eye-catching example of cross combination peaks is found near 3000 μHz (Figure 1), corresponding to linear combinations between the two largest multiplets, $k = 18$ and $k = 12$. Our resolution and sensitivity are sufficient to reveal nine combinations, with amplitudes ranging from 3.4 mma to 1.1 mma. In several cases, multiple parent identifications are possible for each mode. For the following discussion, we include identifications for detected combinations involving at least one large amplitude parent, with most including the 1234 μHz mode in combination with components of $k = 12$ (Table 3). The 1234 μHz mode also produces large amplitude combinations (4.2 and 3.8 mma) with the 1039 ($k = 21$) and 1173 ($k = 19$) μHz modes.

Figure 9 presents observed R_c values and upper limits for first order cross combinations including the dominant 1234 μHz mode as one parent. We include the same theoretical predictions as in Figure 8, adding predictions for $l = 1$, $m = +1, -1$ combinations for inclinations of 20, 40, and 60° (dotted lines), and $m = 0, \pm 1$ combinations (dot/dash line). The R_c values for combinations of 1234 μHz with the high-k modes 21, 19, 15, and one component of $k = 12$ (1739 μHz) are consistent with either $m = 0, 0$ combinations with an inclination of roughly 40° or $m = +1, -1$ combinations with an inclination closer to 50°. Recalling that the harmonic combinations (Figure 8) argue that none of the high-k modes are $m = 0$, the second choice of $m = +1, -1$ combinations seems more likely. This further implies that 1234 μHz is either $m = +1$ or $m = -1$, and the other modes are all the remaining value.

The relative values of R_c among the 3000 μHz combinations ($k = 18$+12), while independent of most model parameters, do depend on inclination, and should reflect their respective projection in our line of sight. We should find R_c values corresponding to combinations of $m = 0, \pm 1$, $m = 0, 0$, $m = -1, +1$, and $m =$ same. However, even incorporating our tenuous identification of 1234 μHz as $m = -1$, given the number of multiplet components and large uncertainties in the inclination angle, our analysis based on Wu (2001) predictions produces no clear identification.

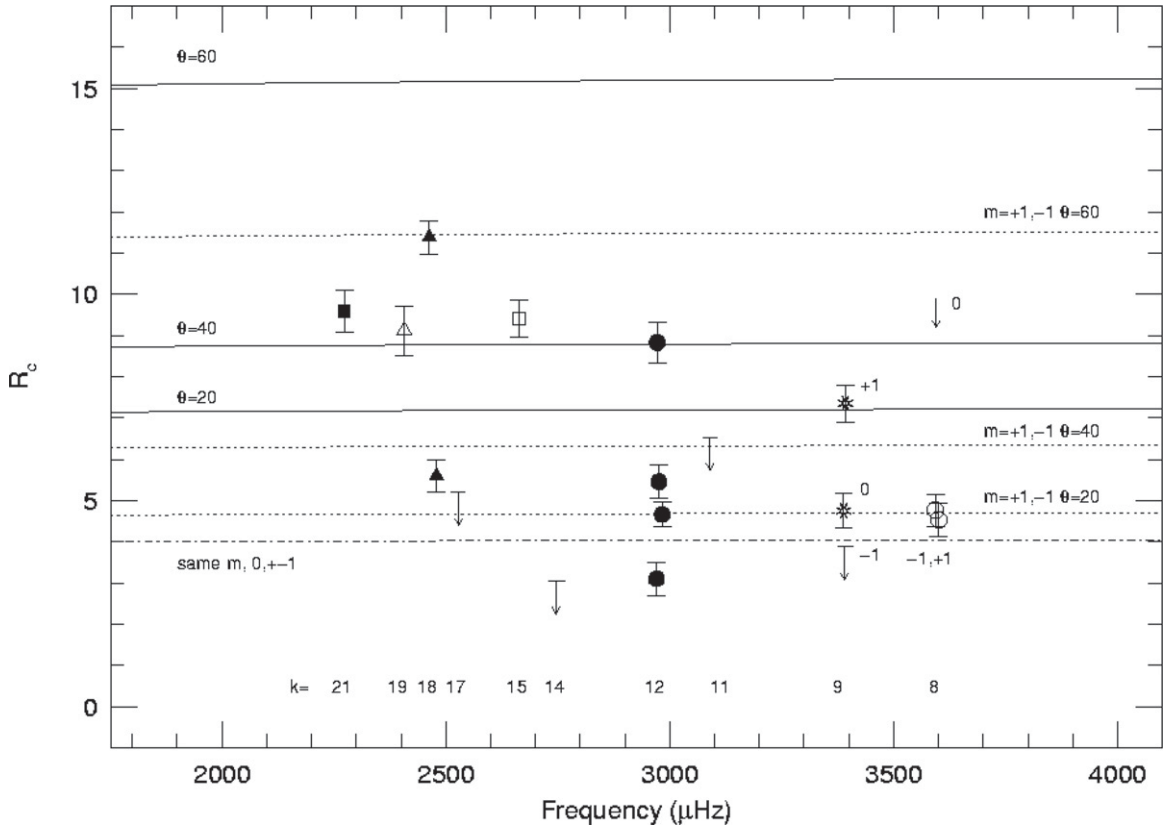

Figure 9. Observed R_c values (ratio of amplitude of the combination to the product of the parent amplitudes) for cross combinations including 1234 μHz as one parent mode. The k value of the second parent is given along the bottom of the figure, and different point types indicate combinations of 1234 μHz with different ks. The solid lines represent theoretical predictions for $m = 0, 0$ combinations with inclinations of 20, 40, and 60°, the dotted lines are for $m = +1, -1$ combinations with the same inclinations, and the dot/dash line represents $m = 1, 1$ and $m = -1, -1$, and $m = 0, \pm 1$ combinations. Error bars are 1σ formal errors.

Our analysis of GD358's combination frequencies is complex. We find a very tenuous identification for the 1234 μHz mode of $m = \pm 1$, requiring the remaining high-k modes' largest component to be the remaining value. We find no clear m identifications for the components of $k = 12$. This mode is clearly more complex than the simple multiplet structure expected in the limit of slow rotation.

There are multiple reasons why GD358's combination frequencies defy simple interpretation. First, this star simply has too many principal modes simultaneously excited to large amplitude. The cross-talk between them is large, and the perturbative treatment of Wu (2001) may not be valid. Second, both Wu (2001) and Yeates et al. (2005) assume the intrinsic amplitudes are the same for every component in a multiplet, and this may simply not be the case for GD358. Third, the theoretical value of R_c relies on correct identification of l and m, although in simpler cases, as in Yeates et al. (2005), it can be used as a mode identification technique. While we are fairly certain that GD358's pulsations are $l = 1$, the assumption of a classical triplet split by rotation is not valid for GD358's high-k modes. Finally, we raise a possibility suggested by the $k = 9$ and 8 components and their harmonics: to first order, the $m = 0$ components sample the radial direction, and the $m = \pm 1$ components sample azimuthal direction. Components of the same mode have the same inclination, so cancellation effects should be the same. The $k = 9$ and 8 multiplet amplitudes and presence/absence of harmonics argue that something is interrupting the azimuthal symmetry of GD358. It is possible that the pulsations do not all share the same inclination, in which case they would not combine as expected by Wu (2001). The oblique pulsator model is well known, especially in the case of roAp stars. For example, Bigot & Dziembowski (2002) show that the main mode of HR 3831, a pulsating roAp star, departs from alignment with the magnetic axis. GD358's combinations are trying to tell us something important about the pulsation geometry, but we do not yet understand how to interpret it.

While the general frequencies of the high-k multiplets agree with the identifications of W94 and K03, the 2006 multiplets themselves are complex, and cannot be explained by simply invoking rotation using standard theory and simple geometric viewing arguments. Except for the $k = 9$ and $k = 8$ modes, we do not find triplet structure as reported in W94 and cannot provide m identifications. The facts that the multiplets do change and the 2006 combinations do not conform to theoretical predictions leads us to expand our investigation to include archival observations of GD358. In the following, we will examine the structure of GD358's multiplets in detail over timescales of years.

5. MULTIPLET STRUCTURE CHANGE AND COMPLEXITY

Each multiplet in GD358's FT should represent a quantized g-mode pulsation, described theoretically by a spherical harmonic of index l and overtone k, which has been split into multiple components $(2l + 1)$ by the star's rotation. As component frequencies are determined by the star's structure and rotation rate, we would expect the multiplet structure to remain stable over long time periods. The classic example is the DO pulsator PG1159-035, which exhibits prototypical triplets, cor-

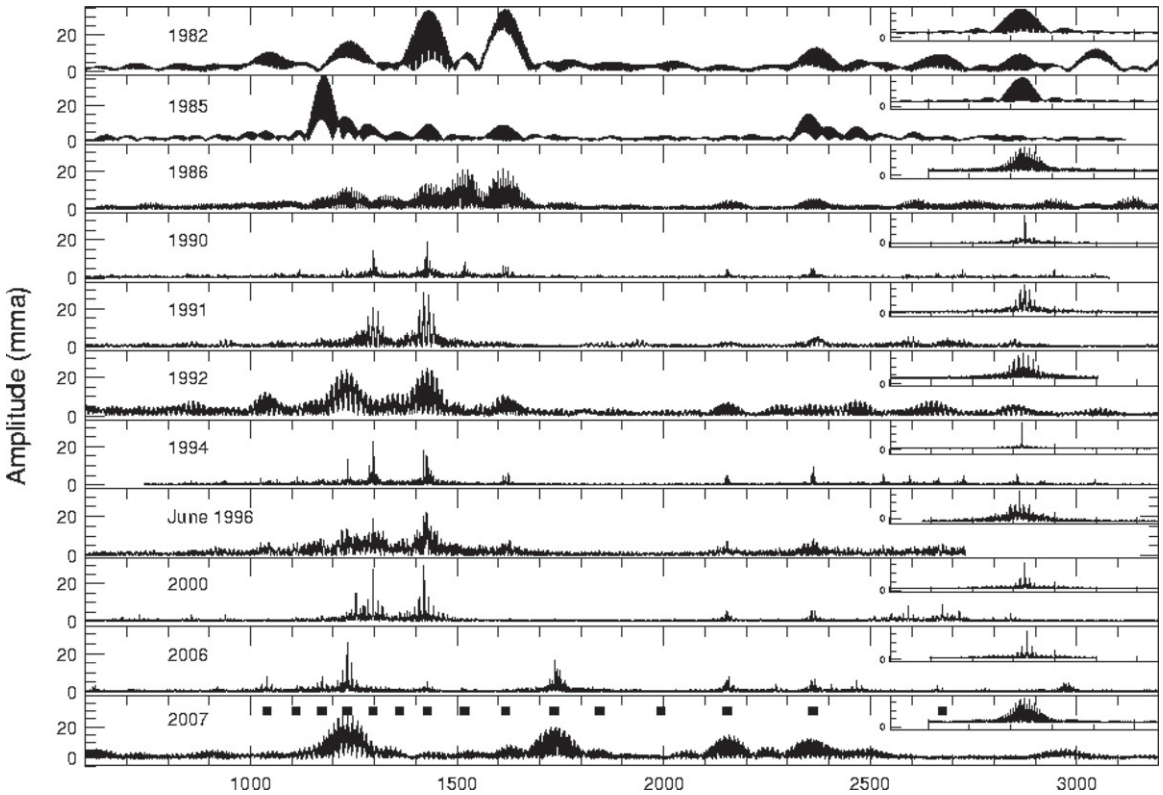

Figure 10. FTs of GD358 from 1982 to 2007, with each spectral window given in the upper right corner of each panel. Each panel spans 2800 μHz. The filled squares in the bottom panel mark the predicted locations of GD358's pulsation modes ($l = 1$). GD358 changes its distribution of amplitudes of the excited modes, but the modes are consistently in the same general locations. High-k modes exhibit the largest variation in amplitude. Note the appearance of $k = 12$ in 2006.

responding to $l = 1$, and quintuplets, corresponding to $l = 2$ (see Figures 5 and 6 in Winget et al. 1991).

W94 based the first asteroseismological analysis of GD358 on the identified modes and multiplet structure in the 1990 data set. The frequency splittings within the 1990 multiplets range from 3.5 to 6.5 μHz, vary as a function of the radial number k, and are not always symmetric with respect to the central frequency. W94 interpreted the trend with k as differential rotation within the star, and used the splitting asymmetry to determine an average magnetic field strength of 1300 ± 300 G. If we assume that GD358's structure is constant in time, then we would expect to find similar multiplet structure in other observing seasons, including XCOV25.

Figure 10 displays FTs for seasons spanning GD358's 1982 discovery to 2007. The 1990 (W94), 1991, 1994, 2000 (K03), and 2006 FTs are from WET runs, while the other FTs are single site, obtained from McDonald Observatory or Mt. Cuba Observatory (2007 season). The large amplitude peaks are consistently found between 1000 and 1800 μHz, and individual modes are close to predicted values for $l = 1$ (the filled boxes in the last panel of Figure 10 marks the periods of the best fit model from Metcalfe et al. 2003). Using the 2006 data set, we calculated an average period spacing of 38.77 s using the measured periods of the lowest and highest k modes. This is consistent with results from previous observations (Table 4), demonstrating that GD358's general internal structure is largely unchanged.

We extracted the $k = 8$, 9, 15, and 17 multiplets from the 1990, 1991, 1992, 1994, 1996, 2000, and 2006 seasons, using the techniques discussed in Section 3. The multiplets are plotted in Figures 11, 12, 13, and 14. The low-order $k = 8$ and 9 modes consistently display the triplet structure expected for $l = 1$ g-modes in the limit of slow rotation (Figures 11 and 12). While the component amplitudes vary from season to season, the frequencies and splitting within the triplets remain roughly the same. The story changes for the $k = 15$ and 17 multiplets (Figures 13 and 14). The multiplet structure of these modes exhibit dramatic changes from year to year. If rotational splitting is the dominant mechanism producing the high-k multiplets, we expect them to share the same splitting with other detected modes within the same data set. We have shown that this is not the case (Figure 7).

We now turn our attention to the frequency stability of the $k = 8$, 9, 15, and 17 mode components. Both W94 and K03 report small but significant frequency changes within the identified multiplets, and Figures 11–14 support this finding. For $k = 8$, 9, and 17 we select the component identified as $m = 0$ in W94. For $k = 15$, however, we choose $m = -1$ since a peak was present near this frequency more often than the $m = 0$ frequency. Figure 15 plots the frequencies of the identified peaks versus time. In all cases, the frequencies shift by several times the statistical errors, where the average error for all the data sets is $\sigma = 0.06$ μHz. The high-k frequencies wander by over 30 σ, much more than the detected 8 σ changes for $k = 8$ and 9. While these variations are small, they point to very definite changes in the g-mode propagation cavity in this star.

Summarizing our results, we find a clear difference between high- and low-k modes. The high-k multiplets are highly variable in amplitude and frequency, and exhibit large changes in multiplet structure. The multiplets within these modes appear to be almost randomly present with the $m = 0$ component not necessarily preferred. The low-k modes typically show a stable triplet structure, but the amplitudes of the components are moderately variable. All the multiplets exhibit significant

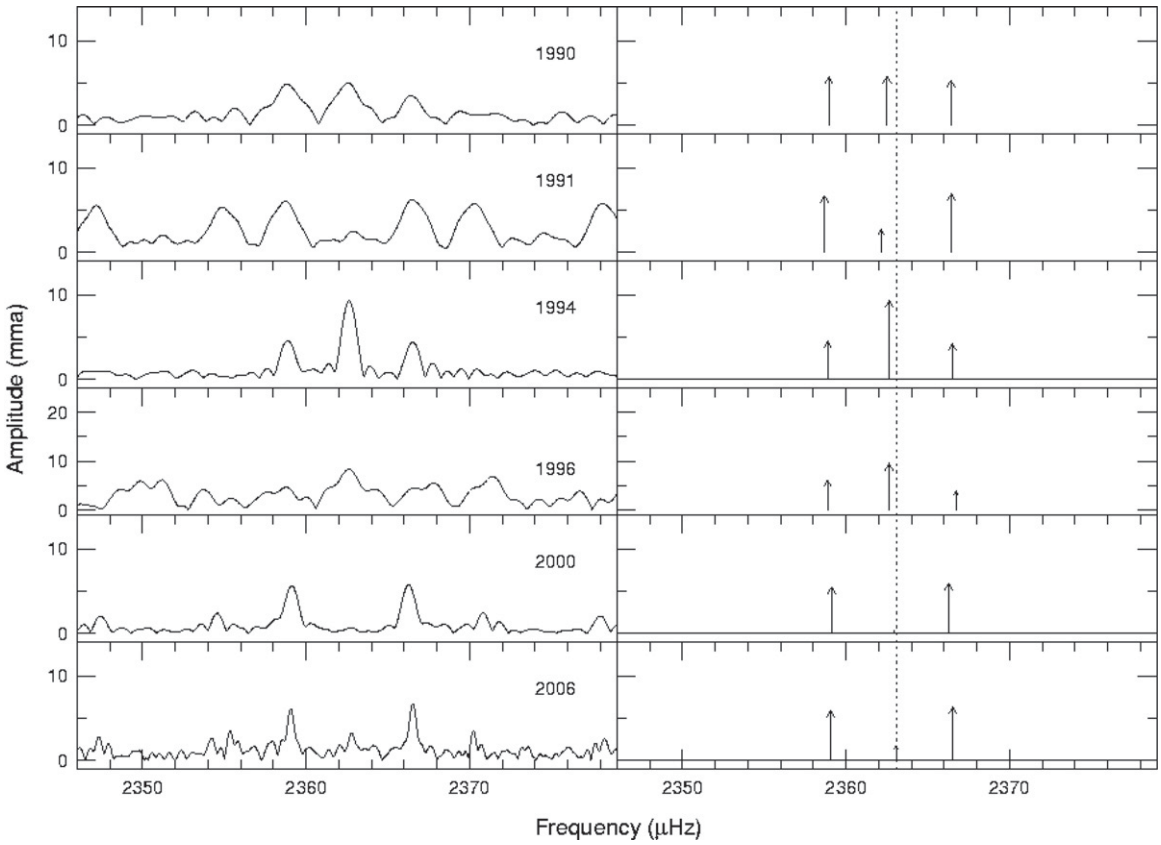

Figure 11. Multiplet structure associated with the $k = 8$ mode in GD358 from different observing seasons. The left panels plot the original FTs, and the right panels give the prewhitening results. The largest 1σ frequency error bar is 0.06 μHz (1996). Each panel spans 18 μHz. The horizontal line through each right panel gives the noise level for that season, and the dotted line marks the 2006 detected frequency.

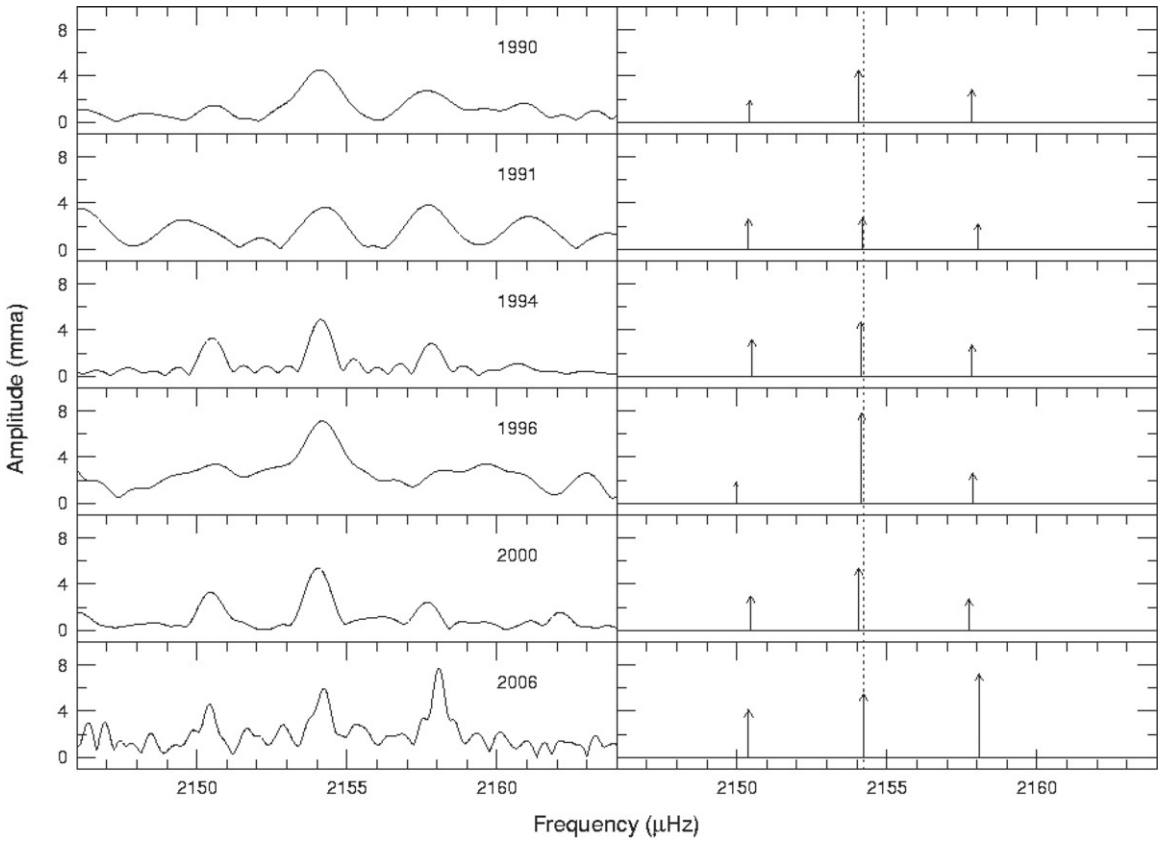

Figure 12. Multiplet structure associated with the $k = 9$ mode in GD358 from different observing seasons. The left panels plot the original FTs, and the right panels give the prewhitening results. The largest 1σ frequency error bar is 0.06 μHz (1996). Each panel spans 18 μHz. The horizontal line through each right panel gives the noise level for that season, and the dotted line marks the 2006 detected frequency.

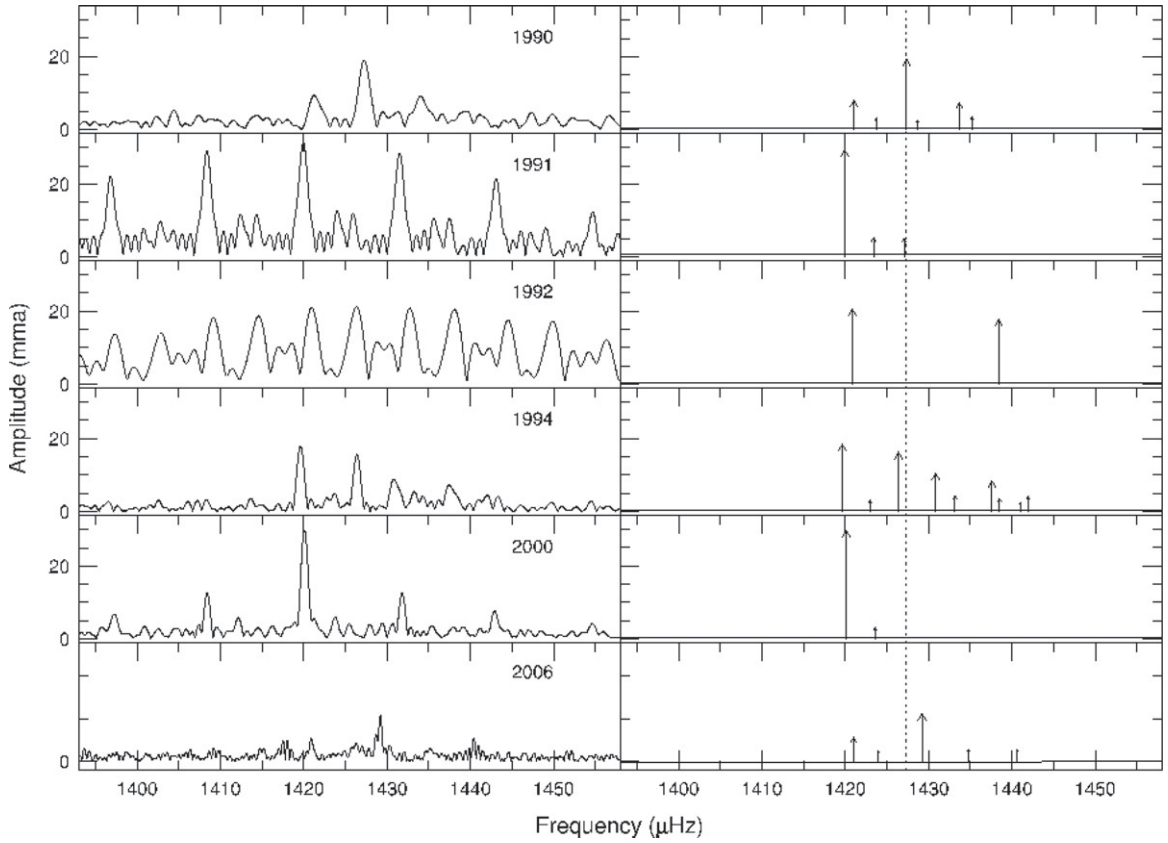

Figure 13. Multiplet structure associated with the $k = 15$ mode in GD358 from different observing seasons. The left panels plot the original FTs, and the right panels give the prewhitening results. The largest 1σ frequency error bar is 0.06 μHz (1992). Each panel spans 65 μHz. The horizontal line through each right panel gives the noise level for that season, and the dotted line marks the 1990 detected frequency.

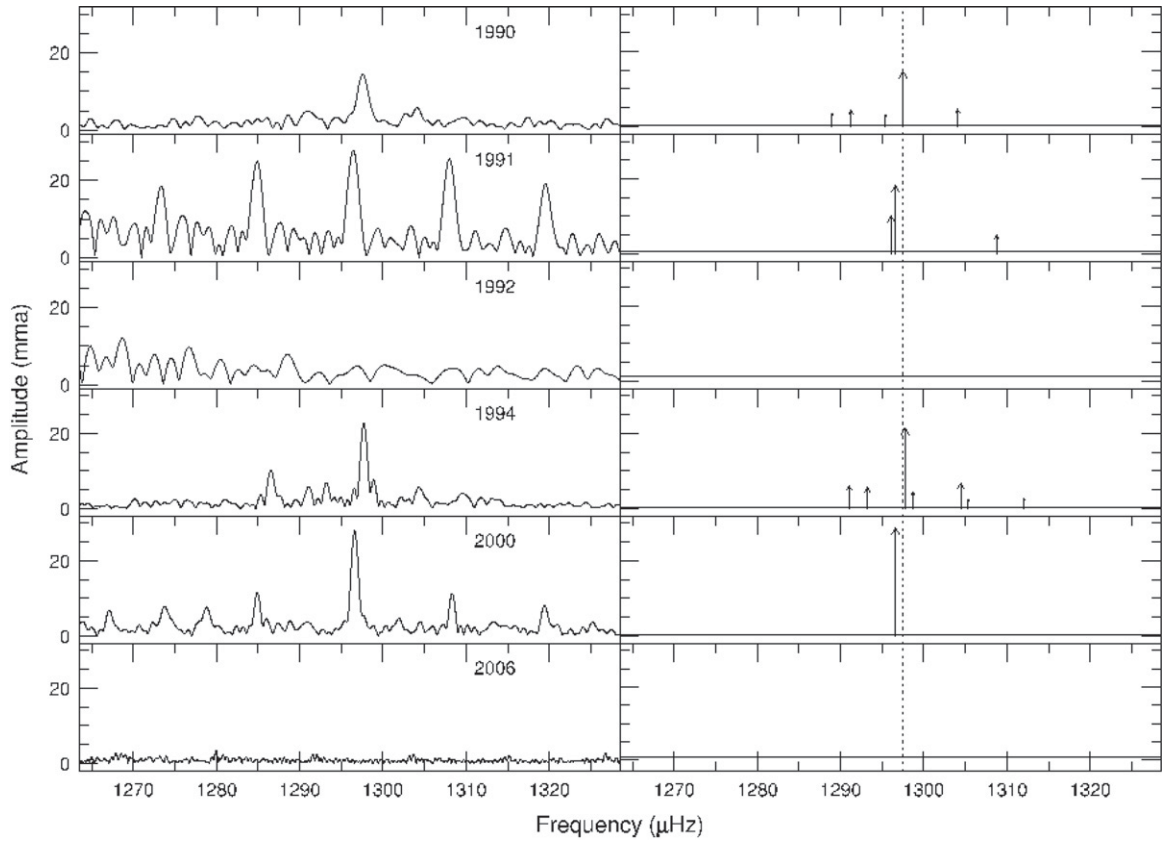

Figure 14. Multiplet structure associated with the $k = 17$ mode in GD358 spanning 1990 to 2006. The left panels present the yearly FTs, and the right panels represent the prewhitening results. The largest 1σ frequency error bar is 0.06 μHz (1992). Each panel spans 65 μHz. The horizontal line through each right panel gives the noise level for that season, and the dotted line marks the 1990 detected frequency. The 2006 peak is difficult to detect due to the y scale.

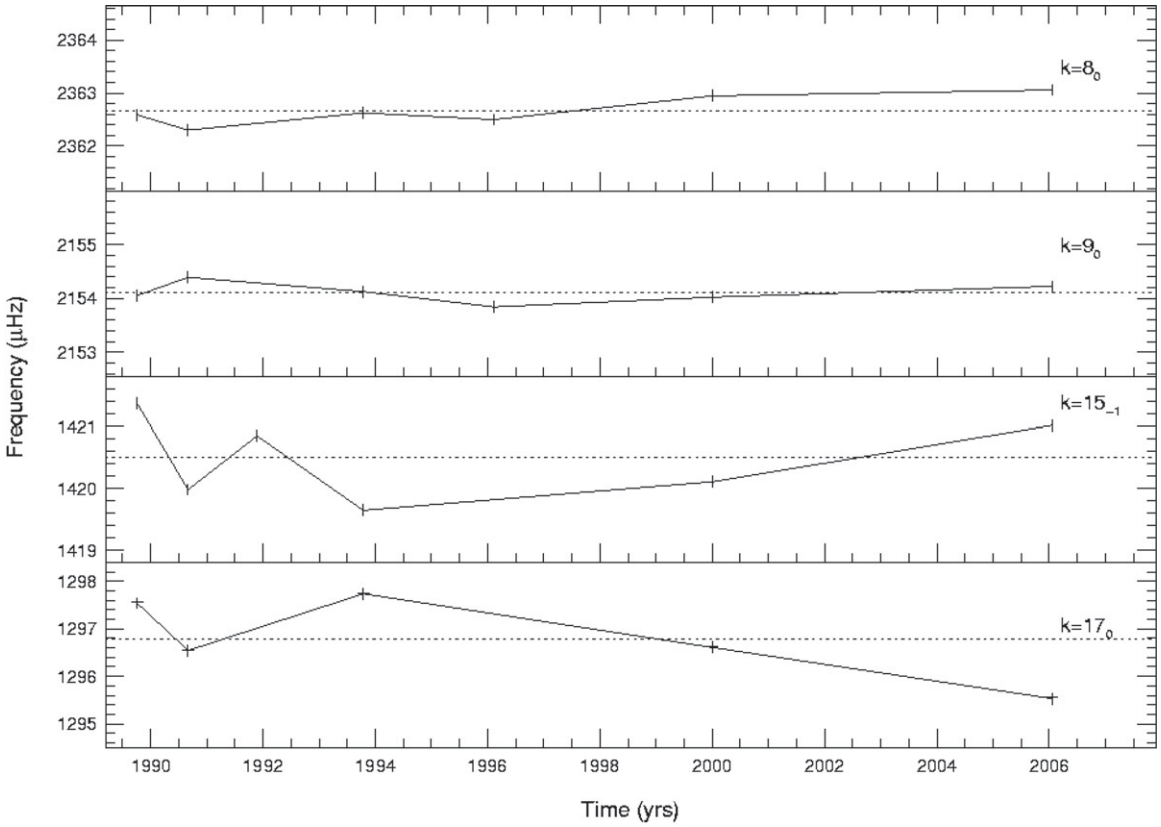

Figure 15. Frequency of the largest component for the $k = 17$, 15, 9, and 8 modes. For $k = 17$, 9, and 8, the $m = 0$ component was selected. For $k = 15$, the $m = -1$ mode was detected more often at larger amplitude. While all modes exhibit some variation in frequency, the high-k modes wander by over 30 σ. The dotted lines mark the reported 1990 frequencies (W94).

wanderings in frequency, with the frequency changes observed in the high-k modes being much larger than those seen in the low-k modes.

6. IMPLICATIONS FOR GD358

GD358's 2006 FT contains 27 independent frequencies distributed in 10 excited modes. The locations of the modes agree with previous observations and predicted values for $l = 1$ g-mode pulsations. The average period spacing $\Delta P_{\rm av}$, calculated using the lowest-k and highest-k modes, is identical from 1990 to 2006 (Table 4). As $\Delta P_{\rm av}$ is fixed by stellar mass and temperature, GD358's basic physical properties have remained unchanged over a timescale of years, as expected. The changes we observe in GD358's pulsation spectra and multiplet structure are not due to gross changes in structure or temperature.

We have shown that the standard model of a pulsating white dwarf in the limit of slow rotation cannot adequately explain the observations of GD358's multiplet structure and behavior. The fine structure of the high-k modes is inconsistent with the expectations of slow rotational splitting, the amplitudes of multiplet components for all ks cannot be explained using simple viewing arguments, and the observed frequency variations imply changes in the g-mode propagation medium that are much more rapid than expected from evolutionary changes.

The qualitative behavior of the low-k and high-k modes can be explained in the context of a general model. g-modes are standing waves of buoyancy in a spherical cavity, and they are thought of as superpositions of traveling waves bouncing back and forth between an inner and an outer turning point. These turning points depend on the mode's period: short period (low-k) modes have deeper outer turning points than long period (high-k) modes, so high-k modes sample the outer regions of the star more than low-k modes. If we introduce an additional, non-spherical structure in the star's outer layers, due to magnetic fields or convection, for example, the effect should be much larger on the high-k modes. In effect, GD358 is telling us where this perturbation to its structure must be, but it is still incumbent upon us to diagnose the actual cause.

We do find a clear difference in the photometric behavior of GD358's high- and low-k modes, leading us to consider a connection between the outer layers and its pulsation changes. The following discussion requires that we draw into the mix a remarkable sequence of events that occurred over ≈30 days in 1996. We follow Castanheira et al. (2005) in calling the event the *sforzando*. In classical music, *sforzando* is an abrupt change in the character of music, usually accompanied by an increase in volume. We begin with a description of the *sforzando*. We will examine the implications and connections between our asteroseismic results, the *sforzando* and two possibilities that may affect GD358's photometric behavior: a surface magnetic field and the convection zone.

6.1. GD358 in 1996

In 1996 June, GD358's light curve (third panel, Figure 16) was typically nonlinear, with a dominant frequency of 1297 μHz corresponding to $k = 17$, and a peak to peak intensity variation of ≈15%. The $k = 9$ and 8 modes were present with amplitudes of 8 and 9 mma, respectively. On August 10 (suh-0055, second panel Figure 16), the light curve was again typical, with a 20% peak to peak intensity varia-

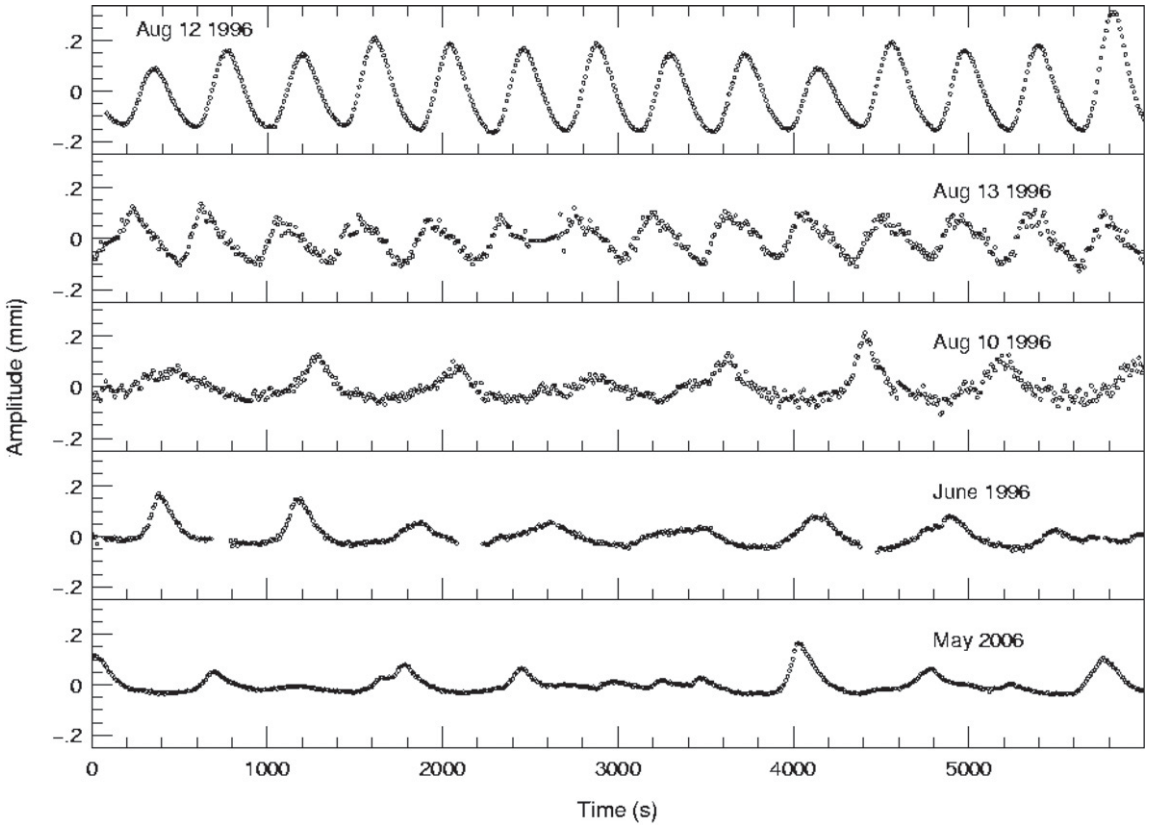

Figure 16. Light curve of GD358 on August 12 (an-0034, top panel) and August 13 (suh-056, second panel), during the 1996 *sforzando*. On 1996 August 10 (suh-0055, third panel), the light curve was typically nonlinear, as it was in 1996 June (fourth panel), and 2006 May (bottom panel).

tion, and main frequencies consistent with previously observed high-k modes. The $k = 9$ and 8 modes had upper amplitude limits of 8 mma. On August 12, 27 hr later, GD358 exhibited completely altered pulsation characteristics (an-0034, top panel Figure 16). The lightcurve was remarkably sinusoidal, with an increased peak to peak intensity variation of ≈50%. The $k = 8$ mode dominated the lightcurve with a amplitude of 180 mma, the highest ever observed for GD358. The $k = 9$ mode was also present, with an amplitude of ≈20 mma. The high-k modes, dominant 27 hr prior, had upper detection limits of 7 mma. Over the next 24 hr, the $k = 8$ mode began to decrease in amplitude (Figure 17). Between Aug 13 and 14, $k = 9$ grew in amplitude as $k = 8$ decreased, reaching a maximum of ≈57 mma, and then began to decrease as the $k = 8$ mode continued to dissipate. By August 16, a mere 96 hr after the *sforzando* began, GD358 was an atypically low amplitude pulsator, with power detected in the $k = 9$ and 8 modes at amplitudes of ≈7 mma, and upper limits of less than 5 mma for the high-k modes. By September 10, less than a month after the start of the *sforzando*, the high-k modes had reappeared, with the dominant mode at ≈1085 μHz at an amplitude of 29 mma.

The only observations we have during the maximum *sforzando* are the PMT photometry (Table 5) observations. Differential photometry does not measure standard stars. However, we can calculate the ratio between the average counts from GD358 and its comparison star, assuming the same comparison star was used each night, and accounting for factors such as extinction and sky variation. In the following, we calculate ratios based on sky subtracted counts obtained within ±1.5 hr of the zenith. We focus on the McDonald 2.1 m runs an-0034, an-0036, an-0038, and an-0040. The ratio between GD358 and the comparison star decreased from 1.23 during the height of the *sforzando* (an-0034, Aug 12) to 1.01 on Aug 15 (an-0040). We also examined observations from Mt. Suhora (Table 5). Suh-0055 was obtained ≈24 hr before the *sforzando*, and the ratio between GD358 and the comparison star was 0.11. Suh-0056 took place 18 hr after the *sforzando* maximum but before the pulsations had completely decayed. For suh-0056, the ratio between GD358 and the comparison star increased to 0.16. For the remaining Mt. Suhora observations, obtained during the

Table 5
GD358 1996 August

Run	CH1 GD358	CH2 Comp	CH1/CH2	Time (BJED)	Date	Length (hr)
McDonald						
an-0034	343727	279268	1.23	2450307.6170160	Aug 12	4.7
an-0036	308308	290898	1.06	2450308.6309639	Aug 13	3.2
an-0038	269937	251923	1.07	2450309.6362315	Aug 14	3.5
an-0040	250813	248479	1.01	2450310.6294625	Aug 15	3.5
Mt. Suhora						
suh-0055	12786	114746	0.11	2450306.4793479	Aug 10	4.8
suh-0056	29408	181597	0.16	2450308.3533174	Aug 12	3.0
suh-0057	20271	158035	0.12	2450309.3015281	Aug 13	5.9
suh-0058	15974	130814	0.12	2450310.4729899	Aug 14	1.0
suh-0059	15434	127672	0.12	2450314.3776294	Aug 18	3.0

Notes. Observations made with McDonald 2.1 m. The same comparison star was used in each instance.

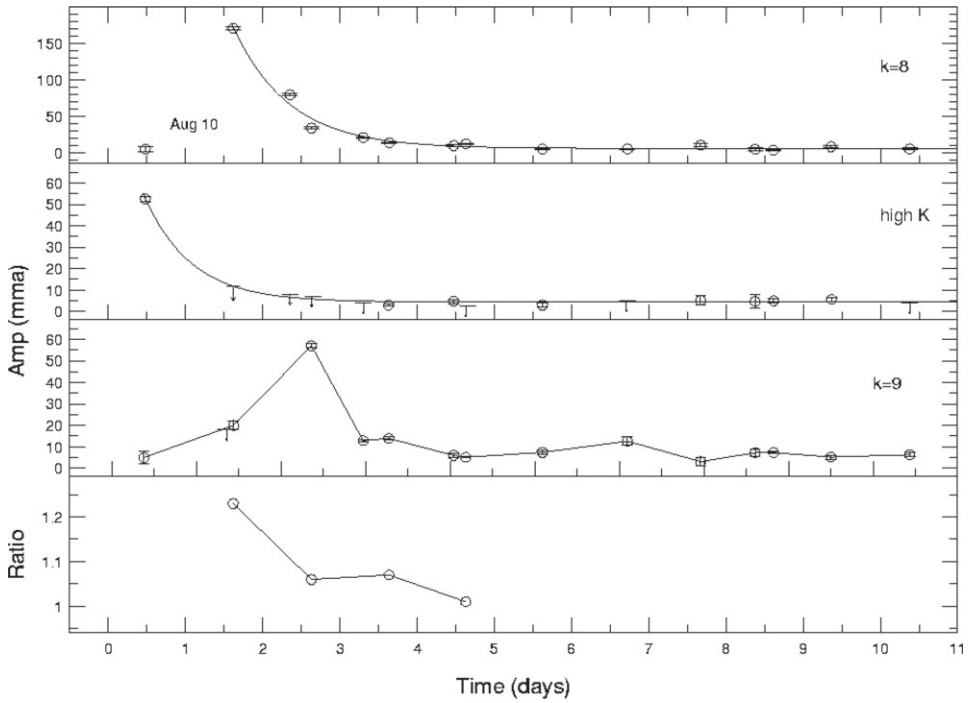

Figure 17. The first three panels give the measured amplitudes for $k = 8$ (top panel), the high-k modes, and $k = 9$ during the 1996 *sforzando*. The solid lines give fits using a simple exponential decay model. For $k = 8$ and the high-k modes, the damping time was 1.4 days. Note that the "high-k" points do not correspond to any particular k value, but give the highest amplitude (or upper limit) between 1000 and 1500 μHz at that time. The $k = 9$ mode grew in amplitude as $k = 8$ decayed. The last panel gives the ratio between GD358 and its comparison star from the McDonald 2.1 m photometry. Note the change in y-axis units.

following days, the ratio between GD358 and the comparison star decreased to 0.12. Observation logbooks at Mt. Suhora demonstrate that the same comparison star, but not the same one used at McDonald, was used each night (Zola 2008). While we cannot pin down any exact numbers due to the nature of differential photometry, the observations of GD358 are consistent with a flux increase in the observed bandpass during the maximum *sforzando*.

6.2. Convection and GD358

The onset of convection goes hand in hand with the initiation of pulsation in both hydrogen and helium white dwarfs (Brickhill 1991; Wu 2000; Montgomery 2005). A primary goal of XCOV25 is to use GD358's nonlinear lightcurve to characterize its convection zone, improving the empirical underpinnings of convective heat transport theory. Our asteroseismological investigation points to evidence that something in the star's outer surface layers is influencing its pulsation modes. The convection zone lies in the outermost regions of GD358, so we are led to consider the relationship between the star's convection zone and its photometric behavior, both typical and during the *sforzando*.

In general, theoretical studies of convective energy transport are based on the mixing length theory (MLT) (Bohm-Vitense 1958). Originally intended to depict turbulent flows in engineering situations, MLT enjoys success in describing stellar convection (Li & Yang 2007). It remains, however, an incomplete model with unresolved problems. The actual mixing length is not provided by the theory itself, but is defined as (αH_p), where H_p is the pressure scale height, and α is an adjustable variable. This adjustable parameter undermines the ability of theoretical models to make useful predictions. Advances in convection theory include stellar turbulent convection (Canuto & Mazzitelli 1991; Canuto et al. 1996), which establishes a full range of turbulent eddy sizes. Work is currently underway employing helioseismology to compare MLT and turbulent convection models (Li & Yang 2007). Our work with convective light curve fitting will also provide important tests for convection theory.

Physical conditions in white dwarf atmospheres differ by orders of magnitude from those in envelopes of main sequence stars like the Sun. For GD358, models indicate that the convection zone is narrow, with a turnover time of ≈1 second and a thermal relaxation timescale of ≈300 s (Montgomery 2008). The pressure scale height is small, limiting the vertical height of the convective elements. Montgomery & Kupka (2004), employing an extension of stellar turbulent convection, calculate that 40–60% of GD358's flux is carried by convection, depending on the adopted effective temperature.

Convective lightcurve fitting is based on the assumption that the convection zone, by varying its depth in response to the pulsations, is responsible for the nonlinearities typically observed in GD358's lightcurves (Montgomery 2005). During the *sforzando*, within an interval of 27 hr, GD358's lightcurve became sinusoidal, arguing that the convection zone was inhibited, at least as sampled by the $k = 8$ mode. For example, if this large amplitude mode was the $m = 0$ member of the triplet, then its brightness variations would be predominantly at the poles and not the equator. Thus, all that is required to produce a sinusoidal lightcurve is a mechanism to inhibit convection near the poles.

How could convection in any star be decreased on such short timescales? The obvious method, but not necessarily the most physical, is to raise GD358's effective temperature, forcing it to the blue edge of the instability strip, and decreasing convection. Such a temperature increase has the observable consequence of increasing the stellar flux. A flux increase of 20% in our effective photometric bandpass would produce an equivalent change in the bolometric flux of ≈40%, corresponding to a temperature change of ≈2200 K. The *sforzando* photometry is consistent

with such an increase in flux, and Weidner & Koester (2003) find that $T_{eff} \approx 27,000$ K is required to simulate GD358's light curve during the maximum *sforzando*. Castanheira et al. (2005) use FOS spectroscopy of GD358 obtained on 1996 August 16 to determine $T_{eff} = 23900 \pm 1100$ K, a number not inconsistent with previous observations (Beauchamp et al. 1999). However, the FOS spectra were acquired after the pulsations had greatly decreased in amplitude (Figures 16 and 17). It is possible that GD358 had cooled by this point. Recent theoretical evidence also indicates that simply "turning off" convection would have minimal observable effects on GD358's spectrum (Koester 2008).

The connection between convection and pulsation during the *sforzando* may also depend on the origin of the event. Was the *sforzando* a short-term change, such as a collision, or a more global event intrinsic to GD358? The growth and dissipation of modes during the *sforzando* could be connected to pulsation growth timescales, or may be governed by a completely different mechanism. Pulsation theory predicts that growth rates for high-k modes are much larger than for low-k modes. This simply means that high-k modes are easier to excite and have growth times (and decay times) of days rather than years (Goldreich & Wu 1999). This makes sense for GD358, where we typically find the high-k modes to be much more unstable in amplitude over time than $k = 9$ and 8 (Figure 10). Figure 17 plots the amplitudes for the $k = 8$, $k = 9$, and "high-k" modes during the *sforzando*. We note that the "high-k" points do not correspond to any particular k value, but give the highest amplitude (or upper limit) between 1000 and 1500 μHz. We fit the observed amplitudes for $k = 8$ and the high ks with a simple exponential decay model $A(t) = A_0 e^{-t/\tau_d} + c$, where A(t) is the amplitude at time t and τ_d is the damping constant. Our fits give a damping timescale of $\tau_d = 1.5 \pm 0.2$ days for both the $k = 8$ mode and the high ks. The $k = 9$ mode, which actually grew in amplitude later, as $k = 8$ decayed, has an upper limit of $\tau_{9^d} < 1.1$ days. We only have a few points measuring the growth timescale (τ_g) of $k = 8$ and 9, so we place an upper limits for $k = 8$ of $\tau_{8^g} \leqslant 1.2$ days. For $k = 9$, we find an upper limit of $\tau_{9^g} \leqslant 2.2$ days. These timescales are all roughly equivalent, are all much longer than the dynamical timescale, and not distributed as predicted by theoretical pulsation growth rates. The results for $k = 9$ and 8 are much shorter than the expected pulsation damping timescale of about two months (Montgomery 2008a), arguing that the source of the *sforzando* was capable of interacting with the pulsations to produce changes on faster timescales than theoretical growth rates.

Our purpose in entering this discussion of the *sforzando* was to provide insight into connections between convection and pulsation in GD358. We find evidence that convection diminished during the *sforzando*. The decreased convection was accompanied by the rapid disappearance of GD358's high-k modes and the transfer of energy to the $k = 8$ and 9 modes. The photometry is consistent with a temperature increase, which would inhibit convection. The sudden transfer of energy from the high-k modes to $k = 9$ and 8 argues that a mechanical (radial or azimuthal) or thermal structural change altered GD358's outer layers, modifying mode selection. We find that the growth/damping timescales during the *sforzando* for the $k = 9$ and 8 modes do not agree with the expectations of pulsation theory, and may be governed by a completely different mechanism.

Magnetic fields have long been known to be capable of inhibiting convection. For example, localized fields associated with sunspots in the Sun are observed to inhibit convection in the surrounding photosphere (Biermann 1941; Houdek et al. 2001). Winget (2008) estimates that the magnetic decay time at the base of the convection zone is ≈3 days. In the next section, we investigate the possible implications of magnetic fields on GD358 and its pulsations.

6.3. Magnetic Fields

Our current understanding of magnetic fields in stars like the Sun invokes the dynamo mechanism, which is believed to function in the narrow region where rotation changes from the latitudinal rotation of the outer convective layers to spherical rotation in the radiative zone (Morin et al. 2008). The solar magnetic field consists of small, rapidly evolving magnetic elements displaying large scale organization, with a cycle time of 22 years during which the polarity of the field switches. Localized fields, with strengths hundreds of times stronger than the global field, exert non-negligible forces on charged particles, influencing convective motion. Solar pulsations are observed to vary in frequency with the solar cycle in these regions (Schunker & Cally 2006). Although the exact mechanism is uncertain, the frequency shifts are interpreted as representing change in the Sun's internal structure or driving (Woodward & Noyes 1985; Kuhn 1998; Houdek et al. 2001).

A pulsating white dwarf represents an extreme environment. The atmosphere and the convection zone are thin, the surface gravity orders of magnitude higher, and differential rotation may or may not play a role (Kawaler et al. 1999). The magnetic field in a typical white dwarf is confined to the nondegenerate outer layers. The field may dominate near the surface, but deeper in the atmosphere, gas pressure will prevail. Drawing an analogy with the Sun, a surface magnetic field in GD358 probably has an associated cycle time similar to the solar cycle. Hansen et al. (1977) and Jones et al. (1989) discuss this topic from a theoretical perspective, predicting cycle times ranging from two to six years.

What are the observable consequences of a magnetic field on white dwarf pulsations? Jones et al. (1989) find that, in the presence of a weak field, defined as strong enough to perturb but not dominate mass motions, multiplet frequencies are increased with respect to the central mode in a manner proportional to m^2. The $m = 0$ mode is also shifted, unlike the case for rotation. Each g-mode pulsation samples the magnetic field at a different depth. A logical expectation is that, for low-k modes with reflection points below the convection zone, we can treat the magnetic field as a perturbation, while for high-k modes such a treatment is not valid.

Our best candidates to investigate the influence of a magnetic field on multiplet structure are GD358's $k = 9$ and 8 modes. These two modes are consistent with rotationally split triplets and we can examine their multiplet structure in detail over 16 years of observations (Figures 18 and 19). From 1990 to 2006, $k = 9$ had an average multiplet width of 7.7 ± 0.1 μHz, while $k = 8$ is similar, at 7.5 ± 0.1 μHz. Figures 18 and 19 show that the complete multiplet width and the splittings with respect to the central mode wander up to 0.5 μHz from the average values. Both Figures 18 and 19 reveal a dramatic change during the *sforzando*. In June 1996, both multiplets increased in total width by ≈1μHz. Prior to August 1996, the retrograde splitting (0, −1) for $k = 8$ was consistently smaller by ≈0.2 μHz than the prograde splitting (0, +1). After 1996 August, the retrograde splitting became consistently larger by ≈0.5 μHz than the prograde splitting and has remained so through 2007, at the

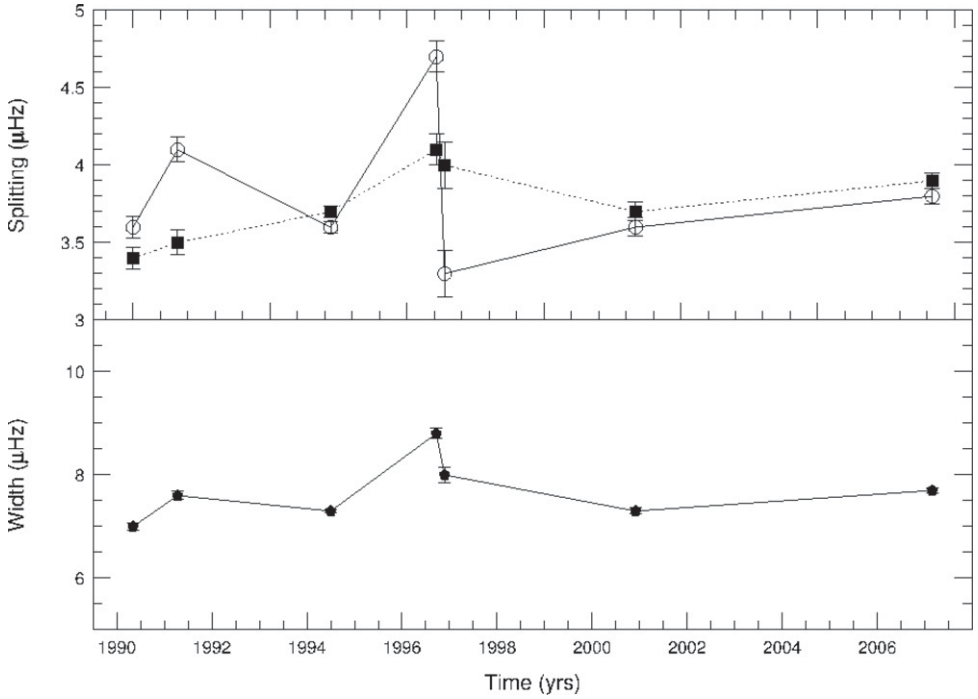

Figure 18. Multiplet structure within the $k = 9$ multiplet. The x-axis is time in years, and the y-axis is in μHz. The bottom panel plots the width of the entire multiplet over time. The top panel examines the $m = 0, +1$ (dotted line) and $m = 0, -1$ (solid line).

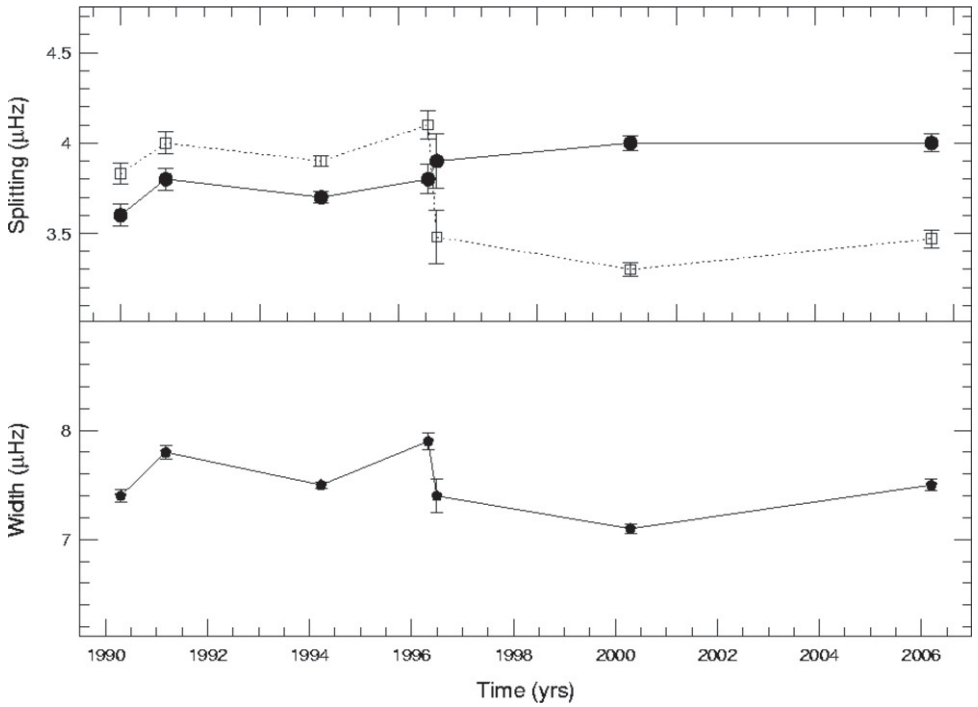

Figure 19. Multiplet structure with $k = 8$ multiplet. The x-axis is time in years, and the y-axis is in μHz. The bottom panel plots the width of the entire multiplet over time. The top panel examines the $m = 0, +1$ (dotted line) and $m = 0, -1$ (solid line).

resolution of our observations. The case is not so straightforward for $k = 9$, but this mode clearly shows a large change in 1996, especially for the $(0, -1)$ splitting (Figure 18). In the previous section, we questioned whether the *sforzando* was a short-term event or a global, enduring change. This analysis of $k = 9$ and 8 points toward a long-term change in GD358's resonance cavity. The changes we observe in the multiplet structure could be explained by a change in magnetic fields.

A magnetic field also introduces an additional symmetry axis. Our analysis of GD358's harmonics and combination frequencies hints that something is disrupting its azimuthal symmetry. It is conceivable that high-k modes would align more or less with the magnetic field, while the low-k modes align with the rotation axis. Wu (2001) & Yeates et al. (2005) do not explore the possibility of multiple axes or the effects of a magnetic field on nonlinear mixing by the convection zone. Future work could

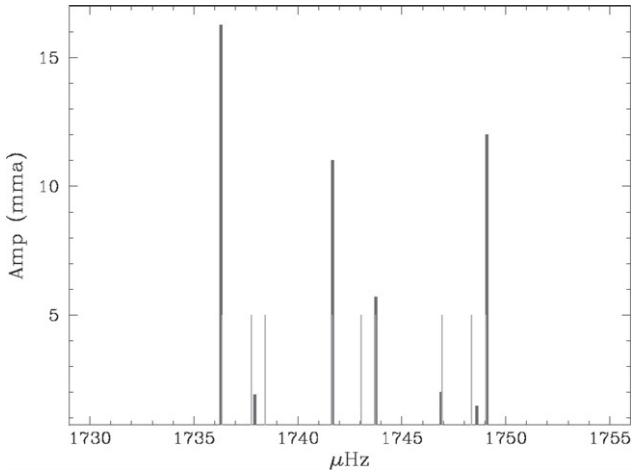

Figure 20. Fit to k=12 components assuming the dominant splitting mechanism is a magnetic field using the model of Unno et al. (1979) rather than rotation. The black lines are the observed multiplet components, including several below our detection limits that are not listed in Table 2. The light gray lines are the theoretical predictions. Theoretical predictions overlap the four largest amplitude peaks, although they are difficult to distinguish in the figure.

explain why GD358's modes do not combine as expected by simple theory.

The presence of the $k = 12$ mode offers a final hint of a possible surface magnetic field. The second largest mode in the 2006 FT, $k = 12$ appears in a region that is normally devoid of significant power. If, for this mode, the magnetic field can no longer be treated as a perturbation, we would expect a multiplet with $(2l + 1)^2$ components, as opposed to the three expected from rotation (Unno et al. 1979). For $l = 1$, this corresponds to nine magnetic components. We do find six peaks above our 4σ limit, with three additional peaks slightly just our criteria. Using the magnetic model of Unno et al. (1979), we are able to match the frequencies of the $k = 12$ mode components, but not the amplitudes (Figure 20).

7. SUMMARY AND CONCLUSIONS

GD358 is the best studied of the DB pulsators, yet our work shows that this object is by no means completely understood. The 2006 XCOV25 observations were obtained with the goal of using GD358's nonlinear lightcurve to characterize its convection zone, but our initial asteroseimological analysis of the data set reveals a great deal of interesting information about GD358's pulsational behavior. Our investigation began with an analysis of GD358's 2006 XCOV25 FT. We explored the identified modes, combination frequencies, and multiplet structure. Difficulties in identifying the m components of the 2006 mode multiplets, both directly and indirectly using the combination frequencies, lead us to examine the multiplet structure in detail over time. Our investigation expanded to include observations of GD358 over the 24 years since its discovery, focusing on the multiplet structure, frequency stability, and photometric behavior of GD358. We summarize our results concerning GD358's pulsation properties:

1. The 2006 FT contains 27 independent frequencies distributed in 10 modes ($k = 21$, 19, 18, 17, 15, 14, 12, 11, 9, and 8). The dominant frequency is at 1234 μHz ($k = 18$) with an amplitude of 24 mma.
2. We find significant power at $k = 12$, a region of the FT previously devoid of significant power.
3. The frequency location of each mode in the 2006 FT is consistent with previous observations and theoretical predictions, assuming $l = 1$.
4. The $k = 9$ and 8 modes exhibit triplets in agreement with theoretical predictions for $l = 1$ in the limit of slow rotation. The amplitudes and frequencies of the components exhibit some variability over time, but much less than the high-k modes.
5. Our analysis of GD358's high-k multiplets over time reveal that they are variable in multiplet structure, amplitude, and frequency. The variability and complexity of the high-k multiplets cannot be interpreted simply as $l = 1$ modes in the limit of slow rotation.
6. We cannot provide m identifications for most of the multiplet components in the 2006 FT, with the exception of $k = 9$ and 8.
7. The 2006 FT contains a rich assortment of combination frequencies. They are potential tools for identifying m values and orientation for each mode. However, their amplitudes do not agree with theoretical predictions from Wu (2001).
8. The $k = 9$ and 8 multiplet amplitudes and presence/absence of harmonics cannot be explained by simple geometric viewing arguments, and argue that something is interrupting GD358's azimuthal symmetry.
9. The linear, sinusoidal shape of the lightcurve indicates that GD358's convection zone was diminished during the 1996 *sforzando*.
10. Photometry taken during the maximum *sforzando* is consistent with a flux increase in the effective bandpass.
11. We find damping/growth timescales during the *sforzando* that are not consistent with the expectations of pulsation theory.
12. Changes in the splittings of the $k = 9$ and 8 multiplets indicate that some mechanism, perhaps a magnetic field, induced a long-term change in the multiplet structure of these modes during the *sforzando*.

Our investigation raises a number of interesting implications for our understanding of the physics of GD358, many beyond the scope of this paper, and some blatantly skirting the realm of speculation. While we cannot pretend that our investigation has unearthed unshakable evidence thereof, we do find tantalizing indications pointing to connections between convection, magnetic fields, and pulsation in GD358. We suggest future investigations:

1. Theoretical investigation of the relationship/connection between magnetic fields, convection, and pulsation will increase our understanding of GD358's photometric behavior. The typical static model of a pulsating white dwarf is too limiting. The dynamic model must accommodate the observed changes in pulsation frequencies and multiplet structure.
2. GD358's multiplets do not conform to theoretical expectations based on rotation. Other mechanisms must be considered. Examination of the influence of a nonspherical asymmetry in the outer layers on the multiplet structure is required to understand GD358's multiplets. Identification of spherical degree by multiplet structure alone should be highly suspect in any large amplitude pulsator.
3. Further work on the theoretical aspects of combination frequencies should explore the effects of multiple symmetry axes and the effects of a magnetic field on nonlinear mixing by the convection zone.

4. Detailed investigation of the FOS spectrum obtained during the *sforzando* for possible metals may provide insight into the mechanism producing the event.
5. Theoretical predictions for growth and damping rates have been calculated using static models. The timing of the growth and decay of $k = 8$ and 9 during the *sforzando* indicates interaction between these two modes. A theoretical examination of growth rates in the presence of other modes, including the interaction of a mode with itself, is necessary to better understand both the growth and dissipation of modes during the *sforzando* and typical mode selection in all large amplitude DB and DA pulsators.
6. A detailed examination of behavior of white dwarf pulsators, both low and high amplitude, spanning both the DA and DB instability strips (and hence a range of convective depths) will improve our understanding of convection's role in mode selection.
7. Theoretical work is needed to improve the treatment of convection. Lightcurve fitting of GD358 and other pulsators is an important step towards that goal.
8. Continued observation of GD358 will better define its dynamic behavior. We would like to observe another *sforzando*.

The practice and theoretical development of asteroseismology of GD358 and other pulsating stars continues to reward us with a rich scientific return. Our focus here on GD358 shows us that stellar seismology can challenge our current paradigm of the interior and behavior of pulsating white dwarfs.

The Delaware Asteroseismic Research Association is grateful for the support of the Crystal Trust Foundation and Mt. Cuba Observatory. DARC also acknowledges the support of the University of Delaware, through their participation in the SMARTS consortium. This work is further supported by the Austrian Fonds zur Förderung der wissenschaftlichen Forschung under grant P18339-N08. We would like to thank the various Telescope Allocation Committees for the awards of telescope time. We also acknowledge the assistance of J. Berghuis, M. David, H. Wade, and U. Burns with the Hawaii 0.6m. D.E.M acknowledges his work as a part of research activity of the Astrophysical Research Center for the Structure and Evolution of the Cosmos (ARCSEC) which is supported by the Korean Science and Engineering Foundation.

Facilities: MCAO:0.6 m, McD:2.1 m, KPNO:2.1 m, UH:0.6 m, BOAO:1.8 m, Lulin:1.8 m, Beijing:2.16 m, Maidanek:1.0 m, Peak Terskol:2.0 m, Moletai:1.65 m, Mt. Suhora:0.6 m, Konkoly:1.0 m, Vienna:0.8 m, Tübingen:0.8 m, OHP:1.93 m, NOT, ING:Herschel, LNA:1.6 m, CTIO:0.9 m, SOAR

REFERENCES

Alves, V. M., et al. 2003, Balt. Astron., 12, 33
Beauchamp, A., Wesemael, F., Bergeron, P., Fontaine, G., Saffer, R., Liebert, J., & Brassard, P. 1999, ApJ, 516, 887
Biermann, L. 1941, Mitt. Ges., 76, 1941
Bigot, L., & Dziembowski, W. A. 2002, A&A, 392, 235
Bohm-Vitense, E. 1958, Z. Astrophys., 46, 108
Bradley, P. A., & Winget, D. E. 1994, ApJ, 430, 850
Breger, M., et al. 1993, A&A, 271, 482
Brickhill, A. J. 1991, MNRAS, 251, 273
Brickhill, A. J. 1992, MNRAS, 259, 519
Canuto, V. M., Goldman, I., & Mazzitelli, I. 1996, ApJ, 473, 550
Canuto, V. M., & Mazzitelli, I. 1991, ApJ, 370, 295
Castanheira, B., Kepler, S. O., Nitta, A., Winget, D. E., & Koester, D. 2005, A&A, 432, 175
Di Mauro, M. P., Christensen-Dalsgaard, J., Kjeldsen, H., Bedding, T. R., & Paterno, L. 2003, A&A, 341
Dolez, N., Vauclair, G., & Kleinman, S. J., et al. 2006, A&A, 446, 237
Goldreich, P., & Wu, Y. 1999, ApJ, 511, 904
Handler, G., Romero-Colmenero, E., & Montgomery, M. H. 2002, MNRAS, 335, 399
Hansen, C. J., Cox, J. P., & Van Horn, H. M. 1977, ApJ, 217, 151
Houdek, G., et al. 2001, MNRAS, 327, 483
Ising, J., & Koester, D. 2001, A&A, 374, 116
Jones, P. W, Pesnell, W. D., Hansen, C. J., & Kawaler, S. D. 1989, ApJ, 336, 403
Kanaan, A., Kepler, S. O., & Winget, D. E. 2002, A&A, 389, 896
Kanaan, A., et al. 2005, A&A, 432, 219
Kawaler, S., Sedekii, T., & Gough, D. 1999, ApJ, 516, 349
Kepler, S. O., et al. 2003, A&A, 401, 639, K03
Kepler, S. O., et al. 2000, ApJL, 534, L185
Kleinman, S. J., et al. 1998, ApJ, 495, 424
Kotak, R., van Kerkwijk, M. H., Clemens, J. C., & Koester, D. 2003, A&A, 397, 1043
Kuhn, J. R. 1998, Proc. SOHO6/GONG 98 Workshop, ESA, SP-418, 871
Lenz, P., & Breger, M. 2005, Commun. Asteroseismol., 146, 53
Li, Y., & Yang, J. Y. 2007, MNRAS, 375, 388
Koester, D. 2008, private communication
Marchenko, S. V. 2008, A&A, 479, 845
Matthews, J. M, et al. 2004, Nature, 430, 51
Metcalfe, T. S., Montgomery, M. H., & Kawaler, S. D. 2003, MNRAS, 344, 88
Montgomery, M., & Kupka, F. 2004, MNRAS, 350, 267
Montgomery, M. H. 2005, ApJ, 633, 1142
Montgomery, M. H. 2006, in ASP Conf. Ser. 352, New Horizons in Astronomy: Frank N. Bash Symp. (San Francisco, CA: ASP), 261
Montgomery, M. H. 2008a, Commun. Asteroseismol., 154, 38
Montgomery, M. H. 2008b, private communication
Morin, J., et al. 2008, MNRAS, 384, 77
Nather, R. E., & Mukadam, A. 2004, ApJ, 605, 846
Nather, R. E., Winget, D. E., & Clemens, J. C. 1990, ApJ, 361, 390
Prada, M., Pier, G., & Straniero, O. 2002, ApJ, 581, 585
Provencal, J. L., et al. 2005, BAAS, 37, 1157
Thompson, S. E., Clemens, J. C., van Kerkwijk, M.H., & Koester, D. 2003, ApJ, 589, 921
Scargle, J. D. 1982, ApJ, 263, 835
Schunker, H., & Cally, P. S. 2006, MNRAS, 372, 551
Unno, W., Osaki, Y., Ando, H, & Shibahashi, H 1979, Nonradial Oscillations of Stars (Tokyo: Univ. Tokyo Press)
van Kerkwijk, M. H., Clemens, J. C., & Wu, Y. 2000, MNRAS, 314, 209
Vuckovic, M., et al. 2006, ApJ, 646, 1230
Weidner, C., & Koeter, D. 2003, A&A, 406, 657
Winget, D. E., et al. 1990, ApJ, 357, 630
Winget, D. E., et al. 1991, ApJ, 378, 326
Winget, D. E., et al. 1994, ApJ, 430, 839, W94
Winget, D. E., Sullivan, D. J., Metcalfe, T. S., Kawaler, S. D., & Montgomery, M. H. 2004, ApJL, 602, 109
Winget, D. E. 2008, private communication
Wood, M. 1992, ApJ, 386, 539
Woodward, M. F., & Noyes, R. W. 1985, Nature, 449, 318
Wu, Y. 2000, ASP Conf. Ser. 203, The Impact of Large-Scale Surveys on Pulsating Star Research, IAU Colloquium 176, ed. L. Szabados & D. Kurtz (San Francisco, CA: ASP), 508
Wu, Y. 2001, MNRAS, 323, 248
Yeates, C. M., Clemens, J. C., Thompson, S. E., & Mullaly, F. 2005, ApJ, 635, 1239
Zola, S. 2008, private communication

The Astrophysical Journal, 695:L203–L207, 2009 April 20 doi:10.1088/0004-637X/695/2/L203

DYNAMICAL PHENOMENA IN THE ATMOSPHERE OF THE PROTO-PLANETARY NEBULA IRAS 22272+5435

L. Začs[1], J. Sperauskas[2], F. A. Musaev[3,4,5], O. Smirnova[1,6,9], T. C. Yang[7], W. P. Chen[7], and M. Schmidt[8]
[1] Faculty of Physics and Mathematics, University of Latvia, Raiņa bulvāris 19, LV-1586 Rīga, Latvia
[2] Vilnius University Observatory, Ciurlionio 29 Vilnius 2009, Lithuania
[3] Special Astrophysical Observatory of the Russian AS, Nizhnij Arkhyz 369167, Russia
[4] Institute of Astronomy of the Russian AS, 48 Pyatnitskaya Street, 119017 Moscow, Russia
[5] Terskol Branch of Institute of Astronomy of the Russian AS, 361605 Peak Terskol, Kabardino-Balkaria, Russia
[6] Institute of Astronomy, University of Latvia, Raiņa bulvāris 19, LV-1586 Rīga, Latvia
[7] Graduate Institute of Astronomy, National Central University, Chung-Li 32054, Taiwan
[8] N. Copernicus Astronomical Center, ul. Rabiańska 8, 87-100 Toruń, Poland
Received 2009 January 28; accepted 2009 March 11; published 2009 April 3

ABSTRACT

Radial velocity monitoring of the star HD 235858 confirmed regular variations with a peak-to-peak amplitude of about 10 km s^{-1} and a period of about 131.2 days. The light, color, and velocity variations are typical for RV Tauri stars. Splitting of low-excitation atomic lines was detected. The components are both blue- and redshifted relative to the systemic velocity. Significant variations are observed in the intensity of C_2 and CN lines. Variable emission in the Hα profile, splitting of low-excitation atomic absorption lines, appearance of CN emission lines, blue wings of strong lines, and recent reddening give evidence of shocks and mass outflow obviously induced by atmospheric pulsations.

Key words: line: profiles – shock waves – stars: AGB and post-AGB – stars: mass loss – stars: oscillations – stars: winds, outflows

1. INTRODUCTION

The protoplanetary nebula (PPN) phase is an important but still poorly understood stage in the evolution of low- and intermediate-mass stars. Objects in this stage are in transition between the asymptotic giant branch (AGB) and planetary nebula (PN) phases. Stars enter the PPN at the moment when the strong AGB mass loss stops; however, up to now it has not been known how the decrease of the mass-loss rates takes place. The difference between envelope morphology in AGB stars and PPNs implies a change in the mass-loss process as the star leaves the AGB (Hrivnak & Bieging 2005, and references therein). Pulsation, dust formation, and mass loss through massive stellar winds are characteristic phenomena of AGB stars. Stellar pulsations cause waves that travel into the outer layers of the atmosphere and develop into shocks with temperature and density variations strong enough to trigger dust formation (Freytag & Höfner 2008, and references therein). Radiation pressure on dust particles is believed to be a major reason for the stellar wind from AGB stars leading to high mass-loss rates. The presence of hot dust and the appearance of emission lines in some PPNs seem to be the results of recent mass loss.

IRAS 22272+5435 is a typical PPN associated in the optical with the carbon-rich star HD 235858, which shows a significant *s*-process enhancement (Hrivnak & Kwok 1991; Začs et al. 1995; Reddy et al. 2002). The star is surrounded by a detached circumstellar envelope (CSE), the result of an earlier mass loss. Radiative transfer calculations showed a significant flux underestimate between 5 and 10 μm in the spectral energy distribution if a single CSE was considered (Szczerba et al. 1997). The best-fit model for the dust shell of IRAS 22272+5435 consists of the central star surrounded by two separate sets of dust shells representing a PPN shell (AGB wind shell + superwind shell) and a post-AGB wind shell located in the inner cavity of the PPN shell (Ueta et al. 2001). The presence of hot dust grains in the inner cavity of the PPN shell was suspected; however, the subarcsecond structure of the post-AGB shell and the nature of a post-AGB mass ejection are not clear (Ueta et al. 2001). The observations performed in 1990 September by Hrivnak et al. (1994) confirmed the post-AGB mass ejection for IRAS 22272+5435. Asymmetry in strong atomic lines was observed in 1992 August by Začs et al. (1995).

The central star left AGB about 380 yr ago (Ueta et al. 2001) and has still a relatively low effective temperature of $T_{\rm eff} = 5600 \pm 250$ K (Začs et al. 1995). The photospheric molecular veiling should be negligible; however, Hrivnak & Kwok (1991) detected prominent molecular absorption features of C_2 and C_3 in the optical low-resolution spectrum of HD 235858. HD 235858 = V354 Lac displays complex light variations with an amplitude of about 0.4 mag in the visual region. Hrivnak & Lu (2000, 2007) found a period of about 127 days both in the magnitude and radial velocity (RV) curve and attributed the variations to pulsations. Arkhipova et al. (2000) retrieved two pulsation periods using long-term UBV observations, $P = 207$ and 145 days. This Letter presents the first results of simultaneous spectroscopy and photometry in the optical region to understand in detail the mechanism of variability.

2. OBSERVATIONS

RV of HD 235858 was monitored using the CORAVEL spectrometer (Upgren et al. 2002) of the Vilnius University installed on the 1.65 m telescope at the Moletai Observatory (Lithuania) and on the 1.6 m and 2.3 m telescopes at the Steward Observatory (Arizona). 75 RV measurements were gathered between 2005 September and 2008 February (JD2453639−4531) with a standard deviation of one measurement of about 0.7 km s^{-1}.

The imaging photometry was carried out on the 1.2 m Schmidt telescope at the Baldone Observatory of the University of Latvia equipped with an SBIG-ST10XME CCD camera in the local *BVRI* system from 2007 October through 2008 January. A few measurements were made with the Lulin 1 m telescope (LOT), equipped with a Princeton Instruments PI 1300B CCD camera in the standard *UBVRI* bands in 2005 October 12 and in 2005

[9] PhD student.

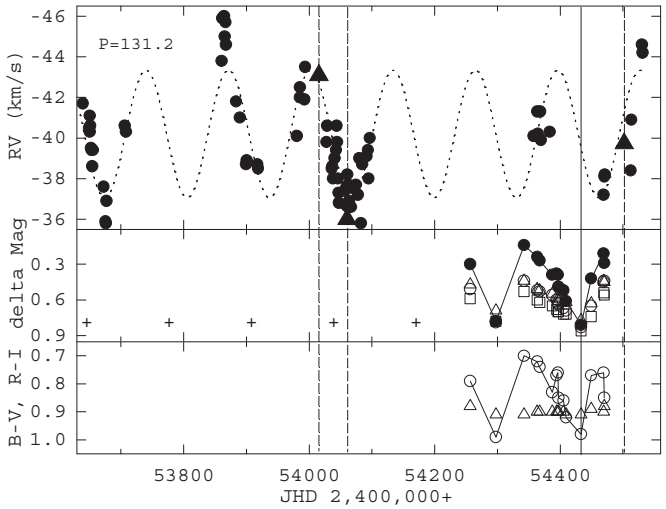

Figure 1. RV variations of HD 235858 measured using the CORAVEL spectrometer (top panel; filled circles) plotted together with a sinusoid fit ($P = 131.2$ days; dotted line) to the velocity data. The velocity values gathered from high-resolution spectra are indicated by filled triangles. The differential variations of magnitude (middle panel: *B*, filled circles; *V*, squares; *R*, triangles; *I*, open circles) and color (bottom panel: $(B - V)$; open circles; $(R - I)$; open triangles) are given. Predicted light minima for the accepted period are indicated by plus signs.

December 19. The images were processed following standard procedures of bias and dark subtraction and flat fielding using the IRAF package.

High-resolution spectra for HD 235858 were obtained with the coudé échelle spectrometer MAESTRO on the 2 m telescope at the observatory on the Terskol Peak in Northern Caucasus (altitude of 3100 m) equipped with a Wright Instruments CCD detector. Four spectra were obtained between 2002 November and 2008 February. In addition, spectra of several hot, rapidly rotating stars were observed to identify the telluric absorption lines. All the spectra covered from about 3600 to 10000 Å. A backside illuminated chip has been used since 2006, therefore the recent spectra longward of about 6700 Å are affected by interference fringes. The resolution inspected using telluric lines agrees for all spectra, FWHM $\simeq$ 0.25 Å near 6900 Å. All spectra were bias subtracted, flat field corrected, and converted to one-dimensional spectra using the standard DECH20T package.

3. ANALYSIS AND RESULTS

3.1. Radial Velocities

The CORAVEL heliocentric radial velocity ($RV_\odot$) measurements are provided in Table 1 and are plotted as a function of time in Figure 1. The best-fitting sinusoid with a period of 131.2 days and an amplitude of 3.1 km s^{-1} is given. The mean residual of observations from this fit is about 1.3 km s^{-1}. The RV curve displays obvious variations in the depth of minima/maxima; therefore, a secondary period was suspected. In the case of two periods (131.5 and 68.9 days) the mean residual is lower—1.0 km s^{-1}. Additional observations are needed to confirm the second period. The mean heliocentric RV of HD 235858 calculated using all RV measurements, $RV_0 = -40.2$ km s^{-1}, is close to the systemic velocity, $RV_\odot = -40.1$ km s^{-1}, measured using CO emission lines of the CSE (Hrivnak & Bieging 2005). In addition, the photospheric RV was measured using a sample of weak (EW $<$ 200 mÅ) and symmetrical atomic lines (FWHM $\simeq$ 0.45 Å) in all high-resolution spectra.

Table 1
Photospheric Heliocentric Radial Velocities

JD 245+	$RV_\odot$ (km s^{-1})	JD 245+	$RV_\odot$ (km s^{-1})	JD 245+	$RV_\odot$ (km s^{-1})
3639.49	−41.7	3917.50	−38.7	4063.70	−36.9
3649.46	−40.5	3918.49	−38.5	4066.62	−36.6
3650.43	−41.1	3980.38	−40.1	4071.55	−37.5
3650.44	−40.3	3985.44	−42.5	4074.56	−37.7
3651.39	−40.6	3985.45	−42.0	4077.65	−37.2
3652.43	−39.5	3992.43	−41.9	4079.61	−39.0
3653.37	−39.4	3993.43	−43.5	4082.58	−35.8
3654.43	−38.6	4027.58	−39.8	4084.59	−38.7
3655.39	−39.4	4028.58	−40.6	4091.59	−39.1
3672.36	−37.6	4035.80	−38.5	4093.61	−39.4
3675.38	−35.9	4036.72	−38.6	4094.64	−38.0
3676.29	−35.8	4037.72	−38.0	4096.59	−40.0
3677.29	−36.9	4040.57	−39.0	4357.46	−40.1
3706.30	−40.6	4042.57	−39.4	4363.46	−41.3
3708.21	−40.3	4043.73	−40.6	4364.40	−40.2
3860.55	−43.8	4044.56	−39.8	4368.40	−41.3
3861.54	−45.9	4045.57	−38.0	4369.39	−39.9
3864.54	−46.0	4046.57	−37.3	4383.43	−40.3
3865.55	−45.0	4047.57	−36.8	4469.27	−37.2
3866.54	−45.7	4056.63	−37.4	4470.23	−38.1
3867.54	−44.6	4058.67	−36.7	4471.19	−38.2
3883.51	−41.8	4059.66	−37.6	4512.27	−38.4
3889.50	−41.0	4060.63	−38.2	4513.20	−40.9
3899.51	−38.7	4061.65	−36.6	4530.22	−44.6
3900.51	−38.9	4062.67	−37.7	4531.22	−44.2

The direct and mirror profile of each line was correlated and the corresponding RV was calculated from the relative shift of the line center from its rest wavelength. These values agree well with the CORAVEL measurements (see Figure 1).

A number of narrow C_2 absorption lines identified in the near-infrared spectrum of HD 235858 (see Section 3.3) were used to measure radial (expansion) velocity of the cool CSE. C_2 lines of the Phillips system are shifted relative to photospheric lines by −4.0 km s^{-1} on average in the spectrum observed in 2002 November 18. The heliocentric photospheric RV of HD 235858 measured at the same time using atomic lines was found to be -44.6 ± 0.5 km s^{-1}. Bearing in mind the photospheric RV relative to systemic velocity during observations, $\Delta RV = -44.6 - (-40.2) = -4.4$ km s^{-1}, the expansion velocity of the CSE was calculated, $V_{exp}(C_2) = -4.4 - 4.0 = -8.4 \pm 0.5$ km s^{-1}. This value agrees with the best model fit of CO (2–1) and (4–3) lines, $V_{exp}(CO) = -8.5$ km s^{-1}, that are formed in the warm and dense interior region of the PPN shell that contains the gas and dust with $T_{kin} = 120$ K ejected in the final AGB stage (Hrivnak & Bieging 2005).

3.2. Photometry

Photometric observations continued over a time interval of about seven months with the main goal of specifying the mechanism of RV variations. The differential light and color variations in the local *BVRI* bands observed at Baldone Observatory are presented in Figure 1. These observations are not converted to the standard system. During observations the magnitude varied from $B = 11.81$–11.14 mag ($\Delta B \sim 0.67$), $V = 8.83$–8.44 mag ($\Delta V \sim 0.39$), $R = 7.77$–7.44 mag ($\Delta R \sim 0.33$), and $I = 6.86$–6.53 mag ($\Delta I \sim 0.33$). The uncertainties are calculated from the errors of individual measurements of standard stars: 0.04 (*B*), 0.03 (*V*), 0.02 (*R*), and 0.03 (*I*). The standard color index $B - V$ observed on 2005 October 12 and

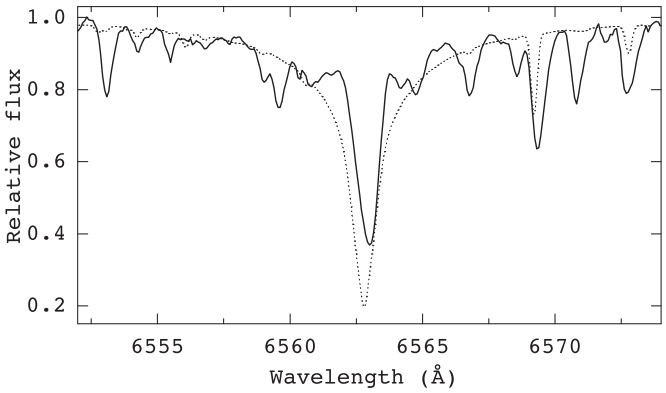

Figure 2. Spectrum of HD 235858 around Hα observed near light maximum in 2008 February along with that calculated (dotted line) using an atmospheric model with $T_{\rm eff} = 5500$ K and $\log g = 0.5$ (cgs). The wavelengths are corrected for photospheric velocity.

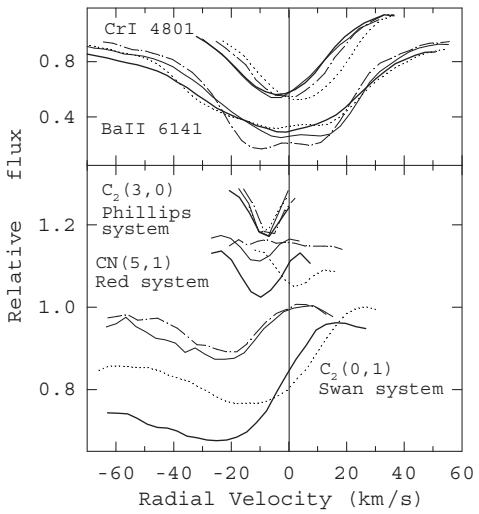

Figure 3. Two representative atomic (top panel) and three molecular (bottom panel) lines in the spectra of HD 235858 observed in 2002 November (thin line), 2006 October (thick), 2006 November (dotted), and 2008 February (dot-dashed) in the RV scale relative to the systemic velocity, $\mathrm{RV}_\odot = -40.2$ km s^{-1}. Splitting of the low-excitation line of barium was observed, indicating an outward and downward motion with a velocity of 10 km s^{-1}. A $C_2(0, 1)$ Swan system band head at 5635.35 Å, a CN(5, 1) Q1 Red system line at 6420.722 Å, and a PPN shell line of $C_2(3, 0)$ Phillips system at 7716.531 Å are provided.

on 2005 December 19 near the predicted primary light minimum and maximum, $B - V = 2.35$ and 2.12 ± 0.01, is larger than previously observed.

3.3. High-Resolution Spectroscopy

The optical spectrum of IRAS22272+5435 was accepted a priori to be stationary (Začs et al. 1995; Bakker et al. 1997; Reddy et al. 2002). However, pulsations of stellar interiors have a strong effect on the atmospheres of cool luminous stars and time series of high-resolution spectra are a useful tool to study atmospheric dynamics (see Nowotny et al. 2005). Variations in profiles and velocities are detected for low-excitation potential (LEP) lines. Strong and variable features of carbon-bearing molecules are detected. A large number of narrow (FWHM $\simeq 0.25$ Å; lines are not resolved) molecular lines are present. The CSE lines of C_2 (1, 0), (2, 0), (3, 0), (4, 0) Phillips system and CN (1, 0), (2, 0), (3, 0), (4, 0) Red System were identified. Thus, the optical spectrum of IRAS22272+5435 originates at various depths throughout different layers in the atmosphere of HD 235858 significantly affected by pulsations and in the CSE. The moments of recent high-resolution observations relative to the RV and light curves are indicated by the dashed vertical lines in Figure 1. The phases were calculated using the 131.2 day period where phase 0.0 defines the time of the primary light minima (JD2454433).

The profile of Hα was found to be asymmetric in all of the spectra. The region around Hα was synthesized using the Kurucz (1993) atmospheric model and compared with the spectrum observed in 2008 February near light maximum: emission wings are visible (Figure 2). The weak variable emissions are present for most, if not all, of the pulsation cycle and might result from emission caused by shock waves. Other shock-related features are observed in low-excitation atomic lines. RV was also measured from the narrow absorption component of the Hα line. This component is redshifted relative to the systemic velocity by about 5–10 km s^{-1} in all of the spectra.

Doubling of strong *s*-process lines was found in the spectrum observed in 2002 November. Additional observations were provided and a number of atomic lines inspected to understand the physical mechanism of splitting. Atomic absorption lines take part in the photospheric pulsations; however, only the profiles of low-excitation lines are disturbed by splitting. Figure 3 shows the profiles of Ba II at 6141.71 Å and of the Cr I line at 4801.025 Å in the RV scale relative to the systemic velocity, $\mathrm{RV}_\odot = -40.2$ km s^{-1}. The Cr I line (LEP = 3.122 eV) with a Gaussian profile in all spectra traces the velocity amplitude of photospheric pulsations around the systemic velocity during the pulsation cycle. The Ba II line (LEP = 0.704 eV) shows splitting. The intensity and velocity of resolved components depend on the pulsation phase. The profile of the barium line observed in 2006 October near the maximum expansion velocity of the photosphere (see Figure 1) is single, much broader and shows an extended wing up to about -70 km s^{-1}. The sequence of profiles indicates that expanding and infalling layers are simultaneously present in the outer atmosphere of HD 235858 and likely a mass outflow exists. It should be noted that the redshifted component of unknown nature relative to the systemic velocity was detected in the resonance lines of three other post-AGB stars ("infalling component A"; see Reddy et al. 1999, 2002).

A time series of high-resolution spectra shows significant changes in the intensity of C_2 and CN "photospheric" features. One representative spectral range is shown in Figure 4 together with the synthetic photospheric spectrum calculated for the C_2 molecule using a spectrum synthesis technique (for details see Začs et al. 2005). The atmospheric model was adopted with parameters suitable for HD 235858: $T_{\rm eff} = 5500$ K, $\log g = 0.5$ (cgs), $\xi_t = 3.7$ km s^{-1}, and [M] $= -0.5$ (Začs et al. 1995). As can be seen, molecular features are stronger than they should be for a standard photosphere of a G5 supergiant, therefore, the temperature of the environment where the molecules have formed is much lower than 5500 K.

Three representative molecular features are displayed here in the RV scale. The band head of the $C_2(0,1)$ Swan system at 5635.35 Å is blueshifted relative to the systemic velocity by about -15–25 km s^{-1} in all of the spectra (see Figure 3). The maximal expansion velocity ($\simeq$25 km s^{-1}) and the maximal C_2 abundance were observed in 2006 October when the photosphere of HD 235858 passed the maximal expansion velocity according to the CORAVEL measurements. The lines of the CN Red system in general vary in step with C_2; however, the Doppler shift relative to the systemic

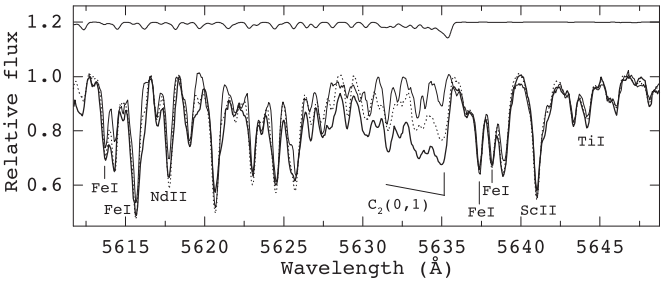

Figure 4. Three high-resolution spectra of HD 235858 in the spectral region around the C_2 Swan system (0, 1) band head at 5635 Å observed on 2008 February 5 (thin line), 2006 October 6 (thick line), and 2006 November 20 (dotted line). The wavelengths are corrected for photospheric velocity. The molecular contribution longward of 5635 Å is negligible. The upper spectrum represents synthetic photospheric spectrum of the C_2 Swan system calculated for an effective temperature of 5500 K.

velocity is lower. The unblended line of the CN Red system (5,1) at 6420.722 Å was blueshifted relative to the systemic velocity by about −10 km s^{-1} in 2006 October when its intensity was largest (see Figure 3). However, in 2006 November this line displays approximately the photospheric velocity. Thus, the "photospheric" molecular features are apparently formed in the cool outflow at a different high scale. The CN lines behave as though they arise near the stellar photosphere. The spectrum observed on 2008 February 5 near the light maximum shows emission in the CN lines (see Figure 3), in support of shock waves. The unblended C_2(3,0) Phillips system line at 7716.531 Å is provided for comparison purposes in Figure 3. Significant variations in the intensity and velocity are not detected in this PPN shell line. Some minor discrepancies in profiles are because of uncertainties in removing the strong CCD fringes and telluric lines longward of 6800 Å. It should be noted that blue- and redshifted C_2 and C_3 lines were detected in the low-resolution spectrum of HD 235858 and similar phenomena were discussed for CRL2688 and some carbon stars by Hrivnak & Kwok (1991).

4. DISCUSSION AND CONCLUSIONS

New spectroscopic and photometric observations of the well-known cool PPN IRAS 22272+5435 in the optical region have strengthened the assumption that this carbon-rich post-AGB star experiences mass-loss episodes probably induced by stellar pulsations.

RV monitoring with the CORAVEL spectrometer revealed variations with a period of about 131.2 days and a peak-to-peak amplitude of about 10 km s^{-1}. The RV curve displays obvious variations in the depth of minima/maxima; therefore, a secondary period was suspected, $P = 68.9$ days. It appears that HD 235858 is pulsating in the fundamental mode with the resonance $P_0 = 2P_1$. This resonance occurs for typical RV Tauri stars (Pollard et al. 1996). Hrivnak & Lu (2000) acknowledge the pulsation period of about 130 days during the last 18 years. Tuchman et al. (1993) found similar periods for the model of a low-mass star (0.7 $M_\odot$) with a thin envelope (less than 0.01 $M_\odot$) and a supergiant luminosity (10^4 $L_\odot$); however, the model is near the limit for the unstable fundamental mode. The fundamental mode of 132.2 days and the luminosity of 1.3×10^4 $L_\odot$ (Ueta et al. 2001) provide a mass of about 0.75 $M_\odot$ for HD 235858 (see Figure 10 of Tuchman et al. 1993). Nonlinear radiative models (Fokin et al. 2001) reproduce reasonable RVs and light curves and acknowledge propagation of the shock (compression) waves throughout the stellar atmosphere; the outward and downward waves reach an amplitude of about 20 and 10–15 km s^{-1}, respectively.

The periods of light and RV variations agree; however, the variations are shifted in phase in agreement with that observed by Hrivnak & Lu (2000). HD 235858 is brightest during expansion and faintest during contraction. The extrema of brightness are at moments when the photosphere reaches the systemic velocity of −40.2 km s^{-1}. The total amplitude of visual light variations during the last 18 years $V \sim 0.4$ mag was found to be stable (Arkhipova et al. 2000). The color index $B - V$ is largest at light minimum in agreement with that observed for Galactic RV Tauri variables. Between 1991 and 2000 the color $B - V$ varied between ∼2.1 and 1.9 mag (Arkhipova et al 2000). Our photometry gives $B - V = 2.35$ and 2.12 in 2005 October/December near the predicted primary light minimum/maximum (predicted phase of 0.08 and 0.60). The recent reddening is probably because of increased circumstellar extinction.

The profile of Hα was found to be asymmetric and variable. The weak emission wings are present for most of the pulsation cycle and may be the result of shock waves. The low-excitation lines display two or more components in the spectra of HD 235858, indicating that shock waves are propagating through the regions of stellar atmosphere where these lines are forming as for typical RV Tauri stars (Pollard et al. 1997). The sequence of profiles indicates that expanding and infalling layers are simultaneously present in the outer atmosphere of HD 235858. The lack of strong line-doubling behavior in high potential lines is most likely because these lines are formed deeper in the atmosphere. A component redshifted relative to the systemic velocity by about 10 km s^{-1} of unknown nature was detected in the resonance lines of Na and Li for other post-AGB stars (Reddy et al. 2002). Thus, the movement of layers in pulsating extended atmospheres influenced by shock waves could be the physical mechanism of blue/redshift.

Photospheric molecular features in the spectrum of HD 235858 are enhanced in comparison with the standard photosphere of a G5 supergiant. Significant changes in the intensities are detected. The C_2 Swan system band heads are blueshifted relative to the systemic velocity by about 10–25 km s^{-1} in all of the spectra. The CN Red system (4,0) and (5,1) lines in general vary in step with C_2; however, the Doppler shift relative to the systemic velocity is lower. The "photospheric" molecular features are apparently formed in the cool outflow of HD 235858 at different high scale. Blue/redshifted C_2 and C_3 lines have been detected in other post-AGB and AGB stars. The intensity changes seem to be typical for RV Tauri stars (Pollard et al. 1996, and references therein). A related star MACHO*04:55:43.2–67:51:10 in the Large Magellanic Cloud (LMC) with a primary period of 112.4 days combines the signatures of post-AGB and RV Tauri stars and shows a strong C_2 band with a pronounced phase dependence (Pollard & Lloyd Evans 2000).

The spectrum of HD 235858 observed in 2008 February near the light maximum shows emission in lines of the CN Red system in support of shock waves. Hrivnak et al. (1994) attributed the emission of highly excited vibrational levels of CO observed in 2000 September to the onset of a sudden mass ejection from the central star. The emission is likely to have originated either at the base of the new wind where the density is high, or at the region of interaction between this flow and the outer dust/molecular envelope where the shock energy is dissipated. Ueta et al. (2001) confirmed post-AGB mass ejection about 10 years ago. Blöcker (1995) considered a nonabrupt

decrease of the AGB mass-loss rates until the pulsation period of 50 days in the fundamental mode is reached. The mass-loss rates beyond the AGB are crucial parameters for evolutionary timescales, therefore time series are required for other cool pulsating PPNs to clarify the post-AGB mass-loss process.

J.S. thanks the Steward Observatory for providing observing time on the 2.3 m and 1.6 m telescopes. This research was partly financed (for L.Z.) by the Latvian Council of Science (grant 05.1863). The collaborative program between Polish and Latvian Academy of Sciences is acknowledged for support.

REFERENCES

Arkhipova, V. P., Ikonnikova, N. P., Noskova, R. I., & Sokol, G. V. 2000, Astron. Lett., 26, 609
Bakker, E. J., van Dishoeck, E. F., Waters, L. B. F. M., & Schoenmaker, T. 1997, A&A, 323, 469
Blöcker, T. 1995, A&A, 299, 755
Fokin, A. B., Lebre, A., Le Coroller, H., & Gillet, D. 2001, A&A, 378, 546
Freytag, B., & Höfner, S. 2008, A&A, 483, 571
Hrivnak, B. J., & Bieging, J. H. 2005, ApJ, 624, 331
Hrivnak, B. J., & Kwok, S. 1991, ApJ, 371, 631
Hrivnak, B. J., Kwok, S., & Geballe, T. R. 1994, ApJ, 420, 783
Hrivnak, B. J., & Lu, W. 2000, in IAU Symp. 177, The Carbon Star Phenomenon, ed. R. F. Wing (Dordrecht: Kluwer), 293
Hrivnak, B. J., & Lu, W. 2007, in ASP Conf. Ser. 378, Why Galaxies Care about AGB Stars, ed. F. Kerschbaum et al. (San Francisco, CA: ASP), 303
Kurucz, R. L. 1993, CD-ROM No. 13, SAO
Nowotny, W., et al. 2005, A&A, 437, 273
Pollard, K. R., Cottrell, P. L., Kilmartin, P. M., & Gilmore, A. C. 1996, MNRAS, 279, 949
Pollard, K. R., & Lloyd Evans, T. 2000, AJ, 120, 3098
Pollard, K. R., et al. 1997, MNRAS, 286, 1
Reddy, B. E., Bakker, E. J., & Hrivnak, B. J. 1999, ApJ, 524, 831
Reddy, B. E., Lambert, D. L., Gonzalez, G., & Yong, D. 2002, ApJ, 564, 482
Szczerba, R., et al. 1997, A&A, 317, 859
Tuchman, Y., Lébre, A., Mennesier, M. O., & Yarri, A. 1993, A&A, 271, 501
Ueta, T., et al. 2001, ApJ, 557, 831
Upgren, A. R., Sperauskas, J., & Boyle, R. P. 2002, Baltic Astron., 11, 91
Začs, L., Klochkova, V. G., & Panchuk, V. E. 1995, MNRAS, 275, 764
Začs, L., et al. 2005, A&A, 441, 303

A&A 504, L9–L12 (2009)
DOI: 10.1051/0004-6361/200912732

Astronomy & Astrophysics

Letter to the Editor

The GASP-WEBT monitoring of 3C 454.3 during the 2008 optical-to-radio and γ-ray outburst⋆

M. Villata[1], C. M. Raiteri[1], M. A. Gurwell[2], V. M. Larionov[3,4,5], O. M. Kurtanidze[6], M. F. Aller[7], A. Lähteenmäki[8], W. P. Chen[9], K. Nilsson[10], I. Agudo[11], H. D. Aller[7], A. A. Arkharov[4], U. Bach[12], R. Bachev[13], P. Beltrame[14], E. Benítez[15], C. S. Buemi[16], M. Böttcher[17], P. Calcidese[18], D. Capezzali[19], D. Carosati[19], D. Da Rio[14], A. Di Paola[20], M. Dolci[21], D. Dultzin[15], E. Forné[22], J. L. Gómez[11], V. A. Hagen-Thorn[3,5], A. Halkola[10], J. Heidt[23], D. Hiriart[15], T. Hovatta[8], H.-Y. Hsiao[9], S. G. Jorstad[24], G. N. Kimeridze[6], T. S. Konstantinova[3], E. N. Kopatskaya[3], E. Koptelova[9], P. Leto[16], R. Ligustri[14], E. Lindfors[10], J. M. Lopez[15], A. P. Marscher[24], M. Mommert[23], R. Mujica[25], M. G. Nikolashvili[6], N. Palma[17], M. Pasanen[10], M. Roca-Sogorb[11], J. A. Ros[22], P. Roustazadeh[17], A. C. Sadun[26], J. Saino[10], L. A. Sigua[6], M. Sorcia[15], L. O. Takalo[10], M. Tornikoski[8], C. Trigilio[16], R. Turchetti[14], and G. Umana[16]

(Affiliations can be found after the references)

Received 19 June 2009 / Accepted 12 August 2009

ABSTRACT

Context. Since 2001, the radio quasar 3C 454.3 has undergone a period of high optical activity, culminating in the brightest optical state ever observed, during the 2004−2005 outburst. The Whole Earth Blazar Telescope (WEBT) consortium has carried out several multifrequency campaigns to follow the source behaviour.

Aims. The GLAST-AGILE Support Program (GASP) was born from the WEBT to provide long-term continuous optical-to-radio monitoring of a sample of γ-loud blazars, during the operation of the AGILE and GLAST (now known as Fermi GST) γ-ray satellites. The main aim is to shed light on the mechanisms producing the high-energy radiation, through correlation analysis with the low-energy emission. Thus, since 2008 the monitoring task on 3C 454.3 passed from the WEBT to the GASP, while both AGILE and Fermi detected strong γ-ray emission from the source.

Methods. We present the main results obtained by the GASP at optical, mm, and radio frequencies in the 2008−2009 season, and compare them with the WEBT results from previous years.

Results. An optical outburst was observed to peak in mid July 2008, when Fermi detected the brightest γ-ray levels. A contemporaneous mm outburst maintained its brightness for a longer time, until the cm emission also reached the maximum levels. The behaviour compared in the three bands suggests that the variable relative brightness of the different-frequency outbursts may be due to the changing orientation of a curved inhomogeneous jet. The optical light curve is very well sampled during the entire season, which is also well covered by the various AGILE and Fermi observing periods. The relevant cross-correlation studies will be very important in constraining high-energy emission models.

Key words. galaxies: active – galaxies: quasars: general – galaxies: quasars: individual: 3C 454.3 – galaxies: jets

1. Introduction

Blazars (i.e. flat-spectrum radio quasars and BL Lacertae objects) constitute a specific class of radio-loud active galactic nuclei whose highly variable emission is dominated by relativistically-beamed non-thermal radiation from a plasma jet. Blazars are detected at all wavelengths, from the radio to the γ-ray band. The low-energy non-thermal emission (from radio to optical, or sometimes to UV/X-rays) is due to synchrotron radiation, while the higher-energy emission is usually ascribed to inverse-Compton scattering of soft photons by the synchrotron-emitting relativistic electrons in the jet. According to synchrotron-self-Compton (SSC) models, the soft photons are the synchrotron photons themselves, while in external-Compton (EC) models, seed photons come from outside the jet, in particular from the accretion disc or the broad line region. The different predictions on the multifrequency behaviour of the source from different models can be tested by the results of coordinated multiwavelength campaigns, coupling the high-energy data from satellite observations with ground-based radio-to-optical data. In 1997, during the operation of the Compton Gamma Ray Observatory (CGRO, 1991−2000) satellite, this was one of the main motivations that led to the birth of the Whole Earth Blazar Telescope (WEBT)[1], which involves a large number of telescopes at different longitudes, to obtain continuous monitoring during campaigns dedicated to single sources. Ten years later, in 2007, following the launch of the γ-ray satellite Astro-rivelatore Gamma a Immagini LEggero (AGILE), and in view of the anticipated launch of the Gamma-ray Large Area Space Telescope (GLAST, then renamed as the Fermi Gamma-ray Space Telescope), the WEBT started a new project: the GLAST-AGILE Support Program (GASP; see e.g. Villata et al. 2008b). Its primary aim is to provide long-term continuous optical-to-radio monitoring of a list of 28 γ-loud blazars, during the operation of these two satellites, by means of selected WEBT telescopes.

⋆ The radio-to-optical data presented in this paper are stored in the GASP-WEBT archive; for questions regarding their availability, please contact the WEBT President Massimo Villata (villata@oato.inaf.it).

[1] http://www.oato.inaf.it/blazars/webt/

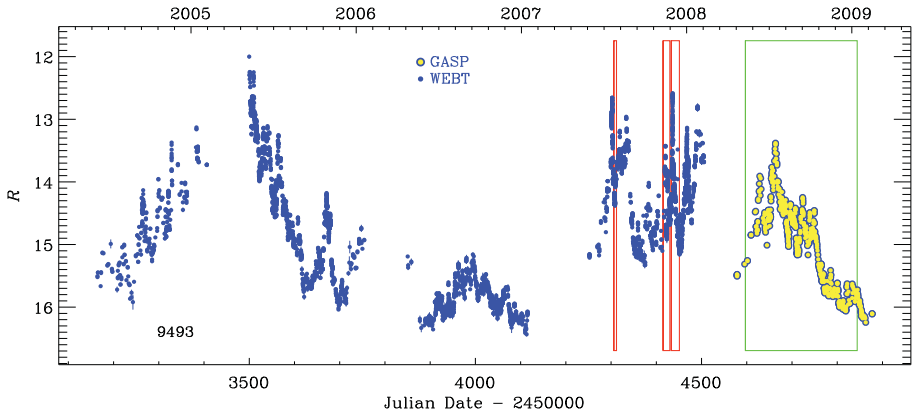

Fig. 1. *R*-band light curve of 3C 454.3 in the last five observing seasons, composed with data from the WEBT campaigns (blue dots) and from the GASP monitoring (yellow-filled circles); the boxes indicate various periods of γ-ray detection, as described in the text.

The flat-spectrum radio quasar 3C 454.3 ($z = 0.859$) is one of the most studied blazars, especially after the observation of an exceptional bright state from the mm band to X-rays in May 2005. That unprecedented outburst was monitored from the radio to the optical band by the WEBT, whose results were published by Villata et al. (2006) together with Chandra observations and VLBA imaging[2]. The WEBT continued to monitor the subsequent high radio activity; an interpretation of the optical-radio correlation was proposed by Villata et al. (2007). The subsequent observing seasons showed an alternation of quiescent and active states; the relevant WEBT monitoring and spectral energy distribution (SED) results were presented and analysed in Raiteri et al. (2007, 2008a,b) together with optical-UV and X-ray observations by the XMM-Newton and Swift satellites and spectroscopic monitoring in the near-IR. During the renewed optical activity of the second half of 2007, AGILE detected the source several times, at the brightest levels ever observed up to that time, as shown by Vercellone et al. (2008, 2009) and Donnarumma et al. (2009). In the last two papers, the authors also performed a cross-correlation analysis between the γ-ray fluxes in November and December 2007 and the corresponding WEBT optical data, showing a possible delay of the γ-ray emission of about 1 day or less. In particular, the detection of an exceptionally fast and strong flare in both the optical and γ-ray bands on December 12 seems to constrain the time lag to be less than 12 h.

Thus, the WEBT followed the radio-to-optical behaviour of 3C 454.3 until February 2008; since then, the GASP continued this task in the last observing season 2008−2009, as part of its 28-source monitoring effort. Between late May and late June 2008, Donnarumma et al. (2008), Vittorini et al. (2008), and Gasparrini et al. (2008) reported on various episodes of γ-ray activity detected by AGILE. In July, the GASP observed a bright optical-NIR flare accompanied by mm and cm radio activity (Villata et al. 2008a). In the meantime, GLAST/Fermi-GST started its operation and the Large Area Telescope (LAT), turned on in late June, promptly detected high γ-ray activity, at unprecedented emission levels, especially during the optical flare (Tosti et al. 2008). Pittori et al. (2008) reported on the further observation by AGILE in late July. Following the optical-to-radio activity detected in July, the GASP continued to observe an increasing flux at high radio frequencies in the subsequent months, leading to the highest levels ever recorded at 43 GHz (Bach et al. 2008).

Abdo et al. (2009) present the results of the first three months of Fermi-LAT observations of 3C 454.3, when the source showed unprecedentedly strong and highly-variable γ-ray emission, with a peak flux of $F_{E>100\,\mathrm{MeV}} \approx 1.2 \times 10^{-5}$ photons cm^{-2} s^{-1}. Their light curve covers (with a quasi-daily sampling) the period July 1−October 5, and the similarities with the optical light curve presented in this letter are evident. However, this letter is focused on the multifrequency behaviour observed by the GASP in the 2008−2009 observing season, and any consideration and analysis on the optical-γ correlation and its impact on theoretical models is deferred to subsequent papers in collaboration with the AGILE and Fermi teams. In Sect. 2 we present the optical-to-radio observations with a selection of light curves; in Sect. 3 we discuss the results.

2. Optical-to-radio observations and results

We calibrated the optical *R*-band magnitudes with respect to Stars 1−4 from the photometric sequence by Raiteri et al. (1998). Figure 1 shows the *R*-band data collected by the GASP in the 2008−2009 observing season (from April 2008 to February 2009; yellow-filled circles), together with WEBT data during the previous four seasons, since the big 2004−2005 outburst (blue dots; data from Villata et al. 2006, 2007; Raiteri et al. 2007, 2008a,b). In total, we assembled about 9500 data points. The participating GASP optical observatories in the 2008−2009 season were: Abastumani, Lulin, Armenzano, Crimean, Roque de los Muchachos (KVA), Belogradchik, San Pedro Martir, St. Petersburg, Kitt Peak (MDM), Teide (BRT), Sabadell, Talmassons, Calar Alto[3], L'Ampolla, New Mexico Skies, Valle d'Aosta, and Tuorla. Near-IR *JHK* data were taken at Campo Imperatore. In the figure, the boxes indicate periods of γ-ray detection: the red ones are those by AGILE in 2007 (Vercellone et al. 2008, 2009; Donnarumma et al. 2009), while the green one represents the total period covered by AGILE and/or Fermi in 2008 – early 2009.

The GASP light curve from April 2008 to February 2009 is better displayed in Fig. 2, where also the details of the γ-ray observing periods are given: red boxes are the AGILE ones, whereas the blue box indicates the July 1−October 5 period covered by the light curve in Abdo et al. (2009)[4]. The optical flux started to increase in mid May and a first, noticeable flare peaked in mid June, at the end of the first AGILE period. A further, brighter flare was observed to double-peak on July 7−10

[2] Observations by the INTEGRAL and Swift satellites and by the REM telescope were presented in Pian et al. (2006), Giommi et al. (2006), and Fuhrmann et al. (2006), respectively.

[3] Calar Alto data were acquired as part of the MAPCAT (Monitoring AGN with Polarimetry at the Calar Alto Telescopes) project.

[4] The Fermi-LAT monitoring has continued beyond this period; preliminary light curves are shown at http://fermi.gsfc.nasa.gov/ssc/data/access/lat/msl_lc/.

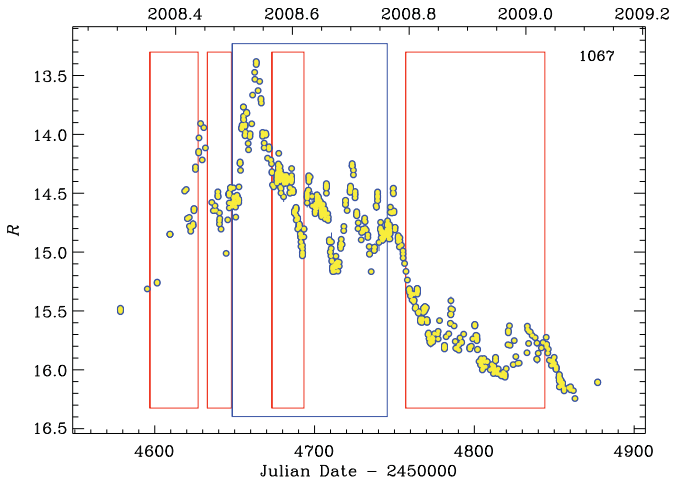

Fig. 2. Enlargement of the last season of the *R*-band light curve shown in Fig. 1, during the GASP monitoring; see text for explanation of the red and blue boxes.

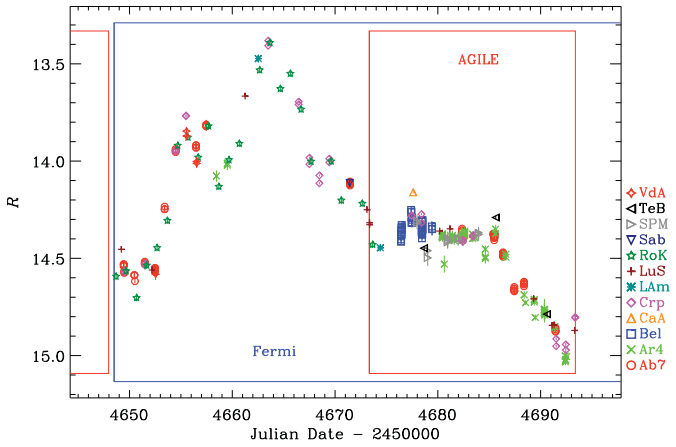

Fig. 3. Further enlargement of the *R*-band light curve around the brightest phase of the 2008 outburst, well monitored also by Fermi and AGILE; different symbols indicate different observatories.

(JD ∼ 2 454 655−57), followed by the brightest phase of the outburst, peaking around July 16.1 (JD ∼ 2 454 663.6). This brightest part of the 2008 outburst is visible in more detail in Fig. 3, which reports the period from the start of the Abdo et al. (2009) γ-ray light curve (July 1.0, JD = 2 454 648.5) until the end of the third 2008 AGILE period (August 14.88, JD = 2 454 693.38), with symbols differentiating the various observatories. Then the optical flux started to drop with a decreasing trend with several flares superposed, until the end of the season.

The GASP monitored the source also at mm and cm wavelengths: 345 and 230 GHz (SMA[5]), 43 GHz (Noto), 37 GHz (Metsähovi), 22 GHz (Medicina), 14.5 GHz (UMRAO), 8 and 5 GHz (UMRAO and Medicina). In Fig. 4, we show the best-sampled and most-significant light curves from late March 2008 to February 2009, at 230, 37, and 14.5 GHz[6]. The optical outburst was accompanied by very high activity at these lower frequencies; in particular, the 37 GHz data show levels never observed before, brighter than the previous historical maximum of early 2006. The mm−cm outbursts appear to be delayed with respect to the optical outburst, especially in the decreasing phase, with the delay increasing with wavelength.

[5] These data were obtained as part of the normal monitoring program initiated by the SMA (see Gurwell et al. 2007).

[6] The other, less-sampled light curves show similar/intermediate trends.

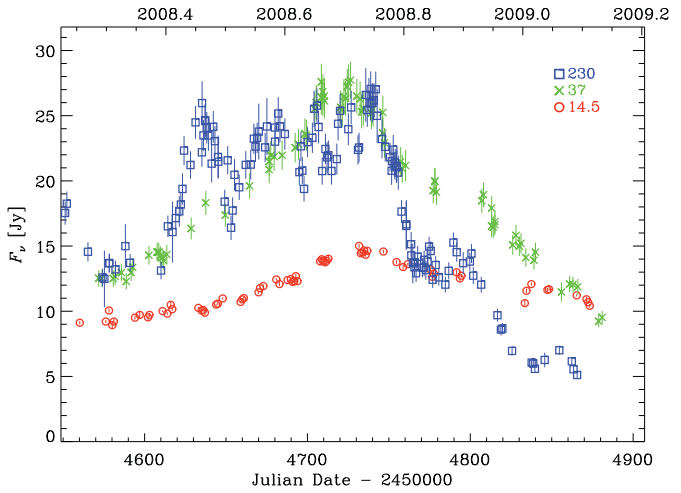

Fig. 4. GASP light curves of 3C 454.3 from late March 2008 to February 2009 at 230 GHz (blue squares), 37 GHz (green crosses), and 14.5 GHz (red circles).

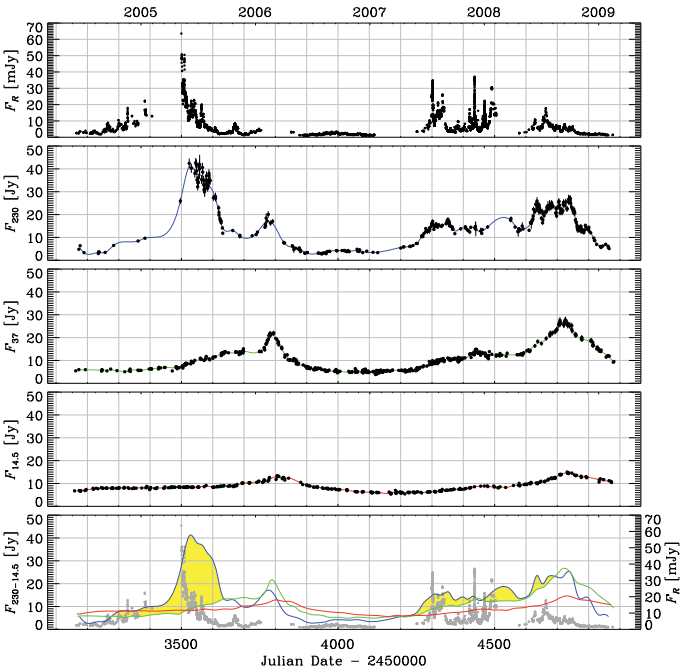

Fig. 5. *R*-band flux-density (de-reddened) light curve (*top*, mJy) and mm−cm light curves (Jy) at 230, 37, and 14.5 GHz from June 2004 to February 2009; in *the bottom panel* the optical data are reported together with the cubic spline interpolations through the 15-day binned data at 230 (blue line), 37 (green line), and 14.5 (red line) GHz; the regions where the 230 GHz spline exceeds the 37 GHz one are highlighted in yellow.

Figure 5 displays the flux behaviour at optical, mm, and radio frequencies in the last five seasons, starting from the 2004−2005 historical outburst, including the WEBT data from Villata et al. (2006, 2007) and Raiteri et al. (2007, 2008a,b). Compared to the previous optical activity, the 2008 outburst appears relatively modest, while the corresponding mm (230 GHz) outburst is much more spectacular, and the radio levels at 37 and 14.5 GHz are higher than in the previous events.

3. Discussion

The unprecedented optical outburst of 2005 was followed by an equally exceptional mm event, but, at lower frequencies, the signature of this event was only a moderate flux increase. According to Villata et al. (2007), the different appearance of the outburst (which is caused by an emitting zone moving along the jet) at different frequencies was due to different viewing angles of the various emitting regions in the (curved) jet: smaller viewing angles yield a stronger Doppler enhancement of the flux. After that, an orientation change of the curved jet provided the extraordinary outburst at high radio frequencies of early 2006, as the counterpart of non-enhanced optical activity. This interpretation predicted a mild mm event, as one can now see in Fig. 5 (see also Raiteri et al. 2008b). In other words, the ratios between the fluxes at different frequencies depend on the curved jet orientation. Following this picture, the strong (but not exceptional) optical activity in the 2007−2008 season, accompanied by mild mm and cm activity, would represent a geometrical configuration slightly favouring high frequencies. Then (2008−2009), the initial optical brightness is soon suppressed in favour of the mm one, which continues to be bright for a longer period, until the radio frequencies also brighten, more than previously, due to a particularly small viewing angle. It seems that the jet curvature can allow only two bands (e.g. optical and mm, or mm and cm) to be contemporaneously strongly Doppler enhanced: if one of the outer bands (i.e. optical and radio) is enhanced, the other is non-enhanced (see also the model for BL Lacertae in Villata et al. 2009 and Fig. 4 therein). To make this evident, in the bottom panel of Fig. 5 we plotted the optical data and cubic spline interpolations through the mm and cm light curves together. The yellow areas highlight the regions where the 230 GHz spline exceeds that at 37 GHz, i.e. when the mm emitting region is better aligned with the line of sight than the cm one. As expected, the larger the 230/37 GHz flux ratio, the higher the corresponding optical activity, and the optical appears always low when the 230/37 GHz ratio is less than 1. A deeper, quantitative analysis of this correlation is beyond the aim of this short letter.

We have reported on the optical-to-radio flux behaviour of 3C 454.3 in the 2008−2009 season, as observed by the GASP, and have compared these results with the WEBT light curves of recent years, finding consistency with the curved jet scenario depicted by Villata et al. (2007). In particular, we have assembled a detailed optical light curve during and around the various detection periods by AGILE and Fermi, which will be very useful for cross-correlation studies with the γ-ray emission.

Acknowledgements. We thank the referee, R. Hartman, for useful suggestions. The Torino team acknowledges financial support by the Italian Space Agency through contract ASI-INAF I/088/06/0 for the Study of High-Energy Astrophysics. The Submillimeter Array is a joint project between the Smithsonian Astrophysical Observatory and the Academia Sinica Institute of Astronomy and Astrophysics and is funded by the Smithsonian Institution and the Academia Sinica. The St. Petersburg team acknowledges support from Russian Foundation for Basic Researches, grant 09-02-00092. AZT-24 observations at Campo Imperatore are made within an agreement between Pulkovo, Rome and Teramo observatories. This research has made use of data from the University of Michigan Radio Astronomy Observatory, which is supported by the National Science Foundation and by funds from the University of Michigan. The Metsähovi team acknowledges the support from the Academy of Finland. The research has been supported by the Taiwan National Science Council grant No. 96-2811-M-008-033. This paper is partly based on observations carried out at the German-Spanish Calar Alto Observatory, which is jointly operated by the MPIA and the IAA-CSIC. Acquisition of the MAPCAT data is supported in part by the Spanish "Ministerio de Ciencia e Innovación" through grant AYA2007-67626-C03-03. This work is partly based on observations with the Medicina and Noto radio telescopes operated by INAF – Istituto di Radioastronomia.

References

Abdo, A. A., Ackermann, M., Ajello, M., et al. 2009, ApJ, 699, 817
Bach, U., Gurwell, M. A., Leto, P., et al. 2008, The Astronomer's Telegram, 1849, 1
Donnarumma, I., D'Ammando, F., Pacciani, L., et al. 2008, The Astronomer's Telegram, 1545, 1
Donnarumma, I., Pucella, G., Vittorini, V., et al. 2009, ApJ, submitted
Fuhrmann, L., Cucchiara, A., Marchili, N., et al. 2006, A&A, 445, L1
Gasparrini, D., Pittori, C., Verrecchia, F., et al. 2008, The Astronomer's Telegram, 1592, 1
Giommi, P., Blustin, A. J., Capalbi, M., et al. 2006, A&A, 456, 911
Gurwell, M. A., Peck, A. B., Hostler, S. R., Darrah, M. R., & Katz, C. A. 2007, in From Z-Machines to ALMA: (Sub)Millimeter Spectroscopy of Galaxies, ed. A. J. Baker, J. Glenn, A. I. Harris, J. G. Mangum, & M. S. Yun, ASP Conf. Ser., 375, 234
Pian, E., Foschini, L., Beckmann, V., et al. 2006, A&A, 449, L21
Pittori, C., Verrecchia, F., Vercellone, S., et al. 2008, The Astronomer's Telegram, 1634, 1
Raiteri, C. M., Villata, M., Lanteri, L., Cavallone, M., & Sobrito, G. 1998, A&AS, 130, 495
Raiteri, C. M., Villata, M., Larionov, V. M., et al. 2007, A&A, 473, 819
Raiteri, C. M., Villata, M., Chen, W. P., et al. 2008a, A&A, 485, L17
Raiteri, C. M., Villata, M., Larionov, V. M., et al. 2008b, A&A, 491, 755
Tosti, G., Chiang, J., Lott, B., et al. 2008, The Astronomer's Telegram, 1628, 1
Vercellone, S., Chen, A. W., Giuliani, A., et al. 2008, ApJ, 676, L13
Vercellone, S., Chen, A. W., Vittorini, V., et al. 2009, ApJ, 690, 1018
Villata, M., Raiteri, C. M., Balonek, T. J., et al. 2006, A&A, 453, 817
Villata, M., Raiteri, C. M., Aller, M. F., et al. 2007, A&A, 464, L5
Villata, M., Raiteri, C. M., Larionov, V. M., et al. 2008a, The Astronomer's Telegram, 1625, 1
Villata, M., Raiteri, C. M., Larionov, V. M., et al. 2008b, A&A, 481, L79
Villata, M., Raiteri, C. M., Larionov, V. M., et al. 2009, A&A, 501, 455
Vittorini, V., Donnarumma, I., D'Ammando, F., et al. 2008, The Astronomer's Telegram, 1581, 1

[1] INAF - Osservatorio Astronomico di Torino, Italy
[2] Harvard-Smithsonian Center for Astrophysics, MA, USA
[3] Astronomical Institute, St.-Petersburg State University, Russia
[4] Pulkovo Observatory, Russia
[5] Isaac Newton Institute of Chile, St.-Petersburg Branch, Russia
[6] Abastumani Astrophysical Observatory, Georgia
[7] Department of Astronomy, University of Michigan, MI, USA
[8] Metsähovi Radio Observatory, Helsinki University of Technology TKK, Finland
[9] Institute of Astronomy, National Central University, Taiwan
[10] Tuorla Observatory, Department of Physics and Astronomy, University of Turku, Finland
[11] Instituto de Astrofísica de Andalucía, CSIC, Spain
[12] Max-Planck-Institut für Radioastronomie, Germany
[13] Institute of Astronomy, Bulgarian Academy of Sciences, Bulgaria
[14] Circolo Astrofili Talmassons, Italy
[15] Instituto de Astronomía, Universidad Nacional Autónoma de México, Mexico
[16] INAF - Osservatorio Astrofisico di Catania, Italy
[17] Astrophysical Institute, Department of Physics and Astronomy, Ohio University, OH, USA
[18] Osservatorio Astronomico della Regione Autonoma Valle d'Aosta, Italy
[19] Armenzano Astronomical Observatory, Italy
[20] INAF - Osservatorio Astronomico di Roma, Italy
[21] INAF - Osservatorio Astronomico di Collurania Teramo, Italy
[22] Agrupació Astronòmica de Sabadell, Spain
[23] ZAH, Landessternwarte Heidelberg-Königstuhl, Germany
[24] Institute for Astrophysical Research, Boston University, MA, USA
[25] INAOE, Mexico
[26] Department of Physics, University of Colorado Denver, CO, USA

A&A 507, 769–779 (2009)
DOI: 10.1051/0004-6361/200912953

Astronomy & Astrophysics

WEBT multiwavelength monitoring and XMM-Newton observations of BL Lacertae in 2007–2008

Unveiling different emission components⋆

C. M. Raiteri[1], M. Villata[1], A. Capetti[1], M. F. Aller[2], U. Bach[3], P. Calcidese[4], M. A. Gurwell[5], V. M. Larionov[6,7], J. Ohlert[8], K. Nilsson[9], A. Strigachev[10], I. Agudo[11], H. D. Aller[2], R. Bachev[10], E. Benítez[12], A. Berdyugin[9], M. Böttcher[13], C. S. Buemi[14], S. Buttiglione[15], D. Carosati[16], P. Charlot[17,18], W. P. Chen[19], D. Dultzin[12], E. Forné[20], L. Fuhrmann[3], J. L. Gómez[11], A. C. Gupta[21], J. Heidt[22], D. Hiriart[12], W.-S. Hsiao[19], M. Jelínek[23], S. G. Jorstad[24], G. N. Kimeridze[25], T. S. Konstantinova[6], E. N. Kopatskaya[6], A. Kostov[10], O. M. Kurtanidze[25], A. Lähteenmäki[26], L. Lanteri[1], L. V. Larionova[6], P. Leto[27,14], G. Latev[28], J.-F. Le Campion[17,18], C.-U. Lee[29], R. Ligustri[30], E. Lindfors[9], A. P. Marscher[31], B. Mihov[10], M. G. Nikolashvili[25], Y. Nikolov[10,28], E. Ovcharov[28], D. Principe[13], T. Pursimo[32], B. Ragozzine[13], R. M. Robb[33], J. A. Ros[20], A. C. Sadun[34], R. Sagar[21], E. Semkov[10], L. A. Sigua[25], R. L. Smart[1], M. Sorcia[12], L. O. Takalo[9], M. Tornikoski[26], C. Trigilio[14], K. Uckert[13], G. Umana[14], A. Valcheva[10], and A. Volvach[35]

(Affiliations can be found after the references)

Received 22 July 2009 / Accepted 3 September 2009

ABSTRACT

Context. BL Lacertae is the prototype of the blazar subclass named after it. Yet, it has occasionally shown a peculiar behaviour that has questioned a simple interpretation of its broad-band emission in terms of synchrotron plus synchrotron self-Compton (SSC) radiation.
Aims. In the 2007–2008 observing season we carried out a new multiwavelength campaign of the Whole Earth Blazar Telescope (WEBT) on BL Lacertae, involving three pointings by the XMM-Newton satellite in July and December 2007, and January 2008, to study its emission properties, particularly in the optical-X-ray energy range.
Methods. The source was monitored in the optical-to-radio bands by 37 telescopes. The brightness level was relatively low. Some episodes of very fast variability were detected in the optical bands. Flux changes had larger amplitude at the higher radio frequencies than at longer wavelengths.
Results. The X-ray spectra acquired by the EPIC instrument onboard XMM-Newton are well fitted by a power law with photon index $\Gamma \sim 2$ and photoelectric absorption exceeding the Galactic value. However, when taking into account the presence of a molecular cloud on the line of sight, the EPIC data are best fitted by a double power law, implying a concave X-ray spectrum. The spectral energy distributions (SEDs) built with simultaneous radio-to-X-ray data at the epochs of the XMM-Newton observations suggest that the peak of the synchrotron emission lies in the near-IR band, and show a prominent UV excess, besides a slight soft-X-ray excess. A comparison with the SEDs corresponding to previous observations with X-ray satellites shows that the X-ray spectrum is very variable, since it can change from extremely steep to extremely hard, and can be more or less curved in intermediate states. We ascribe the UV excess to thermal emission from the accretion disc, and the other broad-band spectral features to the presence of two synchrotron components, with their related SSC emission. We fit the thermal emission with a black body law and the non-thermal components by means of a helical jet model. The fit indicates a disc temperature $\gtrsim$20 000 K and a luminosity $\gtrsim 6 \times 10^{44}$ erg s^{-1}.

Key words. galaxies: active – galaxies: BL Lacertae objects: general – galaxies: BL Lacertae objects: individual: BL Lacertae – galaxies: jets

1. Introduction

BL Lacertae is the prototype of one of the two blazar subclasses, the BL Lac objects, the other subclass being represented by the flat-spectrum radio quasars (FSRQs). Common features of blazars are: i) extreme flux variability at all wavelengths, from radio to γ-ray frequencies, on a wide variety of time scales, from long-term (months, years) oscillations to intra-day variability (IDV); ii) high radio and optical polarization; iii) brightness temperatures exceeding the Compton limit; iv) superluminal motion of the radio components. The commonly accepted paradigm foresees that their non-thermal emission comes from a plasma jet closely aligned with the line of sight. The jet is generated by a supermassive black hole fed by infall of matter from an accretion disc. The broad-band spectral energy distribution (SED) of a blazar, given in the common $\log(\nu F_\nu)$ versus $\log \nu$ representation, shows two wide bumps. The low-energy bump, which extends from the radio to the optical-UV (for some BL Lacs up to X-ray) frequencies, is ascribed to synchrotron radiation by relativistic electrons in the jet. The high-energy bump, covering the X-ray to γ-ray energies, is likely due to inverse-Compton scattering of seed photons off the relativistic electrons. According to the synchrotron self Compton (SSC) model, the seed photons are the synchrotron photons themselves. In contrast, the external Compton (EC) scenario foresees that seed photons may enter the jet either directly from the accretion disc (e.g. Dermer et al. 1992), or reprocessed by the broad line region (e.g. Sikora et al. 1994) or hot corona surrounding the disc (e.g. Ghisellini & Tavecchio 2009). SSC models usually fairly explain the SEDs of the low-luminosity blazars, i.e. the BL Lac objects, while

⋆ The radio-to-optical data presented in this paper are stored in the WEBT archive (http://www.oato.inaf.it/blazars/webt/); for questions regarding their availability, please contact the WEBT President Massimo Villata.

EC models are needed to fit the SEDs of the FSRQs. However, recent multiwavelength studies on a number of blazars, which included observations by the γ-ray satellite AGILE, have shown that multiple SSC and/or EC components are necessary to explain the observed high-energy fluxes (see e.g. Chen et al. 2008; Pucella et al. 2008; Vercellone et al. 2009; D'Ammando et al. 2009; Donnarumma et al. 2009a).

In addition to these two non-thermal jet components, the SEDs of quasar-type blazars sometimes show a "blue bump" in between, which is thought to be the signature of the thermal radiation emitted from the accretion disc. Indeed, the spectra of these objects usually display prominent broad emission lines, which are most likely produced by photoionization of the broad line region due to the disc radiation.

On the contrary, BL Lacs are by definition almost featureless objects (equivalent width less than 5 Å in their rest frame, Stickel et al. 1991). It was hence a surprise when Vermeulen et al. (1995), and soon after Corbett et al. (1996), discovered a broad Hα (and Hβ) emission line in the spectrum of BL Lacertae, whose luminosity ($\sim 10^{41}$ erg s^{-1}) and full-width half-maximum ($\sim$4000 km s^{-1}) are comparable to those of type I Seyfert galaxies such as NGC 4151. Subsequent spectroscopic monitoring of this source by Corbett et al. (2000) showed that the Hα equivalent width is approximately inversely proportional to the optical continuum flux. This suggested that the broad line region is photoionized by a radiation source that is not the same producing the optical continuum. The photoionising radiation would most likely come from the accretion disc.

Another important issue comes from the results obtained by Ravasio et al. (2003). They analyzed the X-ray data acquired by BeppoSAX from October 31 to November 2, 2000, during an extensive multiwavelength campaign. When constructing the source SED with contemporaneous data, it was evident that the steep X-ray spectrum was offset with respect to the extrapolation of the optical one. One possible explanation was the presence of an extra component in addition to the synchrotron and inverse-Compton ones.

Finally, according to Madejski et al. (1999) and Böttcher & Bloom (2000), the explanation of the γ-ray flux detected by the EGRET instrument on board the CGRO satellite during the 1997 optical outburst (see Bloom et al. 1997) requires an EC emission component in addition to the SSC one.

Taken together, these results suggest that in BL Lacertae the interpretation of the broad-band emission may require a more complex scenario than that usually envisaged for the BL Lac objects, involving just one synchrotron plus its SSC emission.

In the last decade, BL Lacertae has been extensively studied by the Whole Earth Blazar Telescope (WEBT) collaboration[1], which has carried out several multiwavelength campaigns on this object (Villata et al. 2002; Ravasio et al. 2002; Böttcher et al. 2003; Villata et al. 2004a,b; Bach et al. 2006; Papadakis et al. 2007; Villata et al. 2009), collecting tens of thousands of optical-to-radio data. These studies were focused on its multiwavelength flux variability, colour behaviour, correlations among flux variations in different bands, possible periodicity of the radio outbursts. The main aim of the new WEBT campaign organized in the 2007–2008 observing season was instead to address the problem of disentangling the possible multiple contributions to the BL Lac flux from the radio band to γ-rays. For this sake, the optical-to-radio monitoring by the WEBT was complemented by three pointings by the XMM-Newton satellite. Moreover, we also obtained optical spectra with the 3.6 m Telescopio Nazionale Galileo (TNG) to investigate the properties of the Hα broad emission line, and possibly infer information on the accretion disc. The results of the spectroscopic study will be reported elsewhere.

[1] http://www.oato.inaf.it/blazars/webt/

Table 1. List of optical, near-IR, and radio observatories contributing data to this work.

Observatory	Tel. size	Bands
Optical		
Abastumani, Georgia	70 cm	*R*
ARIES, India	104 cm	*BVRI*
Armenzano, Italy	35 cm	*BRI*
Armenzano, Italy	40 cm	*BVRI*
Belogradchik, Bulgaria	60 cm	*VRI*
BOOTES-2, Spain	30 cm	*R*
Bordeaux, France	20 cm	*V*
Calar Alto, Spain[a]	220 cm	*R*
Crimean, Ukraine	70 cm	*BVRI*
Kitt Peak (MDM), USA	130 cm	*UBVRI*
L'Ampolla, Spain	36 cm	*R*
Lulin (SLT), Taiwan	40 cm	*R*
Michael Adrian, Germany	120 cm	*R*
Mt. Lemmon, USA	100 cm	*BVRI*
New Mexico Skies, USA	30 cm	*VRI*
Roque (KVA), Spain	35 cm	*R*
Roque (NOT), Spain	256 cm	*UBVRI*
Rozhen, Bulgaria	50/70 cm	*BVR*
Rozhen, Bulgaria	200 cm	*BVRI*
Sabadell, Spain	50 cm	*R*
San Pedro Martir, Mexico	84 cm	*R*
Sobaeksan, South Korea	61 cm	*VRI*
Sommers-Bausch, USA	61 cm	*VRI*
St. Petersburg, Russia	40 cm	*BVRI*
Talmassons, Italy	35 cm	*BVR*
Teide (BRT), Spain	35 cm	*BVR*
Torino, Italy	105 cm	*BVRI*
Tuorla, Finland	103 cm	*R*
Univ. of Victoria, Canada	50 cm	*R*
Valle d'Aosta, Italy	81 cm	*BVRI*
Near-infrared		
Campo Imperatore, Italy	110 cm	*JHK*
Roque (NOT), Spain	256 cm	*HK*
Radio		
Crimean (RT-22), Ukraine	22 m	37 GHz
Mauna Kea (SMA), USA	8×6 m[b]	230, 345 GHz
Medicina, Italy	32 m	5, 8, 22 GHz
Metsähovi, Finland	14 m	37 GHz
Noto, Italy	32 m	43 GHz
UMRAO, USA	26 m	4.8, 8.0, 14.5 GHz

[a] Calar Alto data were acquired as part of the MAPCAT (Monitoring AGN with Polarimetry at the Calar Alto Telescopes) project.
[b] Radio interferometer including 8 dishes of 6 m size.

This paper is organised as follows. In Sect. 2 we present the WEBT optical-to-radio light curves. The analysis of the XMM-Newton data is reported in Sect. 3. In Sect. 4 we show the SEDs corresponding to the XMM-Newton epochs, and compare them with those related to previous observations by X-ray satellites. The interpretation of the XMM-Newton SEDs is discussed in Sect. 5. Finally, Sect. 6 contains a summary and discussion of the main results.

2. Multifrequency observations by the WEBT

The new WEBT campaign on BL Lacertae took place in the 2007–2008 observing season. The participating observatories are listed in Table 1. Optical and near-IR data were collected as instrumental magnitudes of the source and reference stars in

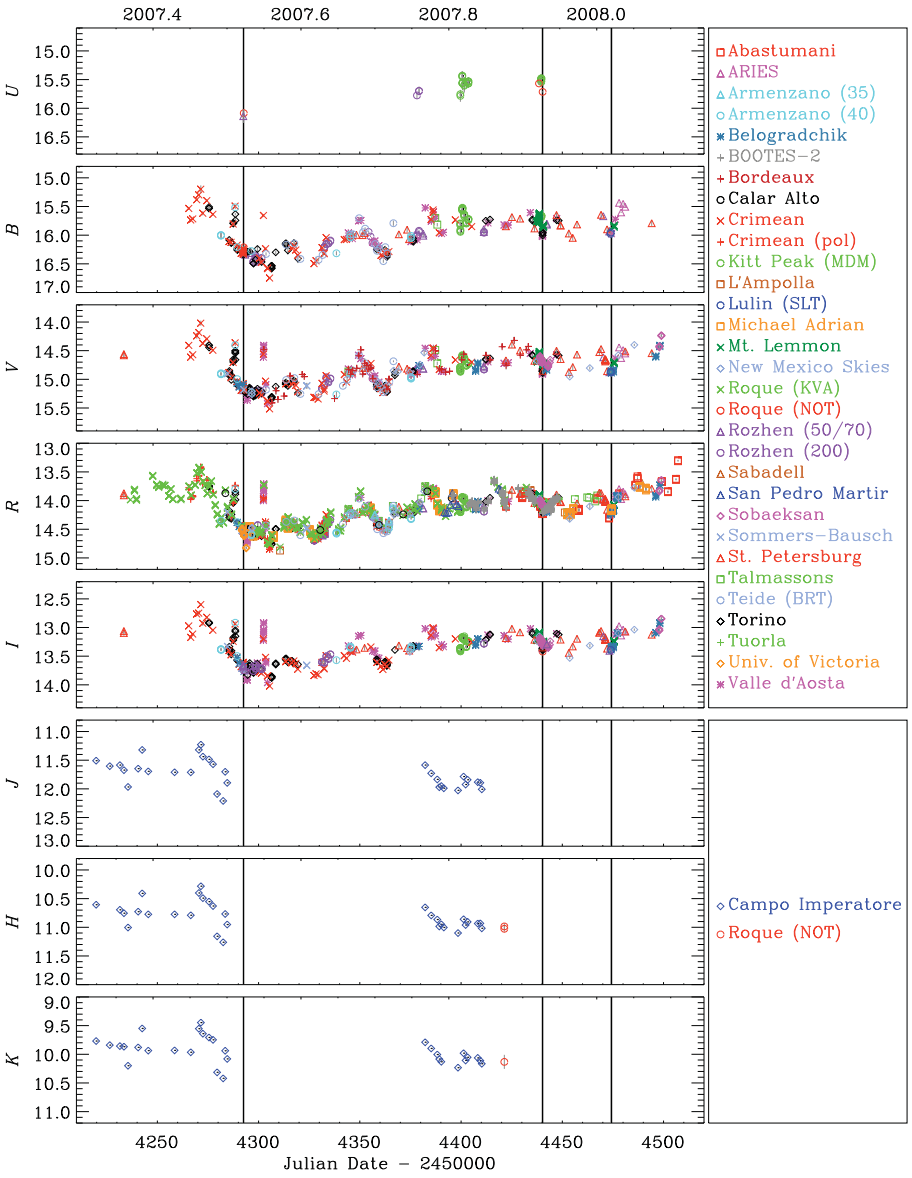

Fig. 1. Optical *UBVRI* and near-IR *JHK* light curves of BL Lacertae in the 2007–2008 observing season. Vertical lines indicate the three XMM-Newton pointings of July 10–11 and December 5, 2007, and January 8, 2008.

the same field to apply the same calibration (Bertaud et al. 1969; Fiorucci & Tosti 1996). The light curves obtained by assembling all datasets were carefully inspected to correct for systematic offsets and to reduce data scatter by binning noisy data taken by the same observer within a few minutes. The results are shown in Fig. 1, where the vertical lines indicate the epochs of the three XMM-Newton pointings. We can see a noticeable flux variability, which progressively increases its amplitude going from the *I* to the *B* band. By considering only the period of common monitoring (before JD = 2 454 500), the maximum variability amplitude (maximum − minimum) is 1.42, 1.46, 1.50, and 1.55 mag in the *I*, *R*, *V*, and *B* bands, respectively. The near-IR time coverage is inferior to the optical one, but the near-IR data are important to add information to the SED (see Sect. 5).

The majority of the variability episodes have a time scale of a few days, but we can also recognise a long-term increasing trend starting from JD ∼ 2 454 300, as well as a few very fast events. One of these involved a brightening of about 0.9 mag in 24 h, from $R \sim 14.6$ on JD = 2 454 301.5 to $R \sim 13.7$ the night after, when observations at the Valle d'Aosta Observatory showed a source brightening of ∼0.3 mag in less than 3 h. This behaviour was confirmed by observations in the *V* and *I* bands, ruling out that this rapid flux increase was an artifact. Similar fast variations are not uncommon in BL Lacertae. When analysing the 13248 *R*-band data acquired by the WEBT (Villata et al. 2002, 2004b,a, 2009, and this paper) during 1500 nights over more than 15 years, though with inhomogeneous sampling, we can distinguish between two kinds of rapid flux variability:

- fast and noticeable intraday variations: we consider variations ≥0.25 mag with rate ≥0.1 mag/h. These were found in 25 nights out of 677 nights where the observing time coverage is ≥2.5 h, with the maximum amplitude episode involving a change $\Delta R = 0.52$ in about 3.9 h;
- large interday variations: we consider variations ≥0.75 mag in ≤36 h. These were observed 6 times, and the above mentioned episode (about 0.9 mag in 24 h) is the most extreme one.

Radio data were collected as already calibrated flux densities. The radio light curves are shown in Fig. 2, where the first panel displays the *R*-band light curve for comparison. We also included data from the VLA/VLBA Polarization Calibration Database (PCD)[2]. As expected, the radio flux variations, which

[2] http://www.vla.nrao.edu/astro/calib/polar/

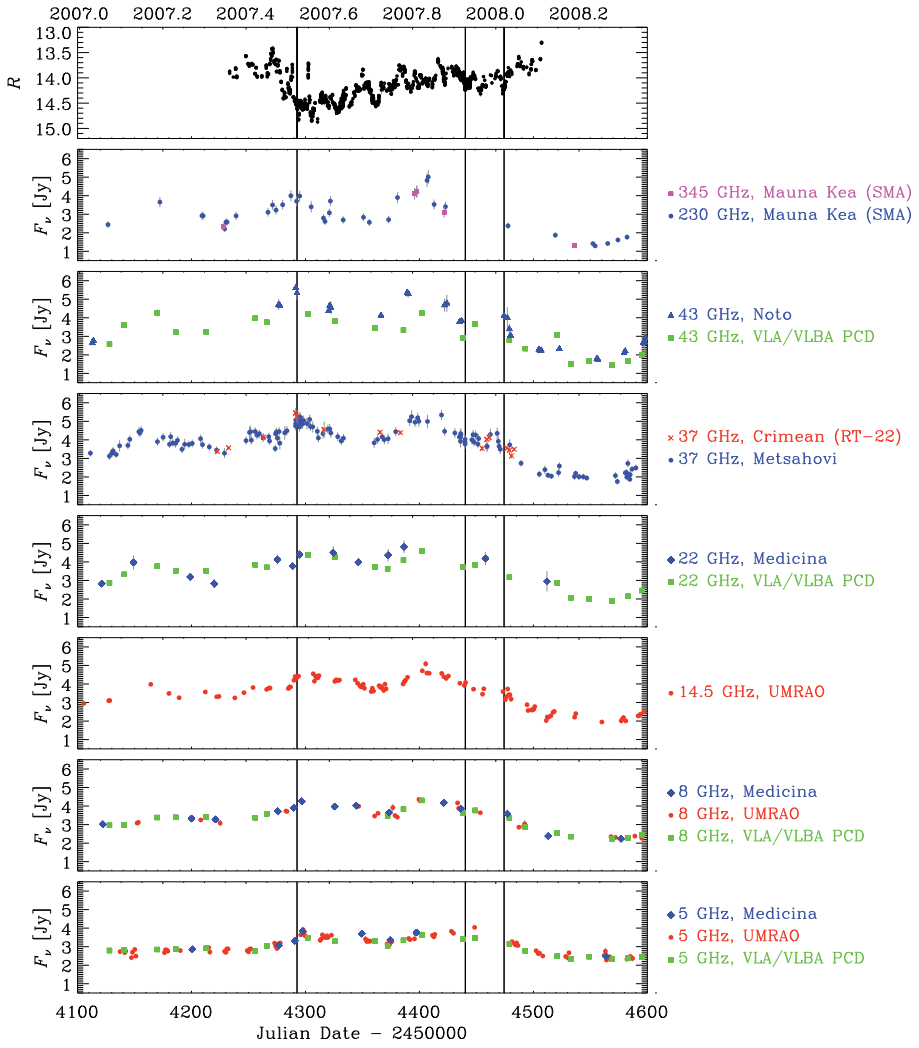

Fig. 2. *R*-band light curve of BL Lacertae in 2007–2008 (*top panel*) compared to the behaviour of the radio flux densities (Jy) at different frequencies. Vertical lines indicate the three XMM-Newton pointings of July 10–11 and December 5, 2007, and January 8, 2008.

are more evident at the shortest wavelengths, are smoother than the optical variations[3], and the radio time scales are longer. Moreover, the long-term increasing trend characterising the optical light curve is not recognisable in the radio band. According to Villata et al. (2009), the optical outbursts of BL Lacertae are usually followed by high-frequency radio events, with time delays of at least 100 days, which can grow to 200 or even 300 days, depending on the relative orientation of the corresponding emitting regions in the jet. Hence, the high optical level observed at the beginning of our observing period, in May–June 2007, might be related to the bright radio state that is visible at the higher radio frequencies around JD = 2 454 400[4].

3. Observations by XMM-Newton

The X-ray Multi-Mirror Mission (XMM) – Newton satellite observed the source on July 10–11 and December 5, 2007, and then on January 8, 2008 (PI: Raiteri).

3.1. EPIC data

The European Photon Imaging Camera (EPIC) onboard XMM-Newton includes three detectors: MOS1, MOS2 (Turner et al. 2001), and pn (Strüder et al. 2001). Since a bright state of the source could not be excluded, we chose a medium filter to avoid possible contamination by lower-energy photons; moreover, we selected a small-window configuration to minimize possible photon pile-up.

Data were reduced with the Science Analysis System (SAS) software, version 8.0.1, following the same standard procedure adopted in Raiteri et al. (2007b). A temporal filtering was applied to discard high-background periods. Source spectra were extracted from circular regions of ∼40 arcsec radius. The MOS background was estimated on external CCDs, while for the pn we selected the largest source-free circle that could be arranged on the same CCD.

The source spectra were binned with the `grppha` task of the FTOOL package, to have a minimum of 25 counts in each bin. The binned spectra were then analysed in the 0.35–12 keV energy range with the `Xspec` task of the XANADU package. We fitted the MOS1, MOS2, and pn spectra of each epoch together to increase the statistics.

We first considered a single power law model with free absorption, where the absorption is modelled according to the Wilms et al. (2000) prescriptions. The results of this spectral fitting for the three epochs are displayed in the top panels of

[3] This is even more evident when comparing radio flux densities to optical flux densities instead of magnitudes.

[4] Indeed, the PCD shows no further radio event until May 2009, the 43 GHz flux density remaining below 3 Jy.

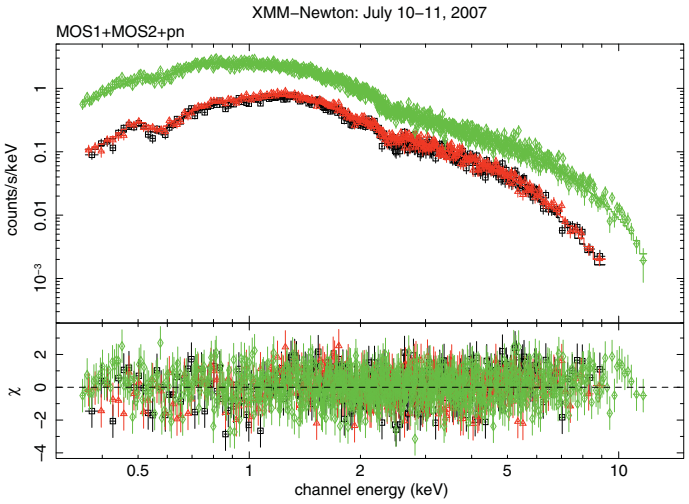

Fig. 3. EPIC spectrum of BL Lacertae on July 10–11, 2007; black squares, red triangles, and green diamonds represent MOS1, MOS2, and pn data, respectively. The bottom panel shows the deviations of the observed data from the folded model (a power law with free absorption) in unit of standard deviations.

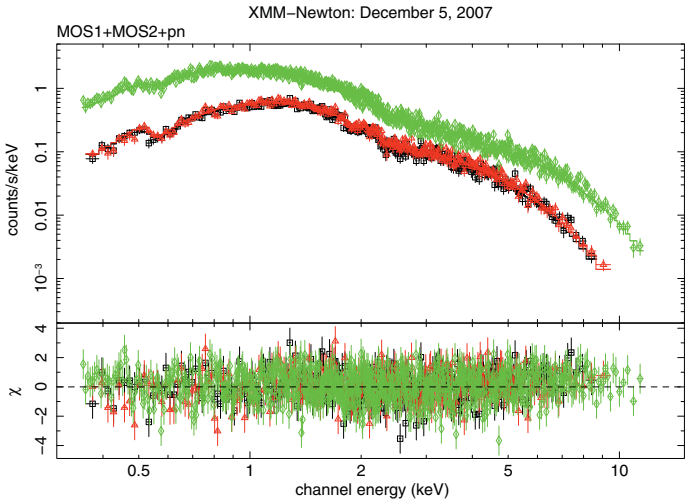

Fig. 4. EPIC spectrum of BL Lacertae on December 5, 2007; black squares, red triangles, and green diamonds represent MOS1, MOS2, and pn data, respectively. *The bottom panel* shows the deviations of the observed data from the folded model (a power law with free absorption) in unit of standard deviations.

Figs. 3–5. The corresponding model parameters are reported in Table 2, where Col. 2 gives the hydrogen column density, Col. 3 the photon spectral index Γ, Col. 4 the unabsorbed flux density at 1 keV, Col. 5 the 2–10 keV observed flux, and Col. 6 the value of χ^2/ν (being ν the number of degrees of freedom). The χ^2/ν values in Table 2 indicate that the model is acceptable. This is also confirmed by the deviations of the observed data from the folded model, which are plotted in the bottom panels of Figs. 3–5. The best-fit value of the hydrogen column density varies between 2.8 and 3.1×10^{21} cm^{-2}, within the range of values found in previous analyses (see Sect. 5).

Actually, the Galactic atomic hydrogen column density toward BL Lacertae is $N_{\rm H} = 1.71 \times 10^{21}$ cm^{-2} (from the Leiden/Argentine/Bonn (LAB) Survey, see Kalberla et al. 2005). However, observations of local interstellar CO toward BL Lac have revealed a molecular cloud (Bania et al. 1991; Lucas & Liszt 1993; Liszt & Lucas 1998). According to Liszt & Lucas (1998), its ^{13}CO column density is $(8.48 \pm 0.78) \times 10^{14}$ cm^{-2}. Assuming that the molecular hydrogen column density $N_{\rm H_2}$ is typically 10^6 times the ^{13}CO one (Lucas & Liszt 1993), we derive an hydrogen column density of $\sim 1.7\times10^{21}$ cm^{-2} due to the molecular cloud. This value depends on the uncertain ratio between CO and H_2[5], but taking it at face value, the total hydrogen column density toward BL Lac becomes $N_{\rm H} = 3.4 \times 10^{21}$ cm^{-2}. This value is not very far from the $N_{\rm H}$ values we found when fitting the EPIC spectra with a power law model with free absorption, but as we will see in Sect. 5 this modest difference can make a difference in the interpretation of the source X-ray spectrum.

We thus fixed $N_{\rm H} = 3.4 \times 10^{21}$ cm^{-2} and re-fitted a single power law model to the EPIC spectra. As expected, the goodness of the new fits is inferior to the previous case, and a slight excess of counts in the soft X-ray domain appears. This could be the signature of a curvature in the source spectra. Indeed, when we adopt a double power law model, the fit improves significantly, as is shown in Table 3, and this suggests that the spectrum is concave.

[5] From the recent paper by Liszt (2007) we can infer that $N_{\rm H_2}/N_{\rm ^{13}CO}$ is most likely in the range $\sim$1–2 $\times 10^6$.

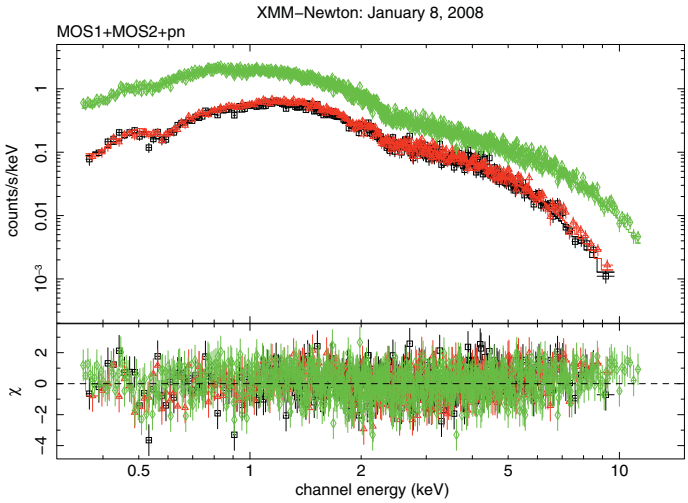

Fig. 5. EPIC spectrum of BL Lacertae on January 8, 2008; black squares, red triangles, and green diamonds represent MOS1, MOS2, and pn data, respectively. *The bottom panel* shows the deviations of the observed data from the folded model (a power law with free absorption) in unit of standard deviations.

The χ^2/ν values in Table 3 are a bit smaller than those in Table 2. To better compare the two model fits, we calculated the F-test probability, which is 1.25×10^{-2} for July 10–11, 2.70×10^{-5} for December 5, and 3.11×10^{-10} for January 8, 2008. These results suggest that the double power law model with fixed absorption may be more appropriate to describe the EPIC spectra than the single power law model with free absorption.

3.2. OM data

XMM-Newton also carries an optical–UV 30 cm telescope, the Optical Monitor (OM, Mason et al. 2001). The BL Lac observations were performed with all its filters: V, B, U, UV$W1$, UV$M2$, and UV$W2$, with long exposures (see Table 4). The OM data were reduced with the SAS software, version 8.0.1. The tasks `omsource` and `omphotom` were used to perform aperture photometry on the images produced by `omichain`. The resulting

Table 2. Results of fitting the EPIC data with a single power law with free absorption.

Date	N_H [10^{21} cm^{-2}]	Γ	$F_{1\,keV}$ [μJy]	$F_{2-10\,keV}$ [erg cm^{-2} s^{-1}]	χ^2/ν (ν)
(1)	(2)	(3)	(4)	(5)	(6)
July 10–11, 2007	3.05 ± 0.06	2.01 ± 0.02	2.58 ± 0.04	9.64×10^{-12}	0.942 (1347)
December 5, 2007	2.92 ± 0.06	1.99 ± 0.02	1.96 ± 0.04	7.65×10^{-12}	1.026 (1250)
January 8, 2008	2.86 ± 0.06	1.91 ± 0.01	1.95 ± 0.03	8.51×10^{-12}	0.905 (1381)

Table 3. Results of fitting the EPIC data with a double power law with fixed total atomic and molecular column density. The two power laws have photon indices Γ^1 and Γ^2 and unabsorbed flux densities at 1 keV $F^1_{1\,keV}$ and $F^2_{1\,keV}$, respectively.

Date	N_H [10^{21} cm^{-2}]	Γ^1	Γ^2	$F^1_{1\,keV}$ [μJy]	$F^2_{1\,keV}$ [μJy]	$F_{2-10\,keV}$ [erg cm^{-2} s^{-1}]	χ^2/ν (ν)
(1)	(2)	(3)	(4)	(5)	(6)		
July 10–11, 2007	3.40	2.48	1.72	1.63	1.14	9.76×10^{-12}	0.939 (1346)
December 5, 2007	3.40	2.58	1.67	1.26	0.90	7.77×10^{-12}	1.013 (1249)
January 8, 2008	3.40	2.48	1.51	1.45	0.73	8.69×10^{-12}	0.880 (1380)

Table 4. Optical-UV magnitudes of BL Lacertae derived from the data analysis of the OM frames.

Date	V	B	U	UV$W1$	UV$M2$	UV$W2$
			Exposure times (s)			
July 10–11, 2007	1498	1499	1499	2601	3098	6257[a]
December 5, 2007	2100	2099	2099	3500	3780	4000
January 8, 2008	1700	1700	1698	2799	3300	7359[b]
			Magnitudes			
July 10–11, 2007	15.33 ± 0.10	16.27 ± 0.10	15.87 ± 0.10	15.99 ± 0.10	16.90 ± 0.10	17.13 ± 0.14
December 5, 2007	14.96 ± 0.10	15.91 ± 0.10	15.52 ± 0.10	15.62 ± 0.10	16.45 ± 0.10	16.98 ± 0.11
January 8, 2008	14.97 ± 0.10	15.90 ± 0.10	15.53 ± 0.10	15.65 ± 0.10	16.47 ± 0.10	16.88 ± 0.14

[a] Two exposures of 3579 and 2678 s.
[b] Two exposures of 3779 and 3580 s.

magnitudes are reported in Table 4. The uncertainties take into account the measure, systematic and calibration errors. In the optical filters, where a comparison with ground-based measurements is possible, the OM magnitudes of the reference stars (B C H K) are within 0.1 mag with respect to the values we adopted for the calibration of the ground data, but they are stable (within 2-3 hundredths of mag) in the three XMM-Newton epochs.

4. Spectral energy distributions

The upper panel of Fig. 6 displays the broad-band SEDs corresponding to the XMM-Newton observations analysed in the previous section. We show both the single power law with free absorption and the double power law with atomic plus molecular Galactic absorption fits to the X-ray spectra. Optical and UV magnitudes were corrected for Galactic extinction by adopting $A_B = 1.42$ from Schlegel et al. (1998) and calculating the values at the other wavelengths according to Cardelli et al. (1989). De-reddened ground-based optical magnitudes were then converted into fluxes using the zero-mag fluxes given by Bessell et al. (1998); as for the optical and UV magnitudes from the OM, this conversion was performed using Vega as calibrator.

The optical flux densities were further corrected for the contribution of the host galaxy. Assuming an R-band magnitude of 15.55 after Scarpa et al. (2000) and the average colour indices for elliptical galaxies by Mannucci et al. (2001), the host galaxy flux densities are: 10.62, 13.97, 11.83, 5.90, 4.23, 2.89, 1.30, and 0.36 mJy in K, H, J, I, R, V, B, and U bands, respectively. Using a De Vaucouleurs' profile, we estimated that the contribution to the observed fluxes is ~60% of the whole galaxy flux (see also Villata et al. 2002). In the UV, the results of spectral evolution modelling of stellar populations by Bruzual & Charlot (2003) allowed us to estimate that the contribution from the host galaxy may be neglected. Indeed, if we consider ages between 4 and 13 Gyr, the galaxy flux density at ~2000 Å is about 50 to 100 times lower than in the R band, i.e. the contribution of the galaxy would affect the measured flux in the UV$W2$ band by ~1–2%.

Optical data are strictly simultaneous to the XMM-Newton observations. Most radio data are simultaneous too, but in some cases we considered data taken a few days earlier or later. We note the excellent agreement between the V, B, and U data taken with ground-based telescopes and the corresponding data acquired by the OM. The main features of the SEDs in the figure are:

- the peak of the synchrotron emission lies in the infrared (see below);
- since a higher radio brightness corresponds to a lower optical state and viceversa, the synchrotron peak likely shifts toward higher frequencies as the optical flux increases;
- there is a strong UV excess, since the UV points do not lie on the extrapolation of the optical trend;
- the X-ray spectrum has either a null slope, or, more likely, it is concave, producing a mild soft-X-ray excess, and suggesting that in this energy region two emission components are intersecting each other;

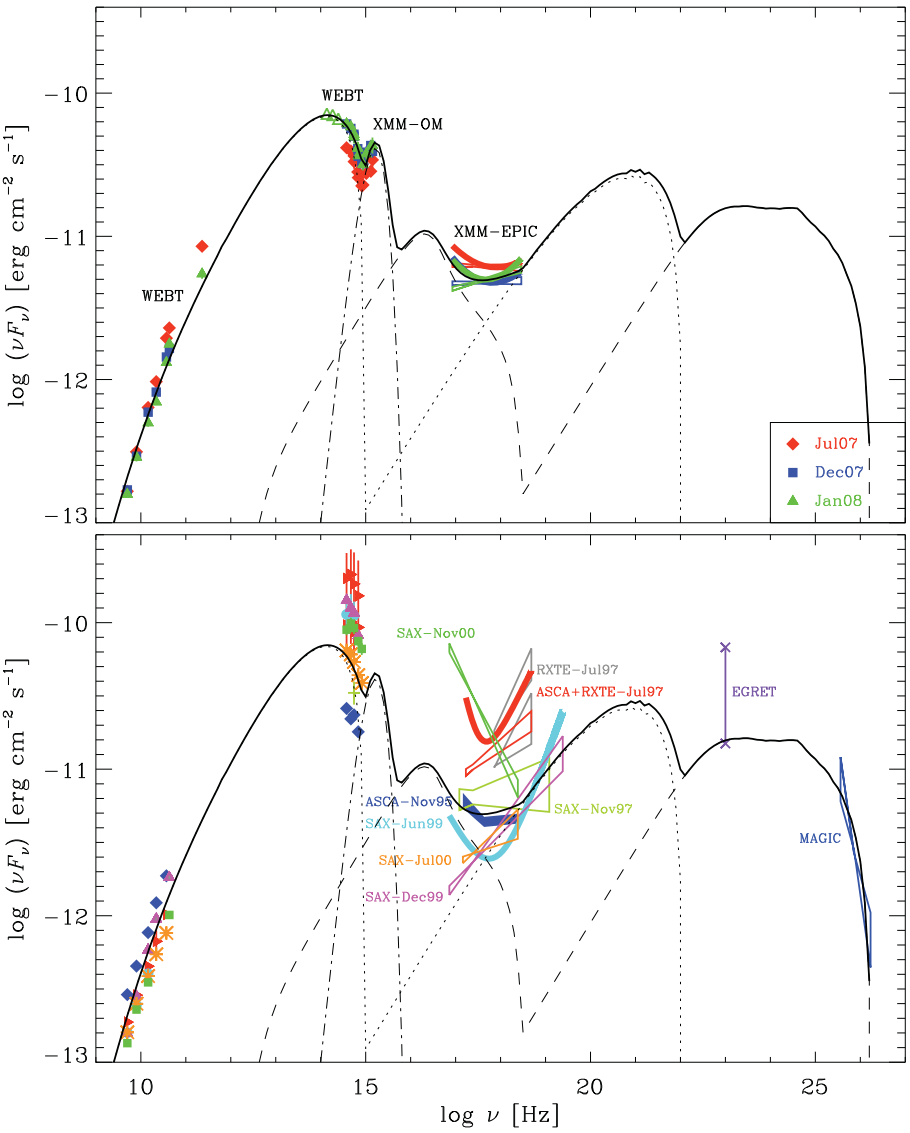

Fig. 6. *Top panel*: broad-band SEDs of BL Lacertae during the three XMM-Newton observations of July and December 2007, and January 2008. Both the single power law with free absorption and the double power law with atomic plus molecular Galactic absorption fits to the X-ray spectra are shown. Bottom panel: SEDs corresponding to epochs of previous X-ray satellites observations: ASCA in November 1995 (blue, Sambruna et al. 1999); RXTE in July 1997 (grey, Madejski et al. 1999); ASCA+RXTE in July 1997 (red, Tanihata et al. 2000); BeppoSAX in November 1997 (light green, Padovani et al. 2001); BeppoSAX in June (cyan) and December (pink) 1999 (Ravasio et al. 2002); BeppoSAX in July (orange) and November (green) 2000 (Ravasio et al. 2003). All radio and optical data are from the WEBT archive; the vertical bars on the red optical points indicate the range of variation of the optical fluxes during the ASCA+RXTE observations in July 1997. The range of flux densities detected by EGRET (Hartman et al. 1999), as well as the TeV spectrum observed by MAGIC (Albert et al. 2007) are also reported. The solid lines represent the sum of different emission contributions: a low-energy synchrotron+SSC component (dotted lines), a high-energy synchrotron+SSC component (dashed lines), and a thermal component from an accretion disc (dotted-dashed line) with a temperature of ∼20 000 K and a luminosity of 6×10^{44} erg s^{-1} (see the text for details).

– the optical steepness makes an interpretation of the soft X-ray excess in terms of the tail of the synchrotron component unlikely.

Details of the near-IR-to-UV SED of BL Lacertae are shown in Fig. 7. Here we can better appreciate the features of the three SEDs obtained at the epochs of the XMM-Newton observations. Moreover, we also report the total uncertainty affecting the UV points, when considering both the error on the data and the sample variance about the Galactic mean extinction curve, following Fitzpatrick & Massa (2007). As stressed by these authors, the sample variance must be taken into account if we want to estimate a realistic error on the de-reddened SEDs. In our case, the lower limit to the UV fluxes that we obtain when considering the total uncertainty indicates that the UV excess might be smaller than shown by the points, but it exists, since the UV points cannot be shifted down enough to lie on the extrapolation of the optical, (quasi-power law) synchrotron trend.

Figure 7 also shows two other SEDs built with simultaneous near-IR and optical data. The near-IR data have been de-reddened and cleaned from the host galaxy contribution similarly to the optical data. In the optical frequency range, these two SEDs confirm the trend shown by the SEDs obtained at the three XMM-Newton epochs, but they add important information in the near-IR. Indeed, they suggest that the peak of the synchrotron component lies in this energy range, or close by.

4.1. Comparison with previous observations

The bottom panel of Fig. 6 shows SEDs corresponding to epochs when various X-ray satellites observed BL Lacertae. The X-ray spectral fits were taken from the literature, while we searched the massive WEBT archive on this source, containing all radio-to-optical data from the previous WEBT campaigns (Villata et al. 2002, 2004b,a, 2009) as well as data from the literature, for contemporaneous low-energy data.

When considering the behaviour of the X-ray spectrum, it is not easy to compare our results to those found by other authors when analysing different X-ray data. The reason is that the shape of the X-ray spectrum strongly depends on the choice of the absorption, i.e. on the $N_{\rm H}$ value adopted to perform the spectral fits. Models where the hydrogen column density is left to vary freely yield a variety of $N_{\rm H}$ values (mostly in the range $1.4–3.5 \times 10^{21}$ cm^{-2}). These are usually lower than the estimated Galactic total absorption, due to both atomic and molecular hydrogen. The point is that the amount of absorption due to molecular hydrogen is not directly measurable, which introduces a

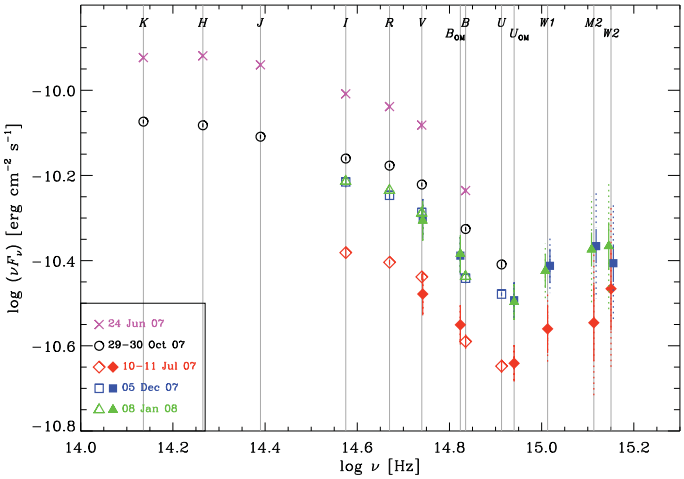

Fig. 7. Details of the near-IR-to-UV SED of BL Lacertae. In the three optical-UV SEDs obtained at the epochs of the XMM-Newton observations of July 10–11, 2007, December 5, 2007, and January 8, 2008, empty symbols represent ground-based observations, while filled symbols refer to data taken by the OM. The dotted error bars on the UV points indicate the total uncertainty, resulting from considering both the data error (solid error bars) and the sample variance about the mean extinction curve, according to Fitzpatrick & Massa (2007). To clearly show the uncertainties holding on the UV data, the UV points corresponding to the December 2007 and January 2008 epochs have been slightly shifted in frequency around the effective value. For comparison, we show other two SEDs obtained with data acquired by ground-based telescopes on June 24 and October 29–30, 2007, when near-IR data contemporaneous to the optical data were available. The near-IR portion of the SEDs shows that the peak of the synchrotron emission probably lies in this energy range, or close by.

further uncertainty (see Sect. 4 and discussion in Madejski et al. 1999). In previous analyses of X-ray data, different authors have followed different prescriptions. An $N_{\rm H}$ value close to the one we assumed was also investigated by Sambruna et al. (1999) when analysing ASCA observations in November 1995, and by Padovani et al. (2001) for observations performed by BeppoSAX in November 1997 (and by ROSAT in 1992). In both epochs the X-ray flux was relatively low and Sambruna et al. (1999) found that the best fit model was a broken power law, leading to a concave X-ray spectrum.

Observations by RXTE and ASCA during the big outburst of July 1997 were analysed by Madejski et al. (1999) and Tanihata et al. (2000). The latter authors combined the data of both satellites and distinguished between a low and a high state. They used a high $N_{\rm H} = 4.6 \times 10^{21}$ cm^{-2}, and found that the high state was best fitted by a double power law model with an extremely steep spectral index below ~1 keV. In contrast to this high value, Ravasio et al. (2002) and Ravasio et al. (2003) preferred an $N_{\rm H} = 2.5 \times 10^{21}$ cm^{-2} to analyse BeppoSAX observations in 1999–2000. Nevertheless, the June 1999 data were best fitted by a double power law model, implying a noticeable upward curvature in the soft X-ray domain. In contrast, in November 2000 the whole X-ray spectrum was steep, and its extrapolation to optical frequencies was not intersecting the simultaneous optical spectrum. This offset was questioned by Böttcher et al. (2003), who warned about the possibility that it was produced by flux averaging in a period of noticeable variability, as shown by the intensive monitoring performed by the WEBT observers during the 2000–2001 observing season (Villata et al. 2002). However, to remove the offset we should have missed one or more big flares, such as to increase the mean optical level by more than 1 mag, which seems unlikely. Hence, if in previous works a soft spectral component at low X-ray energies had always been interpreted as the tail of the synchrotron emission, this was no longer a plausible explanation for the November 2000 SED, as it is not a plausible explanation for the XMM-Newton SEDs presented above. A number of hypotheses were suggested by Ravasio et al. (2003) to justify the optical-X-ray offset: a sudden increase of the dust-to-gas ratio toward BL Lacertae; the detection of a bulk Compton emission; the interplay of two different synchrotron components; Klein-Nishina effect on the synchrotron spectrum.

5. The helical jet model

The availability of broad-band SEDs built with simultaneous data, including UV information, at the epochs of the XMM-Newton observations of 2007–2008 is a formidable tool to investigate the nature of BL Lac multiwavelength emission. The picture that we described in the previous section suggests that the SED behaviour cannot be explained in terms of one synchrotron plus its SSC emission components.

Thermal emission from an accretion disc could account for the UV excess. Indeed, the optical spectrum of this source occasionally shows broad emission lines that are produced in the broad line region, which is most likely photoionised by the radiation coming from the accretion disc (Vermeulen et al. 1995; Corbett et al. 1996, 2000). Moreover, a big blue bump produced in the SED by thermal emission from an accretion disc has already been found for other quasar-type blazars, like 3C 273 (Smith et al. 1993; von Montigny et al. 1997; Grandi & Palumbo 2004; Türler et al. 2006), 3C 279 (Pian et al. 1999), 3C 345 (Bregman et al. 1986), and 3C 454.3 (Raiteri et al. 2007b, 2008).

However, a thermal emission component would hardly be able to explain the extremely variable X-ray spectrum shown in the bottom panel of Fig. 6. Indeed, at 0.3 keV BeppoSAX observed a flux variation of a factor ~50 in about 1 year. We notice that the behaviour of BL Lacertae in the UV-X-ray energy range is similar to that found by Raiteri et al. (2005, 2006b,a) when analysing the SEDs of another BL Lac object, AO 0235+164, which also occasionally shows broad emission lines (see e.g. Raiteri et al. 2007a, and references therein). In that case, the alternative hypothesis of a second, higher-frequency synchrotron component, likely coming from an inner region of the jet, was left open.

We investigated this problem by means of the helical jet model by Villata & Raiteri (1999, see also Raiteri et al. 1999; Raiteri & Villata 2003; and Ostorero et al. 2004). We tried to reproduce the "XMM-Newton" broad-band SEDs of December 2007 and January 2008, which are very similar. To better trace the SED shape, we also added synthetic near-IR data, derived by shifting the October 2007 SED of Fig. 7 to match the above "XMM-Newton" SEDs. This implied a shift of $\log(\nu F_\nu) = -0.07$.

The helical jet model presented in Villata & Raiteri (1999) foresees that orbital motion in a binary black hole system, coupled with the interaction of the plasma jet with the surrounding medium, twists the emitting jet in a rotating helical structure. We here recall the main features of the model. The axis of the helical-shaped jet is assumed to lie along the z-axis of a 3-D reference frame. The pitch angle is ζ and ψ is the angle defined by the helix axis with the line of sight. The non-dimensional length of the helical path can be expressed in terms of the z coordinate along the helix axis:

$$l(z) = \frac{z}{\cos\zeta}, \quad 0 \le z \le 1, \tag{1}$$

which corresponds to an azimuthal angle $\varphi(z) = az$, where the angle a is a constant. The jet viewing angle varies along the helical path as

$$\cos\theta(z) = \cos\psi\cos\zeta + \sin\psi\sin\zeta\cos(\phi - az), \quad (2)$$

where ϕ is the azimuthal difference between the line of sight and the initial direction of the helical path.

The jet is inhomogeneous: it emits radiation at progressively increasing wavelengths by proceeding from its apex outwards. Each slice of the jet can radiate, in the plasma rest reference frame, synchrotron photons from a minimum frequency $\nu'_{\rm s,min}$ to a maximum one $\nu'_{\rm s,max}$. Both these frequency limits decrease for increasing distance from the jet apex following a power law:

$$\nu'_{{\rm s},i}(l) = \nu'_{\rm s}(0)\left(1 + \frac{l}{l_i}\right)^{-c_i}, \quad c_i > 0, \quad (3)$$

where l_i are length scales, and $i = \min, \max$. The high-energy emission producing the second bump in the blazars SED is assumed to be the result of inverse Compton scattering of the synchrotron photons by the same relativistic electrons emitting them (SSC model). Consequently, each portion of the jet emitting synchrotron radiation between $\nu'_{\rm s,min}(l)$ and $\nu'_{\rm s,max}(l)$ will also produce inverse Compton radiation between $\nu'_{\rm c,min}(l)$ and $\nu'_{\rm c,max}(l)$, with $\nu'_{{\rm c},i}(l) = \frac{4}{3}\gamma_i^2(l)\nu'_{{\rm s},i}(l)$. The electron Lorentz factor ranges from $\gamma_{\rm min} = 1$ to $\gamma_{\rm max}(l)$, which has a similar power law dependence as in Eq. (3), with power c_γ and length scale l_γ. As photon energies increase, the classical Thomson scattering cross section is replaced by the Klein-Nishina one, which takes into account quantum effects. Its consequence is to reduce the cross section from its classical value, so that Compton scattering becomes less efficient at high energies. We approximated this effect by requiring that $\nu'_{\rm c,max}(l)$ be averaged with $\nu'^{\rm KN}_{\rm c,max}(l) = \frac{m_{\rm e}c^2}{h}\gamma_{\rm max}(l)$ when $\gamma_{\rm max}(l)\nu'_{\rm s,max}(l) > \frac{3}{4}\frac{m_{\rm e}c^2}{h}$.

We assume a power law dependence of the observed flux density on the frequency and a cubic dependence on the Doppler beaming factor δ: $F_\nu(\nu) \propto \delta^3\nu^{-\alpha_0}$, where α_0 is the power law index of the local synchrotron spectrum, $\delta = [\Gamma(1 - \beta\cos\theta)]^{-1}$, β is the bulk velocity of the emitting plasma in units of the speed of light, $\Gamma = (1 - \beta^2)^{-1/2}$ the corresponding bulk Lorentz factor, and θ is the viewing angle of Eq. (2). Since the viewing angle varies along the helical path, also the beaming factor does. Hence, the flux at ν peaks when the part of the jet mostly contributing to it has minimum θ.

The emissivity decreases along the jet: both the synchrotron and inverse Compton flux densities are allowed to drop when moving from the jet apex outwards. For a jet slice of thickness dl:

$${\rm d}F_{\nu,{\rm s}}(\nu) \propto \delta^3(l)\,\nu^{-\alpha_0}\left(1 + \frac{l}{l_{\rm s}}\right)^{-c_{\rm s}}{\rm d}l, \quad c_{\rm s} > 0, \quad (4)$$

$${\rm d}F_{\nu,{\rm c}}(\nu) \propto \delta^3(l)\,\nu^{-\alpha_0}\left(1 + \frac{l}{l_{\rm c}}\right)^{-c_{\rm c}}\ln\left[\frac{\nu'_{\rm s,max}(l)}{\nu'_{\rm s,min}(l)}\right]{\rm d}l, \quad c_{\rm c} > 0. \quad (5)$$

For both the synchrotron and inverse Compton components, the observed flux densities at frequency ν coming from the whole jet are obtained by integrating over all the jet portions $\Delta z_i(\nu)$ contributing to that observed frequency, i.e. for which $\delta(z)\nu'_{\rm min}(z) \le \nu \le \delta(z)\nu'_{\rm max}(z)$. The total observed flux density at frequency ν is finally obtained by summing the synchrotron and inverse Compton contributions. Notice that the intrinsic jet emission does not vary with time, but the observed one may change as the orientation changes.

Table 5. Main parameters of the helical model for the fit to the "XMM-Newton" broad-band SED of December 2007 – January 2008.

Parameter	Low	High
ζ	30°	30°
ψ	25°	25°
a	110°	110°
ϕ	−8°	20°
$\log\nu'_{\rm s}(0)$	14.0	17.8
$c_{\rm min,max}$	2.5	2.5
$\log l_{\rm min}$	−3.2	−3.2
$\log l_{\rm max}$	−1.6	−1.6
$\log\gamma_{\rm max}(0)$	3.5	4.4
c_γ	1.25	1.25
$\log l_\gamma$	−1.6	−1.6
α_0	0.5	0.5
Γ	10	10
$c_{\rm s}$	1	1
$\log l_{\rm s}$	−1	−1
$c_{\rm c}$	1	1
$\log l_{\rm c}$	−1	−1

The differences between the low- and high-energy synchrotron+SSC components are easily seen.

The fit to the "XMM-Newton" broad-band SED of December 2007 – January 2008 in Fig. 6 (solid line) is obtained by considering two synchrotron emission components from different regions of a helical jet, with their corresponding SSC, plus a thermal component, modelled as a black body. The main parameters of the model are reported in Table 5.

The lower-energy synchrotron+SSC emission (dotted line) comes from a helical portion that is initially fairly aligned with the line of sight ($\phi = -8°$, $\theta(0) \approx 6.2°$), while the higher-energy synchrotron+SSC emission (dashed line) is produced by another helical region that is initially less aligned with the line of sight ($\phi = 20°$, $\theta(0) \approx 10.4°$).

A thermal component that fits the UV excess must have a black body temperature $\gtrsim$20 000 K and a luminosity $\gtrsim 6 \times 10^{44}$ erg s^{-1}. This lower limit to the temperature (and consequently to the luminosity) is constrained by the break of the SED in the optical-UV transition, but much hotter and hence more luminous discs are possible. For comparison, the thermal disc fitted by Pian et al. (1999) to the UV data of 3C 279 has a temperature of 20 000 K and a luminosity of 2×10^{45} erg s^{-1}.

The two synchrotron+SSC components can change a lot for variations e.g. of the angle ϕ, which happens if the helix rotates, allowing us to explain the noticeable spectral variability of the source also in the absence of intrinsic, energetic processes. With reference to the SEDs shown in the bottom panel of Fig. 6, the high-energy synchrotron+SSC emission was giving an exceptional contribution in November 2000, while it was very faint in December 1999. A detailed investigation of the model parameter space to fit the SED shape of BL Lacertae at different epochs goes beyond the scope of this paper. We notice however that our model fit produces a GeV spectrum with photon index $\Gamma \approx 2$ and can fairly reproduce the TeV spectrum observed by the MAGIC telescope in 2005 (Albert et al. 2007).

6. Discussion and conclusions

The WEBT campaign on BL Lacertae in the 2007–2008 observing season involved 37 optical-to-radio telescopes. They observed the source in a relatively faint state. Nevertheless, some fast variability episodes were detected in the optical bands,

superposed to a long-term flux increasing trend. During the campaign, three observations by the XMM-Newton satellite added information on the UV and X-ray states of the source.

The broad-band SEDs built with simultaneous data taken at the epochs of the XMM-Newton observations show a clear UV excess. The high UV fluxes are explained if we assume a contribution by thermal radiation from the accretion disc.

On the other side, the corresponding X-ray spectra indicate a possible soft excess. When comparing our X-ray data with previous data from other satellites, the X-ray spectrum appears to vary dramatically, so the soft excess cannot be ascribed to the accretion disc and/or hot corona surrounding it. A much more variable emission contribution is required.

We found that the broad-band SEDs of BL Lacertae can be explained in terms of two synchrotron emission components with their corresponding SSC radiation, plus a thermal component representing the contribution of the accretion disc. When fitting these two non-thermal components by means of the helical jet model of Villata & Raiteri (1999), and the thermal one with a black body law, we find that the accretion disc has a temperature $\gtrsim$20 000 K and a luminosity $\gtrsim 6 \times 10^{44}$ erg s^{-1}. Taking into account that $L = \eta \dot{M} c^2$, with $\eta \simeq 0.06$ in the case of Schwarzschild's metric (Shakura & Sunyaev 1973), we can derive a lower limit to the accretion rate: $\dot{M} \gtrsim 0.2\, M_\odot\, \mathrm{yr}^{-1}$. And if we assume that the luminosity equals the Eddington's critical luminosity, we can also infer a lower limit to the black hole mass: $M_{\rm BH} \gtrsim 6 \times 10^6\, M_\odot$. This value scales as $L_{\rm Edd}/L$.

A further emission component coming from inverse-Compton scattering on external photons from the disc and/or the broad line region might be present, but it is not needed to fit the observations, so we think that its possible contribution would be a minor one. Its modelling would introduce additional parameters that we could not reliably constrain.

Being aware that also other interpretations might be able to account for the observations reported in this paper, we notice that a helical jet model is motivated by some observing evidence. Indeed, VLBA/VLBI studies of the jet structure in AGNs have revealed bent jet morphologies that are suggestive of streaming motions along a helical path (see e.g. Lister 2001) or that the magnetic field may present a helical geometry (Gabuzda et al. 2004); this is also true for BL Lacertae (Tateyama et al. 1998; Denn et al. 2000; Marscher et al. 2008; O'Sullivan & Gabuzda 2009, see also Stirling et al. 2003). Moreover, a rotating helical path in a curved jet was invoked by Villata et al. (2009) to explain the optical and radio behaviour of BL Lacertae in the last forty years, in particular the alternation of enhanced and suppressed optical activity, accompanied by hard and soft radio events, respectively. If the jet has a helical structure, different portions of the jet may be well aligned with the line of sight, with consequent Doppler beaming of the emitted radiation. The two emission components proposed in our modelling could correspond to two of these regions, the higher-energy one being located closer to the jet apex. An analogous picture was suggested by Villata & Raiteri (1999) for Mkn 501, whose radio-to-X-ray multiepoch SED was explained in terms of two jet regions with different curvature. Alternatively, we can imagine that the two contributions come from two interweaved helical filaments, but we regard this hypothesis as less likely.

Finally, we mention that also in the case of Mkn 421, a possible explanation for its X-ray and optical flux behaviour during the June 2008 flare implies the existence of two different synchrotron emitting regions in the jet (Donnarumma et al. 2009b).

Further multiwavelength observations, including GeV data from the Fermi satellite, and TeV data from ground-based Cherenkov telescopes, will help verify our interpretation.

Acknowledgements. This work is partly based on observations made with the Nordic Optical Telescope, operated on the island of La Palma jointly by Denmark, Finland, Iceland, Norway, and Sweden, in the Spanish Observatorio del Roque de los Muchachos of the Instituto de Astrofisica de Canarias, and on observations collected at the German-Spanish Calar Alto Observatory, jointly operated by the MPIA and the IAA-CSIC. AZT-24 observations are made within an agreement between Pulkovo, Rome and Teramo observatories. The Submillimeter Array is a joint project between the Smithsonian Astrophysical Observatory and the Academia Sinica Institute of Astronomy and Astrophysics and is funded by the Smithsonian Institution and the Academia Sinica. This research has made use of data from the University of Michigan Radio Astronomy Observatory, which is supported by the National Science Foundation and by funds from the University of Michigan. This work is partly based on observation from Medicina and Noto telescopes operated by INAF – Istituto di Radioastronomia. The Torino team acknowledges financial support by the Italian Space Agency through contract ASI-INAF I/088/06/0 for the Study of High-Energy Astrophysics. Acquisition of the MAPCAT data at the Calar Alto Observatory is supported in part by the Spanish "Ministerio de Ciencia e Innovación" through grant AYA2007-67626-C03-03. The Metsähovi team acknowledges the support from the Academy of Finland. This research was partially supported by Scientific Research Fund of the Bulgarian Ministry of Education and Sciences (BIn – 13/09). St.Petersburg University team acknowledges support from RFBR grant 09-02-00092. Observations at the Abastumani 70-cm meniscus were partially supported by the Georgian National Science Foundation grant GNSF/ST-08/4-404. This research has made use of NASA's Astrophysics Data System.

References

Albert, J., Aliu, E., Anderhub, H., et al. 2007, ApJ, 666, L17
Bach, U., Villata, M., Raiteri, C. M., et al. 2006, A&A, 456, 105
Bania, T. M., Marscher, A. P., & Barvainis, R. 1991, AJ, 101, 2147
Bertaud, C., Dumortier, B., Veron, P., et al. 1969, A&A, 3, 436
Bessell, M. S., Castelli, F., & Plez, B. 1998, A&A, 333, 231
Bloom, S. D., Bertsch, D. L., Hartman, R. C., et al. 1997, ApJ, 490, L145
Böttcher, M., & Bloom, S. D. 2000, AJ, 119, 469
Böttcher, M., Marscher, A. P., Ravasio, M., et al. 2003, ApJ, 596, 847
Bregman, J. N., Glassgold, A. E., Huggins, P. J., et al. 1986, ApJ, 301, 708
Bruzual, G., & Charlot, S. 2003, MNRAS, 344, 1000
Cardelli, J. A., Clayton, G. C., & Mathis, J. S. 1989, ApJ, 345, 245
Chen, A. W., D'Ammando, F., Villata, M., et al. 2008, A&A, 489, L37
Corbett, E. A., Robinson, A., Axon, D. J., et al. 1996, MNRAS, 281, 737
Corbett, E. A., Robinson, A., Axon, D. J., & Hough, J. H. 2000, MNRAS, 311, 485
D'Ammando, F., Pucella, G., Raiteri, C. M., et al. 2009, A&A, in press [arXiv:0909.3484]
Denn, G. R., Mutel, R. L., & Marscher, A. P. 2000, ApJS, 129, 61
Dermer, C. D., Schlickeiser, R., & Mastichiadis, A. 1992, A&A, 256, L27
Donnarumma, I., Pucella, G., Vittorini, V., et al. 2009a, ApJ, in press [arXiv:0910.4883]
Donnarumma, I., Vittorini, V., Vercellone, S., et al. 2009b, ApJ, 691, L13
Fiorucci, M., & Tosti, G. 1996, A&AS, 116, 403
Fitzpatrick, E. L., & Massa, D. 2007, ApJ, 663, 320
Gabuzda, D. C., Murray, É., & Cronin, P. 2004, MNRAS, 351, L89
Ghisellini, G., & Tavecchio, F. 2009, MNRAS, 397, 985
Grandi, P., & Palumbo, G. G. C. 2004, Science, 306, 998
Hartman, R. C., Bertsch, D. L., Bloom, S. D., et al. 1999, ApJS, 123, 79
Kalberla, P. M. W., Burton, W. B., Hartmann, D., et al. 2005, A&A, 440, 775
Lister, M. L. 2001, ApJ, 562, 208
Liszt, H. S. 2007, A&A, 476, 291
Liszt, H. S., & Lucas, R. 1998, A&A, 339, 561
Lucas, R., & Liszt, H. S. 1993, A&A, 276, L33
Madejski, G. M., Sikora, M., Jaffe, T., et al. 1999, ApJ, 521, 145
Mannucci, F., Basile, F., Poggianti, B. M., et al. 2001, MNRAS, 326, 745
Marscher, A. P., Jorstad, S. G., D'Arcangelo, F. D., et al. 2008, Nature, 452, 966
Mason, K. O., Breeveld, A., Much, R., et al. 2001, A&A, 365, L36
Ostorero, L., Villata, M., & Raiteri, C. M. 2004, A&A, 419, 913
O'Sullivan, S. P., & Gabuzda, D. C. 2009, MNRAS, 393, 429
Padovani, P., Costamante, L., Giommi, P., et al. 2001, MNRAS, 328, 931
Papadakis, I. E., Villata, M., & Raiteri, C. M. 2007, A&A, 470, 857
Pian, E., Urry, C. M., Maraschi, L., et al. 1999, ApJ, 521, 112
Pucella, G., Vittorini, V., D'Ammando, F., et al. 2008, A&A, 491, L21

Raiteri, C. M., & Villata, M. 2003, in Proc. of the First ENIGMA Meeting, held at Mayschoss, Germany, May 11–14, ed. M. Hauser, U. Bach, & S. Britzen, 326
Raiteri, C. M., Villata, M., Tosti, G., et al. 1999, A&A, 352, 19
Raiteri, C. M., Villata, M., Ibrahimov, M. A., et al. 2005, A&A, 438, 39
Raiteri, C. M., Villata, M., Kadler, M., et al. 2006a, A&A, 459, 731
Raiteri, C. M., Villata, M., Kadler, M., et al. 2006b, A&A, 452, 845
Raiteri, C. M., Villata, M., Capetti, A., et al. 2007a, A&A, 464, 871
Raiteri, C. M., Villata, M., Larionov, V. M., et al. 2007b, A&A, 473, 819
Raiteri, C. M., Villata, M., Larionov, V. M., et al. 2008, A&A, 491, 755
Ravasio, M., Tagliaferri, G., Ghisellini, G., et al. 2002, A&A, 383, 763
Ravasio, M., Tagliaferri, G., Ghisellini, G., et al. 2003, A&A, 408, 479
Sambruna, R. M., Ghisellini, G., Hooper, E., et al. 1999, ApJ, 515, 140
Scarpa, R., Urry, C. M., Falomo, R., Pesce, J. E., & Treves, A. 2000, ApJ, 532, 740
Schlegel, D. J., Finkbeiner, D. P., & Davis, M. 1998, ApJ, 500, 525
Shakura, N. I., & Sunyaev, R. A. 1973, A&A, 24, 337
Sikora, M., Begelman, M. C., & Rees, M. J. 1994, ApJ, 421, 153
Smith, P. S., Schmidt, G. D., & Allen, R. G. 1993, ApJ, 409, 604
Stickel, M., Fried, J. W., Kuehr, H., Padovani, P., & Urry, C. M. 1991, ApJ, 374, 431
Stirling, A. M., Cawthorne, T. V., Stevens, J. A., et al. 2003, MNRAS, 341, 405
Strüder, L., Briel, U., Dennerl, K., et al. 2001, A&A, 365, L18
Tanihata, C., Takahashi, T., Kataoka, J., et al. 2000, ApJ, 543, 124
Tateyama, C. E., Kingham, K. A., Kaufmann, P., et al. 1998, ApJ, 500, 810
Türler, M., Chernyakova, M., Courvoisier, T. J.-L., et al. 2006, A&A, 451, L1
Turner, M. J. L., Abbey, A., Arnaud, M., et al. 2001, A&A, 365, L27
Vercellone, S., Chen, A. W., Vittorini, V., et al. 2009, ApJ, 690, 1018
Vermeulen, R. C., Ogle, P. M., Tran, H. D., et al. 1995, ApJ, 452, L5
Villata, M., & Raiteri, C. M. 1999, A&A, 347, 30
Villata, M., Raiteri, C. M., Kurtanidze, O. M., et al. 2002, A&A, 390, 407
Villata, M., Raiteri, C. M., Aller, H. D., et al. 2004a, A&A, 424, 497
Villata, M., Raiteri, C. M., Kurtanidze, O. M., et al. 2004b, A&A, 421, 103
Villata, M., Raiteri, C. M., Larionov, V. M., et al. 2009, A&A, 501, 455
von Montigny, C., Aller, H., Aller, M., et al. 1997, ApJ, 483, 161
Wilms, J., Allen, A., & McCray, R. 2000, ApJ, 542, 914

[1] INAF, Osservatorio Astronomico di Torino, Italy
e-mail: [raiteri;villata]@oato.inaf.it
[2] Department of Astronomy, University of Michigan, MI, USA
[3] Max-Planck-Institut für Radioastronomie, Bonn, Germany
[4] Osservatorio Astronomico della Regione Autonoma Valle d'Aosta, Italy
[5] Harvard-Smithsonian Center for Astroph., Cambridge, MA, USA
[6] Astron. Inst., St.-Petersburg State Univ., Russia
[7] Pulkovo Observatory, St. Petersburg, Russia
[8] Michael Adrian Observatory, Trebur, Germany
[9] Tuorla Observatory, Dept. of Physics and Astronomy, Univ. of Turku, Piikkiö, Finland
[10] Inst. of Astronomy, Bulgarian Academy of Sciences, Sofia, Bulgaria
[11] Instituto de Astrofísica de Andalucía (CSIC), Granada, Spain
[12] Instituto de Astronomía, Universidad Nacional Autónoma de México, Mexico
[13] Department of Physics and Astronomy, Ohio Univ., OH, USA
[14] INAF, Osservatorio Astrofisico di Catania, Italy
[15] SISSA-ISAS, Trieste, Italy
[16] Armenzano Astronomical Observatory, Italy
[17] Université de Bordeaux, Observatoire Aquitain des Sciences de l'Univers, Floirac, France
[18] CNRS, Laboratoire d'Astrophysique de Bordeaux – UMR 5804, Floirac, France
[19] Institute of Astronomy, National Central University, Taiwan
[20] Agrupació Astronòmica de Sabadell, Spain
[21] ARIES, Manora Peak, Nainital, India
[22] ZAH, Landessternwarte Heidelberg, Heidelberg, Germany
[23] Inst. de Astrofísica de Andalucía, CSIC, Spain
[24] Inst. for Astrophysical Research, Boston University, MA, USA
[25] Abastumani Astrophysical Observatory, Georgia
[26] Metsähovi Radio Obs., Helsinki Univ. of Technology, Finland
[27] INAF, Istituto di Radioastronomia, Sezione di Noto, Italy
[28] Sofia University, Bulgaria
[29] Korea Astronomy and Space Science Institute, South Korea
[30] Circolo Astrofili Talmassons, Italy
[31] Institute for Astrophysical Research, Boston University, MA, USA
[32] Nordic Optical Telescope, Santa Cruz de La Palma, Spain
[33] Dept. of Physics and Astronomy, Univ. of Victoria, Victoria, Canada
[34] Dept. of Phys., Univ. of Colorado Denver, Denver, CO USA
[35] Radio Astronomy Lab. of Crimean Astrophysical Observatory, Ukraine

A&A 508, 181–189 (2009)
DOI: 10.1051/0004-6361/200912560

Astronomy & Astrophysics

AGILE detection of a rapid γ-ray flare from the blazar PKS 1510-089 during the GASP-WEBT monitoring⋆

F. D'Ammando[1,2], G. Pucella[1], C. M. Raiteri[3], M. Villata[3], V. Vittorini[1,4], S. Vercellone[5], I. Donnarumma[1], F. Longo[6], M. Tavani[1,2], A. Argan[1], G. Barbiellini[6], F. Boffelli[7,8], A. Bulgarelli[9], P. Caraveo[10], P. W. Cattaneo[7], A. W. Chen[4,10], V. Cocco[1], E. Costa[1], E. Del Monte[1], G. De Paris[1], G. Di Cocco[9], Y. Evangelista[1], M. Feroci[1], A. Ferrari[11], M. Fiorini[10], T. Froysland[2,4], F. Fuschino[9], M. Galli[12], F. Gianotti[9], A. Giuliani[10], C. Labanti[9], I. Lapshov[1], F. Lazzarotto[1], P. Lipari[13], M. Marisaldi[9], S. Mereghetti[10], A. Morselli[14], L. Pacciani[1], A. Pellizzoni[15], F. Perotti[10], G. Piano[1,2], P. Picozza[14], M. Pilia[15], M. Prest[16], M. Rapisarda[17], A. Rappoldi[7], S. Sabatini[1,2], P. Soffitta[1], M. Trifoglio[9], A. Trois[1], E. Vallazza[6], A. Zambra[1], D. Zanello[13], I. Agudo[18], M. F. Aller[19], H. D. Aller[19], A. A. Arkharov[20], U. Bach[21], E. Benitez[22], A. Berdyugin[23], D. A. Blinov[24], C. S. Buemi[25], W. P. Chen[26,27], A. Di Paola[28], G. Di Rico[29], D. Dultzin[22], L. Fuhrmann[21], J. L. Gómez[18], M. A. Gurwell[30], S. G. Jorstad[31], J. Heidt[32], D. Hiriart[33], H. Y. Hsiao[27], G. Kimeridze[34], T. S. Konstantinova[24], E. N. Kopatskaya[24], E. Koptelova[26,27], O. Kurtanidze[34], V. M. Larionov[20,24], P. Leto[35], E. Lindfors[23], J. M. Lopez[33], A. P. Marscher[31], I. M. McHardy[36], D. A. Melnichuk[24], M. Mommert[32], R. Mujica[37], K. Nilsson[23], M. Pasanen[23], M. Roca-Sogorb[18], M. Sorcia[22], L. O. Takalo[23], B. Taylor[38], C. Trigilio[25], I. S. Troitsky[24], G. Umana[25], L. A. Antonelli[39], S. Colafrancesco[39], S. Cutini[39], D. Gasparrini[39], C. Pittori[39], B. Preger[39], P. Santolamazza[39], F. Verrecchia[39], P. Giommi[39], and L. Salotti[40]

(Affiliations can be found after the references)

Received 23 May 2009 / Accepted 15 September 2009

ABSTRACT

Aims. We report the detection by the AGILE satellite of a rapid γ-ray flare from the source 1AGL J1511−0908, associated with the powerful γ-ray quasar PKS 1510−089, during a pointing centered on the Galactic center region from 1 March to 30 March 2008. This source has been continuosly monitored in the radio-to-optical bands by the GLAST-AGILE Support Program (GASP) of the Whole Earth Blazar Telescope (WEBT). Moreover, the γ-ray flaring episode triggered three ToO observations by the *Swift* satellite in three consecutive days, starting from 20 March 2008. The quasi-simultaneous radio-to-optical, UV, X-ray and γ-ray coverage allows us to make a detailed study of the multifrequency time evolution, the spectral energy distribution of this source, and its theoretical interpretation based on the synchrotron and inverse Compton (IC) emission mechanisms.
Methods. During the radio-to-optical monitoring provided by the GASP-WEBT, AGILE observed the source with its two co-aligned imagers, the gamma-ray imaging detector (GRID) and the hard X-ray imager (SuperAGILE), which are sensitive in the 30 MeV–30 GeV and 18–60 keV energy bands, respectively.
Results. In the period 1–16 March 2008, AGILE detected γ-ray emission from PKS 1510−089 at a significance level of 6.2-σ with an average flux over the entire period of $(84 \pm 17) \times 10^{-8}$ photons cm^{-2} s^{-1} for photon energies above 100 MeV. After a predefined satellite re-pointing, between 17 and 21 March 2008, AGILE detected the source at a significance level of 7.3-σ, with an average flux ($E > 100$ MeV) of $(134 \pm 29) \times 10^{-8}$ photons cm^{-2} s^{-1} and a peak level of $(281 \pm 68) \times 10^{-8}$ photons cm^{-2} s^{-1} with daily integration. During the observing period January-April 2008, the source also showed an intense and variable optical activity, with several flaring episodes and a significant increase in the flux was observed at millimetric frequencies. Moreover, in the X-ray band, the *Swift*/XRT observations seem to show a harder-when-brighter behavior of the source spectrum.
Conclusions. The flat spectrum radio quasar PKS 1510−089 showed strong activity between January and April 2008, with episodes of rapid variability from radio to γ-ray energy bands, in particular with a rapid γ-ray flaring episode. The spectral energy distribution of mid-March 2008 is modeled with a homogeneous one-zone synchrotron self Compton (SSC) emission plus contributions from inverse Compton scattering of external photons from both the accretion disk and the broad line region. Indeed, some features in the optical-UV spectrum seem to indicate Seyfert-like components such as the little and the big blue bumps.

Key words. gamma-rays: observations – radiation mechanisms: non-thermal – quasars: individual: PKS 1510-089

1. Introduction

Blazars are a subclass of AGN characterized by the emission of strong nonthermal radiation across the entire electromagnetic spectrum, from radio to very high energies. Their observational properties include irregular, rapid, and often very high variability, apparent super-luminal motion, flat radio spectrum, high and variable polarization at radio and optical frequencies. These features are interpreted as the result of the emission of electromagnetic radiation from a relativistic jet that is viewed closely aligned to the line of sight (Blandford & Rees 1978; Urry & Padovani 1995). The spectral energy distribution (SED) of blazars is typically double-humped with a first peak occurring in the IR/optical band in the so-called *red blazars* (including flat spectrum radio quasars, FSRQs, and low-energy peaked

⋆ The radio-to-optical data presented in this paper are stored in the GASP-WEBT archive; for questions regarding their availability, please contact the WEBT President Massimo Villata.

Article published by EDP Sciences

BL Lacs, LBLs) and at UV/X-rays in the so-called *blue blazars* (including high-energy peaked BL Lacs, HBLs). The first peak is commonly interpreted as synchrotron radiation from high-energy electrons in a relativistic jet. The second component of the SED, peaking at MeV–GeV energies in *red blazars* and at TeV energies in *blue blazars*, is commonly interpreted as inverse Compton (IC) scattering of seed photons by relativistic electrons (Ulrich et al. 1997), although a different origin of high-energy emission has been proposed in hadronic models (see e.g., Böttcher 2007, for a recent review).

PKS 1510−089 is a nearby ($z = 0.361$) radio-loud, highly polarized quasar (HPQ) already detected also in the MeV–GeV energy band by the EGRET instrument on board *CGRO* (Hartman et al. 1992). The broadband spectrum of the source is representative of the class of FSRQ with the inverse Compton component dominated by the γ-ray emission, and the synchrotron emission peaked around IR frequencies, even if it is clearly visible in this source a pronunced UV bump possibly caused by the thermal emission from the accretion disk (Malkan & Moore 1986; Pian & Treves 1993).

PKS 1510−089 has been extensively observed and studied in the X-ray band by the satellites EXOSAT (Singh et al. 1990; Sambruna et al. 1994), GINGA (Lawson & Turner 1997), ROSAT (Siebert et al. 1998), ASCA (Singh et al. 1997), and *Chandra* (Gambill et al. 2003). The observed X-ray spectrum was very flat in the 2–10 keV band with photon index of $\Gamma \simeq 1.3$, but it was steeper ($\Gamma \simeq 1.9$) in the ROSAT bandpass (0.1–2.4 keV), suggesting a possible spectral break around 1–2 keV. The difference in the photon indices could be caused by a soft X-ray excess. Observations by BeppoSAX (Tavecchio et al. 2000) confirm a possible soft X-ray excess below 1 keV. Evidence of a similar soft X-ray excess has been detected in other blazars such as 3C 273, 3C 279, AO 0235+164, and 3C 454.3, even if the origin of this excess is still an open issue.

During August 2006, PKS 1510−089 was observed in a relatively bright state by *Suzaku* over approximately three days and with *Swift* 10 times during 18 days as a target of opportunity (ToO) with a total duration of 24.3 ks. *Suzaku* measured a very hard X-ray spectrum ($\Gamma < 1.5$), which seems to exclude models in which X-rays are produced by synchrotron radiation of the secondary ultrarelativistic population of electrons and positrons, as predicted by hadronic models. The *Swift*/XRT observations instead revealed significant spectral evolution in the 0.3–10 keV energy band on timescales of one week, with the spectrum that becomes harder as the source gets brighter (Kataoka et al. 2008).

Gamma-ray emission from PKS 1510−089 was detected several times by EGRET with an integrated flux above 100 MeV between (13 ± 5) and $(49 \pm 18) \times 10^{-8}$ photons cm^{-2} s^{-1} and an energy spectrum, integrated over all the EGRET observations, modeled with a power law with photon index $\Gamma = 2.47 \pm 0.21$ (Hartman et al. 1999).

In August 2007, AGILE detected an intense γ-ray activity from PKS 1510−089. In particular, during the period 28 August–1 September 2007 the average γ-ray flux observed was $F_{E>100\ \mathrm{MeV}} = (195 \pm 30) \times 10^{-8}$ photons cm^{-2} s^{-1} (Pucella et al. 2008). Recently, this source was detected again during high γ-ray activity states by both the Large Area Telescope (LAT) onboard the *Fermi* GST (Ciprini et al. 2009; Tramacere 2008; Cutini et al. 2009) and AGILE (D'Ammando et al. 2009; Pucella et al. 2009; Vercellone et al. 2009). The results of the AGILE observations during March 2009 will be published in a forthcoming paper (D'Ammando et al., in preparation).

In this paper we present the analysis of the AGILE data obtained during the observations of PKS 1510−089 from 1 March to 30 March 2008 (see also D'Ammando et al. 2008a). We also present the radio-to-optical monitoring of the GASP-WEBT during the period January-April 2008, and the results of three *Swift* ToO carried out between 20 and 22 March 2008. This broadband coverage over the entire electromagnetic spectrum allows us to build and study the SED of the source in detail.

The paper is organized as follows. Section 2 describes the AGILE observations, and the corresponding data analysis. Section 3 introduces the *Swift* data and the relative analysis. Section 4 is dedicated to the results of the GASP-WEBT observations, while in Sect. 5 we discuss the SED, its implication for the emission mechanisms of the source, and finally we draw our conclusions.

Throughout this paper the quoted uncertainties are given at the 1-σ level, unless otherwise stated, and the photon indices are parameterized as $N(E) \propto E^{-\Gamma}$ (ph cm^{-2} s^{-1} keV^{-1} or MeV^{-1}) with $\Gamma = \alpha + 1$ (α is the spectral index). We adopt a luminosity distance of $d_L = 1915$ Mpc for PKS 1510-089, assuming $z = 0.361$ and a ΛCDM cosmology with $H_0 = 71$ Km s^{-1} Mpc^{-1}, $\Omega_m = 0.27$, and $\Omega_\Lambda = 0.73$.

2. AGILE data

2.1. Observation of PKS 1510−089

The AGILE satellite (Tavani et al. 2008, 2009) is an Italian Space Agency (ASI) Mission devoted to high-energy astrophysics, with four active detectors capable of observing cosmic sources simultaneously in X-ray and γ-ray energy bands.

The gamma-ray imaging detector (GRID) consists of a combination of a pair-production silicon tracker (ST; Prest et al. 2003; Barbiellini et al. 2001), sensitive in the energy range 30 MeV–30 GeV, a non-imaging CsI(Tl) mini-calorimeter (MCAL; Labanti et al. 2009) sensitive in the 0.3–100 MeV energy band, and a segmented anti-coincidence system (ACS) made of plastic scintillator layers that surround all active detectors (Perotti et al. 2006). A co-aligned coded-mask hard X-ray imager (SuperAGILE; Costa et al. 2001; Feroci et al. 2007) ensures coverage in the 18–60 keV energy band.

The AGILE observations of PKS 1510-089 were performed from 1 March 2008 12:45 UT to 21 March 2008 2:04 UT, for a total of 211 h of effective exposure time. In the first period, between 1 and 16 March, the source was located ∼50° off the AGILE pointing direction. In the second period between 17 and 21 March after a satellite re-pointing, the source was located at ∼40° off-axis. Finally, after a gap of 4 days of observation due to technical maintenance of the satellite, the source was observed at ∼50° off axis between 25 March 13:09 UT and 30 March 10:29 UT. Unfortunately, during the observation the source was substantially off-axis in the field of view of SuperAGILE.

2.2. Data reduction and analysis

AGILE-GRID data were analyzed, starting from the Level-1 data, using the AGILE Standard Analysis Pipeline (see Vercellone et al. 2008, for a detailed description of the AGILE data reduction). An ad-hoc implementation of the Kalman Filter technique is used for track identification and event-direction reconstruction in detector coordinates and subsequently a quality flag is assigned to each GRID event, depending on whether it is recognized as a confirmed gamma-ray event, a charged particle event, a single-track event, or as having an uncertain nature.

After the creation of the event files, the AGILE Scientific Analysis Package can be run. Counts, exposure, and Galactic

background γ-ray maps were generated with a bin size of 0.25°× 0.25° for photons with energy $E > 100$ MeV.

To reduce the particle background contamination, we selected only the events flagged as confirmed γ-ray events, so all events collected during the South Atlantic Anomaly were rejected. We also rejected all the γ-ray events whose reconstructed directions form angles with the satellite-Earth vector smaller than 80°, in order to reduce the γ-ray Earth albedo contamination. The most recent version (BUILD-16) of the Calibration files at the time of writing (publicly available at the ASI Science Data Center (ASDC) site[1]) and of the γ-ray diffuse emission model (Giuliani et al. 2004) is used. We ran the AGILE maximum likelihood procedure with a radius of analysis of 10°, on the whole observing period, in order to obtain the average flux in the γ-ray band and estimate the diffuse parameters used to measure the daily fluxes, according to the procedure described in Mattox et al. (1993).

2.3. Results

During the period 1–16 March 2008, AGILE-GRID detected γ-ray emission from a position consistent with the powerful γ-ray quasar PKS 1510−089 at a significance level of 6.2-σ with an average flux over the entire period of $(84 \pm 17) \times 10^{-8}$ photons cm^{-2} s^{-1} for photon energies above 100 MeV.

Instead, in the period 17–21 March 2008, AGILE detected γ-ray emission from a position consistent with the source at a significance level of 7.3-σ. The AGILE 95% maximum likelihood contour level baricenter of the source is $l = 351.49°, b = 40.07°$, with a distance between this position and the radio position ($l = 351.29°, b = 40.14°$) of 0.17°. The overall AGILE error circle, taking both statistical and systematic effects into account, has a radius $r = 0.50°$. The average flux above 100 MeV during this second period, with the source located ∼40° off the AGILE pointing direction, was $(134 \pm 29) \times 10^{-8}$ photons cm^{-2} s^{-1}. The peak level of activity with daily integration was $(281 \pm 68) \times 10^{-8}$ photons cm^{-2} s^{-1}, showing an increase of a factor two in one day and at least three in two days, as the source had not been detected for some days after two episodes of medium intensity. After the sudden increase, the flux rapidly decreased around 19 March 2008.

When fitting the data relative to the period 17–21 March with a simple power law model, we obtain a photon index of $\Gamma = 1.81 \pm 0.34$. This photon index is calculated with the weighted least squares method, considering for the fit three energy bins: 100–200 MeV, 200–400 MeV, and 400–1000 MeV. The photon index obtained for this second period is consistent within the errors with the one observed by AGILE in August 2007 ($\Gamma = 1.98 \pm 0.27$).

Figure 1 shows the γ-ray light curve between 1 and 21 March 2008 with 2-day resolution for the first period and 1-day for the second period, for photons of energy above 100 MeV. The downward arrows represent 2-σ upper limits. Upper limits are calculated when the analysis provides a significance of detection <3-σ (see Mattox et al. 1996). Finally, in the third period between 25 and 30 March 2008 the source was not detected by the GRID and an upper limit with 95% confidence level of 54×10^{-8} photons cm^{-2} s^{-1} is provided.

During August-October 2008, *Fermi*-LAT detected the source with an average flux for $E > 100$ MeV of $(55.8 \pm 3.3) \times 10^{-8}$ photons cm^{-2} s^{-1} and a peak of intensity of $(165.9 \pm 11.7) \times 10^{-8}$ photons cm^{-2} s^{-1} (Abdo et al. 2009). The peak of γ-ray emission corresponds to the first flare observed by *Fermi*-LAT at the end of September 2008 (Tramacere 2008), and the average flux value confirms the flaring state observed by AGILE in mid-March.

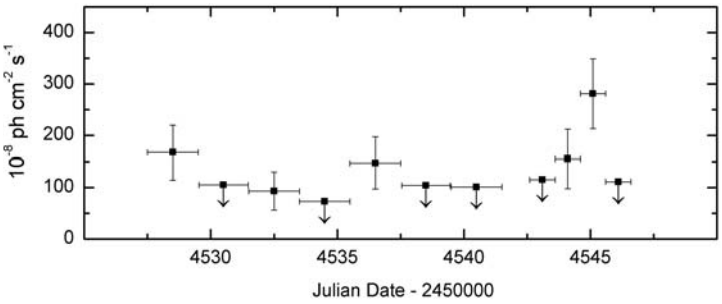

Fig. 1. AGILE-GRID γ-ray light curve between 1 and 21 March 2008 at 1-day or 2-day resolution for $E > 100$ MeV with fluxes in units of 10^{-8} photons cm^{-2} s^{-1}. The downward arrows represent 2-σ upper limits.

Moreover, *Fermi*-LAT observed a softer photon index for this source in August–October 2008, $\Gamma = 2.48 \pm 0.05$ (Abdo et al. 2009), but this value corresponds to an average value over three months of observation in which the source flux was variable, whereas the value reported by us refers to a rapid flaring episode. The value obtained by *Fermi*-LAT is very similar to what was measured by EGRET averaging over all the observations ($\Gamma = 2.47 \pm 0.21$), confirming that the average spectral indexes are softer than those measured during short flaring states. The difference between the value obtained by AGILE and *Fermi* could also be partially due to the different bandpasses of the two intruments.

3. SWIFT observations

The NASA *Swift* gamma-ray burst mission (Gehrels et al. 2004), performed three ToO observations of PKS 1510–089 in three consecutive days with the first occurring on 20 March 2008. The three observations were performed using all three onboard experiments: the X-ray Telescope (XRT; Burrows et al. 2005, 0.2–10 keV), the UV and Optical Telescope (UVOT; Roming et al. 2005, 170–600 nm) and the coded-mask Burst Alert Telescope (BAT; Barthelmy et al. 2005, 15–150 keV). The hard X-ray flux of this source is below the sensitivity of the BAT instrument for so short exposure, so the data from this instruments will not be used.

3.1. Swift/XRT data

The XRT data were processed with standard procedures (`xrtpipeline` v0.12.0), and the filtering and screening criteria were applied by means of the FTOOLS in the `Heasoft` package v6.5. Given the low rate of PKS 1510–089 during the three observations (<0.5 count s^{-1} in the 0.2–10 keV range), we only considered photon counting (PC) data for our analysis, and further selected XRT grades 0–12 (according to *Swift* nomenclature, see Burrows et al. 2005). No pile-up correction was necessary. The ancillary response files were generated with the task `xrtmkarf`, applying corrections for the PSF losses and CCD defects, and we used the latest spectral redistribution matrices (RMF, v011) in the calibration database maintained by HEASARC. The adopted energy range for spectral fitting is 0.3–10 keV, and all data were rebinned with a minimum of

[1] http://agile.asdc.asi.it

Table 1. Observation log and fitting results of *Swift*/XRT observations of PKS 1510-089, with power-law model with $N_{\rm H}$ fixed to Galactic absorption.

Observation date	Exposure time (s)	Counts (0.2–10 keV)	Flux 0.3–10 keV[a] erg cm^{-2} s^{-1}	Photon index Γ	$\chi^2_{\rm red}$ (d.o.f.)/C-stat (%)[b]
20-Mar-2008	1961	306	$12.20^{+1.65}_{-1.65} \times 10^{-12}$	1.16 ± 0.16	0.87 (13)
21-Mar-2008	1966	189	$8.77^{+1.33}_{-1.39} \times 10^{-12}$	1.53 ± 0.17	467 (48.2)[b]
22-Mar-2008	1885	261	$9.48^{+1.13}_{-1.14} \times 10^{-12}$	1.41 ± 0.19	1.34 (11)

[a] Unabsorbed flux; [b] cash statistic (C-stat) and percentage of Montecarlo realizations that had statistic < C-stat, performing 10^4 simulations.

20 counts per energy bin to use the χ^2 minimization fitting technique. An exception is the observation of 21 March 2008, when the number of counts was so low that the Cash statistic (Cash 1979) on ungrouped data was used. *Swift*/XRT uncertainties are given at 90% confidence level for one interesting parameter, unless otherwise stated.

Spectral analysis was performed using the `XSPEC` fitting package 12.4.0 (Arnaud et al. 1996). We fitted the spectra with a power-law model with Galactic absorption fixed to $N_{\rm H} = 6.89 \times 10^{20}$ cm^{-2} (Kalberla et al. 2005). Table 1 summarizes the most important information on XRT observations and the relative spectral fit parameters.

A variability of about 30% in the X-ray flux of the source was observed on a timescale of one day. Notwithstanding the uncertainties due to the errors on fluxes and photon indexes, the XRT data seem to indicate that the X-ray spectrum becomes harder when the source gets brighter, confirming the behavior already observed in this source by Kataoka et al. (2008) during the *Swift*/XRT observations carried out in August 2006. This is a trend often observed in HBL (see e.g. Massaro et al. 2008; Tramacere et al. 2007; Kataoka et al. 1999), but quite rare for quasar-hosted blazars such as PKS 1510−089. For instance, 3C 454.3 shows approximately the same spectral slope in different brightness states (see e.g. Raiteri et al. 2007; Raiteri et al. 2008).

3.2. Swift/UVOT data

During the three *Swift* pointings, the UVOT instrument (Poole et al. 2008) observed PKS 1510−089 in all its optical (V, B, and U) and UV (UV$W1$, UV$M2$, and UV$W2$) photometric bands. Data were reduced with the `uvotmaghist` task of the HEASOFT package. Source counts were extracted from a circular region of 5 arcsec radius, centered on the source, while the background was estimated from a surrounding annulus with 8 and 18 arcsec radii. In the first two days, only one exposure per filter was available, while three exposures per filter were acquired on the last day. With the only exception of UV$M2$, the source brightness turned out to be quite stable in all the UVOT bands, with variations of a few hundredth of mag, well inside the typical UVOT data uncertainty of 0.1 mag due to both systematic and statistical errors. Average values are: $V = 16.94$, $B = 17.19$, $U = 16.31$, UV$W1 = 16.64$, and UV$W2 = 16.55$. The UV$M2$ frames have low signal-to-noise ratios, thus the source magnitude in this band presents a larger dispersion. The average value is UV$M2 = 16.47 \pm 0.14$.

4. Radio-to-optical observations by the GASP

PKS 1510–089 is one of the 28γ-ray-loud blazars that are regularly monitored by the GLAST-AGILE Support Program (GASP; Villata et al. 2008) of the Whole Earth Blazar Telescope (WEBT). Optical and near-IR data are collected as already calibrated magnitudes, according to a common choice of photometric standards from Raiteri et al. (1998). Radio data are provided as calibrated flux densities. The reference optical band for the GASP is the R band. The corresponding light curve in January–April 2008 is shown in the top panel of Fig. 2, with the data provided by the following observatories: Abastumani, Calar Alto[2], Crimean, Lowell (Perkins), Lulin, Roque de los Muchachos (KVA and Liverpool), San Pedro Martir, St. Petersburg, Torino. The source showed intense activity during the entire considered period, with several episodes of fast variability. At the beginning of the optical observing season, the January observations indicate that the source was in a faint state, around $R = 16.6$. A fast brightening of ∼1.3 mag in 8 days led the source to $R = 15.3$ on 15 February. This was followed by a ∼0.6 mag dimming in 4 days. Other minimum brightness states were observed on 23 March and in late April, while peaks were detected on March 29 and April 11.

Near-IR data in the JHK bands were taken at Campo Imperatore and Roque de los Muchachos (Liverpool). Millimetric flux densities at 345 and 230 GHz came from the SubMillimeter Array (SMA) on Mauna Kea. Centimetric radio data were acquired at Medicina (22 and 8 GHz), Noto (43 GHz), and UMRAO (14.5, 8.0, and 4.8 GHz). In Fig. 1 the source radio behavior in different bands is compared to the optical one (top panel). The light curve at high radio frequencies (230–345 GHz) suggests that the mechanism producing the flaring events observed in the optical band in the second half of February and in late March-April 2008 also interested the millimetric emitting zone, with some delay. An estimate of this delay is hampered by the limited data sampling. At lower radio frequencies (22–43 GHz), a hint of flux increase is visible in the second part of the light curve, while the radio flux at 5–15 GHz shows no trend at all. This suggests that the jet regions that are responsible for the emission at the longest radio wavelengths are not affected by the flaring mechanism.

5. Discussion and conclusions

In the past two years, PKS 1510−089 has shown very high activity in γ-ray band with several flaring episodes (see Pucella et al. 2008; Tramacere 2008; Ciprini et al. 2009; D'Ammando et al. 2009; Pucella et al. 2009; Vercellone et al. 2009; Cutini et al. 2009). During the period January-April 2008, the source showed a high variability over the whole electromagnetic spectrum from radio to γ-rays, with several flaring episodes in the optical band and a rapid and intense flare detected in the γ-ray band in mid-March.

[2] Calar Alto data were acquired as part of the MAPCAT (Monitoring AGN with Polarimetry at the Calar Alto Telescopes) project.

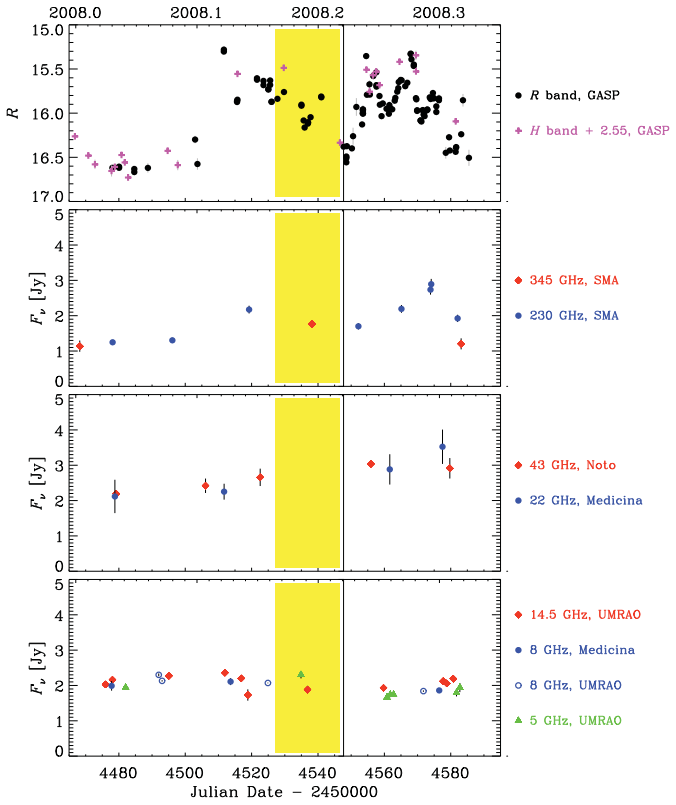

Fig. 2. Optical light curve of PKS 1510-089 (*top panel*) obtained by the GASP–WEBT during the period January-April 2008 compared to its radio flux densities at different frequencies. The vertical bar indicates the time of the *Swift* observations. The yellow shaded region marks the period also covered by the AGILE observation.

5.1. Modeling the spectral energy distribution

Figure 3 shows the SED for the AGILE-GRID observation period 17–21 March 2008, including quasi-simultaneous optical and radio data by GASP and UVOT and X-ray data by *Swift*. Since the source brightness over the three days of UVOT observations remained stable, we built a unique SED for the whole period, including contemporaneous data at other frequencies, in particular radio-to-optical data from the GASP. The optical and near-IR data were acquired exactly in the period of the UVOT observations: one *R*-band datum from Roque (KVA) and *J*, *H*, and *K* data from Campo Imperatore. The UVOT and GASP magnitudes were corrected for Galactic extinction by adopting $A_B = 0.416$ mag, and deriving the values in the other bands according to Cardelli et al. (1989). To convert magnitudes into fluxes, we assumed the zero-mag fluxes by Poole et al. (2008) and Bessel et al. (1998).

Radio light curves are not sampled any more than was the *R*-band one (see Fig. 2), therefore in the SED we show the high-frequency radio data (43–345 GHz) taken within a week from the UVOT observations, while the low-frequency data points were obtained by interpolating between the closest data preceeding and following the UVOT observations. This is justified by the smooth behavior of the low-frequency radio light curves.

The dip in the SED corresponding to the UV*W*1 frequency must be regarded with caution, since it is also found for other blazars with different redshifts and could be systematic. Observations performed by *Swift* and the GASP in March and June 2007, when the source was nearly at the same brightness level, showed the same shape in the near-IR-to-UV part of the SED. A similar trend characterized the optical-UV SED of August 2006 shown by Kataoka et al. (2008). We notice that the shape of the SED in the optical band may be affected by the flux contribution of broad emission lines, including the little blue bump (Neugebauer et al. 1979; Smith et al. 1988). For the SED we used the *Swift*/XRT data collected on 20 March, the observation closest to the γ-ray flare and during which the higher X-ray flux was observed.

Table 2. Parameters for the model used to explain the SED of PKS 1510-089 during the γ-ray flare of 18, 19 March 2008.

Parameter	Value	Units
p_1	2.2	
p_2	4.6	
$\gamma_{\rm min}$	30	
$\gamma_{\rm b}$	290	
$\gamma_{\rm max}$	5200	
K	75	cm^{-3}
R	10	10^{15} cm
B	3.5	G
δ	20.26	
$L_{\rm d}$	5	10^{45} erg s^{-1}
θ	2.86	degrees
Γ	18	

To model the SED we used a homogeneous one-zone synchrotron self Compton (SSC; Marscher & Gear 1985; Maraschi et al. 1992; Bloom & Marscher 1996) model, plus the contribution of external Compton scattering of both direct-disk radiation (ECD; Dermer et al. 1992) and photons from the broad line region (BLR) clouds (ECC; Sikora et al. 1994). The strong thermal features usually observed in FSRQs (and in this blazar in particular, see Neugebauer et al. 1978; Smith et al. 1988) at optical/UV frequencies suggest that the environment is rich in the soft photons produced by the accretion disk and/or reprocessed by the BLR. This implies that the energy density of the external soft radiation is much higher than for the synchrotron radiation; therefore, during the γ-ray flares in FSRQs, the most important processes are the ECC and ECD, and the γ-ray photon index could be determined by the dominant contribution of the two.

We consider a moving spherical blob of radius R, filled by relativistic electrons and embedded in a random magnetic field. We assume that the electron energy density distribution is described by a broken power law:

$$n_{\rm e}(\gamma) = \frac{K\gamma_{\rm b}^{-1}}{(\gamma/\gamma_{\rm b})^{p_1} + (\gamma/\gamma_{\rm b})^{p_2}} \quad (1)$$

where γ is the electron Lorentz factor assumed to vary between $\gamma_{\rm min}$ and $\gamma_{\rm max}$, p_1 and p_2 are pre- and post-break electron distribution spectral indexes, respectively, and $\gamma_{\rm b}$ is the break energy Lorentz factor. We assume that the blob contains a comoving random average magnetic field B with a bulk Lorentz factor Γ at an angle θ with respect to the line of sight. The relativistic Doppler beaming factor is then $\delta = [\Gamma(1\text{-}\beta\cos\theta)]^{-1}$, and K is the normalization density parameter into the blob.

We have chosen an angle of view of 0.05 rad in agreement with both the apparent jet velocities derived from multiepoch Very Long Baseline Array (VLBA) observations of the source (Homan et al. 2001; Wardle et al. 2005; Jorstad et al. 2005; Lister et al. 2009) and the value used by Kataoka et al. (2008).

The short time variability observed in γ-ray band constrains the size of the emitting region to $R < c\Delta t_{\rm var}\delta/(1+z) = 3.86 \times 10^{16}$ cm, where $\Delta t_{\rm var}$ is the observed variation time. An accretion

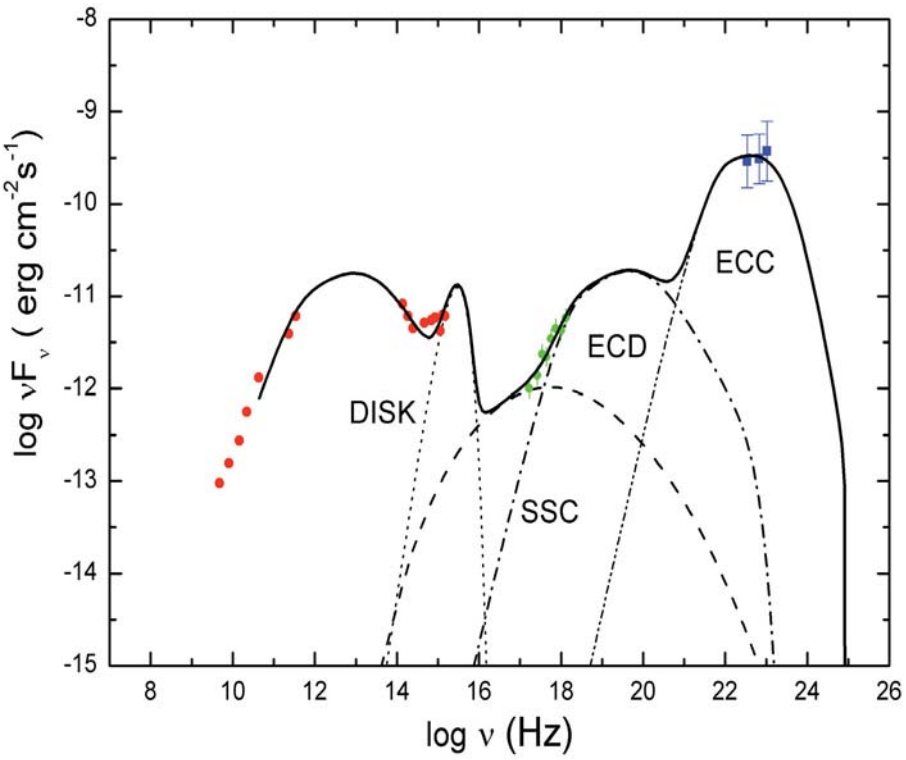

Fig. 3. Spectral energy distribution of PKS 1510-089 for the AGILE-GRID observation of 17–21 March 2008, including quasi-simultaneous GASP radio-to-optical data, the *Swift*/UVOT data of 20–22 March and the *Swift*/XRT data of 20 March. The dotted, dashed, dot-dashed, and double-dot-dashed lines represent the accretion disk black body, the SSC, the ECD, and the ECC radiation, respectively.

disk characterized by a black body spectrum with a luminosity of 5×10^{45} erg s^{-1}, as estimated with UV observations by Pian & Treves (1993), at 0.05 pc from the blob is assumed as one of the sources of external target photons. We also assumed a BLR at 0.2 pc, reprocessing 10% of the irradiating continuum. The IC spectra derived from the approximation of the BLR radiation as a black body reproduces more refined spectra calculated by Tavecchio et al. (2008) quite well when taking the more accurate shape of the BLR into account.

Assuming a model with synchrotron, SSC and EC components plus the contribution from the accretion disk radiation, the SED of mid March 2008 can be represented well with input parameters summarized in Table 2. In the choice of the parameters we were guided by the knowledge of the angle of view, the disk luminosity and the simultaneous observations of the synchrotron and IC peak regions (therefore of the synchrotron and IC peak frequencies and luminosities). In addition, the minimum variability timescale gives an indication of the size of the emitting region. However, even if these quantities are quite tightly constrained by fitting the whole SED, the choice of some parameters is not unique because the simultaneous presence of the synchrotron, SSC, ECC, and ECD components leads to a possible partial degeneration of the parameters.

5.2. X-ray spectral evolution

The spectral evolution detected in X-rays by *Swift* in just two days, soon after the γ-ray flaring episode is another hint of the rapid change in activity by this source. Usually in FSRQs as PKS 1510–089 only little variability is observed in X-rays on short timescales from hours to days, and also on longer timescales the X-ray spectral shape is almost constant with only small variations. The photon indices measured by *Swift*/XRT in March 2008, in particular during the first observation, tend to be lower than usually observed in FSRQs ($\langle\Gamma_{[0.1-2.4]}\rangle = 1.76 \pm 0.06$ and $\langle\Gamma_{[2-10]}\rangle = 1.65 \pm 0.04$, Donato et al. 2001) and are more like those observed in some high-redshift quasars (such as RBS 315, Tavecchio et al. 2007, and Swift J0746+2548, Sambruna et al. 2007). The hard photon indices of high-redshift blazars could be interepreted in terms of absorption by warm plasma in the region surrounding the source, in agreement with a scenario where in the early evolution phases the quasars are substantially obscured by gas subsequently expelled from the host galaxy by powerful winds (see e.g. Fabian 1999). However, considering the low redshift, this interpretation is unlikely for this source.

Instead, the X-ray spectral evolution observed by *Swift*/XRT could be caused by the contamination of an additional component below ~2 keV: the soft X-ray excess. In fact, previous observations with *Chandra* (Gambill et al. 2004) and *Suzaku* (Kataoka et al. 2008) seem to indicate the soft X-ray excess in the spectrum of PKS 1510–089. The soft X-ray excess is an emission in excess of the extrapolation of the power-law component dominating at higher energies, but the origin of this excess in AGNs is still an open issue (see e.g. D'Ammando et al. 2008, for a detailed discussion). In the past, it was often associated with the thermal emission of the accretion disk and then related to the big blue bump. However, it has recently been shown that modeling the soft X-ray excess in non-blazar AGNs with a thermal component yields a remarkably constant disk temperature, around 0.1–0.2 keV, regardless of the central black hole mass and luminosity (Gierlinsky & Done 2004; Crummy et al. 2006). Also in Kataoka et al. (2008) the soft X-ray excess is tentatively described by a black body with temperature $kT \simeq 0.2$ keV. This result is difficult to explain in any model for the soft excess related to disk continuum emission, as the temperature in any disk model is expected to vary with both the black hole mass and the accretion rates.

For FSRQs one possible theoretical explanation is that the soft X-ray excess is a bulk Comptonization feature produced by cold plasma accelerated in a jet (Celotti et al. 2007), even if this

feature has never been positively observed until now. In BL Lac objects the radiative environment is instead too weak to produce the soft X-ray excess via bulk Compton and the soft X-ray excess is likely related to the high-energy tail of the synchrotron emission.

The change in the photon index observed during the *Swift*/XRT observations could stem from the spectral shape of the inverse Compton component in X-ray remaining roughly constant, but the amount of contamination from the soft excess emission varies. The contribution of the soft X-ray excess would be more significant when the source gets fainter, affecting the spectrum at higher energies. Unfortunately, the brief exposure of the *Swift* observation does not allow a detailed spectral modeling of this feature.

One possibility for the origin of this hard power law in PKS 1510-089 is that the photon index observed in X-rays results from the combination of the synchrotron self Compton and external Compton emission, hence from the mismatch of the spectral slopes of these two components, not to a real soft X-ray excess. This is the solution that the data presented in this paper would favor. In this context, the spectral evolution during the three *Swift*/XRT observations could come from the change in contribution of one of the two components and therefore from a different variability of the SSC and EC components.

5.3. Thermal emission components

Even if the SED of the blazars are usually dominated by the beamed nonthermal jet radiation, some of them show the signature of Seyfert-like features such as the little and the big blue bumps. The little blue bump is usually observed in quasars between ~2000 and ~4000 Å in the rest frame and likely stems from the contribution of FeII and MgII emission lines and the Balmer continuum produced in the broad line region (Wills et al. 1985). The big blue bump instead is associated with a rise in the *UV* band commonly interpreted as thermal emission from the accretion disk (see e.g. Laor 1990). Evidence of these thermal components has been found in other quasar-like blazars, such as 3C 273 (Grandi and Palumbo 2004; Türler et al. 2006), 3C 279 (Pian et al. 1999) and 3C 454.3 (Raiteri et al. 2007).

The presence of the emission by the accretion disk is consistent with the scenario in which the seed photons for the IC producing the γ-rays are external to the relativistic jet, but it is usually not observed because hidden by the beamed variable synchrotron emission. That the synchrotron component of PKS 1510−089 peaks around 10^{13} Hz (see Bach et al. 2007; Nieppola et al. 2008) allows us to observe these thermal features in this source. In fact, around 10^{15} Hz, a rising emission is visible in the spectrum and is likely a manifestation of the big blue bump produced by the accretion disk, as already discussed for this source by Malkan & Moore (1986) and Pian & Treves (1993); moreover, a hint of the little blue bump seems to appear in the SED of the source at $10^{14.5}$ Hz.

Given the redshift of PKS 1510–089, the Hα, Hβ, FeII, and MgII lines mostly contribute to the observed spectrum between $10^{14.2}$ and $10^{14.8}$ Hz, and together with the disk emission, could explain the excess of emission observed around $10^{14.5}$ Hz and not modeled from the other components represented in the SED. Moreover these non-jet components in the blue part of the spectrum of this blazar have already been observed by Neugebauer et al. (1979) and Smith et al. (1988) and it agrees with the redder-when-brighter behavior shown by the $B-R$ index versus R-band

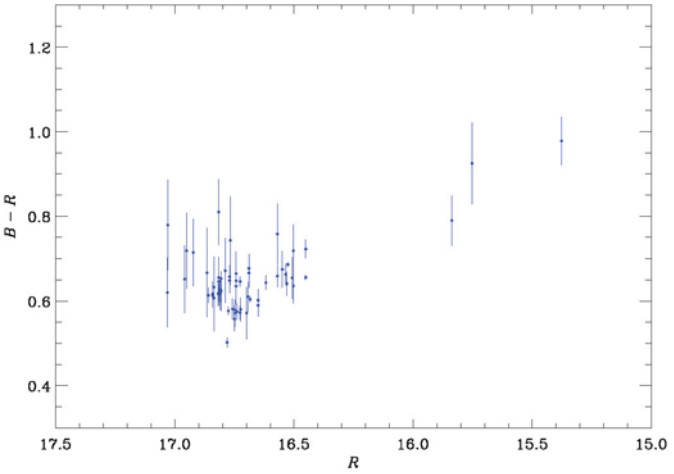

Fig. 4. $B-R$ color index versus R-band magnitude for PKS 1510–089 obtained with archive data of the Torino Observatory.

plot in Fig. 4. The plot has been obtained with archive data stored at the Torino Observatory.

5.4. Energetics and alternative model

Finally, to estimate the energetics of PKS 1510–089, we computed the isotropic luminosity in the γ-ray band, comparing it with the Eddington and bolometric luminosity and the total power transported by the jet. For a given source with redshift z, the isotropic emitted luminosity in the energy band ϵ is defined as

$$L(z)_\epsilon = \frac{4\pi F d_1^2(z)}{(1+z)^{(1-\alpha_\gamma)}}, \quad (2)$$

where, in our case, ϵ is the γ-ray energy band with $E_{\rm min}$ = 100 MeV and $E_{\rm max}$ = 10 GeV, $\alpha_\gamma = \Gamma - 1$, F the γ-ray energy flux between $E_{\rm min}$ and $E_{\rm max}$, calculated from the photon flux F_γ ($E > 100$ MeV) as suggested by Ghisellini et al. (2009):

$$F = 1.6\times10^{-12}\frac{\alpha_\gamma F_\gamma}{1-\alpha_\gamma}\left[100^{1-\alpha_\gamma}-1\right]. \quad (3)$$

The luminosity distance is given by

$$\mathrm{d_l}(z_1,z_2) = (1+z_2)^2 \times \frac{c/H_0}{1+z_2}\int_{z_1}^{z_2}[E(z)]^{-1}\mathrm{d}z, \quad (4)$$

where $z_1 = 0$, $z_2 = z_{\rm src}$, and

$$E(z) = \sqrt{\Omega_{\rm m}(1+z)^3 + (1-\Omega_{\rm m}-\Omega_\Lambda)(1+z)^2 + \Omega_\Lambda}, \quad (5)$$

where H_0 is the Hubble constant, and Ω_m and Ω_Λ are the contribution of the matter and of the cosmological constant, respectively, to the density parameter. Using a luminosity distance d_L = 1915 Mpc and the average γ-ray flux observed by the AGILE-GRID during 17–21 March 2008, we obtained an isotropic luminosity $L_\gamma^{\rm iso} = 5.3\times10^{47}$ erg s^{-1} for PKS 1510–089 ($z = 0.361$).

The power carried by the jet in the form of magnetic field ($L_{\rm B}$), cold protons ($L_{\rm p}$), relativistic electrons ($L_{\rm e}$), and produced radiation ($L_{\rm rad}$), are

$$L_{\rm p} = \pi R^2 \Gamma^2 c \int [N(\gamma)\, m_{\rm p}\, c^2\, \mathrm{d}\gamma] = 3.6\times10^{45}\ \mathrm{erg\,s^{-1}} \quad (6)$$

$$L_{\rm e} = \pi R^2 \Gamma^2 c \int [N(\gamma)\, \gamma\, m_{\rm e}\, c^2\, {\rm d}\gamma] = 1.5 \times 10^{44}\ {\rm erg\ s^{-1}} \quad (7)$$

$$L_{\rm B} = \pi R^2 \Gamma^2 c\, U_{\rm B} = 1.5 \times 10^{45}\ {\rm erg\ s^{-1}} \quad (8)$$

$$L_{\rm rad} \simeq L_{\rm iso} \Gamma^2 / \delta^4 = 5.3 \times 10^{45}\ {\rm erg\ s^{-1}}, \quad (9)$$

where $U_{\rm B}$ is the magnetic energy density. Therefore the total power transported by the jet is $P = L_{\rm B} + L_{\rm p} + L_{\rm e} + L_{\rm rad} = 1.1 \times 10^{46}$ erg s^{-1}.

Assuming a black hole mass $M_{\rm BH} = 4.5 \times 10^8\ M_\odot$ for the source (Woo & Urry 2002), we obtain an Eddington luminosity

$$L_{\rm Edd} = \frac{4\pi\, G\, c\, m_H}{\sigma_T} M_{\rm BH} = 5.7 \times 10^{46}\ {\rm erg\ s^{-1}} \quad (10)$$

to be compared with the bolometric luminosity $L_{\rm bol} = 2.4 \times 10^{46}$ erg s^{-1} reported in Woo & Urry (2002).

An alternative theoretical model has recently been proposed by Kataoka et al. (2008) to interpret the data of PKS 1510–089 collected during August 2006, with the high-energy emission originated by the Comptonization of infrared radiation produced by the molecular torus surrounding the central engine and suggesting that the soft X-ray excess could be produced by the IC scattering of external photons by a population of cold electrons, as discussed by Begelman et al. (1987) and Celotti et al. (2007). An accurate theoretical interpretation of the SED is beyond the scope of this paper; however, our data do not seem to rule out this alternative model. In fact, we do not have simultaneous observations in FIR band that can confirm the excess detected by IRAS (Tanner et al. 1996), interpreted by Kataoka et al. as due to dust radiation from the nuclear torus and assumed to be the main source of seed photons for the IC mechanism. Moreover, the bulk Comptonization feature should not be observable during a high activity state of the source, such as observed in mid-March 2008, because overwhelmed by the SSC and ECD emission, therefore this is not the best situation for testing this hypothesis.

Further X-ray observations with XMM-*Newton* and *Suzaku*, simultaneously with the optical monitoring by means of the REM Telescope and WEBT Consortium, could give strong indications of the emission mechanisms involved in this source, in particular of the real nature of the soft X-ray excess, Seyfert-like features in the spectrum, and the possibility of the bulk Comptonization feature.

Finally, with two γ-ray satellites, AGILE and *Fermi*, in orbit at the same time, we will be able to study the source behavior at high energies in detail on a long timescale, even if a wide multiwavelength coverage is needed to achieve a complete understanding of the structure of the jet, the origin of the seed photons for the inverse Compton process, and all the emission mechanisms working in this blazar.

Acknowledgements. We thank the anonymous referee for the useful comments. The AGILE Mission is funded by the Italian Space Agency (ASI) with scientific participation by the Italian Institute of Astrophysics (INAF) and the Italian Institute of Nuclear Physics (INFN). We acknowledge the use of public data from the Swift data archive. We thank the Swift Team for making these observations possible, particularly the duty scientists and science planners. The Submillimeter Array is a joint project between the Smithsonian Astrophysical Observatory and the Academia Sinica Institute of Astronomy and Astrophysics and is funded by the Smithsonian Institution and the Academia Sinica. UMRAO is funded by a series of grants from the NSF and by the University of Michigan. The research has been supported by the Taiwan National Science Council grant No. 96-2811-M-008-058. This paper is partly based on observations carried out at the German-Spanish Calar Alto Observatory, which is jointly operated by the MPIA and the IAA-CSIC. Acquisition of the MAPCAT data is supported in part by the Spanish "Ministerio de Ciencia e Innovación" through grant AYA2007-67626-C03-03. Some of the authors acknowledge financial support by the Italian Space Agency through contract ASI-INAF I/088/06/0 for the Study of High-Energy Astrophysics.
Facilities: AGILE, *Swift*, UMRAO and WEBT.

References

Abdo, A. A., Ackermann, M., Ajello, M., et al. 2009, ApJ, 700, 597
Arnaud, K. A. 1996, Astronomical Data Analysis Software and Systems V, ed. G. Jacoby, & J. Barnes, ASP Conf. Ser., 101, 17
Bach, U., Raiteri, C. M., Villata, M., et al. 2007, A&A, 464, 175
Barbiellini, G., Bordignon, G., Fedel, G., et al. 2001, Gamma 2001: Gamma-Ray Astrophysics, ed. S. Ritz, N. Gehrels, & C. R. Shrader, Amer. Inst. Phys. Conf. Ser., 587, 754
Barthelmy, S. D., Barbier, L. M., Cummings, J. R., et al. 2005, Space Sci. Rev., 120, 143
Begelman, M. C., & Sikora, M. 1987, ApJ, 322, 650
Bessell, M. S., Castelli, F., & Plez, B. 1998, A&A, 333, 231
Blandford, R. D., & Rees, M. J. 1978, in BL Lac Objects, ed. A. M. Wolfe (Univ. Pittsburgh Press), 328
Bloom, S. D., & Marscher, A. P. 1996, ApJ, 461, 657
Bolton, J. G., & Ekers, J. 1966, Aust. J. Phys., 19, 559
Böttcher, M. 2007, Ap&SS, 309, 95
Burbidge, E. M., & Kinnan, T. D. 1966, ApJ, 145, 654
Burrows, D. N., Hill, J. E., Nousek, J. A., et al. 2005, Space Sci. Rev., 120, 165
Cardelli, J. A., Clayton, G. C., & Mathis, J. S. 1989, ApJ, 345, 245
Cash, W. 1979, ApJ, 228, 939
Celotti, A., Ghisellini, G., & Fabian, A. C. 2007, MNRAS, 375, 417
Ciprini, S., & Corbel, F. 2009, ATel, 1897
Costa, E., Barbanera, L., Feroci, M., et al. 2001, X-ray Astronomy: Stellar Endpoints, AGN, and the Diffuse X-ray Background, ed. N. E. White, et al. (New York: AIP) 599, 582
Crummy, J., Fabian, A. C., Gallo, L., et al. 2006, MNRAS, 365, 1067
Cutini, S., & Hays, E. 2009, ATel, 2033
D'Ammando, F., Bulgarelli, A., Vercellone, S., et al. 2008a, ATel, 1436
D'Ammando, F., Bianchi, S., Jiménez-Bailón, E., et al. 2008b, A&A, 482, 499
D'Ammando, F., Vercellone, S., Tavani, M., et al., 2009, ATel, 1957
Dermer, C. D., Schlickeiser, R., & Mastichiadis, A. 1992, A&A, 256, L27
Donato, D., Ghisellini, G., Tagliaferri, G., et al. 2001, A&A, 375, 739
Fabian, A. C. 1999, MNRAS, 308, L39
Feroci, M., Costa, E., Soffitta, P., et al. 2007, Nucl. Instr. Meth. Phys. Res. A, 581, 728
Gambill, J. K., Sambruna, R. M., Chartas, G., et al. 2003, A&A, 401, 505
Gehrels, N., Chincarini, G., Giommi, P., et al. 2004, ApJ, 611, 1005
Ghisellini, G., Maraschi, L., & Tavecchio, F. 2009, MNRAS, 396, L105
Gierlinski, M., & Done, C. 2004, MNRAS, 349, L7
Giuliani, A., Chen, A., Mereghetti, S., et al. 2004, Mem. Soc. Astron. Italiana Suppl., 5, 135
Giuliani, A., Cocco, V., Mereghetti, S., et al. 2006, Nucl. Instr. Meth. Phys. Res. A, 568, 692
Grandi, P., & Palumbo, G. 2004, Science, 306, 998
Jorstad, S. G., Marscher, A. P., Lister, M. L., et al. 2005, AJ, 130, 1418
Hartman, R. C., Bertsch, D. L., Fichtel, C. E., et al. 1992, NASCP, 3137, 116
Hartman, R. C., Bertsch, D. L., Bloom, S. D., et al. 1999, ApJS, 123, 79
Kalberla, P. M. W., Button, W. B., Hartmann, D., et al. 2005, A&A, 440, 775
Kataoka, J., Mattox, J. R., Quinn, J., et al. 1999, ApJ, 514, 138
Kataoka, J., Madejski, G., Sikora, M., et al. 2008, ApJ, 672, 787
Labanti, C., Marisaldi, M., Fuschino, F., et al. 2009, Nucl. Instr. Meth. Phys. Res. A, 598, 470
Laor, 1990, MNRAS, 246, L369, 5
Lawson, A. J., & Turner, M. J. L. 1997, MNRAS, 288, 920
Lister, M. L., Homan, D. C., Kadler, M., et al. 2009, ApJ, 696, L22
Malkan, M. A., & Moore, R. L. 1986, ApJ, 300, 216
Maraschi, L., Ghisellini, G., & Celotti, A. 1992, ApJ, 397, L5
Marscher, A. P., & Gear, W. K. 1985, ApJ, 298, 114
Massaro, F., Tramacere, A., Cavaliere, A., et al. 2008, A&A, 478, 395
Mattox, J. R. 1993, ApJ, 410, 609
Mattox, J. R., Bertsch, D. L., Chiang, J., et al. 1996, ApJ, 461, 396
Neugebauer, G., Oke, J. B., Becklin, E. E., et al. 1979, ApJ, 230, 79
Nieppola, E., Valtoja, E., Tornikoski, M., et al. 2008, A&A, 488, 867
Perotti, F., Fiorini, M., Incorvaia, S., et al. 2006, Nucl. Instr. Meth. Phys. Res. A, 556, 228
Pian, E., & Treves, A. 1993, ApJ, 416, 130

Pian, E., Urry, C. M., Maraschi, L., et al. 1999, ApJ, 521, 112
Poole, T. S., Breeveld, A. A., Page, M. J., et al. 2008, MNRAS, 383, 627
Prest, M., Barbiellini, G., Bordignon, G., et al. 2003, Nucl. Instr. Meth. Phys. Res. A, 501, 280
Pucella, G., Vittorini, V., D'Ammando, F., et al. 2008, A&A, 491, L21
Pucella, G., D'Ammando, F., Tavani, M., et al., 2009, ATel, 1968
Raiteri, C. M., Villata, M., Lanteri, L., et al. 1998, A&AS, 130, 495
Raiteri, C. M., Villata, M., Larionov, V. M., et al. 2007, A&A, 473, 819
Raiteri, C. M., Villata, M., Larionov, V. M., et al. 2008, A&A, 491, 755
Roming, P. W. A., Kennedy, T. E., Mason, K. O., et al. 2005, Space Sci. Rev., 120, 95
Sambruna, R. M., Barr, P., Giommi, P., et al. 1994, ApJS, 95, 371
Sambruna, R. M., Tavecchio, F., Ghisellini, G., et al. 2007, ApJS, 669, 884
Siebert, J., Brinkmann, W., Drinkwater, M. J., et al. 1998, MNRAS, 301, 261
Sikora, M., Begelman, M. C., & Rees, M. J. 1994, ApJ, 421, 153
Singh, K. P., Rao, A. R., & Vahia, M. N. 1990, ApJ, 365, 455
Singh, K. P., Shrader, C. R., & George, I. M. 1997, ApJ, 491, 515
Smith, P. S., Elston, R., & Berriman, R. G. 1988, ApJ, 326, L39
Tanner, A. M., Bechtold, J., Walker, C. E., et al. 1996, AJ, 112, 62
Tavani, M., Barbiellini, G., Argan, A., et al. 2008, Nucl. Instr. Meth. Phys. Res. A, 588, 52
Tavani, M., Barbiellini, G., Argan, A., et al. 2009, A&A, 502, 995
Tavecchio, F., & Ghisellini, G. 2008, MNRAS, 386, 945 980
Tavecchio, F., Maraschi, L., Ghisellini, G., et al. 2000, ApJ, 543, 535
Tavecchio, F., Maraschi, L., Ghisellini, G., et al. 2007, ApJ, 665, 980
Tramacere, A., Massaro, F., & Cavaliere, A. 2007, A&A, 463, 521
Tramacere, A. 2008, ATel, 1743
Türler, M., Chernyakova, M., Courvoisier, T. J.-L., et al. 2006, A&A , 451, L1
Ulrich, M., Maraschi, L., & Megan, C. M. 1997, ARA&A, 35, 445
Urry, C. M., & Padovani, P. 1995, Publ. Astron. Soc. Pac. J. Phys., 107, 803
Vercellone, S., Chen, A. W., Giuliani, A., et al. 2008, ApJ, 676, L13
Vercellone, S., D'Ammando, F., Pucella, G., et al. 2009, ATel, 1976
Villata, M., Raiteri, C. M., Aller, M. F., et al. 2007, A&A, 464, L5
Villata, M., Raiteri, C. M., Larionov, V. M., et al. 2008, A&A, 481, L79
Wardle, J. F. C., Homan, D. C., Cheung, C. C., et al. 2005, ASPC, 340, 67
Wills, B. J, Netzer, H., & Wills, D. 1985, ApJ, 288, 94
Woo, J., & Urry, C. M. 2002, ApJ, 579, 530

[1] INAF/IASF – Roma, via Fosso del Cavaliere 100, 00133 Roma, Italy
e-mail: filippo.dammando@iasf-roma.inaf.it
[2] Dip. di Fisica, Univ. di Roma "Tor Vergata", via della Ricerca Scientifica 1, 00133 Roma, Italy
[3] INAF, Oss. Astronomico di Torino, via Osservatorio 20, 10025 Pino Torinese (Torino), Italy
[4] CIFS – Torino, viale Settimio Severo 3, 10133 Torino, Italy
[5] INAF, Istituto di Astrofisica Spaziale e Fisica Cosmica, via U. La Malfa 153, 90146 Palermo, Italy
[6] Dip. di Fisica and INFN Trieste, via Valerio 2, 34127 Trieste, Italy
[7] INFN – Pavia, via Bassi 6, 27100 Pavia, Italy
[8] Dip. di Fisica Nucleare e Teorica, Univ. di Pavia, via Bassi 6, 27100 Pavia, Italy
[9] INAF/IASF – Bologna, via Gobetti 101, 40129 Bologna, Italy
[10] INAF/IASF – Milano, via E. Bassini 15, 20133 Milano, Italy
[11] Dip. di Fisica Generale dell'Universitá, via P. Giuria 1, 10125 Torino, Italy
[12] ENEA – Bologna, via dei Martiri di Monte Sole 4, 40129 Bologna, Italy
[13] INFN – Roma "La Sapienza", Piazzale A. Moro 2, 00185 Roma, Italy
[14] INFN – Roma "Tor Vergata", via della Ricerca Scientifica 1, 00133 Roma, Italy
[15] INAF – Oss. Astronomico di Cagliari, loc. Poggio dei Pini, strada 54, 09012 Capoterra (CA), Italy
[16] Dip. di Fisica, Univ. dell'Insubria, via Valleggio 11, 22100 Como, Italy
[17] ENEA – Roma, via E. Fermi 45, 00044 Frascati (Roma), Italy
[18] Instituto de Astrofísica de Andalucía, CSIC, Apartado 3004, 18080 Granada, Spain
[19] Department of Astronomy, University of Michigan, Ann Arbor, MI 48109, USA
[20] Pulkovo Observatory, Russian Academy of Sciences, 196140 St.-Petersburg, Russia
[21] MPIfR, 53121 Bonn, Germany
[22] Instituto de Astronomia, Universidad Nacional Autonoma de Mexico, Mexico, D. F. Mexico
[23] Tuorla Observatory, Department of Physics and Astronomy, University of Turku, Väisäläntie 20, 21500 Piikkiö, Finland
[24] Astron. Inst., St.-Petersburg State Univ., 198504 St.-Petersburg, Russia
[25] INAF – Osservatorio Astrofisico di Catania, via S. Sofia 78, 95123 Catania, Italy
[26] Institute of Astronomy, National Central University, Taiwan
[27] Lulin Observatory, Institute of Astronomy, National Central University, Taiwan
[28] INAF, Osservatorio Astronomico di Roma, via di Frascati 33, 00040, Monte Porzio Catone, Italy
[29] INAF, Osservatorio Astronomico di Collurania, via Mentore Maggini, 64100 Teramo, Italy
[30] Harvard-Smithsonian Center for Astrophysics, Cambridge, Garden st. 60, MA 02138, USA
[31] Institute for Astrophysical Research, Boston University, 725 Commonwealth Avenue, Boston, MA 02215, USA
[32] ZAH, Landessternwarte Heidelberg, Königstuhl, 69117 Heidelberg, Germany
[33] Instituto de Astronomia, Universidad Nacional Autonoma de Mexico, 2280 Ensenada, B.C. Mexico
[34] Abastumani Observatory, 383762 Abastumani, Georgia
[35] INAF – IRA, contrada Renna Bassa, 96017 Noto (SR), Italy
[36] Department of Physics and Astronomy, University of Southampton S17 1BJ, UK
[37] INAOE, Apdo. Postal 51 y 216, 72000 Tonantzintla, Puebla, Mexico
[38] Lowell Observatory, Flagstaff, AZ 86001, USA
[39] ASI-ASDC, via G. Galilei, 00044 Frascati (Roma), Italy
[40] ASI, viale Liegi 26, 00198 Roma, Italy

The Astrophysical Journal, 707:1115–1123, 2009 December 20 doi:10.1088/0004-637X/707/2/1115

MULTIWAVELENGTH OBSERVATIONS OF 3C 454.3. II. THE *AGILE* 2007 DECEMBER CAMPAIGN

I. Donnarumma[1,25], G. Pucella[1], V. Vittorini[1], F. D'Ammando[1,2], S. Vercellone[3], C. M. Raiteri[4], M. Villata[4], M. Perri[5], W. P. Chen[6], R. L. Smart[4], J. Kataoka[7], N. Kawai[7], Y. Mori[7], G. Tosti[8], D. Impiombato[8], T. Takahashi[9], R. Sato[9], M. Tavani[1,2], A. Bulgarelli[10], A. W. Chen[11], A. Giuliani[11], F. Longo[12], L. Pacciani[1], A. Argan[1], G. Barbiellini[12], F. Boffelli[13], P. Caraveo[11], P. W. Cattaneo[13], V. Cocco[1], T. Contessi[11], E. Costa[1], E. Del Monte[1], G. De Paris[1], G. Di Cocco[10], Y. Evangelista[1], M. Feroci[1], A. Ferrari[14,15], M. Fiorini[11], T. Froysland[14], M. Frutti[1], F. Fuschino[10], M. Galli[16], F. Gianotti[10], C. Labanti[10], I. Lapshov[1], F. Lazzarotto[1], P. Lipari[17], M. Marisaldi[10], M. Mastropietro[18], S. Mereghetti[11], E. Morelli[10], E. Moretti[12], A. Morselli[19], A. Pellizzoni[20], F. Perotti[11], G. Piano[1,2], P. Picozza[19], M. Pilia[20,21], G. Porrovecchio[1], M. Prest[21], M. Rapisarda[22], A. Rappoldi[13], A. Rubini[1], S. Sabatini[1], E. Scalise[1], P. Soffitta[1], E. Striani[1,2], M. Trifoglio[10], A. Trois[1], E. Vallazza[12], A. Zambra[11], D. Zanello[17], C. Pittori[5], P. Santolamazza[5], F. Verrecchia[5], P. Giommi[5], L. A. Antonelli[23], S. Colafrancesco[5], and L. Salotti[24]

[1] INAF/IASF–Rome, Via del Fosso del Cavaliere 100, I-00133 Rome, Italy; immacolata.donnarumma@iasf-roma.inaf.it
[2] Dip. di Fisica, Univ. "Tor Vergata," Via della Ricerca Scientifica 1, I-00133 Rome, Italy
[3] INAF/IASF Palermo Via Ugo La Malfa 153, 90146 Palermo, Italy
[4] INAF/OATo, Via Osservatorio 20, I-10025 Pino Torinese, Italy
[5] ASI–ASDC, Via G. Galilei, I-00044 Frascati (Rome), Italy
[6] Institute of Astronomy, National Central University, Taiwan
[7] Department of Physics, Tokyo Institute of Technology, Tokyo, Japan
[8] Dip. di Fisica, Univ. di Perugia, Via Pascoli, I-06123 Perugia, Italy
[9] ISAS/JAXA, 3-1-1 Yoshinodai, Sagamihara, Kanagawa 229-8510, Japan
[10] INAF/IASF–Bologna, Via Gobetti 101, I-40129 Bologna, Italy
[11] INAF/IASF–Milano, Via E. Bassini 15, I-20133 Milan, Italy
[12] Dip. di Fisica and INFN Trieste, Via Valerio 2, I-34127 Trieste, Italy
[13] INFN–Pavia, Via Bassi 6, I-27100 Pavia, Italy
[14] CIFS–Torino, Viale Settimio Severo 63, I-10133 Turin, Italy
[15] Dip. di Fisica Generale dell'Universitá, Via Pietro Giuria 1, I-10125 Turin, Italy
[16] ENEA, Via Martiri di Monte Sole 4, I-40129 Bologna, Italy
[17] INFN–Rome "La Sapienza," Piazzale A. Moro 2, I-00185 Rome, Italy
[18] Consiglio Nazionale delle Ricerche, Istituto Metodologie Inorganiche e dei Plasmi, Area Ricerca Montelibretti (Rome), Italy
[19] INFN–Rome "Tor Vergata," Via della Ricerca Scientifica 1, I-00133 Rome, Italy
[20] INAF-Osservatorio Astronomico di Cagliari, localit Poggio dei Pini, Strada 54, I-09012 Capoterra, Italy
[21] Dip. di Fisica, Univ. dell'Insubria, Via Valleggio 11, I-22100 Como, Italy
[22] ENEA–Rome, Via E. Fermi 45, I-00044 Frascati (Rome), Italy
[23] Osservarorio Astronomico di Rome, Monte Porzio Catone (Rome), Italy
[24] ASI, Viale Liegi 26, I-00198 Rome, Italy
Received 2009 June 23; accepted 2009 October 29; published 2009 December 2

ABSTRACT

We report on the second *Astrorivelatore Gamma a Immagini Leggero* (*AGILE*) multiwavelength campaign of the blazar 3C 454.3 during the first half of 2007 December. This campaign involved *AGILE*, *Spitzer*, *Swift*, *Suzaku*, the Whole Earth Blazar Telescope (WEBT) consortium, the Rapid Eye Mount (REM), and the Multicolor Imaging Telescopes for Survey and Monstrous Explosions (MITSuME) telescopes, offering a broadband coverage that allowed for a simultaneous sampling of the synchrotron and inverse Compton (IC) emissions. The two-week *AGILE* monitoring was accompanied by radio to optical monitoring by WEBT and REM, and by sparse observations in mid-infrared and soft/hard X-ray energy bands performed by means of Target of Opportunity observations by *Spitzer*, *Swift*, and *Suzaku*, respectively. The source was detected with an average flux of $\sim 250 \times 10^{-8}$ photons cm^{-2} s^{-1} above 100 MeV, typical of its flaring states. The simultaneous optical and γ-ray monitoring allowed us to study the time lag associated with the variability in the two energy bands, resulting in a possible $\lesssim$one-day delay of the γ-ray emission with respect to the optical one. From the simultaneous optical and γ-ray fast flare detected on December 12, we can constrain the delay between the γ-ray and optical emissions within 12 hr. Moreover, we obtain three spectral energy distributions (SEDs) with simultaneous data for 2007 December 5, 13, and 15, characterized by the widest multifrequency coverage. We found that a model with an external Compton on seed photons by a standard disk and reprocessed by the broad-line regions does not describe in a satisfactory way the SEDs of 2007 December 5, 13, and 15. An additional contribution, possibly from the hot corona with $T = 10^6$ K surrounding the jet, is required to account simultaneously for the softness of the synchrotron and the hardness of the IC emissions during those epochs.

Key words: galaxies: active – galaxies: individual (3C 454.3) – galaxies: jets – gamma rays: observations – quasars: general – radiation mechanisms: non-thermal

Online-only material: color figures

1. INTRODUCTION

3C 454.3 is a flat spectrum radio quasar at redshift $z = 0.859$. It is one of the brightest extragalactic radio sources with superluminal motion hosting a radio and an X-ray jet. It has been observed in almost all the electromagnetic spectrum from radio up to γ-ray energies; the spectral energy distribution (SED) has the typical double-humped shape of blazars, the first peak occurring at mid-far-infrared frequencies and the second one at MeV–GeV energies (see Ghisellini et al. 1998).

The first peak is commonly interpreted as synchrotron radiation from high-energy electrons in a relativistic jet, while the second component is due to electrons scattering on soft seed photons. In the context of a simple, homogeneous scenario, the emission at the synchrotron and inverse Compton (IC) peaks is produced by the same electron population that can self-scatter the same synchrotron photons (synchrotron self-Compton, SSC). Alternatively, the jet-electrons producing the synchrotron flux can Compton-scatter seed photons produced outside of the jet (external Compton, EC).

3C 454.3 is a highly variable blazar source. In spring 2005, 3C 454.3 experienced a strong outburst in the optical band reaching its historical maximum with $R = 12.0$ mag (Villata et al. 2006). The exceptional event triggered observations at higher energies from *Chandra* (Villata et al. 2006), *Swift* (Giommi et al. 2006), and the *International Gamma-Ray Astrophysics Laboratory* (*INTEGRAL*; Pian et al. 2006). The available data allowed the building of the spectrum of the source up to 200 keV. In particular, *INTEGRAL* detected (2005 May 15–18) the source from 3 up to 200 keV in a very bright state ($\sim 5 \times 10^{-10}$ erg cm^{-2} s^{-1}), being almost a factor of 2–3 higher than the previously observed fluxes (see Tavecchio et al. 2002). Pian et al. (2006) compared the SED in 2000 with that obtained during the 2005 outburst. They were able to describe both observed SEDs with minimal changes in the jet power, assuming that the dissipation region (where most of the radiation is produced) was inside the broad-line region (BLR) in 2000 and outside of it in 2005. On the other hand, Sikora et al. (2008) argued that X-rays and γ-rays could be produced via IC scattering of near- and mid-IR photons emitted by the hot dust: a very moderate energy density of the dust radiation is sufficient to provide the dominance of the EC luminosities over the SSC ones.

In 2007 July, the source woke up again in the optical band, reaching a maximum at $R = 12.6$ mag (Raiteri et al. 2008b). Such an increase in the optical activity triggered observations with *Swift* and the *Astrorivelatore Gamma a Immagini Leggero* (*AGILE*). Although still in its Science Verification phase, *AGILE* repointed at 3C 454.3 and detected it in high γ-ray activity. The average γ-ray flux detected by *AGILE* was the highest γ-ray flux ever detected from this blazar, $(280 \pm 40) \times 10^{-8}$ photons cm^{-2} s^{-1}(see Figure 3, lower panel, in Vercellone et al. 2008).

Ghisellini et al. (2007) reproduced the three source states in 2000, 2005, and 2007 with the model proposed in Katarzyński & Ghisellini (2007). The model assumes that the relative importance of synchrotron and SSC luminosity with respect to the EC one is controlled by the value of the bulk Lorentz factor Γ, which is associated with the compactness of the source.

Villata et al. (2007) and Raiteri et al. (2008b) suggested an alternative interpretation involving changes of the viewing angle of the different emitting regions of the jet.

In both cases, a strong degeneracy of parameters exists in both SSC and EC models especially when the γ-ray data are missing. This is the case of both SEDs in 2000 and 2005 in which historical EGRET data were used to constrain the models.

3C 454.3 exhibited outbursts several times between 2007 and 2008 (see Vercellone et al. 2008; Tosti et al. 2008; Raiteri et al. 2008a, 2008b; Vercellone et al. 2009), posing stringent constraints on its γ-ray duty cycle.

This strengthened the need for simultaneous observations in different energy bands. In the case of 3C 454.3 (and other MeV blazars), it is clear that the dominant contribution in the SED comes from IR–optical bands, where the synchrotron peak lies, and from both X-rays and γ-ray energy range, where the IC emission lies.

In this paper, we present and discuss the result of a multiwavelength campaign on 3C 454.3 during a period of intense γ-ray activity that occurred between 2007 December 1 and 16. In Section 2, we present the multiwavelength campaign, and in Sections 3–7 we present the *AGILE*, *Suzaku*, *Swift*, *Spitzer*, Rapid Eye Mount (REM), Whole Earth Blazar Telescope (WEBT), and Multicolor Imaging Telescopes for Survey and Monstrous Explosions (MITSuME) observations and data analysis; in Section 8, we analyze the γ–optical correlation and present broadband SEDs built with simultaneous data, discussing in details how they are modeled in the framework of SSC and EC scenarios. Throughout this paper, the photon indices are parameterized as $N(E) \propto E^{-\Gamma}$ (photons cm^{-2} s^{-1} keV^{-1} or MeV^{-1}). The uncertainties are given at 1σ level, unless otherwise stated.

2. THE MULTIWAVELENGTH CAMPAIGN

During the period of intense γ-ray activity showed in 2007 November (Vercellone et al. 2009), *AGILE* continued the pointing toward 3C 454.3 for the first half of 2007 December. The persistent high γ-ray activity of the source stimulated us to activate a new multiwavelength campaign.

AGILE data were collected between 2007 December 1 and 2007 December 16. *Suzaku* data were collected during a dedicated Target of Opportunity (ToO) performed on December 5, whereas the *Spitzer* data were collected on December 13 and 15, thanks to a granted Director's Discretionary Time (DDT) observation.

During these two days, a ToO with *Swift* data was activated for a total exposure of 9 ks.

During the whole *AGILE* observation, the source was monitored in radio-to-optical bands by WEBT (see Raiteri et al. 2008a). In addition, observations in the NIR and optical energy bands by REM occurred between December 1 and 8. Moreover, optical data from the MITSuME telescope are available on this source until December 6. In the following sections, we report on the details of the observations and the data analysis for each instrument.

3. *AGILE* OBSERVATION

AGILE (Tavani et al. 2008, 2009) is a mission of the Italian Space Agency (ASI) for the exploration of γ-ray sky, operating in a low Earth orbit since 2007 April 23. The *AGILE* scientific instrument (Prest et al. 2003; Perotti et al. 2006; Labanti et al. 2009) is very compact and combines four active detectors yielding simultaneous coverage in γ-rays, 30 MeV–30 GeV, and in hard X-ray energy band, 18–60 keV (Feroci et al. 2007).

[25] *AGILE* Team corresponding author

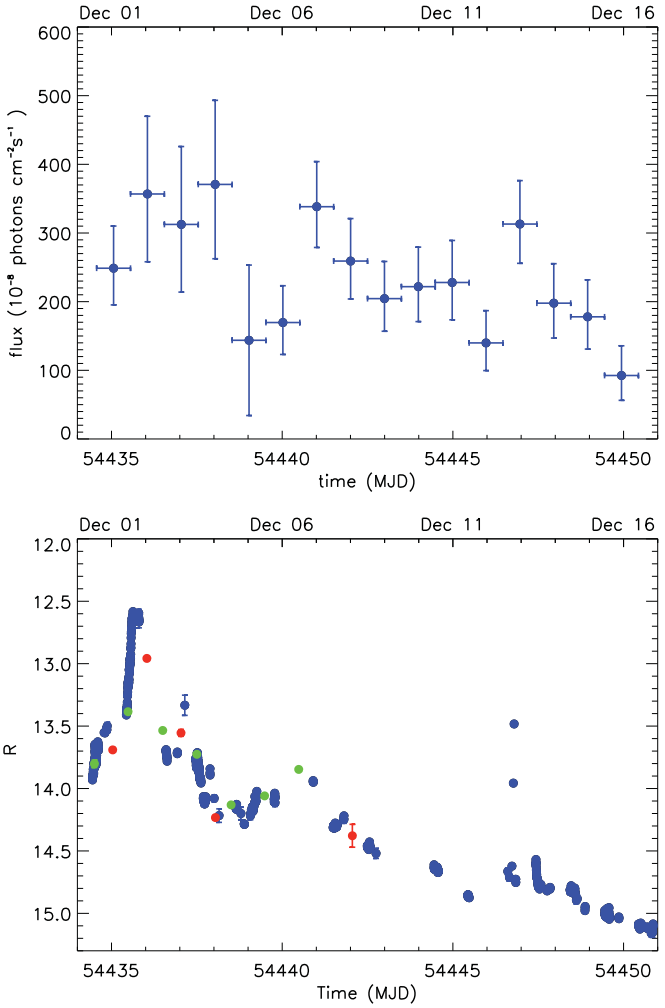

Figure 1. Top panel: *AGILE*-GRID γ-ray light curve of 3C 454.3 at one-day resolution for $E > 100$ MeV in units of 10^{-8} photons cm^{-2} s^{-1} during the period from 2007 November 30 to December 16; bottom panel: *R*-band light curve obtained by WEBT (blue circles), REM (red circles), and MITSuME (green circles) between November 30 and December 16.

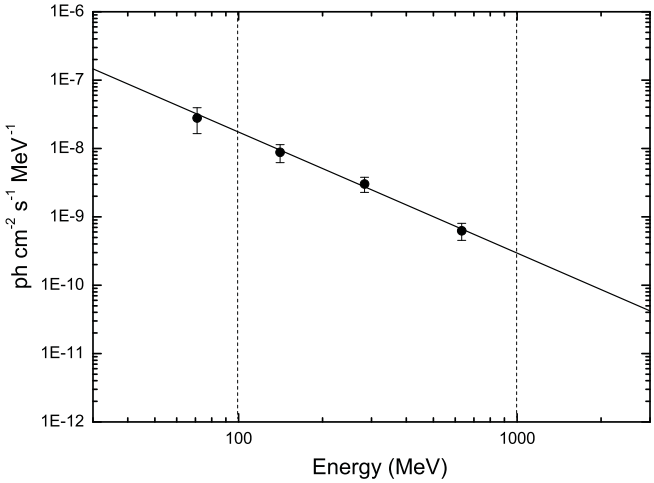

Figure 2. Gamma-ray photon spectrum of 3C 454.3 during the observation period 2007 December 5–16. Only the energy bins above 100 MeV were taken into account in the spectral fitting. The solid line corresponds to a power-law function with a photon index of $\Gamma = 1.78 \pm 0.14$.

The *AGILE* observations of 3C 454.3 were performed between 2007 December 1 and 16, for a two-week total pointing duration. In the first period, between December 1 and 5, the source was located ∼45° off the *AGILE* pointing direction. In the second period, between December 5 and 16, after a satellite re-pointing, the source was located at ∼30° off-axis (variable by ∼1° per day due to the pointing drift) to increase the significance of the detection.

AGILE-Gamma Rays Imaging Detector (*AGILE*-GRID) data were analyzed using the Standard Analysis Pipeline. Counts, exposure, and Galactic background maps were created with a bin size of 0.°3 × 0.°3 for photons with energy greater than 100 MeV. To reduce the particle background contamination we selected only events flagged as confirmed γ-ray events, and all events collected during the South Atlantic Anomaly were rejected. We also reduced the γ-ray Earth albedo contamination by excluding regions within ∼10° from the Earth limb.

The two-week data have been divided into two sets taking into account the two different pointings during which the source shifted from ∼45° to ∼30° off-axis: the first set between UTC 2007 December 1 13:21 and UTC 2007 December 5 12:34; and the second set between UTC 2007 December 5 12:35 and 2007 December 16 10:27 (in Figure 1, top panel, we also report the γ-ray flux of one day before). The first set required a more detailed analysis due to uncertainty on calibration for large off-axis angles in the field of view (FoV).

We ran the *AGILE* maximum likelihood procedure on each data set in order to obtain the average flux as well as the daily values in the γ-ray band, according to Mattox et al. (1996). The average fluxes obtained by integrating separately the two data sets are $(280 \pm 50) \times 10^{-8}$ photons cm^{-2} s^{-1}($\sqrt{(TS)} \sim 8$) and $(210 \pm 16) \times 10^{-8}$ photons cm^{-2} s^{-1}($\sqrt{(TS)} \sim 20$) for the first and second periods, respectively. The source was always detected on the two-week period with a daily integration time. The one-day binned light curve shows three enhancements of the emission around December 4, December 7, and December 13 (see Figure 1, top panel). In particular, the last two enhancements are characterized by a sharp increase of the emission followed by a slow recovery. We accumulated the spectrum over the second set of data in which the source was positioned within 30° in the *AGILE*-GRID FoV, where the most significant energy spectrum can be extracted due to the higher statistical quality. The spectral fit was performed by using only data between 100 MeV and 1 GeV (which are better calibrated) although in Figure 2, we report also the energy bin below 100 MeV. It resulted in a power law with a photon index of $\Gamma = 1.78 \pm 0.14$. We note that the current *AGILE* response is calibrated up to 1 GeV, and that the energy flux above 1 GeV is underestimated by a factor of 2–3. This prevented us from discussing any possible spectral break above 1 GeV as found by *Fermi* (Abdo et al. 2009). However, we note that the *AGILE* spectrum seems to be harder than the one inferred by *Fermi* below ∼3 GeV. The different energy range and the non-simultaneity of the data could explain the difference between the photon indices.

SuperAGILE did not detect the source during the two-week *AGILE* pointing. A deep 3σ upper limit of ∼10 mcrab was derived integrating all the data in which the source was within 30° in the FoV (net source exposure of 360 ks).

4. *SUZAKU* OBSERVATION

Following the *AGILE* detection of the flaring state, 3C 454.3 was observed with *Suzaku* (Mitsuda et al. 2007) on 2007 December 5 as a ToO, with a total duration of 40 ks. *Suzaku*

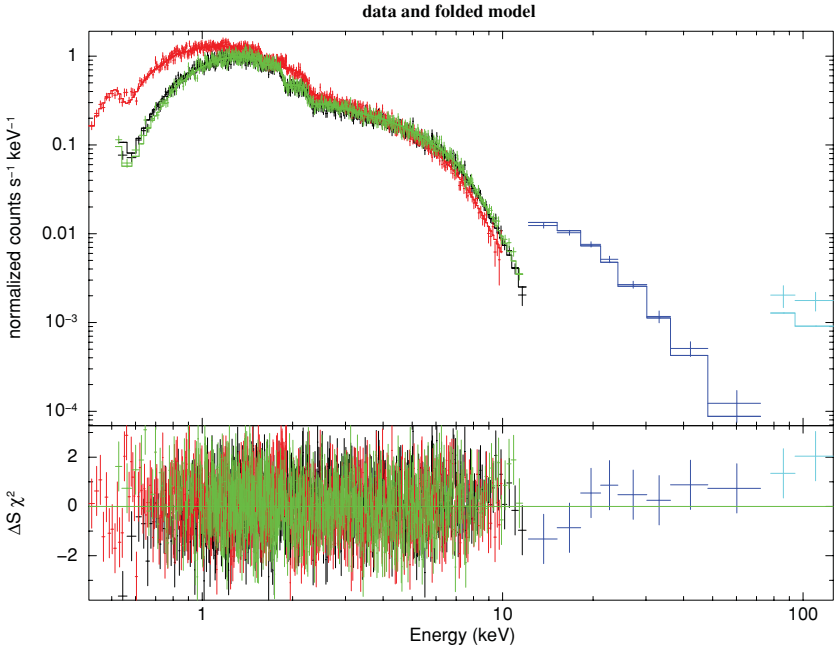

Figure 3. *Suzaku* broadband spectrum (XIS, PIN, GSO) of 3C 454.3 for the observation carried out in 2007 December. In the folded model, a single power law over the whole energy range is assumed; see the text for details. In the online journal, black, red, and green colors refer to XIS0, XIS1, and XIS3, respectively; blue points to PIN; cyan points to GSO.

(A color version of this figure is available in the online journal.)

carries four sets of X-ray telescopes (Serlemitsos et al. 2007), each one equipped with a focal-plane X-ray CCD camera (X-ray Imaging Spectrometer, XIS; Koyama et al. 2007) that is sensitive in the energy range of 0.3–12 keV, together with a non-imaging hard X-ray detector (HXD; Takahashi et al. 2007; Kokubun et al. 2007), which covers the 10–600 keV energy band with Si PIN photodiodes and GSO scintillation detectors. 3C 454.3 was focused on the nominal center position of the XIS detectors.

For the XIS, we analyzed the screened data, reduced via *Suzaku* software version 2.1. The reduction followed the prescriptions described in "The *Suzaku* Data Reduction Guide" provided by the *Suzaku* guest observer facility at NASA/GSFC.[26] The screening was based on the following criteria: (1) only *ASCA*-grade 0, 2, 3, 4, and 6 events are accumulated, while hot and flickering pixels were removed from the XIS image using the CLEANSIS script, (2) the time interval after the passage through the South Atlantic Anomaly (T_SAA_HXD) is greater than 500 s, (3) the object is at least 5° and 20° above the rim of the Earth (ELV) during night and day, respectively. In addition, we also selected the data with a cutoff rigidity (COR) larger than 6 GV. After this screening, the net exposure for good time intervals (GTIs) is 35.1 ks. The XIS events were extracted from a circular region with a radius of 4′.3 centred on the source peak, whereas the background was accumulated in an annulus with inner and outer radii of 5′.0 and 7′.0 pixels, respectively. The response (RMF) and auxiliary (ARF) files are produced using the analysis tools XISRMFGEN and XISSIMARFGEN, which are included in the software package HEAsoft version 6.4.1.

The HXD/PIN event data (version 2.1) are processed with basically the same screening criteria as those for the XIS, except that ELV $\geqslant 5^\circ$ through night and day, and COR $\geqslant 8$ GV. The HXD/PIN instrumental background spectra were generated from a time-dependent model provided by the HXD instrument team for each observation (see Kokubun et al. 2007). Both the source and background spectra were made with identical GTIs and the exposure was corrected for a detector dead time of 6.9%. We used the response files version AE_HXD_PINXINOME_20070914.RSP, provided by the HXD instrumental team. Similarly, the HXD/GSO event data (ver. 2.1) were processed with a standard analysis technique described in the cited "The *Suzaku* Data Reduction Guide." Despite the relatively high instrumental background of the HXD/GSO, the source was marginally detected at 5.5σ level between 80 and 120 keV. We used the response files version AE_HXD_GSOXINOM_20080129.RSP. Spectral analysis was performed using the Xspec fitting package 12.3.1. and we fitted both the soft and hard X-ray spectra with a power law with Galactic absorption free to vary. The XIS spectra are well fitted with a power law with $\Gamma = 1.63$ absorbed with $N_{\rm H} = 1.1 \times 10^{21}$ cm^{-2}, which infers the absorbed fluxes of $4.51^{+0.07}_{-0.03} \times 10^{-11}$ erg cm^{-2} s^{-1} and $3.20^{+0.04}_{-0.01} \times 10^{-11}$ erg cm^{-2} s^{-1} in the energy bands 0.3–10 keV and 2–10 keV, respectively. The hard X-ray spectrum determined by HXD/PIN and GSO seems to be a bit flatter than those determined by the XIS only below 10 keV, as it is shown in the residuals reported in Figure 3 (where a model with a single power law is assumed). We found that it is better fitted by a power-law photon index of $\Gamma = 1.35 \pm 0.14$, which gives $F_{10-100\ \rm keV} = 1.37^{+0.1}_{-0.08} \times 10^{-10}$ erg cm^{-2} s^{-1}. The uncertainties reported above are at 90% confidence level.

5. *SWIFT* OBSERVATION

During our campaign *Swift* (Gehrels et al. 2004) performed two ToO observations of 3C 454.3: the first on 2007 December 13, the second on 2007 December 15. Both observations were performed using all onboard experiments: the X-ray Telescope

[26] http://suzaku.gsfc.nasa.gov/docs/suzaku/analysis/abc. See also seven steps to the *Suzaku* data analysis at http://www.astro.isas.jaxa.jp/suzaku/analysis.

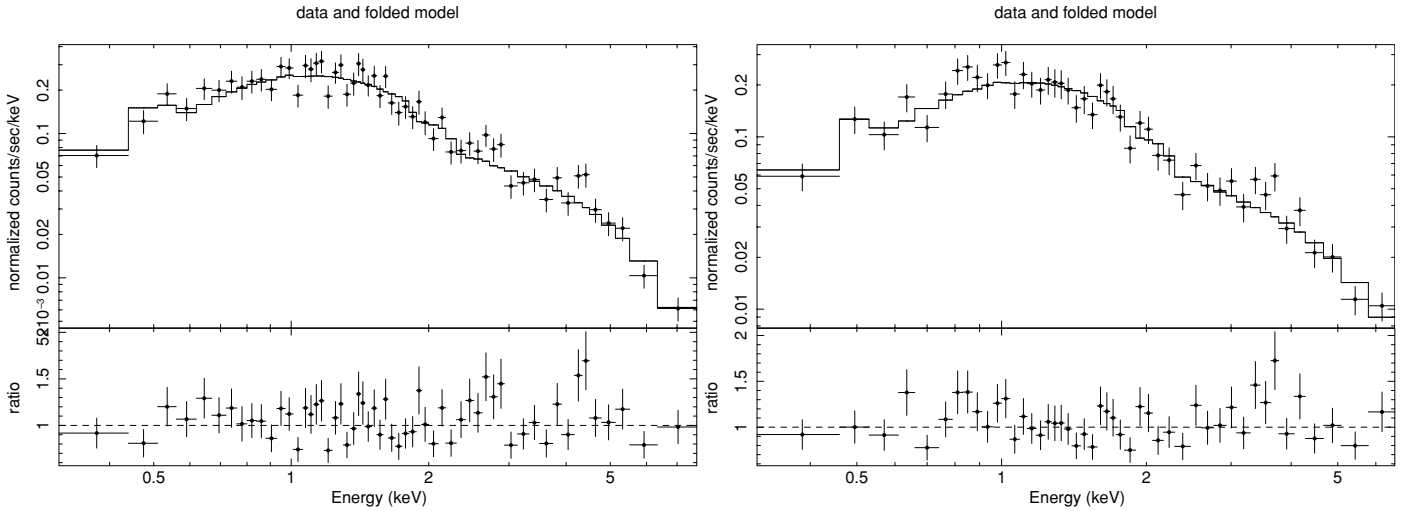

Figure 4. *Swift* data and the folded model of 3C 454.3 for the observation carried out in 2007 December 13 (left panel) and 15 (right panel).

Table 1
Results of XRT Observations of 3C 454.3

Observation Date	N_H (10^{22} cm^{-2})	Flux 0.3–10 keV (erg cm^{-2} s^{-1})	Flux 2–10 keV (erg cm^{-2} s^{-1})	Spectral Slope Γ	χ^2_r/d.o.f.
2007 Dec 13	0.13 ± 0.03	$(4.38 \pm 0.25) \times 10^{-11}$	$(3.04 \pm 0.24) \times 10^{-11}$	1.74 ± 0.10	1.28/54
2007 Dec 15	0.14 ± 0.03	$(3.60 \pm 0.22) \times 10^{-11}$	$(2.49 \pm 0.22) \times 10^{-11}$	1.76 ± 0.12	1.14/44

Note. The power-law model with N_H free to vary.

(XRT; Burrows et al. 2005; 0.2–10 keV), the UV and Optical Telescope (UVOT; Roming et al. 2005; 170–600 nm), and the Burst Alert Telescope (BAT; Barthelmy et al. 2005; 15–150 keV). The hard X-ray flux of this source is below the sensitivity of the BAT instrument for short exposure and therefore the data from this instruments will not be used. We refer to Raiteri et al. (2008a) for a detailed description of data reduction and analysis of the UVOT data.

XRT observations were carried out using the instrument in photon counting (PC) readout mode (see Burrows et al. 2005 and Hill et al. 2004 for details of the XRT observing modes). The XRT data were processed with the XRTDAS software package (ver. 2.2.2) developed at the ASI Science Data Center (ASDC) and distributed by HEASARC within the HEASoft package (ver. 6.4). Event files were calibrated and cleaned with standard filtering criteria with the *xrtpipeline* task using the latest calibration files available in the *Swift* CALDB distributed by HEASARC. Both observations showed an average count rate of >0.5 counts s^{-1} and therefore pile-up correction was required. We extracted the source events from an annulus extraction region with inner and outer radii of 3 and 30 pixels, respectively. To account for the background, we also extracted events within a circular region centred on a region free from background sources and with a radius of 80 pixels. The ancillary response files were generated with the task xrtmkarf. We used the latest spectral redistribution matrices (RMF, ver. 011) in the Calibration Database maintained by HEASARC. The adopted energy range for spectral fitting is 0.3–10 keV, and all data are rebinned with a minimum of 20 counts per energy bin to use the χ^2 statistics. *Swift*/XRT uncertainties are given at 90% confidence level for one interesting parameter, unless otherwise stated.

Spectral analysis was performed using the Xspec fitting package 12.3.1 and we fitted the spectra with a power-law model with galactic absorption left free to vary. In Table 1, we summarize the best-fit parameters and the derived absorbed fluxes in the energy ranges 0.3–10 keV and 2–10 keV. We note that the best-fit N_H values in Table 1 are in agreement with the value 1.34×10^{21} cm^{-2} derived by Villata et al. (2006) when analyzing *Chandra* observations in 2005 May, and adopted by Raiteri et al. (2007, 2008b) when fitting the X-ray spectra acquired by *XMM-Newton* in 2006–2007. In Figure 4, we show the data and the folded models for these observations.

6. OPTICAL MONITORING

6.1. WEBT Observation

The WEBT (http://www.oato.inaf.it/blazars/webt/) is an international collaboration including tens of optical, near-IR, and radio astronomers devoted to blazar studies. An extensive monitoring effort on 3C 454.3 was carried out by the WEBT from 2005 to 2008, to follow the large 2005 outburst and post-outburst phases (Villata et al. 2006, 2007; Raiteri et al. 2007), and the new flaring phase started in mid 2007 (Raiteri et al. 2008a, 2008b). A detailed presentation and discussion of the radio, millimetric, optical, and *SWIFT*-UVOT data collected in 2007 December can be found in Raiteri et al. (2008a). Here we adopt their data analysis in the context of our multifrequency study.

6.2. REM Observation

The photometric optical observations were carried out with the REM (Zerbi et al. 2004), a robotic telescope located at the ESO Cerro La Silla observatory (Chile). The REM telescope has

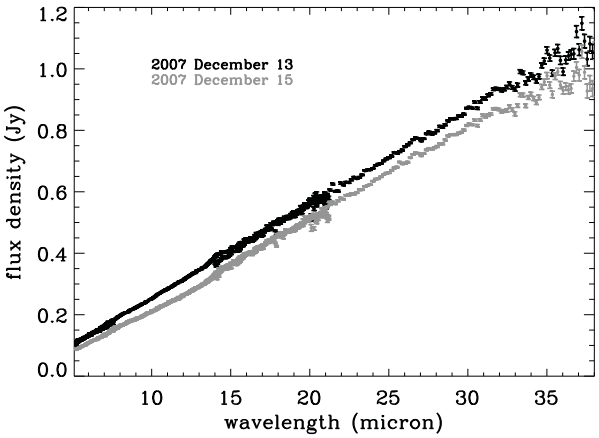

Figure 5. *Spitzer* spectra of 3C 454.3 for the observation carried out in 2007 December 13 (black points) and 15 (gray points).

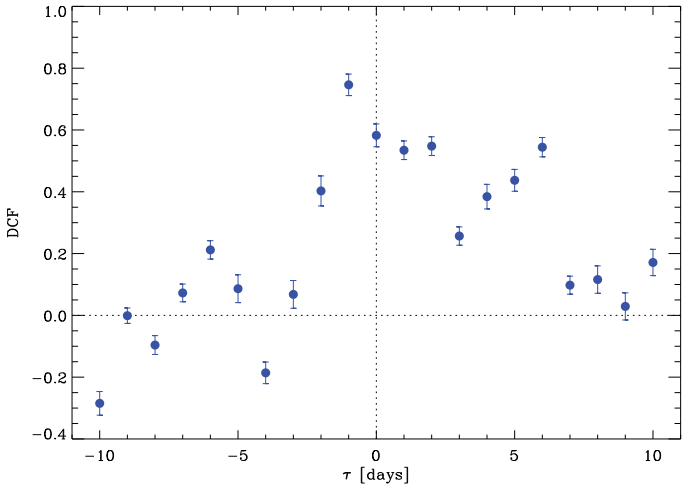

Figure 6. 3C 454.3 DCF between the γ-ray and optical (R-band) magnitudes. (A color version of this figure is available in the online journal.)

a Ritchey–Chretien configuration with a 60 cm $f/2.2$ primary and an overall $f/8$ focal ratio in a fast moving alt-azimuth mount providing two stable Nasmyth focal stations. Two cameras are simultaneously used at the focus of the telescope, by means of a dichroic filter, REMIR for the NIR (Conconi et al. 2004) and ROSS for the optical (Tosti et al. 2004), in order to obtain nearly simultaneous data.

The telescope REM has observed 3C 454.3 between 2007 December 1 and December 8, overlapping with the *AGILE* observation period. The light curve produced by REM in the R band is shown in Figure 1 (bottom panel, red points).

6.3. MitSuME Observation

A contribution of the optical follow-up observations was given also by MITSuME, composed of three robotic telescopes (of 50 cm diameter each) located at the Institute of Cosmic-ray Research (ICRR) Akeno Observatory, Yamanashi, Japan and the Okayama Astrophysical Observatory (OAO). Each MITSuME telescope has a tricolor camera, which allows us to take simultaneous images in g', R_c, and I_c bands. The camera employs three Alta U-6 cameras (Apogee Instruments Inc.) and KAF-1001E CCD (Kodak) with 1024×1024 pixels. The pixel size is 24 μm × 24 μm, or 1.″6 × 1.″6 at the focal plane. It is designed to have a wide field view of 28′ × 28′. The primary motivation of the MITSuME project is a multi-band photometry of γ-ray bursts (GRBs) and their afterglows at very early phases, but the telescopes are also actively used for multi-color optical monitoring of more than 30 blazars and other interesting Galactic or extragalactic sources. These telescopes are automatically operated and respond to GRB alerts and transient events like active galactic nucleus (AGN) flares.

MITSuME observed 3C 454.3 almost every day from 2007 November 22 to December 6 so as to provide simultaneous data with *AGILE* and *Suzaku*. All raw g', R_c, and I_c frames were corrected for the dark, bias and flat field by using IRAF version 2.12 software. Instrumental magnitudes were obtained via aperture photometery using DAOPHOT (Stetson 1987) and SExtractor (Bertin & Arnouts 1996). Calibration of the optical source magnitude was conducted by differential photometry with respect to the comparison stars sequence reported by Raiteri et al. (1998) and González-Pérez et al. (2001). The fluxes are corrected for the Galactic extinction corresponding to a reddening of $E(B-V) = 0.108$ mag (Schlegel et al. 1998). The R_c-optical light curve between November 30 and December 6 is shown in Figure 1 (bottom panel, green circles).

7. MID-INFRARED OBSERVATIONS

Given the high γ-ray activity detected by *AGILE* from 3C 454.3, we also requested and obtained a DDT for a mid-infrared follow-up by *Spitzer* (Werner et al. 2004). The DDT was approved for two epochs for a total duration of 0.8 hr of the Infrared spectrograph (IRS; Houck et al. 2004) providing short-low and long-low observations of 3C 454.3 scheduled for December 13 (starting at MJD 54447.410) and 15 (starting at MJD 54449.403). Both observations provided us with a low-resolution spectrum ($\Delta\lambda/\lambda \sim 80$) in the energy range ∼5–38 μm. Data were acquired in the IRS standard staring mode: observations were obtained at two positions along the slit to enable sky subtraction. Each ramp duration was set to 14.68 s with a number of cycles equal to 5. Each set of data was processed with the IRS Standard Pipeline *SMART* developed at the Spitzer Science Center to produce calibrated data frames (Basic Calibrated Data, BCD, files). Moreover, the BCD files covering the same spectral range were coadded and then sky-subtracted spectra were obtained. The absolute flux calibration was estimated by using the electron-to-Jy conversion polynomial given in the appropriate *Spitzer* calibration file. In Figure 5, we present the two spectra obtained on December 13 and 15. We performed a linear fit of the two, obtaining fluxes equal to $(1.59 \pm 0.02) \times 10^{-10}$ and $(1.38 \pm 0.02) \times 10^{-10}$ erg cm^{-2} s^{-1} for December 13 and 15, respectively.

8. DISCUSSION

8.1. Timing Analysis

We investigated the emission of the blazar 3C 454.3 during a multifrequency campaign performed in the first half of 2007 December. The source was found to be in flaring state with an average γ-ray flux above 100 MeV of ∼250 × 10^{-8} photons cm^{-2} s^{-1}, which is typical of its high γ-ray state (Vercellone et al. 2008, 2009; Anderhub et al. 2009). As in the case of the previous multifrequency campaign (2007 November; Vercellone et al. 2009), the source was continuously monitored in γ-rays as well as in the optical energy bands. In both energy bands, the source exhibited comparable flux variations of the

order of ∼4: this argues for an EC model. Moreover, we deeply studied the optical–γ-ray correlation by means of a discrete correlation function (DCF; Edelson & Krolik 1988; Hufnagel & Bregman 1992) applied to the optical and γ-ray light curves reported in Figure 1. This analysis revealed $\lesssim$one-day delay of the γ-ray emission with respect to the optical one (see Figure 6). Indeed, the DCF maximum at a time lag of $\tau = -1$ day corresponds to a centroid of $\tau = -0.56$ days, whose uncertainty can be estimated by means of the Monte Carlo method known as "flux redistribution/random subset selection" (Peterson et al. 1998; Raiteri et al. 2003). By running 1000 simulations we found $\tau = -0.6^{+0.7}_{-0.5}$ day at 1σ confidence level. We also performed the DCF reducing the data binning down to 12 hr between December 5 and 16, keeping the one-day binned γ-ray light curve for the data before December 5 (MJD = 54,439.524). This shows a peak at -1 day with centroid at -0.54 days which is in agreement with the result obtained with the one-day binned γ-ray light curve. In this case, the Monte Carlo method is not able to provide a reliable estimate of the error on the time lag due to the larger uncertainties on the γ-ray fluxes.

The evidence of this time lag again suggests the dominance of the EC model: such a delay is compatible with the typical blob dimensions and the corresponding crossing time of the external seed photons (Sokolov et al. 2004). We note that this evidence agrees with what was found by Bonning et al. (2009).

Particularly interesting is the source optical flare recorded by WEBT on December 12 (Raiteri et al. 2008a). The source experienced an exceptional variability in less than 3 hr. Raiteri et al. (2008a) interpreted this event as a variation in the properties of the jet emission. This unusual event clearly required an intraday analysis of the γ-ray data. This analysis depends on the source brightness and the instrumental sensitivity. Given the γ-ray flux level of 3C 454.3 reached between 2007 December 5 and 2007 December 16, we obtained a data binning not smaller than 12 hr (Figure 7, top panel). This analysis showed an enhancement of more than a factor of 2 of the γ-ray flux during the second half of 2007 December 12, that remarkably includes the time of the optical event (see vertical lines in Figure 7). The enhancement by a factor of ∼2 of the γ-ray flux was comparable with the 1.1 mag optical brightening. This could support the evidence of a change in the jet emission in the EC scenario. The 12 hr γ-ray light curve could constrain a possible delay between the γ-ray emission and the optical one within 12 hr, shorter than ever observed before for this source.

8.2. Spectral Modeling

As described in the previous section, the 2007 December multifrequency campaign was characterized by ToO carried out in mid-infrared (*Spitzer*), soft X-ray (*Suzaku*, *Swift*), hard X-ray (*Suzaku*) and radio-to-optical, and γ-ray monitoring. These observations allowed us to obtain the SED of this blazar with a wide multifrequency coverage for three different epochs: December 5, 13, and 15. At these dates, the SED in X-rays shows a softening toward lower frequencies that can be due to two causes: (1) a contribution from bulk Comptonization by cold electrons in the jet (Celotti et al. 2007) and (2) the emergence of the SSC contribution in soft X-rays from the more energetic EC component due to the disk and the BLR. The mid-infrared *Spitzer* data and optical data available in December 13 and 15 (which well define the synchrotron peak), combined with the resolved X-ray spectrum and the γ-ray data, constrain the model parameters, arguing for the latter case; the SSC emergence is a natural and inevitable consequence of the simultaneous modeling of the broadband SED. Nevertheless, some contribution from bulk Comptonization cannot be ruled out.

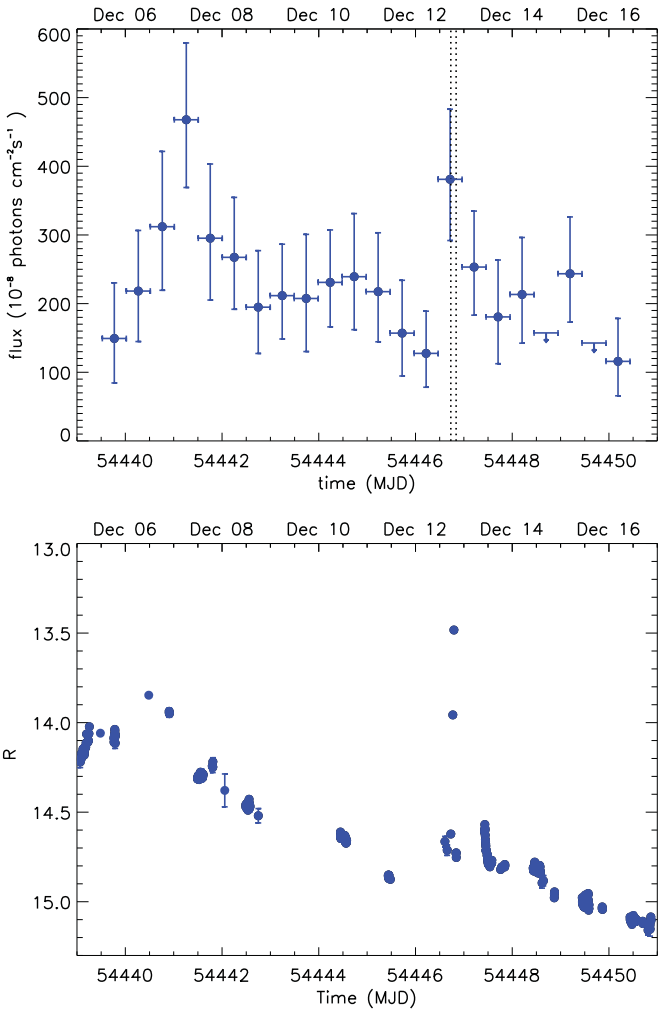

Figure 7. Top panel: γ-ray 12 hr light curve above 100 MeV during the period between 2007 December 5 and 2007 December 16 when the source was at 30° in the *AGILE* FoV. The vertical lines mark the time (<3 hr) of the exceptional optical event of 2007 December 12; bottom panel: *R*-band optical light curve obtained during the period reported above.

(A color version of this figure is available in the online journal.)

We first considered the state of December 13 and 15 in which we have simultaneous radio, mid-infrared, optical, X-ray, and γ-ray data. In these epochs, 3C 454.3 was in a different state with respect to the one analyzed in November: optical and UV fluxes appeared lower by a factor of 2–3, suggesting the synchrotron bump peaking at a frequency 5–10 times lower than the one observed in November, as confirmed also from the mid-infrared data. On the other hand, the soft X-ray data were only a little bit lower than in November. Despite the softer synchrotron bump, γ-ray data showed in the SED the persistence of a hard peak at $\simeq$1 GeV, similar to the higher states observed by *AGILE* in 2007 July and 2007 November (Anderhub et al. 2009; Vercellone et al. 2009). In fact, the December γ-ray spectrum (characterized by a photon index of ∼1.78) is consistent with those obtained during the two previous *AGILE* observations.

We attempted to fit the SEDs with a one-zone SSC model, adding the contribution of external seed photons coming from an accretion disk and a BLR (Raiteri et al. 2007). With this model, we succeeded in fitting the synchrotron peak as well as the X-ray data assuming parameters similar to the November

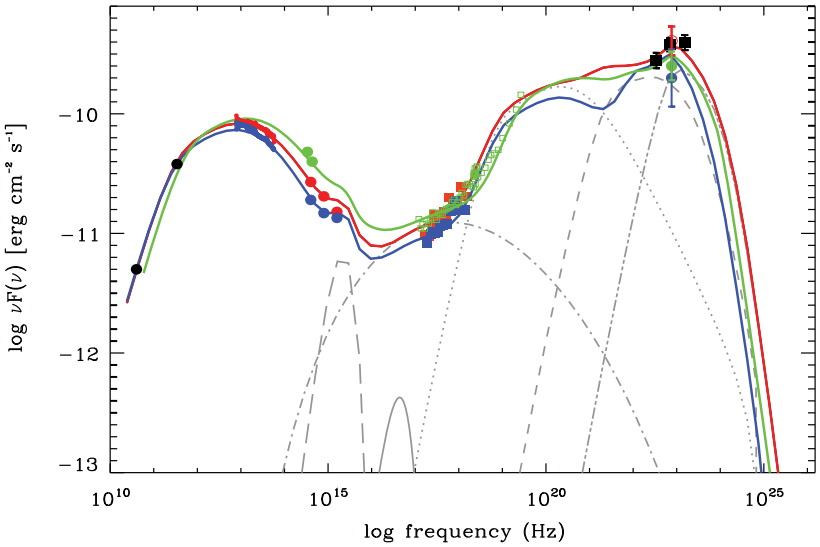

Figure 8. 3C 454.3 SEDs for 2007 December 5, 13, and 15 (green, red, and blue solid lines, respectively). The γ-ray spectrum for $E > 100$ MeV (black squares), extracted from data acquired between December 5 and 16, and the radio points (black circles) from Raiteri et al. (2008a) are also reported. The gray lines represent the contribution of the disk (long dashes), corona (solid), SSC (dot-dashed), EC disk (dotted), EC BLR (dashed), and EC corona (dash dot dot) to the December 13 model.

Table 2
Model Parameters for the December States of 3C 454.3

Observation Date	Γ	B (gauss)	R (cm)	K (cm^{-3})	γ_b	$\gamma_{\rm min}$	a_l	a_h
2007 Dec 5	18	2.5	2.2×10^{16}	50	3×10^2	30	2.3	4.2
2007 Dec 13	18	2	2.2×10^{16}	52	3.5×10^2	38	2.3	4.2
2007 Dec 15	18	2	2.2×10^{16}	52	3.2×10^2	35	2.3	4.2

ones, but a lower $\gamma_b \simeq 350$ was required to account for the softness of the synchrotron bump: with this γ_b the EC from a standard BLR peaks at $h\nu \simeq h\nu_{\rm soft}\Gamma\gamma_b^2\delta/(1+z) \sim 10^8$ eV. This is in contrast to the observed hardness of the γ-ray spectrum up to 1 GeV ($h\nu_{\rm soft} \simeq 10$ eV is the typical energy of the external source as seen by the observer). We note that the EC by the disk can account for the rising hard X-ray portion of the SED, which did not show clear variability. Nevertheless, we note that both the disk and BLR components cannot account for the hardness of the γ-ray spectrum. Thus, we consider a further external source of seed photons.

A possible candidate for this source is the hot extended corona that must be consistently produced in steady accretion/ejection flows as shown by MHD numerical simulations (Tzeferacos et al. 2009). Hence, we considered a one-zone SSC model plus the contribution by external seed photons coming from the accretion disk, the BLR, and the hot corona. We adopted a spherical blob with radius $R = 2.2 \times 10^{16}$ cm and a broken power law for the electron energy density in the blob:

$$n_e(\gamma) = \frac{K\gamma_b^{-1}}{(\gamma/\gamma_b)^{a_l} + (\gamma/\gamma_b)^{a_h}}, \quad (1)$$

where γ is the electron Lorentz factor assumed to vary between $10 < \gamma < 10^4$, while $a_l = 2.3$ and $a_h = 4.2$ are the pre- and post-break electron distribution spectral indices, respectively. We assumed that the blob contained a random magnetic field $B = 2$ gauss and that it moved with the bulk Lorentz Factor $\Gamma = 18$ at an angle $\Theta_0 = 1^\circ$ ($\delta \simeq 33$) with respect to the line of sight. The density parameter into the blob is $K = 52$ cm^{-3}.

The bolometric luminosity of the accretion disk is $L_{\rm d} = 3 \times 10^{46}$ erg s^{-1}, and it is assumed to lie at 0.01 pc from the blob; we assumed a BLR distance of 1.5 pc, reprocessing a 10% of the irradiating continuum. We assumed for the disk a blackbody spectrum peaking in UV (see Tavecchio & Ghisellini 2008; Raiteri et al. 2008b). Finally, we added the hot corona photons surrounding the jet as a blackbody spectrum of $T = 10^6$ K and $L_h = 10^{45}$ erg s^{-1}, and a distance of 0.5 pc from the blob. The SEDs of both December 13 and 15 could be fitted with almost the same parameters (see red and blue solid lines in Figure 8). The high-energy portion of the electron density becomes softer on December 15 as the same electrons should be accelerated with less efficiency than on December 13.

Remarkably, the lower γ_b required in the epochs considered here makes the BLR a too soft contributor at GeV energies, while the contribution of the hot corona succeeded to account for the persistence of the hard γ-ray spectra measured by *AGILE*.

On December 5, the low-energy peak of the SED is less constrained with respect to the December 13 and 15 ones due to the lack of the mid-infrared data. On the other hand, the *Suzaku* X-ray data (green points in Figure 8) better constrain the rise of the IC emission. We fitted this SED with almost the same model assumed for the other two epochs, but the higher optical flux and the lower γ-ray flux detected with respect to December 13 required a higher magnetic field and a lower γ_b (see Table 2).

Given the different γ-ray state of the source analyzed in the November and December campaigns, we compared the particle injection luminosity, $L_{\rm inj}$, measured during the two multiwavelength campaigns. This is expressed by means of the following formula:

$$L_{\rm inj} = \pi\, R^2\, \Gamma^2\, c \int [d\gamma\ m_{\rm e}\, c^2 \gamma\, n(\gamma)]. \quad (2)$$

We found the particle injection luminosity of December to be 6×10^{43}erg s^{-1}, a factor of 5 lower than the November one. This difference is due to both the lower γ_b and $\gamma_{\rm min}$ values needed to reproduce the SED in the states of December.

9. CONCLUSIONS

We reported in this paper the main results of a multifrequency campaign on the blazar 3C 454.3 performed in 2007 December. The source was simultaneously observed in mid-infrared, optical, X-ray, and γ-ray energy bands, which provided us with a wide data set aimed at studying the correlation between the emission properties at lower and higher frequencies. We summarize below the major results.

1. The γ-ray emission from 3C 454.3 shows variations on a daily timescale.
2. The simultaneous monitoring of the source in the optical and γ-ray energy bands allowed us to determine a possible $\lesssim$one-day delay of the γ-ray emission with respect to the optical one.
3. The extraordinary optical activity (lasting less than 3 hr), observed on December 12, has a counterpart in the γ-ray data. A possible delay between the γ-ray emission and the optical one is constrained within 12 hr.
4. We found that a leptonic model with an EC on seed photons from the disk and BLR does not succeed in accounting for both the "hardeness" of the γ-ray spectrum and the "softness" of the synchrotron emission, and requires an additional component. We argued that a possible candidate for it is the hot corona ($T \sim 10^6$ K) surrounding the disk.

AGILE is a mission of the Italian Space Agency, with co-participation of the Istituto Nazionale di Astrofisica (INAF) and the Istituto Nazionale di Fisica Nucleare (INFN). This work was partially supported by ASI grants I/R/045/04, I/089/06/0, I/011/07/0, and by the Italian Ministry of University and Research (PRIN 2005025417). INAF personnel at ASDC are under ASI contract I/024/05/1. This work is partly based on data taken and assembled by the WEBT collaboration and stored in the WEBT archive at the Osservatorio Astronomico di Torino-INAF (http://www.oato.inaf.it/blazars/webt/). This work is based in part on observations made with the *Spitzer Space Telescope*, which is operated by the Jet Propulsion Laboratory, California Institute of Technology under a contract with NASA. The IRS was a collaborative venture between Cornell University and Ball Aerospace Corporation funded by NASA through the Jet Propulsion Laboratory and Ames Research Center. SMART was developed by the IRS Team at Cornell University and is available through the Spitzer Science Center at Caltech.

REFERENCES

Abdo, A. A. (Fermi/LAT Collaboration) 2009, ApJ, 699, 817
Anderhub, H., et al. 2009, A&A, 498, 83
Barthelmy, S. D., et al. 2005, Space Sci. Rev., 120, 143
Bertin, E., & Arnouts, S. 1996, A&AS, 117, 393
Bonning, E. W., et al. 2009, ApJ, 697, L81
Burrows, D. N., et al. 2005, Space Sci. Rev., 120, 165
Celotti, A., Ghisellini, G., & Fabian, A. C. 2007, MNRAS, 375, 417
Conconi, P., et al. 2004, Proc. SPIE, 5492, 1602
Edelson, R. A., & Krolik, J. H. 1988, ApJ, 333, 646
Feroci, M., et al. 2007, Nucl. Instrum. Methods Phys. Res. A., 581, 728
Gehrels, N., et al. 2004, ApJ, 611, 1005
Ghisellini, G., Celotti, A., Fossati, G., Maraschi, L., & Comastri, A. 1998, MNRAS, 301, 451
Ghisellini, G., Foschini, L., Tavecchio, F., & Pian, E. 2007, MNRAS, 382, L82
Giommi, P., et al. 2006, A&A, 456, 911
González-Pérez, J. N., Kidger, M. R., & Martín-Luis, F. 2001, AJ, 122, 2055
Hill, J. E., et al. 2004, Proc. SPIE, 5165, 217
Houck, J. R., et al. 2004, ApJS, 154, 18
Hufnagel, B. R., & Bregman, J. N. 1992, ApJ, 386, 473
Katarzyński, K., & Ghisellini, G. 2007, A&A, 463, 529
Kokubun, M., et al. 2007, PASJ, 59, 53
Koyama, K., et al. 2007, PASJ, 59, 23
Labanti, C., et al. 2009, Nucl. Instrum. Methods Phys. Res. A, 598, 470
Mattox, J. R., et al. 1996, ApJ, 461, 396
Mitsuda, K., et al. 2007, PASJ, 59, 1
Perotti, F., Fiorini, M., Incorvaia, S., Mattaini, E., & Sant'Ambrogio, E. 2006, Nucl. Instrum. Methods Phys. Res. A, 556, 228
Peterson, B. M., Wanders, I., Horne, K., Collier, S., Alexander, T., Kaspi, S., & Maoz, D. 1998, PASP, 110, 660
Pian, E., et al. 2006, A&A, 449, L21
Prest, M., Barbiellini, G., Bordignon, G., Fedel, G., Liello, F., Longo, F., Pontoni, C., & Vallazza, E. 2003, Nucl. Instrum. Methods Phys. Res. A, 501, 280
Raiteri, C. M., Villata, M., Lanteri, L., Cavallone, M., & Sobrito, G. 1998, A&AS, 130, 495
Raiteri, C. M., et al. 2003, A&A, 402, 151
Raiteri, C. M., et al. 2007, A&A, 473, 819
Raiteri, C. M., et al. 2008a, A&A, 491, 755
Raiteri, C. M., et al. 2008b, A&A, 485, L17
Roming, P. W. A., et al. 2005, Space Sci. Rev., 120, 95
Schlegel, D. J., Finkbeiner, D. P., & Davis, M. 1998, ApJ, 500, 525
Serlemitsos, P. J., et al. 2007, PASJ, 59, 9
Sikora, M., Moderski, R., & Madejski, G. M. 2008, ApJ, 675, 71
Sokolov, A., Marscher, A. P., & McHardy, I. M. 2004, ApJ, 613, 725
Stetson, P. B. 1987, PASP, 99, 191
Takahashi, T., et al. 2007, PASJ, 59, 35
Tavani, M., et al. 2008, Nucl. Instrum. Methods Phys. Res. A, 588, 52
Tavani, M., et al. 2009, A&A, 502, 995
Tavecchio, F., & Ghisellini, G. 2008, MNRAS, 386, 945
Tavecchio, F., et al. 2002, ApJ, 575, 137
Tosti, G., Chiang, J., Lott, B., Do Couto E Silva, E., Grove, J. E., & Thayer, J. G. 2008, ATel, 1628, 1
Tosti, G., et al. 2004, Proc. SPIE, 5492, 689
Tzeferacos, P., Ferrari, A., Mignone, A., Bodo, G., & Massaglia, S. P. 2009, MNRAS, 400, 820
Vercellone, S., et al. 2008, ApJ, 676, L13
Vercellone, S., et al. 2009, ApJ, 690, 1018
Villata, M., et al. 2006, A&A, 453, 817
Villata, M., et al. 2007, A&A, 464, L5
Werner, M. W., et al. 2004, ApJS, 154, 1
Zerbi, F. M., et al. 2004, Proc. SPIE, 5492, 1590

儀器室工作報告

鹿林兩米天文望遠鏡儀器研製計畫工作報告
2009 Annual report of Lulin 2-Meter telescope for developing instruments

Daisuke Kinoshita, Ching-Huang Wu, Tse-Chuan Chen, I-Cheng Shen, Ru-Huei Huang

一、簡介

本計畫團隊在 2009 年下半年，沈益承博士、專任助理陳澤銓及研究生黃如慧等三位新成員相繼加入，加上原有的木下大輔老師、工程師吳景煌，儀器室成員共計五位，並依據個人的專長，朝向分工及多元化的方式進行，也同時補足了軟體開發、光電測試以及天文觀測等各方面的技術人才。

以下報告將分別詳述各項儀器設備的採購進度、儀器室建置進度、軟體開發進度，以及利用現有、即將採購和正在開發的多顆 CCD camera 做一性能比較與分析。

二、四波段同步光學與攝像系統說明

1. 系統架構

本系統的示意圖如下，望遠鏡主體下方連接四波段分光光學系統之後，再同步連接到四套攝像系統，再由光纖傳輸到電腦。而真空泵浦與冷卻機的功能是負責維持系統運作的真空與低溫條件。

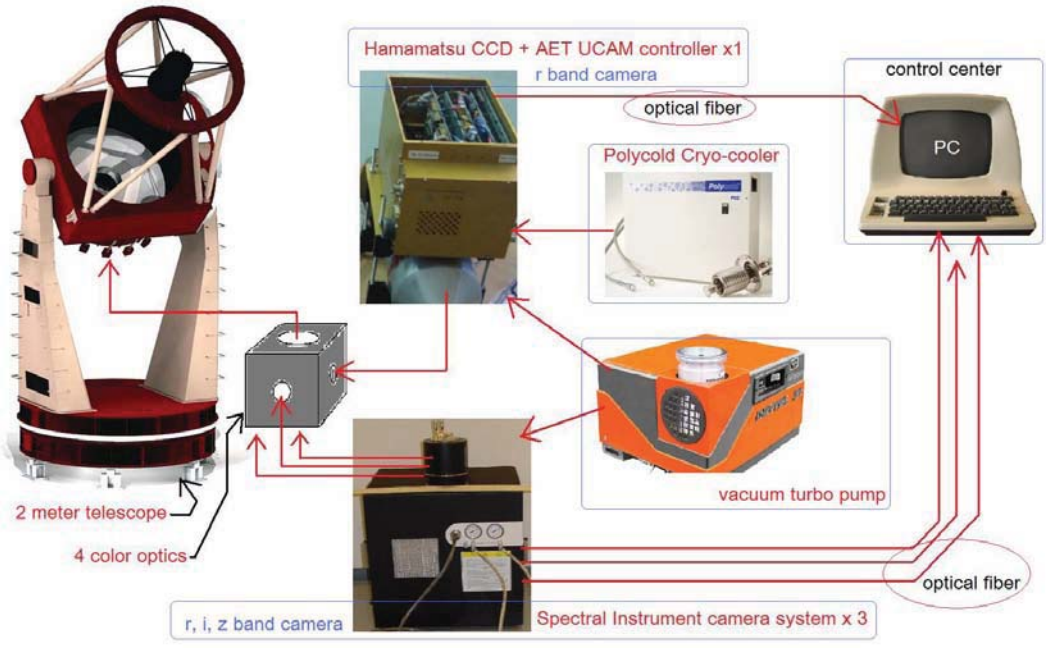

2. 四波段分光架構

上圖中『4-color optics』其內部示意圖如下。

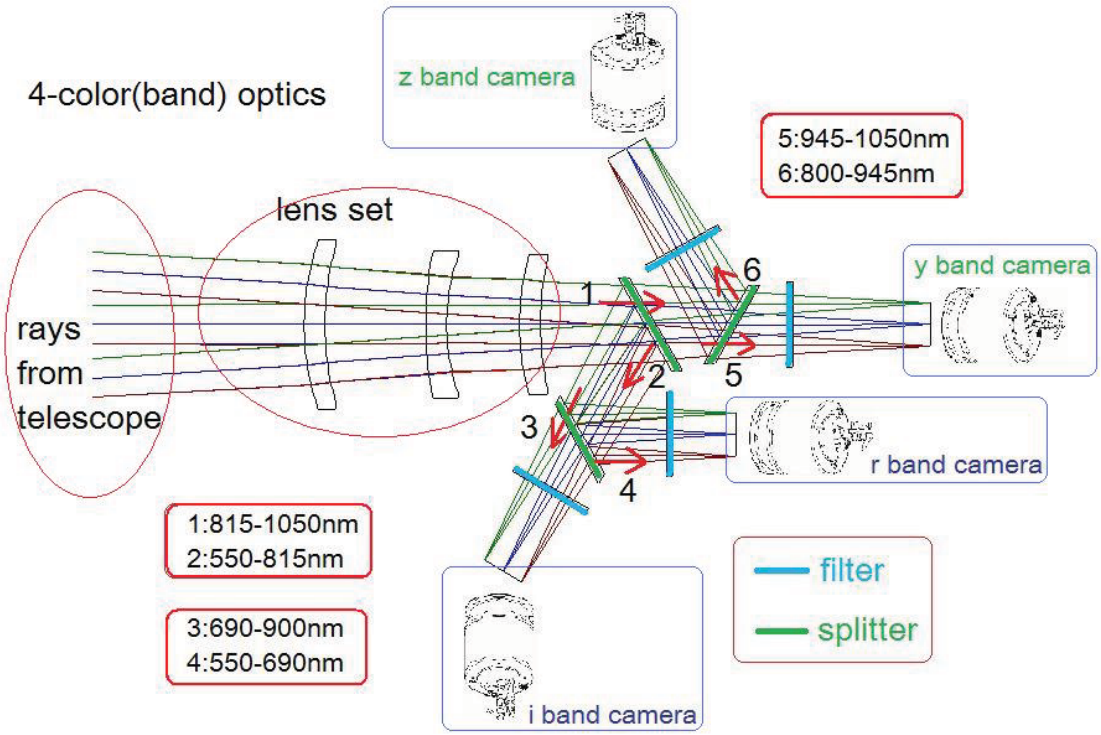

3. r', i', z'攝像系統

經過上圖四色分光系統的分光鏡(splitter)與濾鏡(filter)處理後，入射光將同步分為四個波段，送到四套攝像系統，而其中 r、i、z 波段共計三套，將採用美商 Spectral Instruments 公司 1100 系列的攝像系統，其外觀與系統主要特色如下：

- Simultaneous readout/digitization from 1, 2, or 4 CCD ports, 16-bit digitization using multiple converters per port at low noise,speeds of 50kHz to several MHz.
- Very low readout noise (<6 e- RMS) over a range of pixel readout, rates achieved by correlated double sampling using dual-slope integration, near zero dark current by cryo-cooling to -100°C.
- Gigabit fiber optic, AIA cable, and Camera Link® for computer communication.

4. y 攝像系統

為了在 y 波段有更好的量子效率(QE)，我們將採用日商 Hamamatus 公司的 fully depleted CCD。而 CCD 資料擷取系統將採用美商 Astro Electronics Technology(AET)公司的 ACS-164 UCAM controller。最後，我們將參考國內中研院天文所(IAA)以及日本天文單位有相同 CCD 的使用經驗者，提供我們的資料進行 dewar 設計，用以提供 CCD 在真空與低溫下的環境操作。本攝像系統的設計架構如下圖示。

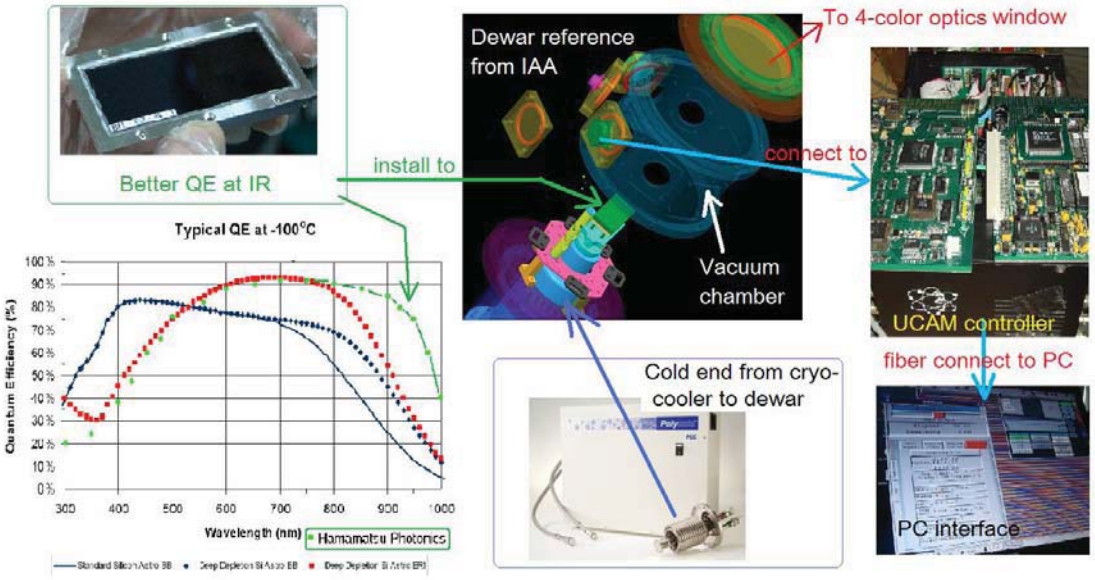

5. 如上圖所示，我們選擇 AET ACS-164 UCAM controller，主要因為其系統雜訊低、開發彈性好(Linux 系統)、維護介面佳，而其主要規格與特色如下：

The System Specifications of **ACS-164** :

(1) Four readout channels with four 1 MHz 16 bit ADCs. Software selectable to use any one amplifier, two amplifiers or four amplifiers.

(2) Can be setup for using any format of different kinds of CCDs. Such as normal CCDs or high resistivity CCDs. (N type or P type)

(3) Can run full-frame mode for scientific observation or high speed frame-transfer mode for telescope-guiding etc.

(4) Multiple readout speeds with variable DCS timing.
The "fast" mode gives up to 1 MHz pixel readout rate.
The "medium" and "slow" modes give low noise readout

(5) Low system noise: < 1 e- (not including CCD noise)

(6) 1% linearity.

(7) Flexible window readout with very high speed skipping of unused rows and pixels.

(8) MPP and NONMPP modes selectable.

(9) Binning: 2x2 or 4x4

(10) System Gain software adjustable.

(11) Negative bias voltages and high n+Vsub voltage available for P type high resistivity CCDs

(12) Build in special erase procedure with variable clock levels and timing can be used to eliminate residual image of high resistivity CCD.

(13) Very flexible and wide range system parameter setting can match different kind CCD requirements and different observation mode requirements. Also easy to optimize CCD working status.
--- All bias and clock voltages programmable.
--- All clock waveforms programmable (timing, raising/falling time and speed, etc)
--- Readout procedures software selectable (high speed skipping, pre-read, baseline readout etc.)
--- Multiple CCD erase procedures software selectable.(normal erase, reverse erase etc.)
--- All parameters can be set and monitored locally or remotely (through Ethernet).

(14) Clock anti – blooming function available (option)

(15) Dewar temperature monitoring and regulation, controller temperature monitoring

(16) 200 MHz high speed fiber optical USB-2 interfacing.

(17) Support for CCD polarimetry test.

(18) Up to 8 outputs and 8 inputs of extra general IO port available.

三、儀器室建置進度

1. 五個工作區介紹

針對天文望遠鏡儀器開發的軟硬體需求，及參考國外多所天文台儀器室的建置方式，將我們的儀器室依不同的用途和功能分成五個工作區(如下圖所示)，分別為無塵室(Clean Room)、光學暗房(Dark Room)、電子焊接區(Electric Welding Area)、軟/硬體測試區(Software & Hardware Test Area)及機構組裝區(Mechanical Assembly Area)。目前已將這五個工作區做一明顯的隔間及標示，將來配合儀器設備的陸續到位，及 2010 年初甫通過的天文所儀器室管理辦法的實施，儀器室已可正常運作，並在不久的將來可發揮其天文儀器開發的功能。

1-1 無塵室(Clean Room)

在 CCD 的封裝過程中，我們需要一個無塵的潔淨環境以防止空間內空氣中的微粒對 CCD 表面造成的不良影響。因此，我們特別獨立出一個空間做為無塵室(如下圖所示)：為隔絕由外部進入系統的汙染源(如空調通風系統、門、窗、牆壁裂縫所導入之微粒)，我們設置一無塵等級為 Class 1000 的無塵工作亭；此外，製程機器與工作人員往往會產生無空間內的汙染源，所以我們除在無塵工作亭內設置一 Class 100 的無塵工作台之外，也嚴格規定工作人員需全程穿戴無塵衣、帽及鞋。

其中 Class 100 表示在一立方公尺內每分鐘流通 0.5μm 直徑以下的微粒應低於 100 個，依此類推。

除了環境上達到無塵的要求外，我們也添購了一台微塵檢查燈(如下圖所示)，這是一台由鹵素燈搭配濾光片的光源組合，可輸出一黃-綠色的光，藉由人眼對黃綠光的敏感來檢測微小的灰塵及刮痕，可精確判定 10μm 以下的刮痕及微粒子。

1-2 光學暗房(Dark Room)

光學暗房(如下圖所示)主要提供 CCD 一個全暗且不受外部雜散光影響的光學測試環境。除先前已採購進來的光學桌外，目前暫時沒有太多的儀器在裡面。

未來，我們計畫添購如白光光源、單光儀(Monochromator)、積分球(Integrating Sphere)等儀器和光學元件，並藉由不同的光路調整和光學架構的組合(如下圖所示)，我們可以作 CCD 的均勻度測試(Uniformity)、CCD 影像測試(Imaging Test)、光源波長分佈測試(Wavelength Distribution)、線性度(Linearity)及量子效率(Quantum Efficiency)等量測工作，用以評估 CCD 的性能。

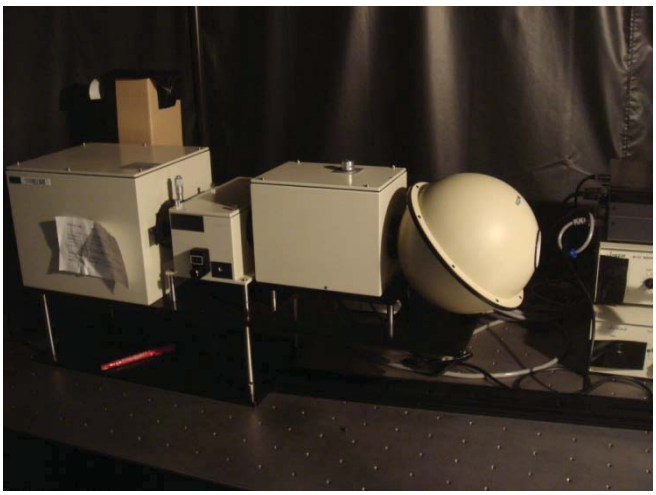

1-3 電子焊接區(Electric Welding Area)

在CCD系統的開發過程中,需要設計相當多的電路,如控制電路、驅動電路、溫控電路..等。因此在電子焊接區，我們購置了直流電源供應器、示波器、各式電表儀器、ESD烙鐵、超音波清洗槽、風扇靜電消除機、PCB及各式手/電動工具等一應具全(如下圖所示)，提供電路設計人員一個完善的工作環境。

1-4 軟/硬體測試區(Software & Hardware Test Area)

在軟/硬體測試區內(如下圖所示)，我們目前配置了二台效能較高的PC，分別做為Windows與Linux的作業平台，以因應軟體開發人員的不同需求。同時整合示波器 、Thermometer等儀器的數據資料，軟體開發人員不但可以獲得更完整的資訊，也可以在此區執行CCD camera及周邊軟硬體連線的測試。

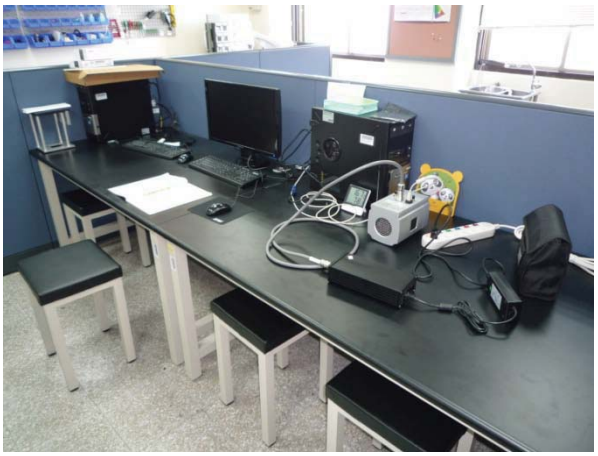

1-5 機構組裝區(Mechanical Assembly Area)

機構組裝區主要目的在做 Dewar(如下圖所示)的設計及機構上的組裝。

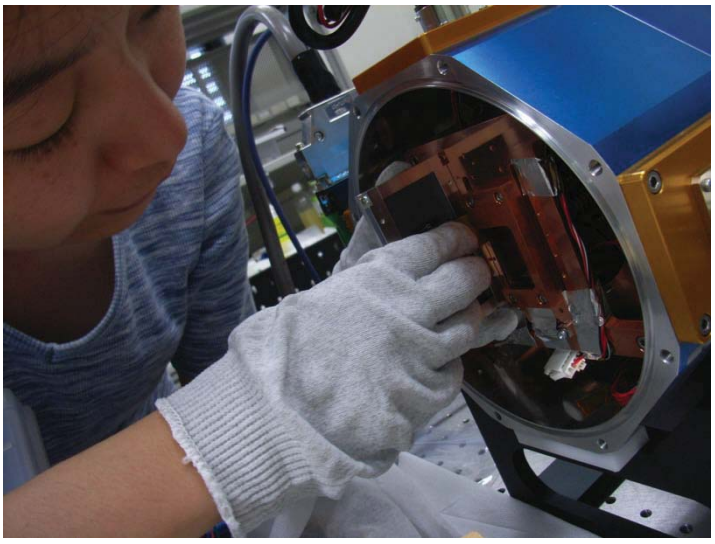

在軟體方面，我們購買了 AutoCAD 2010 製圖軟體，方便我們做機構上的設計及出圖；在硬體方面，此區配置了 Alcatel Drytel 31 的真空幫浦及 Polycold 超低溫機械循環冷卻機(如下圖所示)，以提供 Dewar 一個真空及低溫的操作條件；在人員方面，我們也都具備了車床及洗床的使用概念。

2. 大額採購案

目前正在進行中的採購案有：天文感光檢測器擷取與控制系統(L98-254)、四波段同步光學系統(H98-8082)、可見光多波段成像儀三組(W98-8014A)等三件，除四波段同步光學系統的交期可能長達 15 個月外，其餘二項預計將在 2010 年中左右可到貨。

另一件準備著手進行的是光學濾鏡的採購，計有 r',i',z',y 四個波段，尺寸則為 80mm x 50mm。預計將會向日商 Asahi Spectral 購買，目前正在蒐集廠商報價及確認規格中。

3. 儀器室工程進度

為有效整理和收納儀器室內之耗材用品，我們計畫在儀器室靠窗處及靠配電盤處設置收納櫃(如下圖所示)，目前決定的方案為靠窗處短邊及水槽以訂做木質櫃方式進行，長邊則購買現成的鐵櫃三組；靠配電盤處則訂做整面的木質櫃(但不影響配電盤開關)。

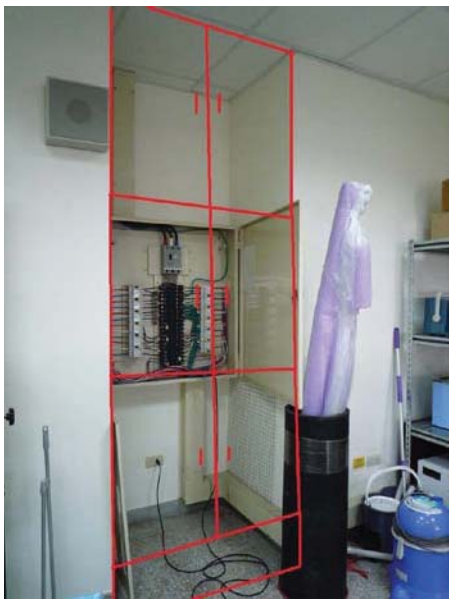

另外為使電子焊接區之銲錫廢氣可向外排出，我們也將在該區的一側設置一排風管及抽風馬達，以將廢氣排至室外(如下圖所示)。

同時為達到儀器設備電源使用的方便性，我們也將在儀器室天花板的

正中央處設置 2~3 條可升降式電源線(如下圖所示之參考樣式)。

以上工程除三組鐵櫃購買現成品外，其餘都將由同一廠商承接及施工，預計將在 2010 年第一季前完成。

4. 天文所儀器室管理辦法

在我剛上任接手儀器室建置的工作之際，便開始著手規劃「天文所儀器室管理辦法」(如附件一)的制訂工作。期間歷經數次的會議討論和修改，以及所長和所上諸位老師的指導與建議，終於在 2010 年 1 月 18 日的所務會議中通過並確定實施。

此辦法除表框張貼在儀器室大門牆上供參閱外，也連同申請書(如附件二)公告於天文所網頁上，以供外賓申請參觀或內部人員欲外借器材設備之用。

附件一

天文所儀器室管理辦法

民國九十九年一月十八日所務會議通過

1. 為有效管理天文所儀器室(以下簡稱儀器室)及提供人員安全之工作環境，特訂定本辦法。

2. 儀器室設負責老師及管理人各一名，人選由所長指派，負責儀器室之管理及維護等相關工作。

3. 儀器室包含下列三個區域：工作區、光學暗房及無塵室。請遵守各個區域之規定。

4. 進入儀器室需換穿室內脫鞋，並經腳踏黏墊除塵；光學暗房與無塵室為靜電防護區域，進入時則需換穿抗靜電鞋(或鞋套)、防靜電衣、頭套、手套及配戴防靜電手環。

5. 儀器室嚴禁吸菸及攜帶任何飲料、食品入內。

6. 欲借用儀器室或設備器材者，請自行至本所網站下載填寫『天文所儀器室暨設備器材借用申請單』,使用時需有管理人或管理人所指定之代理人陪同在場方可使用。

7. 請遵守保護智慧財產權相關法令規定，電腦硬碟中之軟體嚴禁拷貝，並不得下載及安裝任何不合法之套裝軟體至電腦硬碟，下載或安裝軟體應告知管理人。

8. 損壞儀器室內之設備及器材者，需將損壞情況向管理人或負責老師報備，以利後續維修事宜。

9. 設備器材使用後請歸定位，離開儀器室前請隨手關閉冷氣、水電及所使用設備之電源，並將大門鎖上。

10. 欲參訪儀器室之外單位人員(或團體)請遵守下列規定：

    ※外單位係指天文所以外之其他公、私立單位及民間機構。

    a. 參訪人員(或團體)，需於三天前以電話或 email 方式向儀器室管理人提出

申請，經所長同意後，始得入內參觀，因故欲取消參訪行程者，請事先來電告知。

b. 儀器室僅開放 5 人(含)以下之團體參觀，超過 5 人以上請分批辦理，參觀過程需由儀器室管理人陪同導覽與解說。

c. 參觀時間每次以 30 分鐘為限。

d. 參訪人員請遵守本辦法 1-10 項之規定。

本辦法經所務會議核定後實施。

附件二

天文儀器實驗室暨設備器材借用申請單

借用申請人/職稱	
分機或聯絡電話	
借用項目	□儀器室 □設備器材 (名稱：_____)
使用時間	年 月 日(:)~ 年 月 日(:)
使用地點	□儀器室內 □外借 (地點及原因說明：_____)
用途簡述	
*歸還狀態 （由管理人填寫）	單號:IN_____

※※※注意事項※※※

1. 此申請單附屬在『天文所儀器室管理辦法』之下。
2. 申請借用程序：
   借用人自天文所網站下載申請單並逐項填寫 → 申請人簽名 → 儀器室管理人簽名 → 負責老師同意並簽名 → 繳回管理人存查後始可使用 → 使用完畢請告知管理人。
3. 請確實遵守『天文儀器實驗室管理辦法』之規定。
4. 借用設備器材者，請確實填寫『儀器設備使用事件記錄簿』。
5. 有任何問題請洽儀器室管理人。

核准人 （負責老師）	管理人	申請人

5. 天文所儀器室管理辦法

儀器室在第一季相關工程結束後，我們會將儀器室內外做一通盤的打掃和清潔，未來希望藉由「天文所儀器室管理辦法」的實施及儀器室內部人員的嚴格管理，加上所採購之關鍵的天文儀器將陸續到貨，相信儀器室一定會在很短的時間內步上營運軌道，並成為一間很棒的天文儀器開發專用的實驗室。也期許兩米天文台的建案能有突破性的進展，配合我們儀器的開發,希望很快的我們就可以取得兩米望遠鏡的 First-Light。

四、軟體開發進度

1. 前言

傳統天文望遠鏡在觀測天體可見光不同波段的時候，採用更換濾鏡的方式，會造成每個成像之間除了時間的差異，還有環境因素的差異。本計畫將設置的可見光多波段成像儀，該儀器具備幾項特色：這將是本地區目前唯一的可見光多波段成像儀、可同步取得四波段可見光的成像、更快速、更精確、更有效率、較不受環境因素影響、較容易的調校以及提升波長較長部分的靈敏度與其觀測的實現。計畫成果更將用以追隨 Pan-STARRS 的觀測，以及增強本所的儀器能量。這個系統主要有一個四波段同步觀測的分光鏡與濾鏡架構，以及四套攝像系統，還包含了相關的感光元件、控制電路/介面/軟體、真空泵浦、低溫冷卻機等等相關裝置以及軟體開發。

這方面是本計畫中重要的人機介面與機電介面。計畫中是總共使用了三種不同的 Camera，由於不同公司提供的軟體支援完全不同。因此在軟體開發上，需要顧慮到各層面，從最底層的硬體介面溝通（如 PCI/DMA 控制、USB (Universal Serial Bus)控制、序列埠(Serial Port)控制）到最上層的應用程式撰寫。因此面臨的挑戰迥異於在 User Space 下撰寫單純的應用程式。再加上四波段取樣需要精確的時間控制與同步控制，因此軟體上精確的控制，是達到本計畫中消除每個成像時間差異的重要步驟。而因應將來其它計畫的需求，本軟體仍有許多發展空間，成果將輔助本所天文學家，增強本所天文領域上的研究能量。

2. 系統設計

本計畫的軟體系統，其主要結構設計如下圖所示。在這個結構所標示的顏色,其中藍色表示該部分非自製;而綠色部分表示該部分是自製的。而外框線為實線者，表示目前該區塊已經過確認；而虛線者表示該區塊尚未經過確認。無框線者為開發者自己確認。以下將針對該結構分別就最底層(1)到最上層(6)分別介紹。

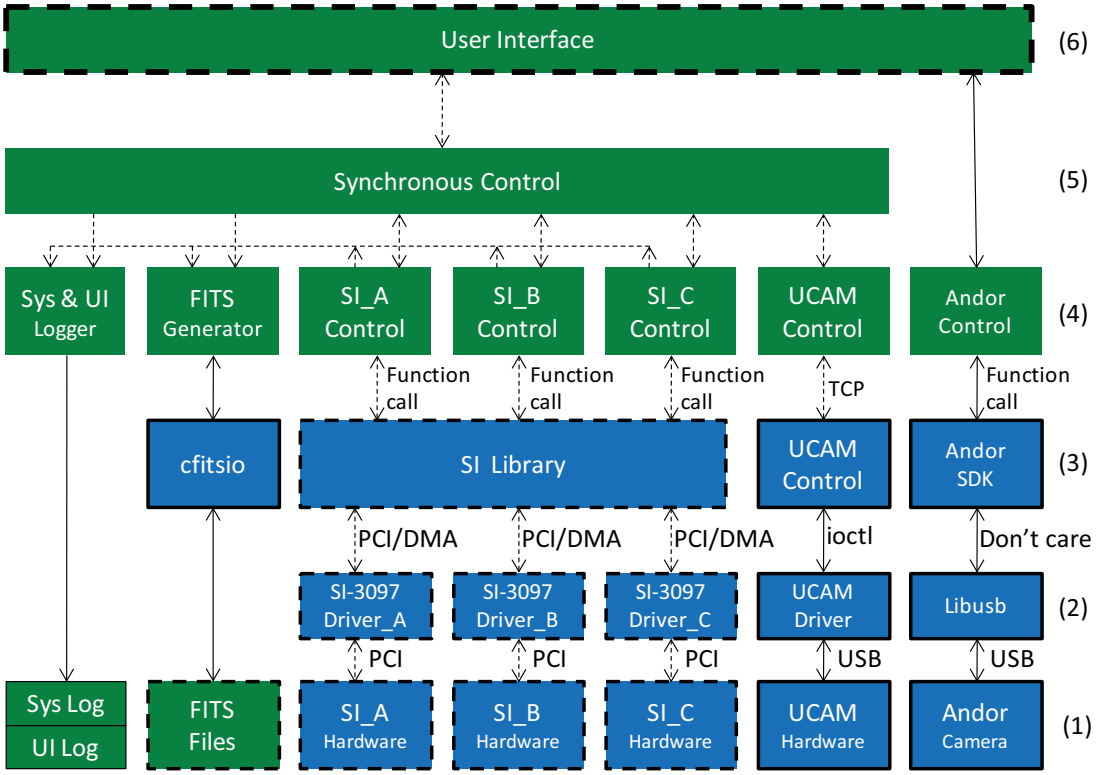

第(1)層為硬體層（Hardware）。在軟體開發系統中，硬體為相機（Camera）。我們所擁有的相機分別為 Spectral Instruments (SI) 1100 Series (以下簡稱 SI-1100) 相機三台；AET UCAM Controller (以下簡稱 UCAM) 一台；實驗用 Andor 936 camera (以下簡稱 Andor)一台，總共五台相機。為了確保軟體系統可以穩定運作，硬體層（Hardware）的運作確認，也列為工作項目之一。其中 Andor 與 UCAM 已經經過確認，確定該系統可運作以取得影像；而 SI 還需要確認。在連結電腦的介面上，SI 採用 PCI 介面，而 UCAM 與 Andor 採用 USB 介面。SI 連結電腦除了相機本身以外，還需要額外一張 SI-3097 介面卡。而 UCAM 與 Andor 則各自整合為單一的 USB 介面連結電腦。

第(2)層為驅動程式層（Driver）。驅動程式需由廠商提供，因為驅動程式內部涉及到許多硬體上面的細節。系統中的硬體是否具備指定之作業系統的驅動程式，以及驅動程式是否能正常載入並運作正常，是這一層需要確認的工作。在這個層級中，SI 由於採用 SI-3097 介面卡，因此需具備 SI-3097 的驅動程式；UCAM 的驅動程式由廠商提供；而 Andor 採用標準的 libusb 驅動程式。目前 Andor 與 UCAM 已經確認其驅動程式可運作正常。

第(3)層為軟體開發套件/函式庫（SDK (Software Development Kit) / Library）。在這一層級仍須廠商提供軟體開發套件/函式庫（SDK / Library）。因為這一層仍為完全脫離硬體上的細節。如果廠商可以提供軟體開發套件/函式庫（SDK / Library），則我們不需考慮第(2)-(3)層之間的控制；反

之，則我們需要考慮第(2)-(3)層的控制細節。在各相機中，由於 Andor 由於有提供完整的軟體開發套件（SDK）與驅動程式（Driver），因此我們不需要考慮 Andor 相機在第(2)-(3)層控制細節；而 UCAM 已具備單獨的控制部分，理想上也不需要顧慮第(2)-(3)層控制技術；SI 原廠並不直接提供我們需要的 SDK，但我們有第三方 Library，未來需要驗證是否能順利運作。確認 SI Library 是否運作正常，以及第(2)-(3)層是否運作正常，是必要的工作項目。如果必要的話，我們必須考慮如何透過 PCI/DMA 的控制技術，自行建構 SI 的第(3)層。

第(4)層為裝置控制層（Device Control）。從此層級往上，都是自己建立的。在此層級中實作的是針對各個 Camera 所需要的各種函式，如：開關 Shutter、初始化/關閉相機、設定曝光時間、讀取影像…等等。而三台相同廠牌相同型號的 SI 相機，也要在此層級中被獨立區分出來。在第(3)-(4)層之間的通訊與控制，除了 UCAM 以外都是透過 Function call 的方式；而 UCAM 是經過 TCP（Transmission Control Protocol）進行溝通。

第(5)、(6)層分別是同步控制介面（Synchronous Control）與使用者介面（User Interface）。同步控制介面（Synchronous Control），確保各相機的控制區塊（Control block）可以獨立運作，並互相不干擾。使用者介面（User Interface）因應天文學家的需求，設計為 CLI（command line interface）方式。

軟體系統預計運作於 Linux 環境下，採用 Kernel 2.6.31 以上。拍攝的影像將儲存為 FITS 格式。我們引用 NASA (National Aeronautics and Space Administration)提供的 cfitsio 來建立我們的 FITS 檔案。

為了完成 Synchronous Control，我們需要將 User Interface 與各相機的控制區塊（Control block）分別設計為獨立的程序（Process），並透過跨程序通訊（IPC，Inter-process communication）與共享記憶體區塊（shm, shared memory）連結起來，如下圖所示。充分利用作業系統本身的多工功能（Mult-tasking），達到同步目的。

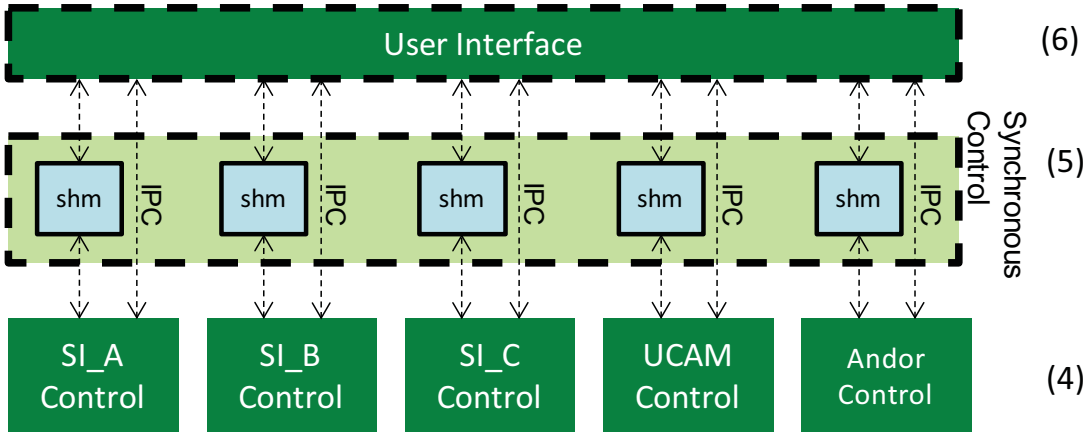

3. 系統實作

我們預備將系統架設於 Linux 下，並採用 CLI (Command Line Interface)

做為我們的使用者介面。以下針對實作部分分別介紹。

- SI Camera

  SI 並未提供 Linux SDK。因此我們對於該相機的控制，需要從驅動程式(Driver)層開始考量起，而無法直接切入 API (Application)層級撰寫相關應用程式。SI Camera 使用了 SI-3097 作為 Camera 連接電腦的介面卡。不過 SI Camera 目前尚未實際取得 Camera，將來 SI Camera 的控制開發需要從 SI-3097 的驅動程式(Driver)驗證開始。Library 方面則取自 ASIAA 溫志懿博士的相關開發經驗，也明白將來還有 PCI 控制和 DMA 控制的難關需要突破。

- AET UCAM Controller

  AET UCAM Controller 屬於我們第四色的相機中，專用於控制部分。這台相機的自製程度較高，軟硬體與 SI Camera 也截然不同。AET 並無提供 SDK，而是由硬體到軟體一整套的整合系統。該控制器的電腦端控制軟體，是由 Lick Observatory 經過約 10 年的發展而來。但由於非商業軟體，因此相關文件相當缺乏，其內部 Functions 也有相當多交互連結使用的程式碼，很難如商業 SDK 般呼叫使用。我在這方面儘量整理出有脈絡可循的文件出來，且在 2010 年四月底曾到北京學習一週，把將來可能運用到的部分整理出文件。總計整理的文件如安裝手冊、軟體說明、軟體結構、硬體結構等。其中安裝手冊的安裝步驟就需要到 37 道步驟，才能建構可使用的軟體出來。其中許多步驟都涉及到權限的轉換，文件檔的編輯和 GUI 畫面的操作，雖然一度想過把安裝步驟寫成 Script，但目前為止撰寫 Script 仍有一定的難度。

- Andor 936 Camera

  Andor 936 並不屬於 4-color camera，而是屬於前期設計，用途是透過此一實際的相機模擬相關 Camera 動作、建立 FITS Keywords 等動作，並用以設計使用者介面（User Interface），如下圖所示：

```
檔案(F)  編輯(E)  檢視(V)  終端機(T)  求助(H)
Camera shell for Andor 936, version 0.9
Graduate Institute of Astronomy, National Central University, Taiwan (ROC)
>init
Initialing camera, please wait...
>a
image is saved in ./image_myFITS.fit
>status
Andor 936 Camera is Online

ShutterMode = Always Close
Exposure Time = 0.1
Image=2048x2048
>shutdown
Andor 936 shutdown.
>exit
bye.
```

Andor 有廠商提供 Linux 下的驅動程式(Driver)與軟體開發套件(SDK)，我們可以直接切入應用程式(Application)的設計。

4. 完成概況

到目前為止，我們完成的系統如下圖所示。我們已經可以透過使用者介面來控制 Andor 936 camera 進行相關控制動作，UCAM Controller 也測試過其獨立的軟硬體系統。等待後續 SI 與 UCAM 相機陸續到達後，我們將著手實作這兩台相機的相關控制細節。

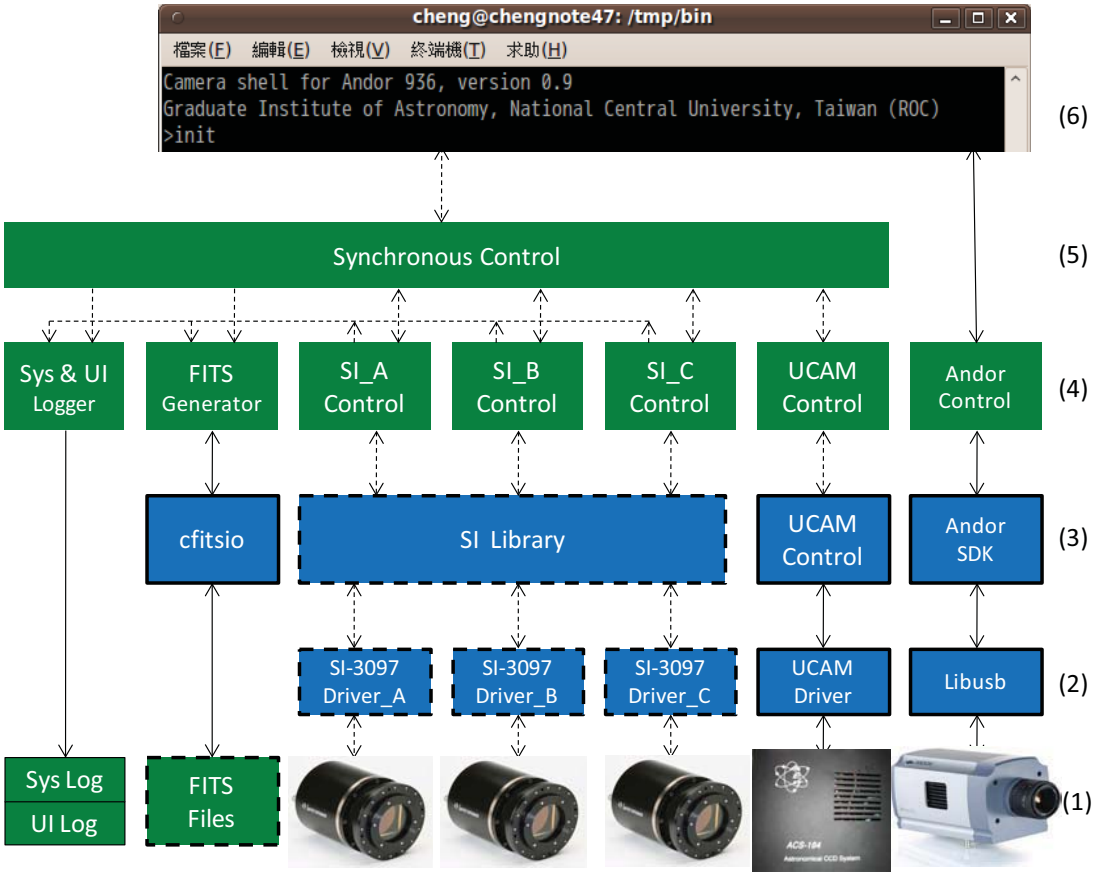

5. 未來工作規劃

將來 SI 與 UCAM 相機陸續到達後。後續工作為(1)驗證 SI 相機介面。(2)驗證 SI Driver 的運作狀況。(3)驗證 SI Library 功能，必要時可能需要修改/重寫 SI Library。(4)建構針對同步控制（Synchronous Control）設計的 SI Control、UCAM Control、Andor Control 等區塊。(5)修改使用者介面（User Interface），使符合四色相機的功能。

五、各種 CCD Camera 性能之比較與分析

CCD (Charge Couple Device) is the most popular detector which is used in astronomical observations. The advantages include low noise, good linearity, high quantum efficiency, and high dynamic range. The limiting magnitude of the instrument is an important index for observation planning. It is essential for efficient execution of observations to know the limiting magnitude prior to the observation.

We focus on two properties of the CCD. One is the cooling temperature of the CCD, and the other is thickness of the depletion layer. The amounts of lower readout noise and dark current strongly depends on the cooling temperature. We could expect significant decrease of the noise at lower CCD operating temperature. There are two common problems for the conventional thinned CCDs. One is that the quantum efficiency (QE) at longer wavelength region is very poor (~ 10% at λ = 900nm ~ 1000nm). The other is the fringe pattern at longer wavelength region is serious and causes larger photometric errors. The thicker deep depletion and fully depleted CCDs achieve higher QE and less fringe pattern.

We have four CCD cameras. Table 1 lists the specifications of the cameras. The PI1300 and Andor936 CCD cameras are for 1-m telescope and SI1100 and NCU-cam CCD cameras are for upcoming 2-m telescope. The specifications and operation conditions of the instrument influence the limiting magnitude.

Before the actual observations, we can use the theoretical calculations to inspect the observational results whether is reliable. Therefore, We use CCD Equation （ Massey 1990 ） as Eq. (1) to estimate limiting magnitude.

$$\frac{S}{N} = \frac{\mathrm{Nt}}{\sqrt{\mathrm{Nt}+\mathrm{n_{pix}}N_S\mathrm{t}+\mathrm{N}_D\mathrm{t}+\mathrm{N}_R^2}} \qquad (1)$$

S/N is signal-to-noise ratio, N is the count rate in electrons per second, $N_S$is the total number of photons per pixel from the background or sky, $N_D$is the total number of dark current electrons per pixel, $N_R$is the total number of electrons per pixel resulting from the readout noise, $n_{\mathrm{pix}}$is pixel number within an aperture area, and t is the CCD integration time. We assume signal-to-noise ratio of 10

within an integration time of 300 sec to calculate limiting magnitude. The calculated limiting magnitudes for Bessel UBVRI bands and SDSS g',r',i',z' bands.

Here report preliminary the results of our calculations. The results show that PI1300 camera seems to have fainter limiting magnitude, it might be because of some specifications and operation conditions is not reliable. However, it is extremely important to measure the dependency of the cooling temperature and depletion layerthickness on the limiting magnitude quantitatively. Therefore, we will use our new cameras to perform a series of observations in 2010A semester. After analyze the observational results, we will make the comparison and the discussion for the theoretical and the actual difference.

Table 1. The specifications of the four cameras. Top is operating temperature of the CCD. The dark current (electron/pixel/sec) and the readout noise (electron/pixel/sec) are derived from previous work (Kinoshita et al. 2005).

	PI1300	Andor936	SI1100	NCU-cam
Pixel number	1340 X 1300	2048 X 2048	2048 X 4096	2048 X 4096
Pixel size	20μm X 20μm	13.5μm X 13.5μm	15μm X 15μm	15μm X 15μm
Thickness	15μm	15μm	40μm	200μm
Dark current	0.064	0.007	0.0001	0.001
Readout noise	4	4	3	5
Top	-50°C	-70°C	-100°C	-100°C

Table 2. Calculated limiting magnitudes for four CCD cameras.

	U	V	B	R	I	g'	r'	i'	z'
PI1300	19.8	21.7	21.2	21.0	20.0	19.1	19.2	19.5	19.2
Andor936	19.3	21.7	21.2	21.0	20.0	19.1	19.2	19.5	19.3
SI1100	19.5	21.6	21.1	21.0	20.1	19.1	19.4	19.5	19.4
NCU-cam	19.6	21.7	21.2	21.0	20.0	19.0	19.2	19.5	19.5

Figs. Those figures plot integration time versus calculated magnitude for Bessel UBVRI bands and SDSS g',r',i',z' bands.

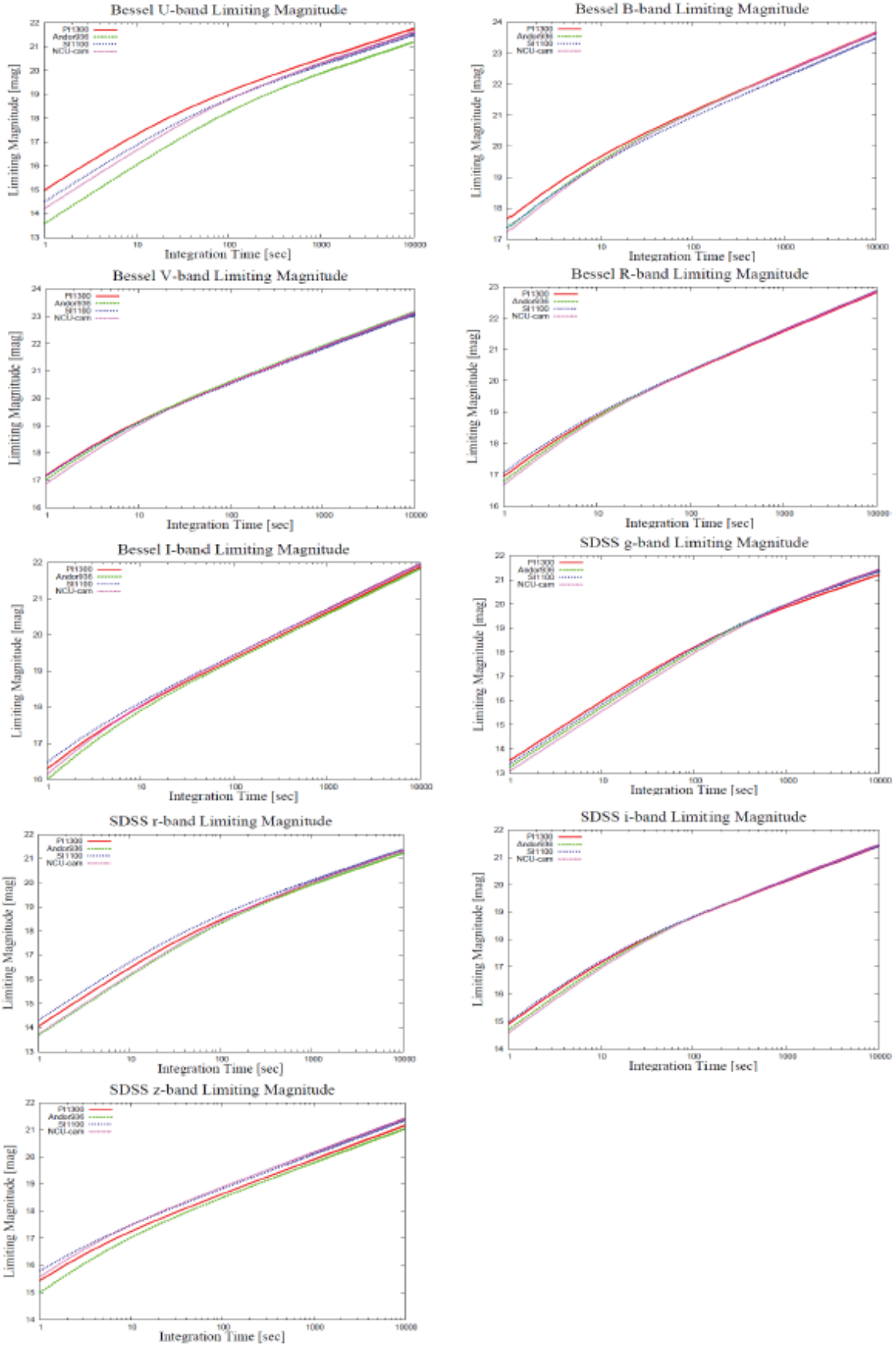

六、儀器計畫總結

1. 已完成部份

真空泵浦、機械冷卻機、電腦硬體、儀器室與相關工具等。

2. 開發中部份

Dewar 真空腔體與外掛控制器機構、溫度檢測與加溫控制電路、壓力檢測電路、溫濕度與露點檢測電路、電壓電流檢測電路、軟體程式開發等。

3. 相關採購案

(1) Spectral Instruments 攝像系統計畫於 2010 年 6 月前取得；

(2) AET 控制器計畫於 2010 年 7 月前取得；

(3) Photocoding 四色光學系統計畫於 2011 年 4 月前取得。

驗收報告（第三項望遠鏡鏡筒部分）

驗收標的：合約第五條第三項，望遠鏡鏡筒與鏡室總成

報告內容：

本項合約標的包含鏡筒與鏡室總成。各大部件如下圖所示，包含主次鏡、次鏡環及支撐架、鏡筒支架、高度軸總成、鏡室總成、像場旋轉裝置等，依目前進度要求，廠商應完成各部件的外型製作，達到可運送至總裝地點的程度。

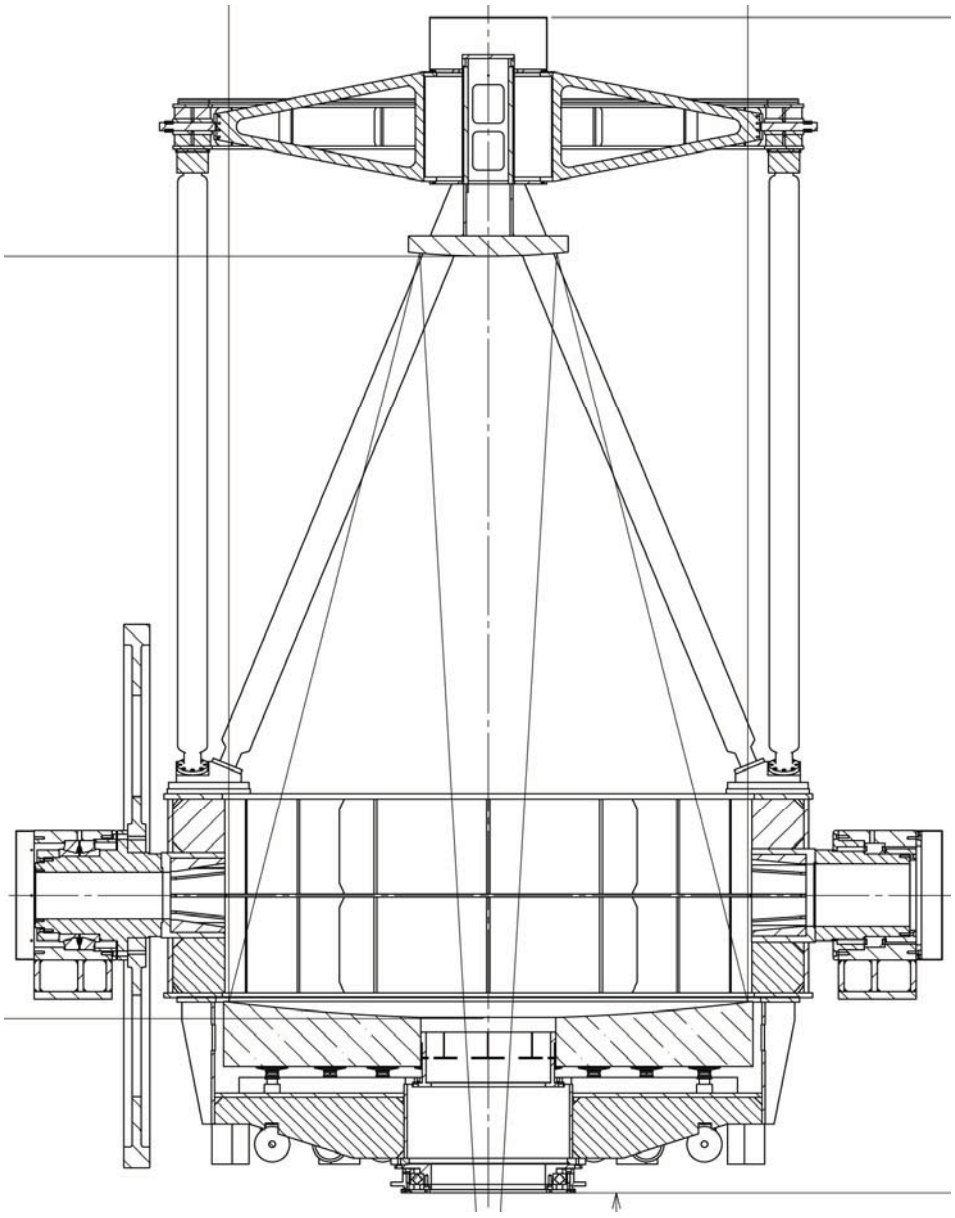

勘驗項目說明如下：

1. 主次鏡

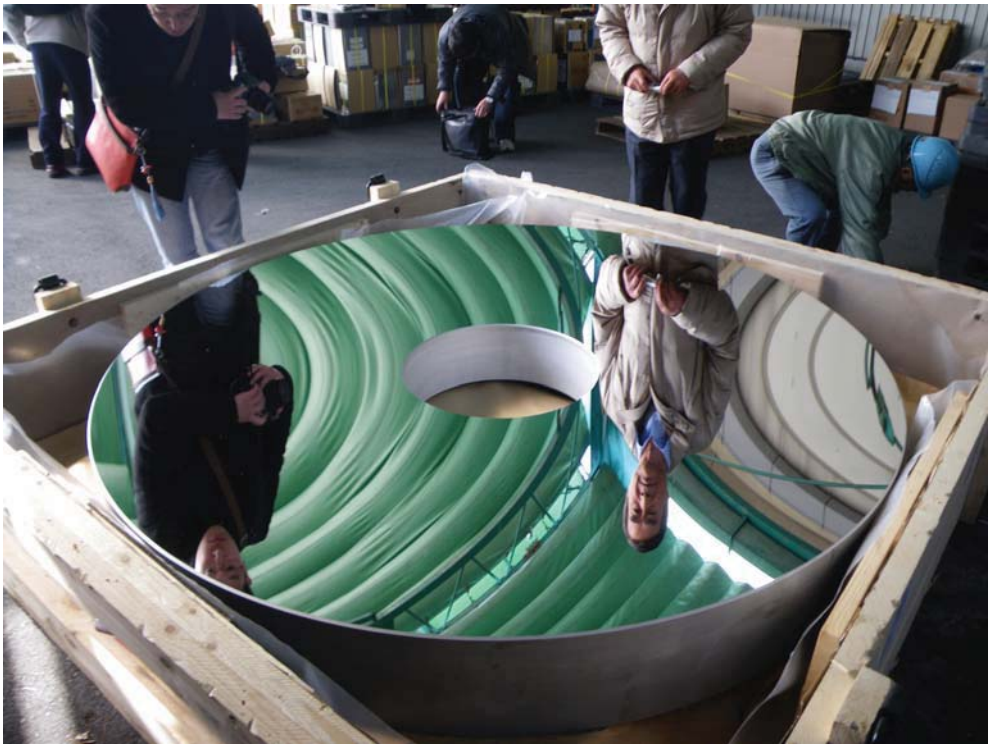

望遠鏡主鏡已由俄羅斯光學鑄鏡廠製作完畢運送至日本，存放於京都市區內的保稅倉庫，等待清關。

已製作完成的次鏡，與主鏡一同存放於保稅倉庫內。

2. 次鏡環與支撐架

次鏡環結構

次鏡支撐架與安裝筒

次鏡支架尺寸量測

3. 鏡筒架

鏡筒架已製作完成，待組裝

鏡筒架尺寸測量

4. 高度軸總成

望遠鏡高度軸安裝座

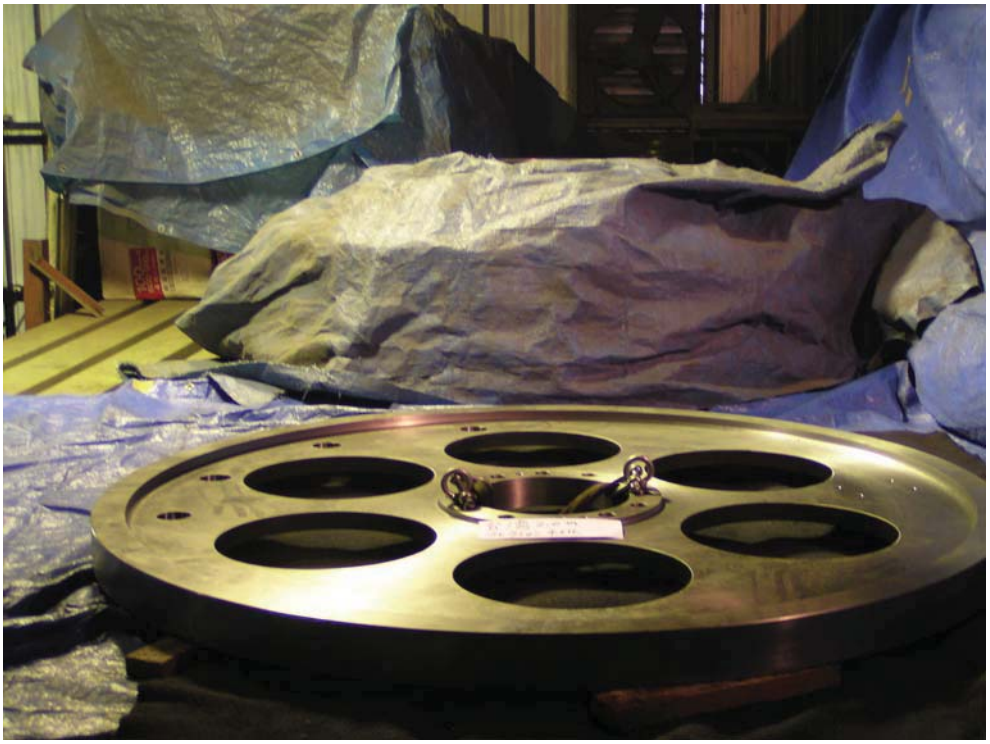

高度軸驅動用摩擦輪

5. 鏡室總成

主鏡室結構

望遠鏡中間塊結構

6. 像場旋轉裝置

像場旋轉裝置的主要齒輪組件

鏡筒與鏡室部份，經查驗各組件已製作完成，應符合進度要求。唯光學鏡片部分，因光學品質部分無法於此次查驗中檢驗，依據合約內針對文件要求的部份，廠商應提供光學檢驗資料。

驗收報告（第四項望遠鏡架台部分）

驗收標的：合約第五條第四項，望遠鏡架台與控制系統機電設備

報告內容：

本項合約標的包含望遠鏡底支撐座、方位旋轉基座、架台底座、叉臂等大型部件與機電控制設備。各大部件如下圖所示黃色部分，依目前進度要求，廠商應完成各部件的外型製作，達到準備組裝之要求。

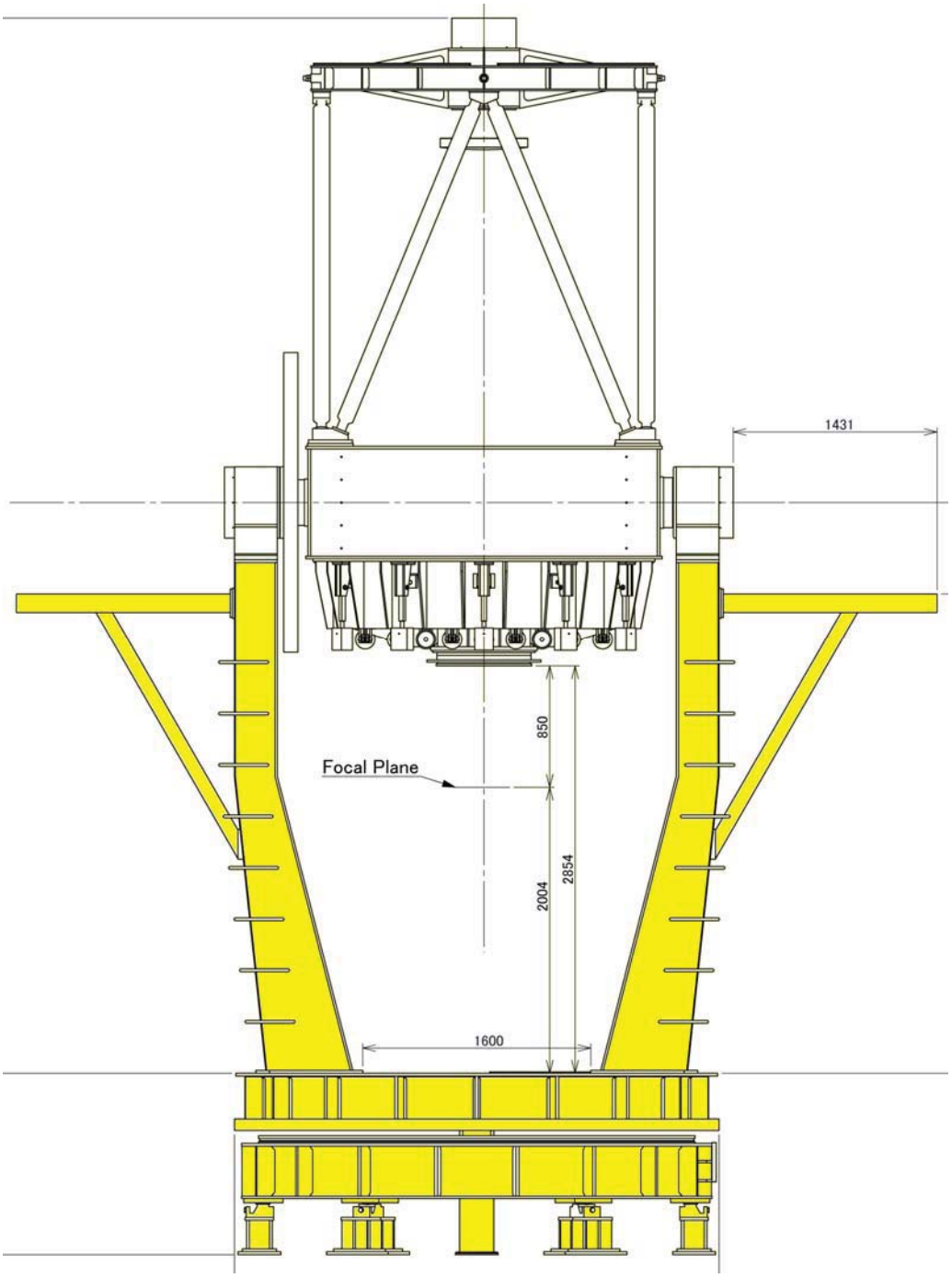

望遠鏡各部件因尺寸不同所需機具有異，由西村公司進行設計後交由不同工廠進行製作與加工，而組裝作業由西村公司人員在西村公司自有工廠進行，由於組裝工作尚未開始，本次針對各別部件的查驗工作在各加工廠進行，於 2/18 日前往姬路市『住本鐵工所株式會社』加工廠勘驗大型物件，2/19 前往城陽『西浦機工有限會社』的加工廠勘驗小型部件，與『內藤運輸株式會社』的倉儲廠勘驗暫存的部件。

經現場實際勘驗各部件製作進度如下：

1. 望遠鏡底支撐座

   如下圖，已完成製作，等待運送至總裝廠進行總裝工作。

望遠鏡底支撐座

望遠鏡底座中心軸

2. 方位旋轉機座

已完成加工、應力釋放等工作，現存於加工廠內，準備運送。

已完成之方位旋轉基座

3. 方位旋轉台

已完成加工與應力釋放工作，現暫存於日本姬路市加工廠內，等待付運至總裝廠進行組裝。

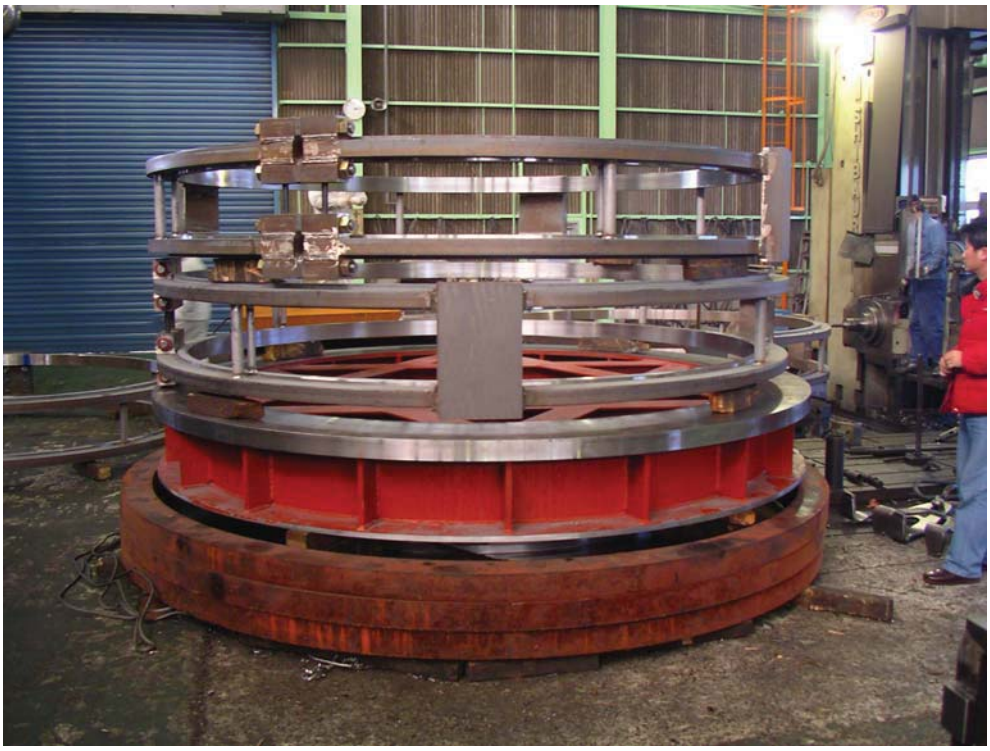

已完成的方位旋轉台

4. 叉臂

已完成製作工作，暫存於倉儲空間內，等待運送至西村公司進行組裝。

望遠鏡叉臂（一）

望遠鏡叉臂（二）

5. 控制系統機電設備

望遠鏡的機電設備於組裝時方配合安裝於各部件預定位置，已完成控制器的製作，並完成馬達與編碼器等備料工作。

機電與控制系統已於西村公司內準備組裝

驅動單元

驅動單元內部線路

望遠鏡控制單元

伺服馬達與讀、編碼器、纜線等控制系統配件

結論：

依據合約精神與天文所行前會議討論，本次驗收屬於望遠鏡各部件的進度檢視，應對主件進行完成度檢驗，且望遠鏡組裝有其特定工序與未來運輸上的考量，因此訂立驗收標準為：

I. 大型焊接件應完成整體外型與應力處理。

II. 小型的加工件與組合件應完成工件。

III. 機電與控制系統單元應完成線路組裝並備齊相關料件。

IV. 一次性安裝組件或有運輸問題考量，廠商應提出說明。

依據現場勘驗結果，本項廠商所製之大型部件均已製作完成，已達可配合組裝進度付運至西村公司進行組裝之程度。機電控制系統也已於西村公司組裝廠內完成備料與組裝準備，符合合約進度規範，查驗合格。

附錄

NCU/LULIN LOT/1m OBSERVING PROPOSAL

Semester:

※ Observing time is allocated on a 6month basis, September-January (B), for this semester.
※ The proposal, either in Chinese or English, should be sent to the Time Allocation Committee, preferably via email at tac_lulin@astro.ncu.edu.tw, or via post to Graduate Institute of Astronomy, National Central University, 300 Jungda Road, Chung-Li 32054 Taiwan. Inquiries regarding observing requests or instrumentation can be directed to the same email contact.
※ If time is granted, please fill out the Lulin Lodging Request Form before the observing run (http://www.lulin.ncu.edu.tw/TAC/LulinApplication.htm).
※ At times a time-honored event may require interruption of an ongoing project. The observer will be notified, and consulted for service observations if a mutual agreement can be reached.

---

1. Title of the Proposed Observing Program

---

2. Abstract (limited to 200 words)

---

3. Category

☐Solar System ☐Exoplanets ☐Stars Star Formation ☐Compact Objects
☐Interstellar Medium ☐Nearby Galaxies ☐AGN ☐Cosmology
☐Cluster of Galaxies ☐Gravitational Lenses ☐Large Scale Structure ☐Distant Galaxies
☐Others

---

4. Principal Investigator

Name:
Institute:
Address:
E-mail:
Phone/Fax:

5. Co-Investigators

Name / Institute	Name / Institute	Name / Institute

6. Link to Thesis Work

☐This observing program is linked to a PhD thesis

☐This observing program is linked to a master thesis

Name of the student(s):

7. Time Request

Instrument (LCI/LCS)	Number of Nights	Moon Phase (D/G/B)	Preferred Date	Acceptable Date	Remarks (Hi or Lo-Res for LCS)

Total requested number of nights:

Minimum acceptable number of nights:

8. Scheduling Constraints

9. Instrument Requirements

10. Observing Experiences

11. Backup Program in Poor Weather Conditions

12. Publications related to LOT usage

13. Status of Previous Observations if LOT observing time has been allocated to P.I. before

14. Target List

Object	RA (2000.0)	Dec (2000.0)	Magnitude	Angular Size	Exposure	Remarks

15. Scientific and Technical Justifications (limited to two additional A4 pages, including figures)

相關報導

全球天文年 26日環食 2/9半影月食

【記者蔡明樺台北報導】

二〇〇九是全球「天文年」！中央氣象局表示，今年除了六月之外，每個月都有天文現象發生，元旦假期的象限儀座流星雨後，一月二十六日還有「日環食」，二月九日的「半影月食」台灣可見到全部過程，有興趣的民眾可大飽眼福。

一月二十六日大年初一當天，日環食的環食帶起自南大西洋，自非洲南方海面橫跨印度洋，最後在菲律賓南方海面結束，氣象局說，台灣可以在日沒前見到二十五到三十五分鐘的偏食現象，七月二十二日還有一次「日全食」現象，但台灣並非位於全食帶區，僅能見到日偏食。

由中央大學天文所發現的「鹿林彗星」，是二〇〇九年最值得關注的彗星，二月二十四日最接近地球，預估可達肉眼能見的亮度，屆時民眾可以直接用簡易型望遠鏡欣賞鹿林彗星。

原文轉載自【2009-01-02/台灣新生報/3版/兩岸・航貿】

新年看流星雨 明晚象限儀座極大值

【記者郭曉蓓台北報導】

昨天是元旦，也是新年的開始；氣象局指出：今年天文星象相當精采，天空流星雨爲今年的豐富星象拉開序幕，尤其明天是「象限儀座流星雨」的極大值，民眾在光害少的空曠地區，看到流星雨的機率很大。

新年開始，就有流星雨報到，象限儀座流星雨是年度三大流星雨的第一群，活躍期間一直持續至五日，其中極大期將在明天，根據國際流星組織（IMO）預測極大期發生在明天二十時五十分，預計條件最佳的狀況下，流星數量最多可達每小時一百二十顆。

中央氣象局也表示，此次「象限儀座流星雨」輻射點位於牧夫座北側，在午夜過後才從東北方升起，由於見到輻射點升起時間與極大期相差近三個小時，因此台灣無法見到極大期的數量，但氣象局說，這個流星群特色是相當的明亮，在明天三日午夜過後至四日凌晨仍值得留意。

新年來到，今年天文星象很熱鬧，氣象局表示，今年預估有九個流星雨較值得留意，其中，中央大學天文所鹿林天文台所發現的「鹿林彗星」也是今年開始最受矚目的彗星，它將在一月十日通過近日點，並在二月二十四日最接近地球，預估達肉眼能見的亮度，台灣民眾屆時直接用簡易望遠鏡，便可欣賞第一顆彗星。

氣象局公布整年度的天文星象指出，今年全球計有一次日環食、一次日全食、一次月偏食及三次半影月食現象，台灣將可以看到二次日食，以及一次半影月食，民眾可以留意觀賞天文現象。

原文轉載自【2009-01-02/青年日報/9版/生活新聞】

日食 月食 流星雨…天文迷 今年看個夠

【記者楊正敏台北報導】

今年是全球天文年，各種天文現象彷彿在慶祝似的一起湊熱鬧，不只日食、月食全都有，還有台灣中央大學鹿林天文台發現的鹿林彗星，今年二月將最靠近地球，用簡單的望遠鏡就能看到這顆彗星。

中央氣象局表示，今年全球有一次日環食、一次日全食、一次月偏食及三次半影月食現象。台灣可以看到二次日食及一次半影月食。

氣象局天文站技士鄭振豐指出，日環食將在一月廿六日出現，當天農曆大年初一，環食帶起自南大西洋，從非洲南方海面橫跨印度洋，最後在菲律賓南方海面結束，台灣僅能在日落前廿五到卅五分鐘看見偏食。

較值得注意的是七月廿二日的日全食，鄭振豐說，這次日食帶起自印度，經過中國大陸及日本南方海面，最後在南太平洋結束，中國的長江流域附近城市如上海就可以看到日全食；就算不到對岸，台灣可以看到約八成日偏食。

月食部分，今年元宵節，台灣可以看到半影月食全部過程，所謂的月影半食是月亮通過地球的半影區，會看到亮度變化。開始時間爲晚上的八時卅七分，隔日凌晨零時四十分結束。

中央大學鹿林天文台所發現的鹿林彗星，將於一月十日通過近日點，二月廿四日接近地球，預估可以達到肉眼能見的亮度，約在四到五等間。

另外，年九月四日會因土星環橫面正對地球，在視線上好像消失的天文現象。全年還有九個流星雨，明晚八時五十分是象限儀座流星雨極大期。

這兩天台灣天氣受大陸冷氣團影響，看流星雨，要做好保暖準備。

原文轉載自【2009-01-02/聯合報/A7版/生活】

兩岸合作發現首顆彗星 10日通過軌道近日點

【中央社記者孫承武台北 5 日電】

台北市立天文館今天表示，兩岸在 2007 年合作發現的第一顆彗星「鹿林」，將於 1 月 10 日通過軌道近日點，亮度約 6 至 7 等，且 2 月下旬最接近地球時可亮達 5 至 6 等、甚至更亮。

天文館表示，在這段期間內，利用雙筒或小型望遠鏡可觀賞這顆在宇宙間高速奔馳的另類「台灣之光」。

鹿林彗星是在 2007 年 7 月 11 日由國立中央大學天文研究所的「鹿林巡天計畫」（Lulin Sky Survey, LUSS）觀測助理林啓生與中國大陸廣州中山大學葉泉志，使用鹿林天文台 41 公分望遠鏡共同發現。

國際彗星組織依非週期彗星、2007 年 7 月上半個月發現的第 3 顆新彗星的特性，將其編號 C/2007 N3，並以發現的天文台爲其命名「鹿林（Lulin）」。鹿林彗星是台灣本土所發現及命名的第一顆彗星，也是海峽兩岸合作發現的第一顆彗星。

依天文館資料，鹿林彗星軌道特性顯示，鹿林彗星是來自太陽系外圍歐特雲區的極長週期彗星，繞太陽公轉一圈長達 2850 萬年。

換言之，鹿林彗星上一次來到太陽系內側時，當時地球上才剛要演化出人類與猿猴類的共同祖先—埃及猿，地球南北兩極的冰冠才剛開始形成，地球最高的山脈喜馬拉雅山才正要從板塊互撞的造山運動中向上隆起成山，而當時的台灣還深埋在海底。

原文轉載自【2009-01-05/中央社】

鹿林彗星 1-4 月　進入最佳觀測期

【林麗玉報導】

由臺灣天文研究團隊發現的第一顆彗星「鹿林彗星」，這個月 10 號就會通過軌道近日點，亮度大約在 6~7 等左右，預測 2 月下旬最接近地球時，亮度還可以達到 5~6 等左右、甚至更亮，民眾利用雙筒或小型望遠鏡，就可以觀賞到鹿林彗星，而今年 1 月到 4 月，都是鹿林彗星的最佳觀測期。

台北市立天文教育館表示，鹿林彗星是在 2007 年 7 月 11 日，是中央大學天文研究所的鹿林巡天計畫時，使用鹿林天文台 41 公分望遠鏡發現，當時位在寶瓶座，亮度只有 19 等。而俗稱掃把星的彗星，環繞太陽公轉，當逐漸靠近太陽時，會受到太陽光與熱的影響，表面物質蒸發形成彗髮與彗尾；愈靠近太陽，彗髮愈寬、彗尾愈長。而今年一月到四月，正是鹿林彗星的最佳觀察期，1 月初時，它位在天蝎座與天秤座之間，天亮前可以發現它位於東南方天空，而元月 10 號晚間 11 點，以 1.212AU 的距離通過近日點，隨後移動速度加快，2 月初位在天秤向獅子座移動；2 月 24 號最接近地球，這個時候的鹿林彗星不僅整晚可見，觀測條件也相當良好，不過到 4 月底時，鹿林彗星的亮度預計會快速降至 8-9 等左右，得用口徑 15 公分以上的望遠鏡才比較容易看見，天文教育館表示，鹿林彗星繞陽公轉一圈必須花長達 2850 萬年時間，民眾可要好好把握這次鹿林彗星通過軌道近日點的最佳觀測機會。

原文轉載自【2009-01-05/中廣新聞網】

鹿林彗星接近地球　僅此一次

【張勵德／台北報導】

第一顆由台灣望遠鏡發現並獲國際命名權的「鹿林彗星」，將於下月二十四日抵達最接近地球的近地點，由於屬長周期軌道彗星，離開近地點後可能不再出現，這將是台灣民眾此生唯一可見鹿林彗星的機會。

鹿林彗星是二〇〇七年七月十一日，中央大學天文所鹿林天文台執行「巡天計劃」時，由觀測員林啓生與中國廣州中山大學學生葉泉志一起發現，編號「C/2007N3」，後正式命名爲鹿林（Lulin），是首顆由台灣本土望遠鏡觀測、兩岸合作發現的彗星。

搭配星座盤較好找

中央氣象局天文站技士鄭振豐說，鹿林彗星本月十日將通過離太陽最近的近日點，之後慢慢接近地球，下月二十四日抵達與地球距離最近的近地點，春節期間到下月底都很適合觀賞；亮度估計可達四到五等（數字越大越暗，人類肉眼最低可見約六等），用雙筒望遠鏡即可看見。

鄭振豐指出，目前鹿林彗星在天秤座東側靠天蠍座頭部，每天約凌晨三到四時自東南東方升起，「建議用雙筒望遠鏡，尋找天空中帶有朦朦彗髮的星體，本月底到下月初還可看見拖著尾巴的彗星，但那時彗尾對著地球，反而不易看見整顆彗星。」

林啓生建議，下月二十三、二十四日觀賞較清楚，屆時彗星在日沒後即從東南方升起，「但彗星亮度不高，尋找可能有些困難，最好搭配星座盤，甚至彗星軌道圖，先找到彗星所在的星座位置，再尋找彗星。」

●鹿林彗星觀測資訊

・通過近地點時間：02/24

・最佳觀測期：1 月下旬農曆春節至 2 月底

・觀測方式：本月底前每天清晨 4 時許，向東南東方上空觀測、找尋帶有朦朦彗髮的星體

・建議事項：使用雙筒望遠鏡或高倍數望遠鏡觀測

資料來源：氣象局天文站技士鄭振豐、鹿林天文台觀測員林啓生

原文轉載自【2009-01-05/蘋果日報/A4 版/要聞】

中國時報「鄒族」小行星　月中正式命名

【記者謝璧蓮報導】

中國時報；「台灣原住民族」在太空也找得到！中央大學鹿林天文台因爲與鄒族的「緣份」，也爲了鼓勵更多原住民投入天文科學的行列，決定把最近新發現的一個小行星命名爲「鄒族」，本月十四、十五日舉行命名儀式。

這是第一個以台灣原住民族命名的小行星。

原文轉載自【2009-01-02/台視新聞】

「鄒族」小行星　月中正式命名

【邱莉苓報導】

「台灣原住民族」在太空也找得到！中央大學鹿林天文台爲了鼓勵更多原住民投入天文科學的行列，決定把最近新發現的一個小行星命名爲「鄒族」，14、15 日舉行命名儀式。這是第一個以台灣原住民族命名的小行星。特別的是，命名當天，將邀請同爲鄒族的星光二班安欽雲到現場觀禮，儀式可謂「星光熠熠」。

中央大學的鹿林天文台自 2006 年 3 月開始「鹿林巡天計畫」，利用有限的經費與人力，藉小型望遠鏡與台灣擁有的經緯度觀測條件的優勢，短短 2 年內已發現 800 多顆小行星，成果相當豐碩。

中央大學天文所所長黃崇源說，「鄒族」與鹿林天文台的所在地、嘉義阿里山鄉關係密切，台內 7 名成員中，有 4 人是鄒族人，「緣分不淺」。

天文台發現小行星後，行星軌道經國際小行星中心（ＭＰＣ）確認，再由國際天文聯合會(ＩＡＵ)編號才擁有命名權。鹿林天文台目前擁有將近 30 顆的小行星命名權，但受限於國際天文聯合會每兩個月才召開一次會議，每次會議只能提報兩個行星名。爲了鼓勵更多的原住民能夠一起加入科學領域，才選用「鄒族」這個名字。

此外，繼「嘉義」後，此次發現的另外一個小行星也再度以台灣地名「南投」命名，將在 1 月中旬的世界天文年慶祝活動中一併公布。

原文轉載自【2009-01-02/中央廣播電台_新聞】

鹿林彗星來了　錯過不再來

【記者謝蕙蓮/台北報導】

第一顆由台灣望遠鏡發現並命名的彗星「鹿林彗星」，2 月 24 日最接近地球。由於鹿林彗星的軌道呈拋物線，可能一去不回，今年是這輩子唯一有機會親眼見到鹿林彗星，民眾千萬不能錯過。

中央氣象局技士鄭振豐利用元旦假期上山「追星」，昨天凌晨終於在攝氏零度低溫中，在新中橫橫石山停車場，拍攝到鹿林彗星最近的影像。照片中的鹿林彗星，已經可以明顯看見，彗核四圍包圍著一團綠色的「彗髮」，一般彗星最顯著的特徵—長長的「彗尾」，現在還不明顯。

鹿林彗星是在前年 7 月 11 日，中央大學天文所鹿林天文台執行鹿林巡天計畫 (Lulin Sky Survey,LUSS)時，由鹿林天文台觀測員林啓生、大陸廣州中山大學學生葉泉志，使用鹿林天文台 41 公分望遠鏡發現的新彗星，編號爲「C/2007 N3」，後來命名爲「鹿林」，是第一顆在台灣本土觀測、命名，由兩岸合作發現的彗星。

鄭振豐表示，鹿林彗星 10 日通過近日點，今年 2 月 24 日最接近地球，屆時和地球的距離大約是地球和月亮距離的 14.5 倍，預估亮度可達 4 等左右，肉眼就能看見。台灣的民眾只要透過簡易望遠鏡，就可以清楚觀測第一顆由台灣發現、命名的彗星。

鄭振豐說，這個月底接近春節期間，是民眾觀測鹿林彗星較佳的時機。因爲鹿林彗星在 1 月底、2 月初時，「彗尾」最明顯、拖得最長；2 月 24 日鹿林彗星最接近地球時，彗尾正好背對著我們，那時觀測反而看不清楚它的全貌。

鹿林彗星 1 月的位置在天秤座緩慢向西移動，2 月會加速經過室女座，2 月下旬進入獅子座內。大約在黎明前，會出現在東南東方低空。鹿林天文台人員表示，鹿林彗星未來的角度會愈升愈高，到 2 月 24 日時，位置大約在西偏南方仰角 30 度的天空，民眾使用一般的雙筒望遠鏡就可以看到。

原文轉載自【2009-01-04/聯合晚報/A3 版/話題】

鹿林彗星　下月最接近地球

【李宗祐台北報導】

二〇〇九年是「全球天文年」，紀念伽利略首次以望遠鏡進行天文觀測四百周年，對台灣天文迷更具特別意義。首顆由國人發現並命名的「鹿林彗星」本月十日通過近日點後，將逐漸向地球接近，這是「鹿林彗星」被發現後，首次接近地球，可望掀起國內觀測熱潮。

中央氣象局表示，二〇〇九年是全球天文年，有許多天文景觀值得期待。台灣地區看得到二次日食和一次半影月食，最令人期待的應是由中央大學鹿林天文台前年觀測發現的「鹿林彗星」（C/2007 N3）本月十日通過近日點後，預計二月廿四日最接近地球。

原文轉載自【2009-01-02/中國時報/A10 版/生活新聞】

「鄒族」小行星　月中正式命名

【唐鎮宇台北報導】

「台灣原住民族」在太空也找得到！中央大學鹿林天文台因爲與鄒族的「緣份」，也爲了鼓勵更多原住民投入天

文科學的行列，決定把最近新發現的一個小行星命名爲「鄒族」，本月十四、十五日舉行命名儀式。這是第一個以台灣原住民族命名的小行星。

特別的是，命名當天，將邀請同爲鄒族的星光二班安欽雲到現場觀禮，儀式可謂「星光熠熠」。

星光熠熠　鼓勵原住民投入

中央大學的鹿林天文台自九十五年三月開始「鹿林巡天計畫」，利用有限的經費與人力，藉小型望遠鏡與台灣擁有的經緯度觀測條件的優勢，短短兩年內已發現八百多顆小行星，成果相當豐碩。

中央大學天文所所長黃崇源說，「鄒族」與鹿林天文台的所在地、嘉義阿里山鄉關係密切，台內七名成員中，有四人是鄒族人，「緣分不淺」。

「南投」也將繼「嘉義」後翱翔

天文台發現小行星後，行星軌道經國際小行星中心（ＭＰＣ）確認，再由國際天文聯合會(ＩＡＵ)編號才擁有命名權。鹿林天文台目前擁有將近卅顆的小行星命名權，但受限於國際天文聯合會每兩個月才召開一次會議，每次會議只能提報兩個行星名。爲了鼓勵更多的原住民能夠一起加入科學領域，才選用「鄒族」這個名字。

此外，繼「嘉義」後，此次發現的另外一個小行星也再度以台灣地名「南投」命名，將在一月中旬的世界天文年慶祝活動中一併公布。

原文轉載自【2009-01-02/中國時報/A10 版/生活新聞】

鹿林彗星十日通過軌道近日點　閃耀台灣之光

【記者楊麗雪台北報導】

我研究團隊發現的第一顆彗星－鹿林彗星，本月十日將通過軌道近日點，兩度約六至七等，且在二月下旬最接近地球時可亮達五至六等、甚至更亮。台北市立天文館指出，此期間，利用雙筒或小型望遠鏡，就可觀賞這個在宇宙間高速奔馳的另類「台灣之光」。

俗稱「掃把星」的彗星是太陽系中，環繞太陽公轉的冰雪球，當逐漸靠近太陽時，會受到太陽光與熱的影響而使表面物質蒸發形成彗髮與彗尾；愈靠近太陽，彗愈寬、彗尾愈長。

天文館指出，今年一至四月是鹿林彗星的最佳觀察期，它於本月初時位在天蝎座與天秤座之間，可在天亮前見於東南方天空；十日深夜十一時以一點二一二 AU(天文單位，爲日地平均距離，約爲一億五千萬公里)的距離通過近日點，隨後移動速度加快，二月初位在天秤，經室女向獅子移動；二月廿四日最接近地球(約零點四一 AU)，此時不僅整晚可見，月相幾乎逢朔，觀測條件非常良好，且再二月廿四日凌晨與土星近至僅約三度距離。

之後，鹿林彗星將繼續西移，三月五、六日掠過巨蟹中央著名的鬼宿星團；三月中旬後進入雙子座，三月十六日與九點一等的愛斯基摩星雲（或稱「丑臉星雲」）相距不到四十角分，相當適合做爲天文攝影的目標。四月底時，亮度預計會快速降至八至九等左右，得用口徑十五公分以上的望遠鏡才比較容易看見，且彗星在約午夜時便已西沈。

天文館表示，鹿林彗星是在二○○七年七月時一日由國立中央大學天文研究所的鹿林巡天計畫(Lulin Sky Survey,LUSS)觀測助理林啓生與大陸廣州中山大學葉泉志，使用鹿林天文台四十一公分望遠鏡共同發現；發現當時位在寶瓶座，亮度僅十九等。

國際彗星組織按其身爲非週期彗星、二○○七年七月上半個月發現的第三顆新彗星的特性，將其編號爲 C/2007 N3，並以發現的天文台爲其命名爲「鹿林(Lulin)」。鹿林彗星是台灣本土所發現及被命名的第一顆彗星，也是海峽兩岸合作發現的第一顆彗星。

原文轉載自【2008-01-06/青年日報/6 版/新視界】

鹿林天文台 2 米望遠鏡　2 月動工

【圖：中央大學提供　文：記者陳宣瑜】

中央大學將斥資一點七六億，在鹿林天文台打造全東南亞最高的兩米望遠鏡，於「二○○九國際天文年」二月將正式動工，預計二○一○年完工，昨由原住民鄒族長老舉辦祈福儀式，期盼工程順利。

中央大學天文研究所所長黃崇源表示，鹿林天文台位於海拔二八六二公尺高山，光害少，是全台最適合觀星地點，但因所有運輸均靠索道工程，施工難度頗高。

未來二米望遠鏡集光能力高四倍，可觀測的星體體積達十倍，將可完整觀測到銀河系外的天體變化。中央大學副校長葉永烜表示，以一○一的煙火爲例，一米望遠鏡看不到，但兩米就能看得一清二楚。

未來兩米望遠鏡將與美國「泛星計畫」結合，負責搜尋太空中可能撞擊地球的天體，擔任守護地球的哨兵。）

原文轉載自【2009-01-15/自由時報/A10 版/生活新聞】

鹿林天文台 2 米望遠鏡　東南亞最高

【記者湯雅雯嘉義報導】

中央大學位於鹿林天文台的 2 米望遠鏡將於 2 月動工，預計明年完工。這座位於海拔 2862 公尺高的 2 米望遠鏡，不僅是全台口徑最大的望遠鏡，更是全東南亞海拔最高的天文台，且沒道路直達，須靠索道運輸，施工難度更高。

中央大學天文所所長黃崇源表示，因爲海拔高，鹿林天文台是全球唯一沒有車道可達的研究型天文台，必須花半小時

爬完 600 公尺的步道才能抵達，這對工程的挑戰極大，物資運輸需靠「索道」吊運，採取傳統工法，施工難度相當高。黃崇源指出，2 米望遠鏡計畫所需經費高達 1.76 億元，由教育部 5 年 500 億計畫補助一半，剩下的由國科會補助及中央大學自籌，光主鏡就高達 8000 萬元；主鏡目前在俄羅斯磨片，預計今年內送往日本組裝。

黃崇源說，2 米望遠鏡集光能力是 1 米的 4 倍，可看到更暗的星星，看到星空的範圍，也將是 1 米望遠鏡的 8 倍，讓台灣晉升中大型望遠鏡之列。且目前也和美國夏威夷大學共同推動「泛星計畫」，將讓台灣在全球天文觀測占有一席之地。

「泛星計畫」由美國空軍委託夏威夷大學在夏威夷建置望遠鏡，用來搜尋太空中任何可能撞擊地球的天體。預計花 10 年時間，找出會威脅地球的小行星，即時將它清除。

原文轉載自【2009-01-15/聯合報/C3 版/教育】

世界第一顆！　發現行星命名「鄒族」

【記者辜士陞嘉義報導】

台灣原住民之一的鄒族，現在在天空也找得到！中央大學鹿林天文台新發現一顆小行星，因爲平常研究員的生活受到鄒族人照顧，決定把這顆行星命名爲鄒族小行星，也成爲第一顆以台灣原住民爲名的星球。

就是這顆，位在金牛座和白羊座中間的小行星，被中央大學天文所研究人員發現，現在決定以命名爲「鄒族」小行星。中央大學副校長：「我們是第一個把小行星，命名給原住民的國家，所以在這方面，台灣可以作爲全世界的榜樣。」

由於研究人員發現小行星的地點就是在嘉義鹿林，而這裡不但是鄒族大本營，就連研究人員的生活起居，全都要靠鄒族的 4 位青年打理，爲了感謝原住民才興起命名的念頭。文史工作者梁景德：「真的非常高興，也非常感動，在這部分有占一個空間，所以地球上有鄒族，太空也有鄒族，把鄒族往外推。」

鄒族原住民開心，也希望透過這座天文台，讓更多原住民的小朋友加入觀星的行列。

原文轉載自【2009-01-16/TVBS】

中大贈阿里山鄒族小行星模型

【台北訊】

中央大學 2007 年發現小行星，取名爲「鄒族小行星」，去年底國際接受這項命名，成爲首顆以台灣原住民族群命名的小行星，中大昨天頒贈鄒族小行星模型給阿里山鄉公所。

中大表示，鹿林天文台在 95 年 10 月 15 日發現的 175586 號小行星，發現時位置在牡羊座，目前位於室女座；去年 12 月 12 日經國際天文聯合會(IAU)的國際小行星命名委員會通過，正式命名爲「鄒族」(175586 =Tsou = 2006 TU106)。

中大指出，今年是聯合國的「國際天文年」，昨天是國際天文年的開幕日，所以在這個特別的日子舉行頒贈儀式，由阿里山鄉長陳明利代表接受，阿里山地區達邦、樂野、來吉、十字、香林等 5 所小學的校長與學生參與盛會。

中大副校長葉永烜表示，台灣原住民有豐富的天文知識，引領他們航向未知；鹿林天文台的背後是許多原住民的付出，鹿林海拔 2862 公尺，建設之初，端賴布農族和鄒族原住民披荊斬棘，一磚一瓦揹上山頭。成立至今，全賴 4 位鄒族青年 365 天 24 小時輪班守候。

中大表示，「鄒族小行星」是由中央大學天文所觀測員林啓生與大陸廣州中山大學大氣科學系研究生葉泉志在鹿林天文台所發現，國際永久編號爲 175586。

中大指出，「鄒族小行星」位於火星和木星之間的小行星帶，最接近太陽時距離約 4.6 億公里（近日點），離太陽最遠時，距離約 4.8 億公里（遠日點），繞太陽一圈約 5.6 年（軌道週期）。

原文轉載自【2009-01-16/台灣立報】

接受中央大學發現的小行星命名爲鄒族

【中央社記者林思宇台北 15 日電】

中央大學 2007 年發現小行星，取名爲「鄒族小行星」，2008 年底國際接受這項命名，成爲第一顆以台灣原住民族群命名的小行星，中央大學今天頒贈鄒族小行星模型給阿里山鄉公所。

中大表示，鹿林天文台在 95 年 10 月 15 日發現的 175586 號小行星，發現時位置在牡羊座，目前位於室女座；去年 12 月 12 日經國際天文聯合會 (IAU)的國際小行星命名委員會通過，正式命名爲「鄒族」(175586 =Tsou = 2006 TU106)。

中大指出，今年是聯合國的「國際天文年」，今天是國際天文年的開幕日，所以在這個特別的日子舉行頒贈儀式，由阿里山鄉長陳明利代表接受，阿里山地區達邦、樂野、來吉、十字、香林五所小學的校長與學生參與盛會。

中大副校長葉永烜表示，台灣原住民有豐富的天文知識，引領他們航向未知；鹿林天文台的背後是許多原住民的付出，鹿林海拔 2862 公尺，建設之初，端賴布農族和鄒族原住民披荊斬棘，一磚一瓦揹上山頭。成立至今，全賴 4 位鄒族青年 365 天 24 小時輪班守候。

中大表示，「鄒族小行星」是由中央大學天文所觀測員林啓生與大陸廣州中山大學大氣科學系研究生葉泉志在鹿林天文台所發現，國際永久編號爲 175586。

中大指出，「鄒族小行星」位於火星和木星之間的小行星

帶，最接近太陽時距離約 4.6 億公里（近日點），離太陽最遠時，距離約 4.8 億公里（遠日點），繞太陽一圈約 5.6 年（軌道週期）。

原文轉載自【2009-01-15/中央社】

首以原住民命名　鄒族小行星誕生

【記者湯雅雯】

「現在不只地上有鄒族、天上也有鄒族。」繼鹿林、中大、嘉義、鄭崇華小行星後，中央大學鹿林天文台發現編號 175586 小行星，正式命名爲「鄒族（Tsou）」，成爲首顆以台灣原住民爲名的小行星。

鹿林天文台已對 12 顆小行星命名，其中 7 顆星名是中大取的，另 5 顆由共同發現者，中國籍的業餘天文學家葉泉志享有。

中央大學天文研究所所長黃崇源說，發現小行星無法立即命名，再確定行星軌道後，才能提報國際天文聯合會（IAU）編號，發現單位才有命名權。阿里山鄉鄉長陳明利是鄒族原住民，他昨天帶領香林、來吉、十字、樂野、達邦等五所鄒族原住民小學共 50 多名學童參加「鄒族小行星」的命名頒贈典禮，希望從小灌輸他們天文科學概念，培養成爲「天文新兵」。

鄒族小行星　蘊涵感恩之心

【本報嘉義訊】

中央大學天文所鹿林天文台九十五年發現一顆小行星，取名爲「鄒族」，去年經國際天文聯合會通過，成爲首顆以台灣原住民族族群命名的小行星。

今年是國際天文年，中央大學昨天選在阿里山鄉公所舉辦命名頒贈典禮，邀請數十位鄒族小朋友參與。

九十五年十月十五日，中大天文所觀測員林啓生、大陸廣州中山大學大氣科學系研究生葉泉志，在鹿林天文台發現一顆小行星，國際永久編號爲「一七五五八六」。

爲何要命名爲「鄒族」？中大副校長葉永烜表示，鹿林天文台的背後是許多原住民的付出，鹿林海拔二千八百六十二公尺，建設之初，端賴布農族和鄒族原住民披荆斬棘，一磚一瓦揹上山頭。

他說，一般人很難在這麼高的地方工作，鹿林天文台成立至今，全賴四位鄒族青年全天輪班守候，無論颱風來襲或除夕過年，他們都堅守崗位，取名「鄒族」是爲了感恩，也希望大家了解原住民有豐富的天文知識。

中大指出，鄒族小行星位於火星和木星之間的小行星帶，最接近太陽時，距離約四點六億公里（近日點），離太陽最遠時，距離約四點八億公里（遠日點），繞太陽一圈約五點六年。

原文轉載自【2009-01-16/人間福報/3 版/綜合/社區】

台灣鄒族登上太空　小行星正式命名

【記者陳宣瑜嘉義報導】

「台灣鄒族登上太空！」國立中央大學天文所鹿林天文台以台灣原住民「鄒族」爲名，爲中大發現的一七五五八六號小行星命名，今天在嘉義縣阿里鄉公所舉行頒贈儀式，這是第一個以台灣原住民族命名的小行星。

中央大學表示，「鄒族小行星」是由中央大學天文研究所專任助理林啓生與中國廣州中山大學大氣科學系葉泉志，在九十五年十月十五日共同發現，行星軌道經國際小行星中心（MPC）確認後，再由國際天文聯合會(IAU)編號才擁有命名權，中大在去年十月提出命名申請，在十二月十二日經國際天文聯合會(IAU)國際小行星命名委員會通過，正式命名爲「鄒族」（175586 = Tsou = 2006 TU106），成爲第一顆以台灣原住民族群命名的小行星。

中央大學天文所所長黃崇源說，「鄒族」與鹿林天文台的所在地、嘉義阿里山鄉關係匪淺，除了地緣關係外，天文台內七位成員中，有四位是鄒族青年，他們一年三百六十五天、二十四小時輪班守候，無論颱風來襲或除夕過年，在鹿林山上堅守著崗位。

黃崇源表示，鹿林天文台一直受到嘉義縣的幫助，期望能夠回饋地方，結合嘉義縣太陽館等地方資源，合作推廣天文與科學教育，邀請當地小學，香林國小、達邦國小、樂野國小學生造訪鹿林天文台設備，一窺浩瀚星空的奧秘，培育天文教育、天文研究的種子。

此外，繼以台灣地名「嘉義」命名的「嘉義小行星」後，與「鄒族小行星」同時發現發現的另外一個小行星也再度以台灣地名「南投」命名，將在一月十八日的世界天文年慶祝活動中一併公布。

原文轉載自【2009-01-15/自由電子報 即時新聞】

小行星命名　台灣「鄒族」飛越穹蒼

「台灣鄒族登上太空！」國立中央大學天文所鹿林天文台以台灣原住民「鄒族」爲名，爲中大發現的一七五五八六號小行星命名，昨天在嘉義縣阿里鄉公所舉行頒贈儀式，這是第一個以台灣原住民族名命名的小行星。

中央大學天文所所長黃崇源指出，「鄒族」與鹿林天文台的所在地、嘉義阿里山鄉關係匪淺，除地緣關係外，天文台內七位成員中，有四位是鄒族青年，他們一年三百六十五天、二十四小時輪班守候、堅守崗位。　（圖文：記者陳宣瑜）

原文轉載自【2009-01-16/自由時報/A10 版/生活新聞】

「鄒族」耀夜空　不只是傳說……

【張朝欣嘉義報導】

國立中央大學天文所鹿林天文台，將所發現的小行星命名爲「鄒族」，十五日在阿里山鄉公所舉行命名頒贈儀式，這是全世界首次以原住民做爲小行星名稱的創舉，「鄒族」從此在夜空中閃耀光芒。

鹿林天文台興建之初，全賴鄒族與布農族原住民披荊斬棘，一磚一瓦揹上山頭，四名天文台所屬鄒族工作人員，三百六十五天廿四小時輪班守候，無論颱風來襲或除夕過年，都在山之巔堅守崗位，爲感謝他們的付出與努力，將天文台發現的小行星命名爲「鄒族」。

昨天中央大學副校長葉永烜、天文所所長黃崇源等學者，前往阿里山鄉公所，舉辦命名頒贈儀式，由阿里山鄉長陳明利代表接受，阿里山地區達邦、樂野、來吉、十字、香林五所國小師生共同參與。

葉永烜說，命名爲「鄒族」小行星，還與鄒族一個美麗傳說有關，很久以前，六名鄒族勇士因耽擱時間而趕不及參與祭典，被拒絕進入大社，最後六人與一隻獵狗變成了天上的七顆星星，一同守候著北方，這個古老的傳說，也巧合的呼應著「鄒族」小行星。

葉永烜表示，經學者考證，東南亞原住民應是台灣原住民的移民，在沒有精密儀器的領航之下，能夠跨洋越海遷移，顯見台灣原住民有豐富的天文知識，才得以引領他們航向未知的大海。

天文所所長黃崇源指出，鹿林天文台一直受到嘉義縣民幫助，天文台除了研究工作外，也積極回饋地方，結合地方資源共同推廣天文與科學教育，經常邀請香林國小、達邦國小、樂野國小學生，一窺浩瀚星空奧秘，培育天文教育與研究種子。

原文轉載自【2009-01-16/中國時報/C3 版/社會新聞】

這顆星　叫它鄒族小行星

【記者湯雅雯嘉義縣報導】

「現在不只地上有鄒族、天上也有鄒族。」繼鹿林、中大、嘉義、鄭崇華小行星後，中央大學鹿林天文台發現編號一七五五八六小行星，正式命名爲「鄒族（Tsou）」，成爲首顆以台灣原住民爲名的小行星。

鹿林天文台已對十二顆小行星命名，其中七顆星名是中大取的，另五顆由共同發現者，中國籍的業餘天文學家葉泉志享有。

中央大學天文研究所所長黃崇源說，發現小行星無法立即命名，要再確定行星軌道後，才能提報國際天文聯合會（IAU）編號，而且是發現單位才有命名權。副校長葉永烜指出，嘉義鹿林是鄒族大本營，小行星以「鄒族」爲名，別具意義。

阿里山鄉鄉長陳明利是鄒族原住民，他昨天帶領香林、來吉、十字、樂野、達邦等五所鄒族原住民小學五十多名學童參加行星命名典禮。

陳明利說，當地學童要登上玉山、塔塔山才能畢業，未來將多要求學生考察星象才能畢業。香林國小四年級湯佳臻說，希望「鄒族小行星」能保佑她念書，考試考滿分。

【記者湯雅雯嘉義縣報導】鄒族人相信，北斗七星源於六名鄒族勇士因打獵耽擱而趕不及回家參與祭典，而被拒絕進入大社，抱憾而亡，最後與同行的獵狗變成天上的七顆星星，永遠守候著北方。

這則傳說，伴著四名與鹿林天文台一起打拚的鄒族青年。他們是汪榮進、石皓偉、林進全與石俊雄，十年前鹿林天文台還只是鐵皮屋，他們跟著中央大學教授們，登上海拔二千八百六十二公尺高山，再緩步走完六百公尺步道，將一磚一瓦背上山頭。

「仰望滿天星斗，看到守護族人的北斗七星，一切都值得了。」四名鄒族青年全年廿四小時輪班守護天文台，石俊雄說，雖然辛苦，想到背後的意義，一切都值得。

除了輪班守護鹿林天文台，四人從廚師、司機到技工，他們無所不能，熱情款待觀測人員，讓隻身進入高山寒境的學者，在海拔近三千公尺處，也感受到溫暖人情味。

天文台預計興建一座二米望遠鏡，想完工，還得靠這四名鄒族勇士。從設備到物資上山都靠索道吊掛，原料到位，再採傳統工法施作，中大教授說，有鄒族朋友的協助，鹿林天文台才得以完成。

●二〇〇六年十月十五日由中央大學天文所助理林啓生與大陸業餘天文學家葉泉志於鹿林天文台共同發現。爲感謝鄒族對鹿林天文台的貢獻，故命名「鄒族（Tsou）」。

「鄒族小行星」位於火星和木星的小行星帶，它最接近太陽的距離爲四點六億公里（近日點），離太陽最遠爲四點八億公里（遠日點），繞行太陽一圈（軌道周期）約五點六年，發現時位置在牡羊座附近，目前位於處女座。

原文轉載自【2009-01-16/聯合報/A6 版/生活】

全球天文年台灣啓動　18 日登場會迷友

【中央社記者郭美瑜台北 16 日電】

1609 年伽利略首次用望遠鏡觀測天文現象，今年剛好滿 400 年。台北市立天文館將於 18 日舉辦「2009 全球天文年台灣啓動儀式」，另借展 18 世紀至今的天文儀器以饗天文迷。

天文館將於 18 日下午 3 時 30 分舉辦 2009 全球天文年台灣啓動儀式暨「窺天」特展、多媒體展揭幕典禮，其間包括中央大學「南投小行星」命名儀式，中大鹿林天文台命名的「鄭

崇華小行星」，也將於現場同步展出，台達電子董事長鄭崇華也將親臨現場見證。此外，天文館也準備 1 萬份小型望遠鏡贈送遊客。

天文館長邱國光表示，「窺天」特展從奇美博物館借展 10 種以上的古董天文儀器，包括 18 世紀的太陽系儀鐘、最有造型的 19 世紀折射式腳架天文望遠鏡、造價百萬的 19 世紀晚期折射式天文望遠鏡等。

另外還有望遠鏡 DIY，讓民眾體驗望遠鏡發明之初的感動。

原文轉載自【2009-01-16/中央社】

鹿林天文台發現小行星　中央大學命名爲「鄒族」

【生活中心綜合報導】

中央大學在嘉義鹿林的天文台發現了新的小行星，由於鹿林地區是鄒族的活動區域，天文台的成立又是靠鄒族青年辛苦爬山送物資，因此這顆最新被發現的小行星，就被命名爲「鄒族」(Tsou)，來感謝鄒族人的付出，也是首顆以台灣原住民命名的行星。

小行星「鄒族」在 2006 年時被發現的位置，是介於金牛座與白羊座中間，並且編號爲 175586 號；現在它的位置則是在處女座下方，而且還被正式命名爲「鄒族」。

中央大學鹿林天文台因爲設在嘉義海拔 2862 公尺高山上，爲了感念鄒族人平常爬山運送物資，以及協助觀測的貢獻，因此當小行星被發現時，就讓它成爲首顆以台灣原住民當名字的小行星。

對此，文史工作者梁錦德表示，「鹿林天文台有四位鄒族的助理觀測員，從開始興建天文台的時候，他們就在那邊開始幫忙，到現在將近十年了，都是駐守在那裡。」據了解，四位鄒族助理觀測員分別是汪榮進、石皓偉、林進全與石俊雄。

正式命名當天，幾位鄒族的天文觀測員全都笑開懷，因爲有前人與他們默默的努力，現在不只地上有鄒族，就連天上也有鄒族了。(新聞來源：東森新聞記者吳瑞興)

原文轉載自【2009-01-17/NOWnews 重點新聞】

全球天文年　骨董儀器特展

【記者莊琇閔台北報導】

今年是「全球天文年」，台灣地區一整年的天文相關活動在昨天起跑，同時也舉行中央大學發現的「南投小行星」命名活動。

今年一整年的相關活動由台大孫維新教授號召，並獲得國科會及教育部的大力支持，藉此向一般大眾傳達科學發現的欣喜，及分享知識提升的喜悅。

台北市立天文館昨天起推出「小眼睛‧大宇宙－窺天特展」及「從地球到宇宙多媒體展」，爲台灣天文年活動揭開序幕。

「窺天特展」展出國內外望遠鏡，奇美博物館及國立科學工藝博物館還特別外借價值不斐的骨董天文儀器，再搭配台北圓山天文台時代的望遠鏡，懷舊展出。

同時也介紹台灣天文科學的研究成果，包含中研院天文所與中央大學鹿林天文台等單位，正在進行的尖端天文研究等，展期到 3 月 15 日止。

另外，中央大學天文所鹿林天文台在 96 年 2 月 6 日發現的 160493 號小行星，在去年 12 月 1 日經國際天文聯合會(ＩＡＵ)的國際小行星命名委員會通過，正式命名爲「南投小行星」，昨天也在天文館舉行命名活動。

未來一整年的天文活動，可上網查詢 2009 全球天文年台灣官方網站：http://www.astronomy2009.tw/，2009 全球天文年天文館活動網站：http://tamweb.tam.gov.tw/astro2009/，台北天文館網址：www.tam.gov.tw。

原文轉載自【2009-01-19/聯合報/C2 版/北市綜合新聞】

迎接全球天文年　台灣天文界總動員

【記者黃淑芬、盧歌綜合報導】

2009 年 1 月 18 日市政府首日發放消費券來振興經濟，同時也是 2009 全球天文年台灣地區啓動的大日子。當天，天文館館長邱國光爲了迎接 2009 全球天文年，幾乎讓台灣的天文界總動員！當天率先推出「小眼睛．大宇宙－窺天特展」及「從地球到宇宙多媒體展」，爲台灣天文年活動揭開序幕。「窺天特展」承蒙廣達文教基金會、新光人壽慈善基金會等單位協助，以伽利略觀天的角度出發，展出國內外望遠鏡，爲充實展品的豐富性，特別向奇美博物館及國立科學工藝博物館商借價值不斐的骨董天文儀器，再搭配臺北圓山天文台時代的望遠鏡做懷舊展出，同時亦介紹臺灣天文科學的研究成果，包含中研院天文所與中央大學鹿林天文台等單位正在進行的尖端天文研究等，內容豐富可期。展期維持至 3 月 15 日止，敬請民眾把握時間前往參觀。

早在 2007 年底，第 62 屆聯合國大會上正是決議將 2009 年定爲「全球天文年」，來紀念 1609 年伽利略首次用望遠鏡進行天文觀測 400 週年。由台大孫維新教授號召，臺灣各領域天文相關人士也開始著手規劃 2009 一整年的相關活動，並獲得行政院國家科學委員會及教育部的大力支持，讓臺灣不匯在這個重要的全球性活動上缺席，同時也向一般大眾傳達科學發現的欣喜及分享知識提升的喜悅。

於 1 月 15、16 日，全世界的天文學家齊聚法國巴黎位 2009 全球天文年揭幕後，1 月 18 日隨即於市立天文科學教育館宇宙劇場舉行臺灣地區的起跑活動，除了有多項展覽的揭幕活動及全球開幕活動的內容分享，同時並有中央大學「南投小

行星」的命名活動。

天文館館長邱國光表示，除了慶祝「2009 全球天文年」的活動正式開始，也爲了呼應政府發放消費券美意，凡於即日起，出示消費券即可免費參觀展示場（包含相關特展）及搭乘宇宙探險軌道車，前 500 名來賓再加碼贈送天文年限量紀念品紙製望遠鏡，以紀念天文望遠鏡發明 400 週年。

台達電鄭崇華董事長對於推廣「環保節能愛地球」一向不遺餘力，爲了追求環境永續、善盡綠色公民責任，於 2007 年國際天文聯合會（IAU）特地將編號 168126 小行星命名爲「Chengbruce（鄭崇華）」。於 1 月 18 日 2009 全球天文年，台達電子更特地出借 Chengbruce 小行星模型，讓社會大眾參觀「2009 全球天文年」相關展覽活動時，能一睹小行星的風采。相信您一定在網路或書本上看過宛如藝術品的天文圖片，讓人不禁讚嘆這番美景是真正存在於宇宙中，還是只是虛幻的影像？爲了 2009 全球天文年，全世界的天文學家精選出百餘張兼具科學意涵與藝術價值的天文圖片，集結於「從地球到宇宙」網站（ http://www.fromearthtotheuniverse.org ），讓更多人能領略宇宙之奇、之美。但小小的 17 吋電腦螢幕實在無法表現出宇宙的浩瀚，這些精選圖片如能透過大螢幕播出，更有絕佳的視覺震撼。台達電子文教基金會並特別提供麗訊科技 Vivitek 47 吋 Full HD 高畫質數位電子看板，於天文館展示場入口展示--「從地球到宇宙多媒體展」，將高畫質的天文圖片完美呈現，讓參觀者更能清楚得欣賞宇宙之美。

「2009 全球天文年」的主題爲「我的宇宙，我來探索！」，臺北市立天文科學教育館推出『小眼睛、大宇宙-窺天特展』，紀念伽利略，使用望遠鏡觀測天空 400 週年。期望引領您走進伽利略的異想天空，瞭解人們如何從原始生活中，透過經驗的累積及星辰運行的觀察，造就了科學知識的萌芽，發展出的時間、曆法及最初的宇宙觀；認識窺天工具-望遠鏡如何的誕生，天文科學的突飛猛進及望遠鏡科技的精進，有著什麼樣的密切關係；體驗 400 年前伽利略觀天的感動，明白人們的宇宙觀，如何從對天空神話的崇拜，到積極想揭開宇宙真面目的過程；鑑賞古今望遠鏡的精緻設計，探究現代化望遠鏡的觀測能力，透析望遠鏡對天文觀測扮演的角色；回顧及展望臺灣天文科學推廣及研究過程中，圓山天文台、鹿林山天文台及中研院天文台所扮演的角色及其研究成果；並透過模型、實物、多媒體影片及去位天文迷宮等。希望您能重新找回科學的基本價值，更期望大家大手牽小手一起仰望天際，體驗那宇宙萬物最原始的感動。

原文轉載自【2009-01-20/民眾日報/18 版/都會萬象】

南投小行星命名　李朝卿與會

【記者蔡榮宗投縣報導】

國立中央大學天文研究所人員，在位於南投縣的鹿林天文台發現一顆小行星，經國際天文台聯合會小行星命名委員會通過，正式命名爲「南投小行星」。南投縣長李朝卿 18 日特別北上，參加「2009 全球天文年台灣啓動儀式」，並接受中央大學副校長葉永烜致贈之「南投小行星」紀念銘牌。

原文轉載自【2009-01-20/台灣新生報/6 版/綜合新聞】

全球天文年　「南投星」揭開序幕

未來，「南投」不再只是縣市的名字，更成爲天上的星星！國立中央大學天文研究所人員，在位於南投縣的鹿林天文台發現 1 顆小行星，經國際天文台聯合會小行星命名委員會通過，正式命名爲「南投小行星」。南投縣長李朝卿特別北上，參加「2009 全球天文年臺灣啓動儀式」，並接受中央大學副校長葉永烜致贈之「南投小行星」紀念銘牌，完成命名儀式。

2009 年爲「全球天文年」，全球一百多個國家將用一整年的時間，來慶祝天文學對社會、文化、教育所帶來的貢獻。台灣部分由台大孫維新教授號召臺灣各領域天文相關人士，特別規劃未來一整年的相關活動，其中重頭就是中央大學「南投小行星」的命名活動。

位於南投縣的鹿林天文台於 96 年 2 月 6 日發現 160493 號的小行星，因地處南投，研究人員欣喜之餘命名爲「南投小行星」，並於翌年呈報國際天文聯合會小行星命名委員會通過。中央大學目前已陸續取得 30 多顆小行星命名權，「南投小行星」在命名序中第 6，是除嘉義之外，唯二以國內縣市命名的小行星。

李朝卿縣長對「南投小行星」能以縣名獲得命名深表榮耀，他指出，南投縣境內 3000 公尺以上的高山就有 41 座，是觀測天文的最佳縣份，縣府支持天文科學教育，合作國小也將繼續扮演「星光小學」的角色，深信一定能在南投縣的天空發現更多、最燦爛的星球。

原文轉載自【2009-01-20/全國廣播】

鹿林天文台發現小行星以「南投」命名

【張文祿報導】

「南投」不再只是縣市的名字，它也是宇宙中一顆小行星。位於南投縣的鹿林天文台，在 96 年 2 月 6 號發現一顆小行星，研究人員命名爲「南投小行星」，並在去年呈報國際天文聯合會小行星命名委員會審查通過。南投縣長李朝卿北上接受中央大學副校長葉永烜致贈「南投小行星」紀念銘牌，完成命名儀式。

國立中央大學天文研究所人員，在位於南投縣的鹿林天文台發現 1 顆小行星，經國際天文台聯合會小行星命名委員會

通過，正式命名爲「南投小行星」。

中央大學目前已陸續取得 30 多顆小行星命名權，目前只有兩顆小行星是以縣名命名，分別是嘉義跟南投。

由鹿林天文台發現並命名的 6 顆小行星，依序分別名爲鹿林、中大、嘉義、鄭崇華、溫世仁、南投。第 6 顆小行星之所以命名爲南投，是爲感謝南投縣政府長期對天文台的協助。鹿林天文台團隊，也將仁愛鄉合作國小列爲「星光小學」，未來不僅可打造學校特色，也讓當地學童學習豐富的天文知識。

李朝卿縣長對於「南投小行星」能以縣名獲得命名深表榮耀，他指出，南投縣境內 3000 公尺以上的高山就有 41 座，是觀測天文的最佳地點，縣府支持天文科學教育，合作國小也將繼續扮演「星光小學」的角色，相信一定能在南投縣的天空發現更多、最燦爛的星球。

鹿林天文台，海拔 2862 公尺，設置 2 米望遠鏡，是全台最大口徑的望遠鏡。在這裡，總計發現 700 多顆小行星、1 顆近地小行星、1 顆彗星。

原文轉載自【2009-01-19/中廣新聞網】

南投鹿林天文台發現小行星　命名「南投」

【劉文珍報導】

「南投」不再只是縣市的名字，更成爲天上的星星！國立中央大學天文研究所人員，在位於南投縣的鹿林天文台發現 1 顆小行星，經國際天文台聯合會小行星命名委員會通過，正式命名爲「南投小行星」。

位於南投縣的鹿林天文台於 96 年 2 月 6 日發現 160493 號的小行星，因地處南投，研究人員欣喜之餘命名爲「南投小行星」，是除嘉義之外，唯二以國內縣市命名的小行星。中央大學天文所長黃崇源即表示，中央大學在 95 年 3 月起啓動「鹿林巡天計畫」，於位於海拔 2862 公尺的鹿林天文台設置 2 米望遠鏡，爲全台最大口徑的望遠鏡，天文台天文團隊也將天文科學教育深入南投縣偏遠地區學校，將仁愛鄉合作國小列爲「星光小學」，未來不僅可打造學校特色，也讓當地學童學習豐富的天文知識，並建立天文科學教育平台，讓天文教學成爲南投縣教育的一大特色。

原文轉載自【2009-01-20/國立教育廣播電台－【文教新聞】】

綠色彗星 2 月 24 來訪太陽系

【大公報訊】

據英國《每日郵報》網絡版九日報道：一顆像外星人飛船般發出綠光的奇特彗星將於兩星期後逼近地球，專家估計它只能在某些漆黑一片的郊區中用肉眼觀看，不過亦不排除它可以更容易看見。美國一名業餘天文學家日前用望遠鏡爲這顆彗星拍了一張照片，令人對它興趣大增。

這顆彗星名叫「鹿林」（見圖），因爲它是在二〇〇七年七月被當時年僅十九歲的廣州中山大學學生葉泉志於台灣中央大學的鹿林天文台發現。它綠色的外觀來自一種在木星大氣層發現的氣體氰氣。彗核噴出的氰氣（許多彗星都有的毒氣）和雙原子碳，在太空中被陽光照射時都會發出綠光。

據了解，「鹿林」快將首次進入內太陽系。美國太空總署的發言人稱，它將於本月二十四日（周二）最接近地球，並進入距地球六千一百一十萬公里（火星最接近地球時的距離爲五千五百七十萬公里）的軌跡。他又說，由於距離甚遠，天文愛好者大概要在漆黑一片的郊區看才可用肉眼觀看「鹿林」，不過由於這是「鹿林」第一次進入太陽系，所以它說不定會爲大家帶來更大的驚喜。專家估計它將會在日出前數小時出現於地球上空。

本月一日，美國亞利桑那州業餘天文學家傑克・牛頓在自家後園的天文台用一台十四吋望遠鏡清晰地拍攝到「鹿林」的奇觀。他說它十分刺眼，它不能以肉眼觀看，只能透過拍照間接觀看。「鹿林」的發現者葉泉志說，有了照片後，我們可以隨時用肉眼觀賞它那「綠色美感」了。

原文轉載自【2009-02-11/中央社】

【探索天文】走進伽利略的異想天空　探尋真宇宙

【台北市立天文科學教育館解說員林琦峰】

伽利略・伽利萊（Galileo Galilei），義大利人，400 年前他使用自製望遠鏡指向天空，看見了從來沒有人見過的月面坑洞及山脈（圖{1}，古今月面圖，林琦峰提供）；發現銀河不是霧氣，而是許多星星構成的地方；看見了木星的四顆大衛星，現在更稱爲「伽利略衛星」；發現了土星旁邊總是跟著兩顆星星，現在我們知道那是「土星環」。並從觀測木星的衛星系統，與金星像月球一樣有盈虧變化等現象，加強了他支持哥白尼的「日心說」，也稱爲「地動說」的信念（圖{2}，19 世紀太陽系儀鐘，奇美博物館提供）——地球被視爲一具有衛星的行星，宇宙有超過一個以上的運動中心。伽利略開啓了天文學家，利用望遠鏡觀測天文的風氣，讓人們對宇宙觀有了更清楚的認知。望遠鏡的誕生，更增進了人們視野，拉近與宇宙的距離。

爲了表揚伽利略，並鼓勵全球合作及發揚探索精神，義大利首先提出了「2009 全球天文年」的活動概念，並由國際天文學聯合會（IAU）及聯合國教科文組織（UNESCO）所共同提案，在 2007 年底聯合國第 62 屆會員大會通過了 2009 全球天文年這項議題。

台灣天文年活動已經在 2009 年 1 月 18 日，於台北市立天

文科學教育館熱鬧開幕。同時天文館推出「小眼睛，大宇宙——窺天特展」，這次的展覽分成「伽利略的異想天空」、「古今望遠鏡」、「臺灣之光」、「窺天特區」、「科學劇場」及「天文迷宮」共六區。藉此帶領大眾走進伽利略的異想天空，了解人們如何從原始生活中，透過經驗的累積及星辰運行的觀察，造就了科學知識的萌芽，發展出生活中時間、曆法及航海對天文的依賴，同時發展出神話般的宇宙觀，這是人類與天文的第一類接觸。

而窺天工具——望遠鏡的誕生更影響天文科學的突飛猛進。為豐富特展展品，特別向奇美博物館借展 19 世紀時期的古董望遠鏡及天文儀器（圖{3}，全台最古老的望遠鏡，奇美博物館提供），現場並將展出台灣早期圓山天文台時期使用的望遠鏡及高雄科學工藝博物館典藏的子午儀。本特展著重在台灣地區重要的光學天文觀測發展，包含早期扮演天文科學推廣的圓山天文台，負責教學及研究用的中央大學鹿林天文台，及參與國際天文觀測研究的中研院天文所等三個重要機構。

另一方面，特展也邀請到中央大學天文所及中研院天文所協助，提供近年來的研究成果及未來展望。並展出圓山天文台時期的重力式赤道儀及鹿林天文台 76 公分望遠鏡主鏡，讓現場參與民眾可以體驗早期觀測天文時導星的方式，從中一窺難得一見的天文望遠鏡主鏡面貌。

而特展也將透過多媒體及巨型影像投影，在特展現場播放世界各地天文台的實際影像輪流播放，了解天文學家是如何使用大型望遠鏡來進行觀測。　值得一提的是，特展現場還有針對小朋友設計「天文迷宮」透過寓教於樂方式與迷宮特性，讓小朋友可以心領神會用肉眼和用望遠鏡所看到的宇宙，有何不一樣。

原文轉載自【2009-02-13/人間福報/13 版/遇見科學】

臺灣之光鹿林彗星　24 日最閃亮

【楊惠芳臺北報導】

今年是世界天文年，由國人發現和命名的鹿林彗星，今年是最亮的一年。發現這顆彗星的中央大學天文研究所觀測員林啓生表示，鹿林彗星在二十四日將是最接近地球的時候，如果錯過這次，可能要再等兩千一百萬年。

中央大學天文所所長陳文屏表示，今年是世界天文年，國際天文界相當注意鹿林彗星的動態，鹿林天文臺已經將拍到的影像資料傳給國際彗星組織。鹿林彗星預定二十四日出現在獅子座附近，當天沒有月亮的光害，幾乎用肉眼就可以看到。

中央大學教授葉永烜表示，鹿林彗星的彗核為十公里，相當於臺北市大小。但彗星接近太陽後，受熱蒸發出的氣體和塵埃所組成的彗髮，包覆在彗核外，卻可以達到百萬公里，比地球還大；形成的藍色離子尾和扇形的塵埃尾，也相當壯觀。

臺北市立天文館等單位自即日起推出活動，歡迎民眾參加。

原文轉載自【2009-02-18/國語日報/2 版/文教新聞】

一輩子就看這次　鹿林彗星 24 日最接近地球

【本報綜合報導】

一輩子就這麼一次。全世界矚目、由台灣人發現的鹿林彗星，是 2009 年上半年最耀眼的彗星，24 日將最靠近地球，民眾當天晚上往南方獅子座與土星附近，用肉眼就能看見。

中央大學昨天就召開記者會說明鹿林彗星初訪太陽系的現況，他們在新聞稿中指出，台灣人首度以本地儀器觀測發現並命名的「C/2007 N3（Lulin）鹿林彗星」初訪太陽系，綠色的光芒顯示這顆彗星很新鮮。

中央大學天文所教授陳文屏表示，根據推算，鹿林彗星軌道特性顯示它是來自太陽系外圍歐特雲區的彗星。鹿林彗星軌道可能為雙曲線或拋物線，表示這是它第一次、也是最後一次進入太陽系，也可能是週期性，這週期長達 2800 萬年，不管如何，現代人這輩子只有一次機會親眼目睹。民眾只要當天晚上 10 點以後，面對南方，找到獅子座與土星，鹿林彗星就在附近，雖然亮度不如土星，但肉眼還是看得見。

原文轉載自【2009-02-18/民眾日報/1 版/頭版】

一生一次觀賞鹿林彗星機會　24 日最佳

【韓啓賢報導】

國人第一次以本地儀器觀測發現並冠名的「鹿林(Lulin)彗星」，初訪太陽系，將在下週二(24 日)運行到最接近地球的地方。中央大學天文研究所教授陳文屏表示，由於鹿林彗星是長週期或非週期的彗星，這輩子只有一次機會，親眼目睹它的容顏。

中央大學指出，根據預測資料，鹿林彗星軌道特性顯示它是來自太陽系外圍，歐特雲區的極長週期彗星，繞太陽公轉一圈長達 2850 萬年。鹿林彗星在今年 1 月通過近日點後，將於 2 月 24 日運行到最接近地球的地方；屆時的預測亮度達 6 等左右，位在獅子座附近，幾乎肉眼可見，是今年上半年最耀眼的彗星。

根據計算，鹿林彗星軌道可能為雙曲線或拋物線，或是週期長達 2000 多萬年的狹長橢圓；也就是說，這是它第一次、也可能是最後一次進入太陽系。中央大學天文所教授陳文屏說：『多半不會來了，如果它會來，它是一個很狹長橢圓，也是幾千萬年以後的事情；所以，一般目前認為它是雙曲線

或者是拋物線，意思就是說，它來這麼一次就沒有了，所以我們運氣很好，我們能夠看到它，是非常有緣分的。』

陳文屏還說，鹿林彗星在 24 日最接近地球時，距離約 0.41 天文單位，也就是 6100 萬公里，亮度有可能達 4、5 等，整晚可見；沒有月亮光的干擾，觀測條件良好，凌晨與土星相近僅約 3 度，非常適合觀測。天文迷可以挑選沒有光害的地方，準備一個觀賞球賽或者看表演的小望遠鏡觀賞彗星。

原文轉載自【2009-02-17/中央廣播電台_新聞】

鹿林彗星訪台　24 日肉眼可見

【記者嚴文廷台北報導】

國人首度以本地儀器發現命名的「鹿林彗星」即將訪問太陽系，預計 24 日最接近地球，屆時，以肉眼就能在獅子座附近觀測到綠色霧光，錯過這次，要等 2 千 8 百萬年才能再見面。

2007 年由國人利用望遠鏡發現鹿林彗星的蹤影，本月底是千載難逢的最佳觀測機會。鹿林彗星發現者、中央大學鹿林天文台觀測員林啓生表示，24 日晚上，在光害少的地方，抬頭望著獅子座，就能看到一個綠色光點，周圍散發霧狀光線，這就是「鹿林彗星」，該彗星含有大量氨與氫氣體，現身時會呈現鮮綠色。

尋找獅子座有點難度，林啓生建議民眾，如果有朋友能找到確定座標，再帶著雙筒望眼鏡，就能一窺真面目。如果想觀測彗星尾巴，林啓生建議到山區觀測，仔細看就會發現一團綠色棉花後面出現一條光尾，就是彗星尾巴。

錯過要等 2 千 8 百萬年

中央大學天文所教授陳文屏指出，鹿林彗星從 2 月開始，軌道相當接近於黃道面，就是地球繞太陽公轉的軌道，24 日當天和地球僅相差 6 千萬公里，可能 2 千 8 百萬年才來地球一次，比起知名的「哈雷彗星」，繞行太陽系的週期約 76 年還要久。

陳文屏建議，24 日晚上 9 點後就可觀察，直到凌晨 4 點，都可以憑肉眼看到鹿林彗星。他強調，當天沒有月亮光干擾，非常適合觀測，只要到空曠的海邊，或是高樓都可看到難得一見的鹿林彗星。

「鹿林彗星」的「彗核」只有 10 公里，相當於台北市大小，接近太陽後受熱昇華，蒸發出的氣體與塵埃組成的彗髮，包覆在彗核之外，卻可以達到百萬公里比地球還大，形成的藍色離子尾和扇形的塵埃尾相當壯觀。

中央大學教授、國際知名天文學者葉永烜表示，探索彗星的結構、化學物質、大小分布及軌道分布情形，可了解地球乃至於太陽系的過去，更可探索未來，鹿林彗星提供絕佳的觀測機會，堪稱是台灣今年天文界的一大盛事。

原文轉載自【2009-02-17/立報新聞】

鹿林彗星接近地球　2 月 24 日最適合觀測

【康紀漢報導】

今年是世界天文年，由國人發現及命名的鹿林彗星，將於 2 月 24 號最接近地球，屆時在獅子座附近，幾乎達到用肉眼就可以看到的亮度，民眾可千萬不要錯過這一輩子只能親眼看到它一次的難得機會。

鹿林彗星來自於太陽系外圍的歐特雲區，軌道相當接近黃道面，今年 1 月 10 號通過近日點最接近太陽後，將在 2 月 24 號運行到最接近地球的地方，到時候因爲月相逢朔，沒有月亮光的干擾，非常適合觀測 。

中央大學天文所教授陳文屏表示，鹿林彗星的彗核只有 10 公里，相當於台北市大小，可是接近太陽後受熱昇華，蒸發昇華出的氣體與塵埃組成的彗髮，包覆在彗核之外，卻可以達到百萬公里比地球還大，並且所形成的藍色離子尾和扇形的塵埃尾相當壯觀，由於它是長週期或沒有固定週期的彗星，又含有大量氣體，顏色特別鮮綠，這可能是它第一次，也是最後一次進入太陽系。

陳文屏教授進一步指出，爲了搜索對地球可能造成撞擊威脅的彗星和小行星，中央大學也參與泛星巡天計畫，並在將來投入露西達登陸彗核計畫，藉以對彗星的結構與形成更瞭解。

原文轉載自【2009-02-17/國立教育廣播電台－【文教新聞】】

24 日深夜向南　可觀測鹿林彗星

二千八百萬年可能才來一次的鹿林彗星，二月二十四日將運行至最接近地球的地方，台灣民眾當天晚上十點後，面向南方，只要在天空找到獅子座和土星，肉眼就可以觀測到鹿林彗星。中央大學天文研究所教授陳文屏形容，「這顆幾乎是從『永恆』而來的彗星」，當今人類有幸親眼目睹它的容顏，而且因爲角度好，可看到明顯彗尾，畫面華麗。

形容鹿林彗星爲「台灣之光」再合適不過，因它是首顆由本土觀測並命名的彗星。

陳文屏指出，鹿林彗星是來自太陽系外圍歐特雲區的彗星，二月二十四日最近地球，「鹿林彗星的光線散開，肉眼看起來會像棉花球般鬆鬆的」，當天不但距離地球最近、接近土星，恰好正值新月，光線暗、仰角高，天時地利十分合適觀星。（圖：中央大學天文所提供文：記者林嘉琪）

原文轉載自【2009-02-18/自由時報/A11 版/生活新聞】

鹿林彗星　下周二最接近地球

【記者林進修/台北報導】

「錯過這一次，再等 2100 萬年！」國人首度以本地儀器觀測發現並命名的鹿林彗星，24 日最接近地球。發現這顆彗星的中央大學天文研究所觀測員林啓生建議把握難得機會，近距離把鹿林彗星看個夠，因爲錯過這次，今生再無機會。

鹿林彗星是前年 7 月 11 日由林啓生及大陸廣州中山大學葉泉志，使用鹿林天文台 41 公分望遠鏡進行鹿林巡天計畫時共同發現。鹿林彗星也是海峽兩岸合作發現的首顆彗星，意義非凡。

中央大學天文研究所教授陳文屏表示，鹿林彗星去年逐漸受到全球天文界的注意。根據計算，這顆彗星的運行軌道可能是雙曲線、拋物線或狹長橢圓，因其離心率趨近於零，預計運行周期長達 2100 萬年。

林啓生表示，全球知名的「哈雷」彗星，繞行太陽系的運行週期約 76 年，大多數人一生只有觀賞一次的機會；鹿林彗星下一次再度繞近地球時，人類恐已滅絕，地球也可能不復存在。 林啓生昨晚守在海拔 2800 公尺的鹿林天文台，透過高倍望遠鏡記錄這顆讓他揚名的彗星，並把拍下來的影像資料，立即傳到國際彗星組織，供其他研究者參考。

陳文屏表示，鹿林彗星 16 日離室女座主星角宿一約 3 度。到了 2 月 24 日，鹿林彗星最接近地球，距離約 0.41 個天文單位，也就是 6100 萬公里，亮度可能達 4、5 等，整晚可見。即日起的兩個星期均可觀賞鹿林彗星，24 日前後恰逢朔月，月亮的亮度最低，光害最小，應是最好的觀賞時機。

中央大學教授、國際知名天文學者葉永烜表示，探索彗星的結構、化學物質、大小分布及軌道分布情形，可了解地球乃至於太陽系的過去，更可探索未來，鹿林彗星提供我們絕佳的觀測機會，不容錯過。

原文轉載自【2009-02-17/聯合晚報/A8 版/焦點】

鹿林彗星 24 日到　今生只一次

【楊桂華／台北報導】

首顆由台灣望遠鏡於二〇〇七年發現、並獲國際命名權的鹿林彗星，下周二將最接近地球，幸運的話，只要位在高處憑肉眼就可看到。鹿林彗星含有大量氫氣，呈耀眼鮮綠色，因運行軌道周期長達兩千八百萬年，發現此彗星的中央大學鹿林天文台成員和教授，昨鼓勵民眾把握一生僅此一次的機會欣賞。

在獅子座附近出現

中央大學天文研究所教授陳文屏說，下周二（二十四日）鹿林彗星和地球將僅相距六千萬公里，是有史以來最接近的一次，當天鹿林彗星會在獅子座附近出現，是今年上半年最耀眼的彗星。由於鹿林彗星逐漸接近太陽，彗星的兩個氣團相撞，彗星尾巴部分產生明顯的離子尾與塵埃尾，都非常值得觀察。

周三凌晨升到天頂

鹿林天文台觀測員林啓生建議，下周二晚上九時後，可先搭配星座盤找到獅子座，再從獅子座中找到黃色土星，位於土星南側、略帶朦朦彗髮的鮮綠色星體，便是鹿林彗星。他提醒若要在平地觀測，用肉眼看到的機會可能不大，最好還是使用望遠鏡。

陳文屏預估，下周三（二十五日）約凌晨四時，鹿林彗星將爬升到天頂，幸運的話，屆時只要到空曠海邊或高樓處，就可憑肉眼欣賞。根據計算，鹿林彗星軌道可能呈現雙曲線、拋物線，或周期長達兩千八百萬年的狹長橢圓，若錯過此次觀測，今生將再無機會得見。

◎鹿林彗星小檔案

資料來源：中央大學

原文轉載自【2009-02-18/蘋果日報/A6 版/要聞】

鹿林彗星觀測指南

新浪科技訊 北京時間 2 月 18 日消息，據美國宇航局網站報道， 一顆名爲鹿林彗星的綠色彗星正在接近地球，2 月 24 日，這顆彗星與地球之間的距離達到最小值。據估計，它的亮度將達 4~5 等，這意味著，在鄉村黑暗的天空中將能看到這顆彗星靚麗的身影。

2 月 6 日：鹿林彗星將從氐宿一(Zubenelgenubi)旁邊滑過，氐宿一是天秤座里的一顆雙星。氐宿一不僅是一個津津樂道的有趣話題，而且它還是一個唾手可及的向導。你可以利用肉眼看到氐宿一，它大約跟大熊星座里的北斗七星一樣明亮；利用雙孔望遠鏡，可以非常清楚地看到鹿林彗星。

2 月 16 日：這一天，鹿林彗星將飛越室女座里的角宿一。角宿一是一顆最亮的恆星，同時也是一個路標，即使城市里的天文學家，也能看到它。尋星鏡指向角宿一，不需移動望遠鏡，就可以通過這個光學器械觀測到鹿林彗星。

2 月 24 日：這個特殊一天的早晨，鹿林彗星將以最近距離飛越地球。屆時，鹿林彗星將與土星齊聚獅子座。人們利用裸眼很容易看到土星，鹿林彗星也很容易看到。如果這還不足以把你從溫暖的床上拉起來，就沒有什麼能吸引你早早起床了。

原文轉載自【2009-02-18/北美新浪財經】

新快報：今年最亮彗星肉眼或都可見

【新快報訊記者邢冉冉 實習生劉潔 通訊員李建基】

今年最明亮的彗星——『鹿林』正在飛臨地球！來自廣東省天氣學會的觀測資料顯示，『鹿林』將在 2 月 23 日最亮，並且有可能被肉眼目睹。

天文專家稱，如果天色晴朗，本月 28 日之前，在零時至天亮前觀測最佳；3 月 1 日以後，在天黑後至 24 時(上半夜)觀測最佳。這顆『鹿林』彗星是海峽兩岸天文科技共同合作的傑出成果。2007 年 7 月 11 日，『鹿林』彗星被臺灣鹿林天文台天文攝影師林啓生拍攝、並由廣州中山大學本科生、廣東天文學會會員葉泉志通過圖片中發現的。隨後，被國際天文聯合會命名爲 C/2007N3(Lulin)彗星。『鹿林』彗星于今年 1 月 10 日過近日點，2 月 24 日距離地球最近，大約只有 6100 萬公里。

原文轉載自【2009-02-19/北京新浪網】

鹿林彗星逼近　中央大學週六辦天文講座

【記者成漢桃園報導】

由國人所發現的首顆彗星－鹿林彗星，下週二將最接近地球，爲迎接 2009 上半年最耀眼之彗星，中央大學天文所特地發起一系列科普演講，本週六(21 日)在中大科學四館，分別由葉永烜教授和林建賢先生主講「彗星天文觀測與太空探測」、「太陽系的遊俠－彗星」，兩場科普講座完全免費入場，喜愛天文的民眾不要錯過！

鹿林彗星（C/2007 N3 (LULIN)），兩年前由中央大學鹿林天文台所發現，初訪太陽系，已經長出尾巴，發出鮮綠色的光芒，繞太陽公轉一圈長達 2850 萬年，屬於長週期彗星，錯過這一次觀測，這輩子就看不到了。

原文轉載自【2009-02-19/青年日報/13 版/桃竹苗地方通訊】

鹿林彗星　綠光奇景

【文／楊桂華 • 圖／張君宏提供】

首顆由台灣發現、命名，每 2800 萬年才造訪地球一次的鹿林彗星，下周二（24 日）晚上 9 時到隔天清晨 4 時，將是最接近地球時。前晚已有讀者在合歡山上搶拍到鹿林彗星發出綠光的天文奇景（圖）。中央大學表示，鹿林彗星因含有大量的氫氣，現身時會呈現鮮綠色，下周二晚上若天氣好，民眾有機會憑肉眼就可在空曠的海邊、高樓或高山上欣賞鹿林彗星。

鹿林天文台觀測員林啓生建議，觀星時要搭配星座盤來找尋，從星座盤先找出獅子座中的土星，而在土星南側略帶朦朧彗髮的鮮綠色星體，便是鹿林彗星。

◎鹿林彗星觀看資訊

時間：即日起至 2 月底皆可觀察，但以 2/24 晚上 9 時至隔天清晨 4 時爲鹿林彗星最接近地球時候，觀測效果最好

地點：全台空曠無光害的海邊、高樓、高山

方式：用雙筒鏡或高倍數望遠鏡觀測，搭配星座盤先找到獅子座，再從獅子座中找到黃色土星，自土星南處找尋有朦朧彗髮的鮮綠色星體即是

資料來源：中央大學

原文轉載自【2009-02-19/蘋果日報/A6 版/要聞】

下周二看彗星　錯過要等 2800 萬年

【記者吳政諺、江昭青報導】

鹿林彗星 24 日最接近地球，要怎麼看？中央大學天文所教授陳文屏表示，當晚 10 點後到天亮前都可見，且若當天沒有月光干擾，用肉眼就可以觀測，而且可觀測期直到三月中！

陳文屏解釋，星的亮度通常會分等級，等級越小亮度越強，而最暗到肉眼可見的亮度爲六等，所以，鹿林彗星比起其他肉眼可見的星星亮度還高。不過，也要看當時環境而論，他建議，用一般望遠鏡就可以看到。

去年七月 11 日，鹿林天文台進行「巡天計畫」時，天文所專任助理林啓生與大陸廣州中山大學的合作伙伴葉泉志，使用鹿林天文台直徑 41 公分望遠鏡，發現一顆軌道疑似彗星的新天體，經美國天文學家 James Young 以桌山天文台（Table Mountain Observatory）直徑 61 公分望遠鏡觀測證實的確是一顆彗星，因而正式命名爲「鹿林」，編號 C/2007 N3。

鹿林天文台台長林宏欽指出，彗星發現機率極低，平均發現 1000 個小行星，才有 1 個彗星，本次台灣發現鹿林彗星，十分難能可貴。鹿林彗星是第一顆被台灣發現、命名的彗星。也是海峽兩岸合作發現的第一顆彗星。林宏欽說，這證明我們有能力可以發現彗星這類特殊的天體。

鹿林彗星第一次造訪太陽系，陳文屏說，鹿林彗星其中含有大量的氰等有毒氣體，所以會發出鮮綠色光芒，但有毒氣體並不會影響地球，可是若錯過這一次，下次要再看到它，至少要等兩千八百萬年。

第一顆小行星是 1801 年由義大利天文學家皮亞齊發現的，後來命名爲穀神星。小行星是目前各類天體中唯一可以由發現者進行命名並得到世界公認的天體。

台灣自從鹿林天文台建立後，有系統的展開小行星巡天計畫，第一顆發現並獲得命名的小行星，就稱爲鹿林小行星。林肯近地小行星研究中心已發現上萬顆小行星，且規定只要是美國英特爾科學獎得主，都可以得到一顆以得獎者名字命

名的小行星；台灣已經有許多年輕學生獲得這份榮耀。

原文轉載自【2009-02-18/台灣醒報】

觀看鹿林彗星　一輩子就這次!

【民視新聞崔立潔綜合報導】

台灣中央大學鹿林天文台，在 2007 年發現的鹿林彗星，24 日將會最靠近地球，屆時大家在郊外沒有光害的地方，甚至可以直接用肉眼看到這顆閃耀青綠色光芒的彗星，如果錯過這一次，下次想要看到鹿林彗星，將會是 2800 萬年後。

日本岩手縣，黑夜中群星閃耀，仔細看，這當中有一顆顏色呈現青綠色的彗星，這就是 2007 年由台灣的中央大學鹿林天文台所發現的鹿林彗星，從 1 月開始，鹿林彗星就逐漸接近地球。

由日本群馬縣立天文台，在 18 日拍攝到的鹿林彗星，影像更加清晰，不過卻看不見彗尾，這是因爲從地球的方向望去，彗尾剛好在反方向，鹿林彗星會呈現這樣特殊的青綠色，代表它是顆非常年輕的彗星，內含大量的氰等有毒氣體。

2 月 24 日它將最靠近地球，亮度可能達到 4、5 等，也就是說，只要到郊外等沒有光害的地方，用肉眼，都有可能看見鹿林彗星。

會說一輩子只能看到一次，是因爲鹿林彗星是極長週期彗星，繞太陽公轉一圈，下次再接近地球，恐怕是 2800 萬年以後的事了。

24 日晚間 10 點過後，鹿林彗星會從獅子座附近的地平線升起，當晚土星會很亮，鹿林彗星就會在土星附近，記住這些觀星要點，天文迷可千萬別錯過了。

原文轉載自【2009-02-19/民視新聞網】

2009 全球天文年系列活動起跑

【劉文珍報導】

爲了提供民眾對彗星科學知識的瞭解，並見證國人在天文觀測上的傑出成果，國立自然科學博物館 21、24、28 日分別在清境農場遊客中心及台中都會公園星象廣場舉辦《尋找夜空中的台灣之光－鹿林彗星》觀測活動，利用 35 公分口徑望遠鏡及天文望遠鏡，和民眾，一起尋找夜空中的台灣之光－鹿林彗星。

2007 年 7 月 11 日，國立中央大學的林啓生及廣州中山大學的葉泉志兩位先生，利用鹿林天文台的 41 公分望遠鏡，在寶瓶座附近發現疑似彗星的天體。後來經由美國天文學家詹姆士・楊確認爲彗星，並正式命名爲「鹿林彗星」（Comet Lulin），編號爲 C/2007 N3，成爲台灣研究團隊所發現的第一顆彗星。

科博館助理研究員黃釗俊表示，俗稱「掃把星」的彗星是太陽系中環繞太陽公轉的冰雪球，當逐漸靠近太陽時，會受到太陽光與熱的影響，使表面物質蒸發形成彗髮與彗尾；愈靠近太陽，彗髮愈寬，彗尾愈長。「鹿林彗星」於 2009 年 1 月 10 日通過軌道近日點，亮度約 6 至 7 等，且在 2 月下旬最接近地球時亮度可達 5 至 6 等左右、甚至更亮。這段期間內，利用雙筒或小型望遠鏡就可以觀賞到這個在宇宙間高速奔馳的另類「臺灣之光」。由於它預期將是 2009 年天空中最亮的彗星，因此頗受國際注目。

爲了響應 2009 全球天文年，並且帶領觀眾一起探索鹿林彗星的奧秘，國立自然科學博物館除了規劃辦理三場鹿林彗星觀測活動之外，也將在 2 月 21 日下午 2：10 邀請中央大學天文所陳文屏教授於科學中心演講廳發表演講，介紹鹿林彗星的發現過程。此外，中央大學天文所目前也正在台中都會公園展出多幅彗星海報，歡迎民眾踴躍前往參加。

原文轉載自【2009-02-19/國立教育廣播電台－【文教新聞】】

北市天文科教館開放民眾觀測鹿林彗星

【台北訊】

天文界的台灣之光——鹿林彗星，今天來到距離地球最近距離，星等將暴增至約 5 等左右，北市天文科學教育館今晚 7 點半到 9 點半開放觀測，歡迎民眾前來一睹風采。

由中央大學鹿林天文臺觀測員與中國大陸廣州中山大學學生合力發現的鹿林彗星，是台灣發現的第一顆彗星，天文館除派員到高山觀測外，將在今晚最接近地球時，利用天文望遠鏡觀測，天文館開放 4 樓第 2 觀測室供民眾觀測，週六晚上也將在 7 點到 9 點開放。

民眾如果想自行觀賞，可利用雙筒望遠鏡觀測，在太陽下山、晚上 6 點 40 分後，朝獅子座方向尋找，目前星等約 0.5 等的土星，正位於獅子座的尾部，只要看到這顆明亮的行星，在上方不遠處可看到一團霧狀星體，就是鹿林彗星。欲知相關天文訊息可上臺北市立天文科學教育館網站查詢 http://www.tam.gov.tw。

嘉義市天文協會也特別和中央大學天文所鹿林山天文台合作，即日起至 27 日，將配合鹿林彗星升起的時間，透過網路直播鹿林彗星即時影像，28 日將全天候重播鹿林彗星發現人之一林啓生解說，讓民眾對彗星組成的成分、構造，以及對於地球的影響，有進一步的認識。

「鹿林彗星網路直播節目」播出時間爲今晚 8 到 9 點；25、26 及 27 日晚上 7 點半到 8 點半，播出網址諸羅城的星空天文頻道 Http://webcast.ltes.cy.edu.tw/Ch-astro。

原文轉載自【2009-02-23/立報新聞】

鹿林彗星飛臨地球　2850 萬年一遇

2 月 24 號，2009 年上半年已知最亮的彗星「 鹿林」飛到離地球最近的地方，成爲一顆肉眼可見的彗星。

天文資料稱，「鹿林」彗星來自非常遙遠的奧爾特雲，歷經上千萬年向太陽的漫長「朝聖」旅途，於今年 1 月 10 日到達離太陽最近的地方，2 月 24 日距離地球最近，大約 6000 萬公里。23 日天文學家在美國北卡羅來納州使用 300 毫米長焦鏡頭拍攝到的「鹿林」彗 星照片。

鹿林彗星的被發現純屬巧合。2007 年 7 月，一名台灣天文愛好者將拍攝的一批「夜空圖」發送給廣東天文愛好者，研究過程中意外發現了一個傳統星圖外的天體，經最終確認，這是顆從未被 觀測過的新彗星。由於彗星的首次發現是在中國台灣鹿林天文台拍攝的照片上，因此這顆編號爲 C/2007N3 的彗星擁有了一個永久的中文名字——鹿林彗星。據說該彗星再次飛臨地球，要等 2850 萬年 。

原文轉載自【2009-02-24/希望之聲電台/新聞頻道>天下縱橫】

中央大學周五晚　看鹿林彗星活動

鹿林彗星接近地球，中央大學 27 號晚間七點三十分起，在校內大草坪舉辦觀星活動，現場將介紹鹿林天文台、當季的星空導覽，同時遠端遙控鹿林天文台 SLT 望遠鏡觀測鹿林彗星。

中央大學指出，中央大學鹿林天文台所發現的鹿林彗星，在今年 1 月 10 號通過近日點，這個月 24 號通過近地點，距離只有 6,000 萬公里，在沒有光害的晴朗夜空下觀測，用肉眼即可在獅子座與土星附近看到她的芳蹤，看起來像是一團可愛的綠色小棉花球。

中央大學表示，鹿林天文台這幾天所拍攝到的鹿林彗星影像，好像一支疾速升空中的火箭，尖尖的逆向彗尾朝向左上方，是伸展在彗星軌道上的塵埃尾。在彗核右下方是朝太陽反方向的離子尾，鹿林彗星的離子尾可能在受到太陽風磁場的影響，而呈現複雜的分叉開花現象。

原文轉載自【2009-02-26/中廣新聞網】

鹿林彗星造訪太陽系　錯過這次再等千萬年

【記者羅智華專題報導】

2/24 日晚上，一群又一群的天文迷呼朋引伴上山追星，準備一睹千載難逢的穹蒼之美，他們所爭相觀看的天文景象並不是我們所熟悉的流星雨，而是兩千多萬年才會造訪太陽系一次的新嬌客——「鹿林彗星」。適逢 2009 年是全球天文年，鹿林彗星的到訪更讓今年顯得意義非凡。 第一顆本土命名的彗星

事實上，「鹿林彗星」此次造訪太陽系不只受到世界各國矚目，更是國人引以爲傲的「台灣之光」！中央大學天文研究所教授陳文屏表示，「鹿林彗星」是 2007 年 7 月 11 日由鹿林天文台觀測員林啓生及大陸廣州中山大學學生葉泉志，使用鹿林天文台望遠鏡所發現。編號爲 C/2007 N3，經確認後命名爲「鹿林」，成爲第一顆在台灣本土觀測、命名的彗星。

彗星又俗稱「掃把星」，顧名思義，彗星後頭總是拖著長長的尾巴，讓人印象深刻。陳文屏表示，彗星本身是形狀不規則的天體，像哈雷彗星外觀就長得像顆馬鈴薯般。

根據科學家計算，鹿林彗星軌道周期長達數千萬年，甚至可能是雙曲線或拋物線，也有可能是狹長橢圓，而這也意味著這可能是鹿林彗星第一次、也是最後一次進入太陽系，因此，格外受全球天文迷矚目；不只台灣，歐美日等地的天文愛好者引頸期盼它的到來，各國天文學家也展開對鹿林彗星的觀測行動。

爲何天文學家會對觀測彗星這麼感興趣？身爲國際知名天文學者的中央大學天文所教授葉永烜表示，回溯過去歷史，國際有關彗星的科學研究一路走來迄今已有兩百多年的歷史，尤其是 1986 年，俄國與歐洲太空局、日本宇航局等單位分別發射太空船來觀測哈雷彗星，更將彗星研究推向另一個高峰。

一般人可能不知道，其實彗星的形成與太陽系形成的早期非常類似；彗星、地球與太陽系都是同一時期所發展而成的天體，年紀相仿，都是接近 46 億年。

而有別於地球本身的不斷變化，葉永烜表示，由於彗星的星體小，加上一直維持在低溫狀態，因此仍然保留了當初生成時的原始元素，如碳、氰等成分，就像時空膠囊一樣。而這項特點也成爲天文學家在探索宇宙源起與天體生成時的有力依據。透過探索彗星的結構、化學物質、大小分布、軌道分布的情況，可以幫助現代科學家了解地球，以及太陽系的過去發展脈絡。

因爲這個特點，也讓陳文屏忍不住幽默表示，鹿林彗星此次造訪太陽系就如同是「少小離家老大回」，在闊別多年後，才回來看看當初一起同時間誕生的老朋友。鹿林彗星接近太陽系時，其所含的氰會直接昇華爲鮮綠氣體，因此照片所拍攝到的都是帶著綠光的天體。

研究彗星有助探索未來

不只「了解過去」，彗星研究也有助於我們「探索未來」。不少科技電影常以「彗星撞地球」爲題材，讓許多看過的民眾忍不住好奇究竟彗星會不會真的有一天撞上地球？對此，葉永烜表示，答案是可能的！

葉永烜說，地球過去也曾遭受許多天體撞擊過，因此難保彗星會不會有一天真的跑來撞地球。這也是爲什麼科學家希望多了解彗星天體結構與運行軌道的原因所在，目地就是希

望能早日發現可能的危機，即時作出因應與對策。像是台灣天文學界參與的「泛星計畫」，目標之一就是在搜索對地球有碰撞威脅性的小行星和彗星，讓「地球人」可以提早「未雨綢繆」。

原文轉載自【2009-02-27/人間福報/13 版/遇見科學】

鹿林彗星歷經2850萬年重返地球　天象奇觀不間斷

【北京晚報 周健森 責任編輯：劉鎏】

守望鹿林彗星之夜

今年是世界天文年天象盛事將持續全年

當人們沉浸于夢鄉的時候，他們正在城市以外的某個角落，專注地仰望天空；他們可以牢牢地記住每個星座的名字，並且滔滔不絕地告訴你這其中的來龍去脈。每當有天象奇觀出現，他們便會爲之激動，因爲那一天註定會成爲他們的節日。他們是一群天文愛好者，他們是真正的追星族。

最近一週是北京觀測鹿林彗星的最佳時期，本報記者前晚與北京巡天會的會員們前往平谷金海湖，見證了他們如何守望這顆散發綠色光芒的美麗星體。

出發

從“哈雷”到“鹿林”

晚 8 時剛過，三元大廈樓下。當 33 歲的王震石驅車趕過來時，何景陽和另外幾個朋友已經在此等候多時。“今天晚上應該不錯。”何景陽抬頭看了看漸顯的夜色，“城堹酮揝ㄣX顆星星就不容易了。”

正是下班時間，站在行色匆匆的人流中，他們看上去並不出眾，但是在北京天文愛好者的圈子堹 A 何景陽和王震石都算是頗有名氣的人物。他們都是北京巡天會的會員，這個民間自發的天文愛好者組織挂靠于北京天文學會名下；追溯淵源，他們都曾參加過東城區青少年科技館天文組。

1986 年，光臨地球的哈雷彗星暗淡得幾乎看不到，但是卻足以照亮王震石與何景陽的興趣。20 多年後，他們從小學生變成了公務員、貿易公司白領，是當初那批天文愛好者中爲數不多堅持下來的。

1997 年 3 月海爾-波普彗星回歸，北京巡天會第一次集體行動。何景陽用相機拍攝下一幅彗星的照片：“兩條彗尾看上去非常壯觀，用肉眼看上去漂亮極了！”雖然那張照片不算完美，但是王震石至今仍保留在自己的手機堹 C

昨晚的目標是鹿林彗星，這是由海峽兩岸共同發現的第一顆彗星。湊巧的是，作爲發現者之一的台灣“中央大學”鹿林天文臺觀測員林啓生，正是巡天會的老朋友。王震石貼在巡天會網上論壇堛漱@幅鹿林彗星照片，就是林啓生親自拍攝並通過電子郵件發送過來的。

波折

險些錯過觀測

出發沿京平高速一路前行，燈火輝煌的城市漸漸甩在身後，除了路燈燈光，車窗外遠處已是一片黑暗。何景陽已經習慣了這種黑暗：“天文觀測最容易受到的干擾，一是天氣，二是光害。”他們觀測天象時都會選擇懷柔、密雲、興隆等人口稀少的地方。

抵達平谷金海湖岸邊的一處觀景臺時，已近晚 9 時 40 分。一下車就有人興奮地叫喊起來。抬頭仰望，星辰漫天密布，久居城市的人們恐怕早已忘記了這樣的景象。有人掏出鐳射指星筆，熟練地指點起獵戶、雙子、獅子座等星座。王震石則調出安裝在手機堛漪 P 空圖軟體，開始和夥伴們調試天文望遠鏡。

這群發燒友級的天文愛好者，手中的裝備全部價格不菲。一部日本產天文望遠鏡的價格，據說得 4 萬元人民幣以上，“是會員堛漱@個‘大款’捐的”；另一部天文望遠鏡和天文攝影用的專業赤道儀，也是身價數萬的傢夥，都是會員們湊起來購買的，而平時活動的費用，則由參加活動的會員平攤。

鹿林彗星位於東方，此時東南方向的一抹淡淡的雲霧令王震石緊張起來。上週六在懷柔，王震石和夥伴就因爲雲塊遮擋未能觀測到鹿林彗星，他擔心今晚又要重蹈覆轍。幾分鐘後，雲霧漸漸散去，他才放下心來。

目擊

肉眼難以分辨

因爲自身化學成分而呈現綠色，鹿林彗星又被許多媒體稱爲“綠色彗星”。此時鹿林彗星亮度可以達到 4 至 5 等星，正是最佳觀測時期，不少媒體都聲稱用肉眼就能欣賞到它。

然而即使來到遠郊，用肉眼仍難以將鹿林彗星辨認出來，記者通過天文望遠鏡只能隱約看到一個淡灰色棉花狀的光團。王震石說，只有通過照相機長時間曝光拍攝，才能真正看到它綠色的本來面目。不過面對這顆歷經 2850 萬年才重返地球的彗星，這樣的景象已屬彌足珍貴。

鹿林彗星的另一位發現者是廣州中山大學本科生葉泉志，他也是一位天文愛好者。何景陽說，發現彗星的方法行話叫做“尋彗”，是一項非常艱苦的專業工作。巡天會很少組織這樣的技術活兒，大家更享受欣賞星空的過程。

計劃

組織“路邊天文”

從 20 多年前的哈雷彗星之夜到眼前的鹿林彗星之夜，這些追星族仍然說不清自己爲何著迷于星空。“也許是小時候探索宇宙奧秘的那點兒野心還沒丟掉吧。”一位會員半開玩笑地說，“越看星空就越會覺得好奇，想要看得再近些。”

巡天會當初開始活動時，多數人只是 20 歲出頭，如今有人已經四十不惑。用王震石的話說，“越來越老啦”。他的師兄老邵提起這事兒有些激動：“小孩兒都喜歡去天文館看星星，可是等他們大了，有幾個還能留下來？都去學英語、搞奧數、彈鋼琴了，覺得天文這個愛好沒用！”

王震石希望能有更多的人加入進來。他說，等到天氣暖和的時候，巡天會打算組織“路邊天文”活動，把天文望遠鏡支在大街上，誰感興趣都可以來看，他最希望能讓小孩子們從中體會到追星的樂趣。

晚 10 時 40 分，夜色漸深，山風吹得人瑟瑟發抖。巡天會的會員們仍舊沒有去意。“其實我們明天都要去上班，但是今天晚上一定要把鹿林彗星拍下來，”何景陽說，“拍到我們滿意爲止，大概要一兩點鐘才能完活。”

第二天早晨一睜眼，這些追星族又成了穿梭在城市中的上班族，只是每個人都懷揣著一個有關星星的夢。

今年是世界天文年，告別美麗的鹿林彗星之後，年內仍將有大量的天文奇觀上演：■3 月 8 日：土星衝日。■7 月 7 日：半影月食。■7 月 22 日：日全食。■8 月 6 日：半影月食。■8 月 14 日：木星衝日。■8 月 17 日：海王星衝日。■9 月 17 日：天王星衝日。■10 月 13 日：金星合土星。■12 月 31 日：月偏食。

原文轉載自【2009-02-27/中國經濟網>新聞中心>國內時政】

星迷開趴　賞鹿林彗星

【陳方瑩／南投報導】

爲慶祝台灣人發現並命名的第一顆彗星「鹿林彗星」靠近地球，一群熱愛天文愛好者昨凌晨聚集在玉山國家公園塔塔加停車場辦星空派對，躺在星空下喝紅酒賞星，好不浪漫。謝長廷：很漂亮

「鹿林彗星」發現者林啓生，前天晚上號召四十多名天文熱愛者，聚集在海拔二千七百公尺的塔塔加舉辦星空派對，各式各樣專業天文望遠鏡一字排開，配合數位相機，徹夜捕捉彗星的軌跡。

林啓生說，今年一月至四月是「鹿林彗星」最佳觀賞期，二月下旬利用雙筒或小型望遠鏡就可觀賞，二月二十四日雖是「鹿林彗星」最接近地球的時間，因當天雲層太厚看不到才改期。

昨天凌晨零時過後，雲層散盡，天空星光閃閃，天文愛好者除了用天文器材觀星拍照，也在星空下品嘗紅酒，清晨還可從東方看到閃耀的銀河光芒。

星迷一族的行政院前院長謝長廷，前天晚上也跟妻子上山賞星，但避談政治議題。他說，曾多次到高雄市港和國小天文台看星星，但因光害看不到，才到深山來拜訪彗星，在林啓生引介下，如願看到「鹿林彗星」，還有他的星座「雙子星」，真的很漂亮。

原文轉載自【2009-03-02/蘋果日報/A13 版/生活】

鹿林彗星 2 日後　永遠消失地球視線

據新華社報道，「鹿林」彗星上月 24 日最接近地球。天文專家表示，目前，鹿林彗星正從獅子座向巨蟹座運行，作爲一顆非周期彗星，後日（5 日）後它將永遠脫離地球「視線」。

廣州中山大學本科生葉泉志，於 07 年 7 月 11 日，與台灣「中央大學」天文研究所鹿林天文台的觀測助理林啓生共同發現鹿林彗星。

原文轉載自【2009-03-03/蘋果動新聞】

“鹿林”彗星 3 月 5 日後將永遠離開地球“視線”

【記者周潤健、蔡玉高】

２００９年上半年已知最亮的彗星“鹿林”２月２４日飛到離地球最近的地方。連日來，我國不少公眾都欣賞到了“鹿林”彗星的絕世風採。

天文專家表示，目前，“鹿林”彗星正從獅子座向巨蟹座運行，作爲一顆非周期彗星，３月５日後它將永遠脫離地球“視線”。因此，有興趣的公眾要抓緊這兩天欣賞，用最美好的祝福送它一程。

“鹿林”彗星是近年來由我國業余天文愛好者參與發現的３顆彗星之一。該彗星由廣州中山大學本科生葉泉志和臺灣“中央大學”天文研究所鹿林天文臺的觀測助理林啓生合作，于２００７年７月１１日發現。

天津市天文愛好者馬強等人連日來多次通過望遠鏡對“鹿林”彗星進行了觀測。他告訴記者，鏡頭塌滿妊尷L”彗星非常漂亮，散發著綠色的光芒，倣佛一大塊璀璨的寶石。

記者登錄同好、牧夫、天之星等國內知名天文網站發現，“鹿林”彗星成爲近期的“主角”，吉林長春、河北、內蒙古、山東、福建、廣東等地的一些天文愛好者紛紛將各自的觀測和拍攝情況“曬”出來與大家分享。

有報道說，下次“鹿林”彗星再次光臨地球需要等２５８０萬年。對此，天文專家表示，“鹿林”彗星是一顆非周期彗星，它沒有準確的回歸時間，可以說，此次一別就是永別。

如何尋找“鹿林”彗星“最後的身影”呢？天文專家提醒說，公眾先尋找到獅子座，獅子座中最亮甯Ｐ軒轅十四的西南方，就是正在緩慢移動的“鹿林”彗星。用大口徑雙筒望遠鏡不難找到，但要注意避開城市光害。

原文轉載自【2009-03-03/新華網】

天文 100 小時　今夜，星空辦網趴

【記者楊正敏台北報導】

今天晚上犧牲一下睡眠，守在電腦前就能一窺台灣的星空之美。中央大學鹿林天文台將在今晚六時到明日上午六時進行星空觀測網路直播，透過鹿林天文台的專業望遠鏡，就能與全球一起來場夜未眠的天文網「趴」。

全球天文年活動之一「天文一百小時」活動即日登場，超過八十個世界級的大型天文望遠鏡馬拉松接力進行天文觀測網路直播。許多知名天文台，與太空上的哈伯、史匹茲（Spitzer）與錢卓（Chandra）等太空望遠鏡將以接力轉播觀測畫面，難得一見。

直播的十二小時中，除了星空觀測直播外，還有國內天文專家同步解說，也會有小遊戲，每個小時還有抽獎活動。

這次直播活動登錄在全球天文年的官方網站，和世界其他的天文慶典一同呈現。

●想了解全球八十支望遠鏡的接力觀測，可上網：
http://www.100hoursofastronomy.org/

或全球華語網路直播天文頻道：
http://webcast.ltes.cy.edu.tw/ch-astruo/

●鹿林天文台觀測直播網址：
http://www.atlaspost.com/groups/starry99

原文轉載自【2009-04-04/聯合報/A6 版/生活】

「沈君山」小行星　3 年前發現　台灣目前看不到

【郭淑敏台北報導】

鹿林天文台台長林宏欽表示，已被命名爲「沈君山」的小行星，是於二〇〇六年四月十八日被發現。這顆小行星目前距離地球約七億公里，它與地球一樣，同是繞著太陽轉，白天在太陽附近，與太陽同時升起與落下，所以目前在台灣看不到這顆小行星。

林宏欽表示，大部分的小行星分布在小行星帶，它們軌道介於木星與火星之間，屬於太陽系的一部分，都是繞著太陽轉。

林宏欽強調，當我們不斷找到小行星後，可以對太陽系的組成有更多的了解；其次，確認小行星的運行軌道，也有助於了解它對地球是否存在威脅。鹿林天文台預計在未來十年內，會有將近二百顆小行星由台灣來命名。而「沈君山」小行星則是鹿林天文台發現並且命名的第十三顆小行星。

林宏欽說，中央大學鹿林天文台從二〇〇六年開始尋找小行星，到目前爲止，已陸續找到了八百多顆，發現小行星後，必須先做軌道確認，通常這道程序需歷時多年，之後才能開始進行命名。

這顆永久編號爲二〇二六〇五小行星在經過軌道確認後，發現者有權將其提交國際天文學聯合會（ＩＡＵ）下命名委員會進行命名工作。發現者每次可以提交兩顆小行星進行命名，命名委員會每二個月開會審查。

除了政治、軍事與商業有關的名稱之外，命名委員會通常不會否決發現者所建議的名稱。林宏欽透露，政治人物除非死後一百年，不然不可能被命名；還有命名委員會曾經否決小行星被命名爲ＹＡＨＯＯ，因爲要避免出現任何商業利益的爭議。

原文轉載自【2009-05-09/中國時報/A3 版/焦點新聞】

天文研究最高榮耀　小行星命名「沈君山」

【陳至中台北報導】

浩瀚宇宙中將有一顆「沈君山」小行星！中央大學鹿林天文台決定，以前清華大學校長、天文物理學家沈君山命名最新發現的小行星，理由爲「帶動一代人對天文學的興趣」。不過現年七十六歲的沈君山，兩年前三度中風後、至今昏迷不醒，無從得知該消息。

編號二〇二六〇五的小行星，於九十五年由中央大學天文所楊庭彰及中國中山大學葉泉志共同發現，九十八年四月九日正式命名爲「沈君山」（Shenchunshan）；五月廿三日天文學會在墾丁舉行年會，同時在當天舉行「贈星儀式」。

中大鹿林天文台台長林宏欽表示，按照國際慣例，發現者擁有命名權，中大決定將之命名爲「沈君山」，是爲了表彰其對天文學的貢獻。在這之前，中大曾以台達電創辦人鄭崇華、英業達集團總裁溫世仁等命名小行星。

沈君山畢業於台大物理系，隨後赴美，於馬里蘭大學取得物理博士學位，先後在普林斯頓大學、美國太空總署和普度大學歷練。回國後，寫作《天文新語》及《天文漫說》二書，影響國內天文學界極深。中大天文所教授葉永烜表示，沈君山以一根禿筆，影響一代的天文學研究，在台灣很多人，都是因爲看了他的書，選擇投入天文學研究。

葉永烜表示，沈君山對台灣的貢獻是「衝擊性」的，中大只是在天上發現一些石頭，拿來做文章「沾沾光」。中大鹿林天文台近來發現的小行星，都盡量以和本土有關的名字命名，例如去年命名的「鄒族」小行星，即是表彰原住民的精神。

清大歷史系教授、中研院院士黃一農表示，沈君山的成就不僅在科學，他的文筆極好，將天文學以「極漂亮」的文字作介紹，門外漢都看得懂。他也曾在華視製作科普節目，對啓迪台灣學生對天文的興趣貢獻極大，黃一農當時即在其麾下擔任助教。

黃一農表示，中大告知小行星命名一事後，家人已在沈君

山的耳邊告知，但他昏迷不醒、無從答覆。不過黃一農說，就他對沈君山的認識，沈君山一定非常高興，必將視爲人生中的最高榮耀之一。

「沈君山」爲第二顆以清大校長命名的小行星，在此之前還有「徐遐生」。其他以華人命名的小行星，包括「林青霞」、「金庸」、「溫世仁」。而中大鹿林天文台發現的小行星，多以地名命名，包括「中大」、「南投」、「嘉義」、「鹿林」等。（相關新聞刊Ａ３）

原文轉載自【2009-05-09/中國時報/A1 版/要聞】

建造鹿林２米望遠鏡 募款不順利 葉永烜賣畫籌錢

【李宗祐台北報導】

中央大學天文研究所教授葉永烜近年爲籌措經費在鹿林天文台建造兩米口徑望遠鏡，備極艱辛，又碰到金融海嘯，募款更困難。但葉永烜樂觀地說，募款不順並不會讓他感到挫折。

鹿林天文台兩米望遠鏡建造計畫在二○○六年啓動，教育部補助九千六百萬元，其餘六千萬元由中央大學自行籌募。去年完成工程設計、準備募款時，遭逢金融風暴。

葉永烜說，在六千萬元自籌款還沒募齊之前，中央決定先從校務基金墊付，暫時不影響望遠鏡建造進度。在鹿林天文台建造兩米望遠鏡，是東亞最大望遠鏡之一，但這僅是表徵意義，最重要的是，我國可以透過這個觀測平台，培育優秀天文科學人才。

葉永烜在研究和教學之外鑽研油畫創作，還開過畫展，爲爭取捐款，他拾起畫筆以玉山和鹿林天文台爲主題創作兩幅油畫，再捐出兩幅夏荷義賣，卻還是激不起回響。葉永烜說：「現在只希望金融海嘯趕快過去。」

原文轉載自【2009-06-09/中國時報/A6 版/生活】

新發現小行星 中央大學命名「玉山」

【本報訊】

世界新七大奇景網路票選進入第二階段，就在國人持續爲玉山催票衝刺，希望能擠進前 28 強的同時，中央大學今天也特別將新發現的編號 185546 小行星命名爲「Yushan」，希望能增加玉山在國際上的曝光度。

在玉山設立「鹿林天文台」的中央大學表示，今天發現新的小行星標號 185546，既然是在玉山發現，也希望增加玉山的曝光度，特地將這顆小行星命名爲「Yushan」，成爲全球第一顆以台灣高山爲名的小行星，讓玉山同時在地面與太空揚名全球。

原文轉載自【2009-07-14/自由電子報 即時新聞】

小行星命名「玉山」 彰顯台灣獨特觀測條件

【陳奕華報導】

第一顆以台灣高山命名的小行星正式誕生，中央大學經國際天文學會(IAU)通過，把 2007 年 12 月 28 號發現的小行星，正式命名爲「玉山」(Yushan)，彰顯玉山在台灣獨特的象徵意義，以及台灣國內天文研究上獨一無二的觀測條件

玉山是台灣的聖山，海拔 3952 公尺，海拔高、緯度低又接近赤道，空氣清新無污染，非常適合天文觀測。

中央大學副校長劉振榮表示，中央大學從民國 78 年開始籌設的鹿林天文台，在三年多前開始有計畫觀測小行星，短時間內獲得豐富成果。

「我們在 2006 年 3 月啓動了一個『鹿林巡天計畫』，這個巡天計畫啓動之後，其實在短短幾年內，我們大概有近八百顆的小行星被我們發現，全世界是很少見的，所以我們也成爲世界上發現小行星最活躍的一個地區。」

軌道介在火星與木星之間的玉山小行星，目前位置在天秤座，距離地球約 3 億公里，研究團隊預估大小與玉山差不多，不過詳細資訊還要持續觀測分析確認，亮度是在 20 星等左右，一般民眾就算攀登上玉山頂峰，也不容易用肉眼看見，需要專業望遠鏡。

這次以玉山小行星定名，得到小行星中心給予的永久編號爲 185546，也代表永恆見證台灣天文成就與自然生態的永續發展，尤其目前玉山正在爭取成爲世界新七大奇景，玉管處也呼籲國人支持台灣聖山，讓玉山在地球與宇宙發光。

原文轉載自【2009-07-14/中廣新聞網】

亞洲最活躍 鹿林天文台 發現 800 顆小行星

【記者黃玉芳/台北報導】

在玉山上的「鹿林天文台」，讓台灣成爲亞洲發現小行星最活躍的地方，迄今累計發現近 800 顆。

中央大學天文所長黃崇源表示，小行星就是未形成的行星，除了透過觀測等數據收集，未來太空船降落在小行星，可進一步瞭解如地球、火星等行星的原始狀態與形成之謎。

所有的小行星命名，須報經國際小行星中心和小行星命名委員會審議通過後，才公諸於世，成爲該天體的永久名字，並爲世界各國公認。

台灣發現的近 800 顆小行星中，有 9 顆已取得正式編號和命名，分別名爲「鹿林」、「溫世仁」、「鄒族」、「沈君山」、「玉山」等。

中央大學也透過鹿林天文台參與多項重要的國際天文計畫，例如和美國夏威夷大學合作泛星計畫(Pan-STARRS)，搜尋及發現在太空中運行、可能撞上地球的小行星或彗星。

原文轉載自【2009-07-14/聯合晚報/A7 版/焦點】

台灣中央大學發現小行星　命名玉山

【中央社記者謝佳珍台北 14 日電】

台灣中央大學今天表示，2007 年底發現的編號 185546 號小行星，經國際天文學聯合會通過，正式命名爲「玉山（Yushan）」，成爲第一顆以台灣高山爲名的小行星。

玉山國家公園管理處、中央大學今天舉行「玉山小行星」命名記者會，除宣布小行星命名玉山外，也呼籲全民支持玉山競選世界新七大奇景活動。

中央大學副校長劉振榮表示，玉山小行星是 2007 年 12 月 28 日，由中央大學鹿林天文台觀測助理林啓生與大陸廣州中山大學葉泉志以 41 公分的望遠鏡所發現，國際編號爲 185546。

中央大學天文所所長黃崇源說，今年 4 月向國際天文學聯合會送件，將小行星命名爲玉山，6 月正式核准；玉山小行星軌道位於火星與木星之間，以亮度、距離推估，大小與玉山差不多，直徑約 4 公里。

出席記者會的內政部長廖了以表示，天上有顆玉山小行星，地上有座玉山，兩者連結在一起，相互呼應；營建署長葉世文則說，玉山與台灣密不可分，玉山讓台灣走向國際，他深受感動。

另外，玉山在新七大自然奇景票選活動中順利晉級，將繼續往專家評選階段挺進，爭取進入前 28 名，葉世文與玉管處長陳隆陞都希望全民繼續努力，將玉山推向國際。

中央大學鹿林天文台設立於 1999 年，地點位在海拔 2862 公尺的鹿林前山，2002 年發現第一顆小行星，迄今累計發現近 800 顆，其中有 9 顆已取得正式命名，分別爲鹿林、中大、嘉義、鄭崇華、溫世仁、鄒族、南投、沈君山、玉山。

原文轉載自【2009-07-14/大紀元】

彰顯天文貢獻　小行星命名「玉山」

【李宗祐台北報導】

中央大學在玉山山系進行的「鹿林巡天計畫」，陸續發現近八百顆小行星。爲彰顯玉山對台灣天文研究的重要意義，中央大學昨日宣布，二〇〇七年底發現、編號一八五五四六號的小行星命名「玉山」，成爲首顆以台灣高山命名的小行星。

積極推動玉山參與瑞士新七大奇景基金會「新世界七大自然景觀」全球票選活動的內政部長廖了以昨日也出席「玉山」小行星命名記者會，呼籲國人繼續支持玉山進入最後廿八個決選名單，讓「玉山」在天地之間相互輝映，「星星恆永遠、玉山永留傳」。

鹿林巡天計畫　發現近八百顆小行星

營建署長葉世文補充說，「天上多了一個星星，讓我們更有信心，玉山在這個月底一定會進入前廿八名。」

「玉山」小行星於二〇〇七年十二月廿八日由鹿林天文台觀測助理林啓生和廣州中山大學學生葉泉志合作發現，經國際天文學聯合會確認後，由中央和中山大學取得編號及命名權。

中央大學副校長劉振榮指出，「鹿林巡天計畫」從二〇〇六年三月啓動，已陸續發現八百顆小行星，成爲亞洲發現小行星最活躍的地方，爲彰顯玉山對國內天文研究的重要性，「我們決定把編號一八五五四六號小行星命名爲玉山，一提出去，很快就獲得認可！」

爭取新七大奇景　多顆星造勢加把勁

中央天文研究所長黃崇源表示，小行星命名如果與政治或戰爭行爲相關，或涉及商業行爲都會被駁回，玉山命名在今年四月向國際天文學聯合會遞件，六月即通過命名審查。

玉山國家公園管理處長陳隆陞透露，中央大學原本計畫六月廿五舉行「玉山」小行星命名記者會，爲玉山角逐「新世界七大自然景觀」加油造勢。但當時玉山的網路選票已衝到第一名，爲保留實力，玉管處協商中央把記者會延到昨天，「希望透過『玉山』小行星命名經過國際認證的過程，讓學者專家組成的新七大第二階段評選委員更了解玉山。」

原文轉載自【2009-07-15/中國時報/A8 版/生活】

中央大學發現小行星命名玉山

【記者潘昱帆／綜合報導】

內政部營建署玉山國家公園管理處日昨表示，玉山國家公園爲台灣天文研究發展的搖籃，其海拔高、緯度低、接近赤道，空氣清新無污染，非常適合天文觀測。民國七十八年國立中央大學於本園鹿林前山設置天文觀測點迄今，已發現近千顆小行星，並有多顆獲得國際天文學界認可擁有命名權。

爲彰顯台灣卓越之國際天文研究能力，以及玉山地區獨特的天文景象，本次中央大學應玉管處所請，將二〇〇七年十二月二十八日於鹿林天文台所發現的一八五五四六號小行星，以台灣地標與精神象徵意義的「玉山」命名，更於二〇〇九年六月七日經國際天文學聯合會小天體命名委員會通過，正式命名爲「玉山 Yushan」——首顆以台灣高山命名的小行星。

玉管處指出，玉山爲台灣的聖山，海拔三,九五二公尺，爲台灣中央山脈最高峰，由玉山主峰、北峰、東峰等 11 連峰構成玉山群峰。亦爲冠絕東北亞，睥睨雲天，誠爲斯土斯民堅毅卓絕的精神象徵，及以豐富的生態、奇特的地形著稱。今年的大學指考，英文科翻譯正以玉山爲題，更增添玉山在

全體國民心中的重要性。

時值玉山爭取瑞士新七大奇景基金會（N7W）舉辦的「世界新七大自然奇景」活動，經全世界公民長達四個月的全球網路票選，一直穩居山岳類之首，目前已順利晉級前七十七名。該基金會將再由專家選出二十八個入圍名單進入決賽，並於二〇一一年公布最後的結果。玉管處期望藉由玉山小行星的命名，突顯玉山獨特的天文景象，增強評審專家對玉山的瞭解與認同。同時也呼籲全民團結一致，以代表台灣的玉山參選世界新七大奇景，躍向國際，在宇宙間永垂不朽。

原文轉載自【2009-07-19/台灣新生報/11 版/人物・采風】

發現小行星！　以高雄命名

【記者徐如宜/高雄報導】

台灣業餘天文愛好者蔡元生與團隊，今年 3 月 20 日發現的臨時編號為 2009 X18 的小行星，經國際天文學聯合會小天體命名委員會審核，最後命名為「高雄小行星，蔡元生今天將「高雄小行星」的模型，贈送給高雄市長陳菊。

蔡元生與中央大學天文所長黃崇源，共同申請了臺灣中央大學鹿林天文臺的天體搜尋計畫，「高雄小行星」便是在此計畫中所發現。今年 3 月 20 日由蔡元生組成「天體搜尋團隊」，與中央大學鹿林天文臺觀測助理林啓生，共同使用鹿林天文臺口徑 41 公分的望遠鏡與天文專用數位影像，發現了新天體。

蔡元生表示，為了紀念自己土生土長的故鄉高雄，及高雄市成功舉辦的 2009 世界運動會，於是他將已發現的 13 顆小行星中，第一顆得到 IAU CSBN 永久編號的星體命名為「高雄」，並希望能將此榮耀與全體的高雄市民共同分享。

陳菊很肯定蔡元生及團隊的努力與用心，代表全體高雄市民，接受蔡元生致贈其所發現並命名的「高雄小行星」立體模型。她表示，不論是專業的天文學家或業餘的天文愛好者，發現新的星體是大家夢寐以求的心願，此次「高雄小行星」的發現與命名，不但是高雄之光，也是台灣之光。

「多抬頭看星星吧！」蔡元生給想觀星的孩子一個建議，市區雖然有光害，但還是看得到星星，只要用心觀察，就能感受到星星的美好。

目前台灣發現並命名的小行星，包含鹿林、玉山、高雄等 12 顆。蔡元生表示，雖然此次小行星中心公布的「高雄小行星」發現者為蔡元生(Tsai, Y.-S.)與林啓生(Lin, C.-S.)兩人，但這次的發現屬於團隊的功勞，每個參與者都有其不可替代的重要性與貢獻。

原文轉載自【2009-10-19/聯合晚報/A8 版/生活】

台發現小行星命名「高雄」

【大公報訊】

據中央社高雄十九日消息：高雄市業餘天文愛好者蔡元生發現一顆新的小行星，命名「高雄」，並獲國際天文界承認。

「高雄」是第一顆由台灣業餘天文愛好者發現並命名的小行星。蔡元生說，為紀念故鄉高雄，於是將連月來已發現的十三顆小行星中，第一顆得到國際天文學聯合會小天體命名委員會（IAU CSBN）永久編號的星體命名為「高雄」（Kaohsiung）。

蔡元生長期與台灣中央大學天文所長黃崇源合作，進行中央大學鹿林天文台天體搜尋計劃。蔡元生另與三名中國大陸天文網友同好共同組成「天體搜尋團隊」全力投入這項計劃，四人正於新疆烏魯木齊共同籌建一座大型天文台。

蔡元生今年三月二十日與鹿林天文台觀測助理林啓生，共同以鹿林天文台的天文望遠鏡與天文專用數碼影像擷取設備。他們在火星與木星間發現一顆小行星，約與高雄機場同大。近日點距離約三點五億公里，遠日點距離約四點五億公里，繞太陽公轉一圈約四年。

蔡元生說，他當時發現小行星與地球一樣會自轉，也繞著太陽公轉，每天座標位置都不一樣，於是連續拍下照片比對，確認是天文界未曾發現的太陽系小行星。

他指出，目前銀河系的大行星幾乎都已發現，尚待人類探索的行星，大概只剩小行星。由於小行星肉眼無法觀測，就算用大型天文望遠鏡也不易看到，因此得先連續拍照，再比對移動星點座標，觀測行星移動位置。

四十歲的蔡元生就讀中正預校夜間站衛兵時，就經常仰望星空，成為追星族。為了更自由接觸天體，甚至放棄海軍官校學位及日後軍職，一頭栽進天體觀測。他婚後更經常帶妻子及女兒上山觀星。

原文轉載自【2009-10-20/大公網/兩岸->兩岸新聞】

天文愛好者發現小行星　命名高雄

【中央社記者程啓峰高雄 19 日電】

高市業餘天文愛好者蔡元生發現一顆新的小行星，命名「高雄」，並獲國際天文界承認。他今天將小行星模型贈予高雄市長陳菊，希望將「高雄」的榮耀與全體市民分享。

「高雄」是國內第一顆由台灣業餘天文愛好者發現並命名的小行星。蔡元生說，為紀念故鄉高雄，於是將連月來已發現的 13 顆小行星中，第一顆得到（IAU CSBN）永久編號的星體命名為「高雄」。

蔡元生發現「高雄」興奮之餘，希望能與全體高雄市民分享這份榮耀，於是將小行星立體模型送給陳菊。

模型致贈儀式是在高市港和國小舉行。陳菊說，發現新星

體是天文家夢寐以求的心願，「高雄」的發現與命名，不但是高雄之光，也是台灣之光。

蔡元生長期與中央大學天文所長黃崇源合作，進行中央大學鹿林天文台天體搜尋計畫。蔡元生另與 3 名中國大陸天文網友同好共同組成「天體搜尋團隊」全力投入這項計畫，4 人正於新疆烏魯木齊共同籌建一座大型天文台。

蔡元生今年 3 月 20 日與鹿林天文台觀測助理林啓生，共同以鹿林天文台的天文望遠鏡與天文專用數位影像擷取設備。他們在火星與木星間發現一顆小行星，約與高雄機場同大。近日點距離約 3.5 億公里，遠日點距離約 4.5 億公里，繞著太陽公轉一圈約 4 年。

蔡元生將 3 月 20 日發現，臨時編號爲 2009FX18 的小行星，命名爲「高雄」（Kaohsiung）。今年 8 月獲國際天文學聯合會小天體命名委員會（IAU CSBN）審核通過，永久編號爲 215080。

蔡元生說，他當時發現小行星與地球一樣會自轉，也繞著太陽公轉，每天座標位置都不一樣，於是連續拍下照片比對，確認是天文界未曾發現的太陽系小行星。

他指出，目前銀河系的大行星幾乎都已發現，尚待人類探索的行星，大概只剩小行星。由於小行星肉眼無法觀測，就算用大型天文望遠鏡也不易看到，因此得先連續拍照，再比對移動星點座標，觀測行星移動位置。

40 歲的蔡元生就讀中正預校夜間站衛兵時，就經常仰望星空，成爲追星族。爲了更自由接觸天體，甚至放棄海軍官校學位及日後軍職，一頭栽進天體觀測。他婚後更經常帶妻子及女兒上山觀星，皇天不負苦心人，終於讓他找到爲高雄發光的機會。981019

原文轉載自【2009-10-19/中央社/頭條新聞】

12 顆小行星　台灣發現命名

【呂素麗高雄報導】

到目前爲止，在台灣發現並命名的小行星有十二顆，除了高雄，另有以嘉義、南投、台南縣歸仁等地命名的星星。

十二顆小行星全部在中央大學鹿林山天文台觀測發現，除了以地名命名，也有以鹿林、中大爲名的行星；更有以人名命名，如已故英業達電子副董事長溫世仁、台達電董事長鄭崇華、前清大校長沈君山等。鹿林觀測員張敏悌將他發現的小行星以母親「馬碧霞」命名；中央天文研究所專任助理林啓生將他發現的小行星以故鄉命名爲「歸仁」，目前還未正式公開。

其他還有以台灣最高峰「玉山」爲名的小行星，爲中央所命名；另有以阿里山「鄒族」爲名的小行星，相當特別。

原文轉載自【2009-10-20/中國時報/A8 版/生活新聞】